THE APPLICATION OF SYNTHETIC SEISMOGRAMS TO THE INTERPRETATION OF CRUSTAL AND UPPER MANTLE STRUCTURE.

by

James Howard Leven

A thesis submitted for the degree of
Doctor of Philosophy
to the
Australian National University

Research School of Earth Sciences

August 1980.

STATEMENT

This thesis is a description of a research project undertaken during the period January 1977 to July 1980, while I was a full time student in the Research School of Earth Sciences at the Australian National University.

The work described in Chapter 9 was performed in collaboration with Dr. I. Jackson and Prof. A.E. Ringwood. Other than this, the work described in this thesis is entirely my own, except as acknowledged in the text. This thesis has never been submitted to another university or similar institution.

.....

J. H. Leven
July 1980

ACKNOWLEDGEMENTS.

I am indebted to my supervisors, Dr. K.J. Muirhead, and for the first 18 months, Prof. A.L. Hales, for their support and encouragement. I have profited from discussion with many members of Research School of Earth Sciences, and to all these people I wish to express my sincere thanks. The crustal refraction survey would not have been possible without the help of numerous people,and I particularly wish to thank those members of the Coal Industry, together with Dr. J. Webb, Dr. J. Rynn, Mr. S. Hearn, and Mr. T. Richie for their assistance in this respect. Both Mr C. Collins and Dr. J. Rynn provided additional data, and this is gratefully acknowledged.

This project has, of necessity, been oriented around computers and I am grateful for the assistance and facilities provided by the Computer Services Centre. I also wish to thank those associated with the maintenance of the Datacraft computer.

Drs. C.H. Chapman, V.F. Cormier, D.V. Helmberger, R. Kind, P.G. Richards, & R.A. Wiggins provided source copies of the programmes used in this study, and I thank them for the unselfish distribution of these programmes. To the secretaries who have helped me produce this thesis, I am indebted. Mrs. Edna Hopkins undertook the horrific task of correcting the English of this thesis, and for this and the hospitality that she and Lister have extended to me, I express my sincere thanks.

Finally, I wish to thanks my parents for the educational opportunities that they have provided for me.

ABSTRACT

Synthetic seismograms have been applied to the interpretation of crustal and upper mantle velocity structure. An analysis of the data from a crustal refraction survey in Central Queensland has indicated that the Mohorovicic discontinuity in this area possesses a more complicated structure than a first order discontinuity. Re-interpretation of data from the Central Australia Project using the additional constraints provided by synthetic seismograms has led to the postulation of a new velocity model (CAPRI). It is suggested that the low velocity zone beneath the "200 km" discontinuity commences more abruptly than previously inferred. The analysis also suggests that the "400 km" discontinuity is a first order velocity increase, whereas all other upper mantle discontinuities are more satisfactorily modelled by second order velocity structures. The diminutive amplitudes observed on short period retrograde branches have been investigated. It is inferred that a low Q zone above the discontinuity is responsible for this attenuation of the retrograde energy, and mechanisms which may be responsible are reviewed. The "200 km" discontinuity has been found to possess a peculiar structure, and it is suggested that this seismic feature may be the result of the anisotropic alignment of olivine crystals, associated with the decoupling of continents from the underlying mantle.

CONTENTS

FIGURES.

Chapter 7.

Chapter 8.

Chapter 9.

TABLES.

CHAPTER 1

1.1 INTRODUCTION.

The use of synthetic seismograms has become widespread in refraction seismology over the past decade, with synthetic seismograms assuming the role of a routine tool in the interpretation of crustal and upper mantle refraction studies. Several different applications of synthetic seismograms have evolved. These are:- the application to modelling amplitudes of crustal (eg. Kennett, 1977) or upper mantle phases (eg. McMechan, 1979); the application to complete waveform synthesis (eg. Burdick and Helmberger, 1979); and the application to the investigation of special wave propagation effects (eg. Cormier and Richards, 1977; Fuchs and Schulz, 1976).

Several different classes of synthetic seismograms have been developed, each taking a slightly different approach to what is essentially the solution of the wave-equation, subject to various "boundary" and radiation conditions. The problem of how the answers from each of these methods differ in their application to the same problem has recently been investigated by several authors, including Burdick and Orcutt (1979), Cerveny (1979), and Choy et al. (1979). These studies have indicated that there are only minor and generally insignificant differences between the results of the various synthetic techniques, when they are employed within their range of applicability.

Where these differences do occur, they can usually be attributed to the way in which the algorithm for the synthetic seismogram is set up. For routine applications, however, the choice of which method was used, has commonly rested with which technique was locally available.

1.2 SCOPE OF THESIS.

Synthetic seismograms have been applied to the problem of understanding the structure of the crust and upper mantle. Data for the crust and uppermost mantle have been gathered from a crustal refraction profile in Central Queensland, while data used for the study of the upper mantle was from the Central Australia Project conducted by the Research School of Earth Sciences seismology group, under the direction of Professor A.L. Hales.

Chapter 2 reviews the synthetic techniques which have been used in

this study. A simplified outline of the algorithms of the four major methods is given, and some of the assumptions inherent in the use of synthetic seismograms are discussed. Chapter 3 describes the field work, data reduction, and interpretation in terms of ray tracing, of the Central Queensland crustal refraction survey. Chapter 4 describes a time term analysis of the data from these Central Queensland surveys, and two other crustal refraction surveys conducted in this region. Both the Pn and Pg wavegroups have been analysed using the time term method, and the resulting structure is discussed in relation to the known geological structure of the Central Queensland region. Chapter 5 applies synthetic seismograms to selected portions of the Central Queensland crustal data, in order to study the nature of particular wavegroups. The synthetic seismogram techniques employed for this study assume a laterally homogeneous Earth structure, and the region over which the two surveys discussed in Chapter 3 extend is structurally complicated by the presence of the Bowen Basin. The results of the time term analysis have therefore been used to select that portion of this data for which synthetic seismogram modelling is applicable.

Using Full Wave theory, the amplitude of the Pn wavegroup in explosion seismology is investigated in Chapter 6. The importance of non-ray theoretical phenomena is evaluated in the context of the velocity structure associated with the Moho.

In chapter 7, synthetic seismograms are applied to the re-interpretation of the Central Australia Project data. Amplitudes are used to further refine the upper mantle velocity profile beneath northern Australia. Various petrological models of the upper mantle have been discussed in relation to the proposed velocity structure.

If an attempt is made to match amplitudes of recorded short period data with the synthetic seismograms, it becomes apparent that there is a marked discrepancy between the observed amplitudes on the retrograde refraction branches, and those amplitudes predicted by the synthetics. In Chapter 8, this disparity is investigated using synthetic seismograms, and possible explanations in terms of physical mechanisms are discussed.

Chapter 9 looks in detail at the upper mantle seismic feature at about 200 km depth, which is observed under northern Australia, and investigates various explanations of this feature in terms of the petrology of the upper mantle.

Chapter 10 concludes by reviewing the application of synthetic seismograms to crustal and upper mantle refraction studies, and discusses

the future of these interpretational tools in the understanding of Earth structure.

CHAPTER 2

SYNTHETIC SEISMOGRAMS.

2.1 INTRODUCTION.

The relatively recent advent of synthetic seismograms has revolutionized interpretation techniques in seismology. This is paticularly evident in the areas of crustal and upper mantle refraction studies, where synthetic seismograms have become a routine tool in the inverse modelling procedure. Classical interpretation techniques of seismic refraction data have used the travel times of the first onsets (ie, first breaks in the seismic records) to derive the velocity model. This constitutes a very small proportion of the total information contained in a record section, and consequently limits the constraints which may be imposed on the knowledge of the Earth structure. The logical extension is the use of information in the later arrival branches, particularly such information as the form of the retrograde branches and the location of the cusp points of any triplications.

Still further information can be obtained from the amplitudes and waveforms of the seismic arrivals on the various branches. Both these wave characteristics are determined by the velocity structure sampled by the seismic wave, and are particularly influenced by the velocity structure near the turning point of the wave. Although the information about the Earth structure is incorporated in this detailed form of the seismic traces, no inversion technique has yet been devised to directly recover this information. Phinney et al. (1979) have recently advocated the transformation of refraction data into the τ-p domain before comparison with the synthetic data, and this technique holds promise for the future development of a direct inversion method. An advantage of this approach is that it becomes far easier to calculate synthetic seismograms in the τ-p domain. Mellman (1979) is also believed to have approached the direct inversion problem, but his thesis has not been sighted.

It is common practice in refraction studies to construct a velocity model using travel time information. The model is then perturbed by comparing its calculated synthetic response with the original seismic data, thereby iteratively improving the velocity model. Synthetic seismograms play an important role in this procedure, as without their use the

interpretation of seismic refraction data becomes an open-ended process. The synthetic seismograms provide the necessary feedback to ensure a stable convergence of the model to a realization of the actual Earth structure. An example of the benefits arising from more common use of synthetic seismograms in crustal and upper mantle refraction studies is the increased awareness of the necessity of positive velocity gradients in Earth models, rather than first order discontinuities separated by homogeneous layers, in order to more accurately model the amplitude of the prograde branches. In this manner, synthetic seismograms have been responsible for the construction of more realistic Earth models, which ultimately lead to a greater understanding of the Earth.

2.2 DEVELOPMENT OF SYNTHETIC SEISMOGRAMS.

The wave equation in an inhomogeneous isotropic medium, is a coupled second order partial differential equation. The three types of body wave motion (P,SV, and SH) can all be thought of as having an associated wave-equation, but in general these wave equations are coupled together. In a homogeneous medium, the far field wave solutions are effectively uncoupled, and these body waves therefore propagate independently of one another. This suggests that in a weakly inhomogeneous medium, the wave equation may be approximately decoupled. If attention is restricted to the P-SV wave-system in a vertically inhomogeneous medium, then the two coupled wave equations can be uncoupled at the expense of raising the partial differential equation to a fourth order equation (see Pilant, 1979, page 35). Alternatively, the problem of solving fourth order partial differential equations can be avoided by making an asymptotic expansion in terms of the inverse frequency, as at infinite frequency, the wave equations are decoupled.

Richards (1974) has shown that for a vertically inhomogeneous medium having velocity gradients less than 0.0005 km/s/km, the P-SV coupling at periods under one minute amounted to less than 5% of the total displacement. Ansell (1979) has derived expressions for the P-SV coupling for a wave propagating in a general inhomogeneous medium. His analysis demonstrates that the coupling of the P-SV wave types is strongest when the wave is propagating parallel to the direction of maximum velocity gradient, (ie. in a vertically inhomogeneous medium - a vertical ray path).

Most synthetic seismogram methods which deal with an inhomogeneous medium implicitly assume that the P-SV waves in this medium are decoupled;

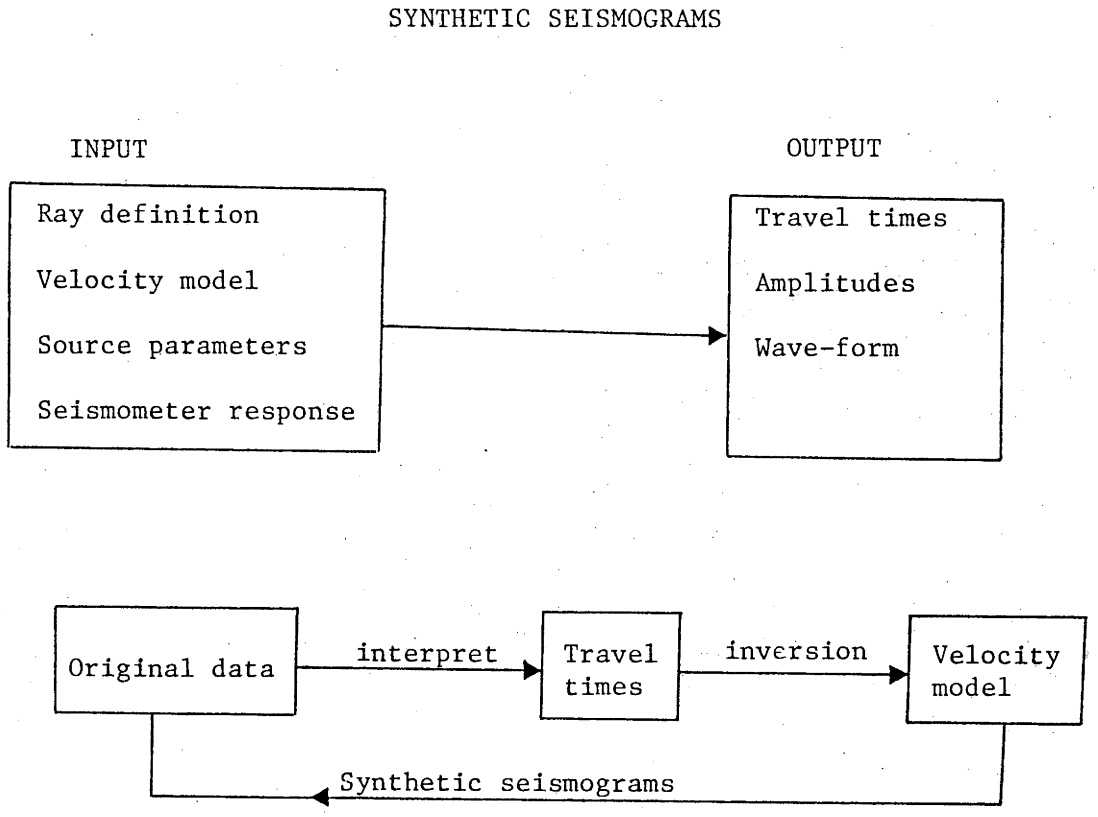

Fig. 2-1. An overview of synthetic seismograms.

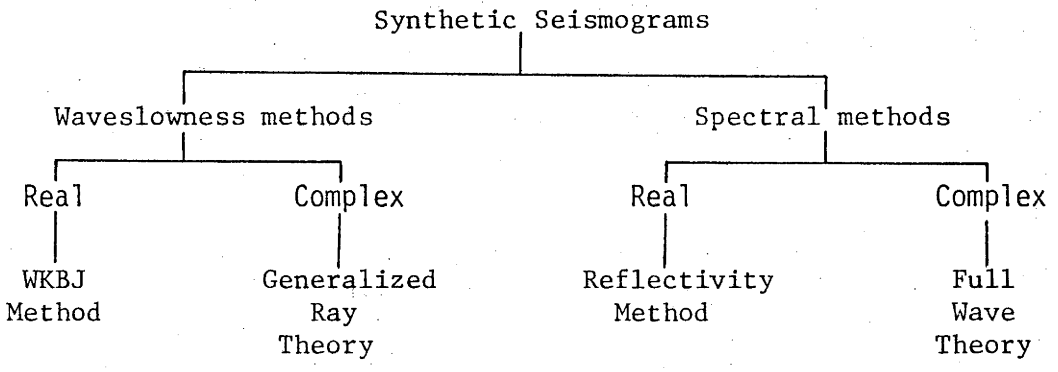

Fig. 2-2. A classification of synthetic seismogram methods; see text for an explanation.

however, this assumption becomes invalid in strong velocity gradients. The implications of this assumption of total decoupling will be discussed in more detail in a later chapter.

Assuming that the wave equation can be decoupled in the medium under consideration, and without loss of generality restricting attention to the P wave motion, the decoupled equation of compressional motion is a second order partial differential equation. To solve this equation two transformations are applied, these being (in general), a transformation from the time to the frequency domain, and from a spacial coordinate into the waveslowness domain (see Grant & West, 1965). The application of these two transformations converts the second order partial differential equation into a second order ordinary differential equation which can be solved by a variety of well known techniques. The appropiate boundary and radiation conditions are applied to this solution, and to complete the generation of the synthetic seismogram the results must then be transformed back into the time-distance domain.

In practice, these inverse transformations are performed numerically, as only in the simplest of cases is it possible to analytically transform the derived solutions. Four alternatives exist as to the manner in which these two inverse transformations may be numerically evaluated, and the four major synthetic seismogram techniques can be classified accordingly. Chapman (1978) has defined two classes of synthetic seismogram methods, namely the spectral and waveslowness methods, depending on whether the waveslowness-to-distance, or frequency-to-time transformation is first applied. These two classes can be further sub-divided, according to whether the contour of the integration involved in the transformation from the waveslowness-to-distance is constrained to lie on the real waveslowness axis. Figure 2-2 shows the four synthetic seismogram techniques categorized on the basis of this classification scheme.

2.3 THE REFLECTIVITY METHOD.

This method of generating synthetic seismograms is based upon a matrix formalism for the calculation of P and S wave reflection/transmission coefficients for a vertical stack of homogeneous layers. The formalism was initially developed by Thompson (1950), and after subsequent simplification and correction by Haskell (1953), it became known as the Thompson-Haskell method. Previous attempts to calculate the total

reflectivity involved the solution of simultaneous equations, and as the number of these simultaneous equations becomes unmanageably large when more than a few layers are considered, it was only possible to analyse simple models using this approach. Knopoff (1964) developed an alternative approach to the Thompson-Haskell method for the calculation of the propagation matrices, and his approach, using subdeterminants, removed a numerical problem inherent in the original Thompson-Haskell formulation. Dunkin (1965) also reformulated the Thompson-Haskel method to remove the numerical loss of precision problem, but used a similar approach to the Thompson-Haskell formalism.

Early applications of the Thompson-Haskell method were restricted to the calculation of surface wave dispersion functions (Haskell, 1953; Harkrider, 1964; Dunkin, 1965). Fuchs (1968) first applied this method to the calculation of body wave synthetics, and in particular to the interpretation of reflected and refracted body waves. Fuchs and Muller (1971) subsequently presented a detailed algorithm for the synthetic seismogram technique which has commonly become known as the Reflectivity method. A brief outline of the algorithm is presented below.

Given a vertical stack of homogeneous layers, the Thompson-Haskell matrix technique enables the calculation of the reflectivity function; i.e. the relative amplitude of the total signal that would be reflected back to the surface from the stack of layers, if a continuous signal of single frequency and angle of incidence was applied at the top of the stack. The angle of incidence is related to the horizontal waveslowness, so the Thompson-Haskell technique gives the solution of the wave equation in the doubly transformed frequency-waveslowness domain, having applied all the relevant boundary conditions appropiate to the interfaces between layers. The calculation of this reflectivity function is a relatively time-consuming process within the algorithm; however, the resulting reflectivity of a particular model is independent of the source - receiver distance, and hence the reflectivity calculations need only be performed once for each frequency and waveslowness considered. An efficient algorithm for the calculation of this reflectivity function in a non-attenuating medium has been published by Kind (1976); this programme uses the delta decomposition of the Thompson-Haskell matrix to avoid the numerical loss of precision problem mentioned above.

For an impulsive point source in a homogeneous layer, the compressional wave potential can be expressed as

$$\phi(r,z,t) = \frac{1}{R}\ \delta\ (t - {}^{R}/_{\alpha}) \qquad (2.1)$$

where $R^2 = r^2 + z^2$. Taking the Fourier transform of this, and using the Sommerfeld integral, we obtain

$$\tilde{\phi}(r,k,\omega) = \int_0^\infty \frac{k}{i\nu_1}\ J_o(kr)\ \exp\ (i\ \nu_1\ z)\ dk \qquad (2.2)$$

where J_o is the Bessel function of zero order, k is the horizontal waveslowness, $\nu_1 = (k_{\alpha_i}^2 - k^2)^{\frac{1}{2}}$, and $k_{\alpha_i} = \omega/\alpha_i$, where α_i is the P wave velocity in the ith layer.

Equation 2.2 gives the compressional wave potential of the source in an infinite medium, in the ω-k domain. The Thompson-Haskell matrix method allows the introduction of interfaces into this formulation, such that the waves from the source interact with these interfaces. This is achieved by multiplying the integrand of equation 2.2 by the reflectivity R_{pp}. Other factors may also be incorporated, and these include the free surface conversion coefficient r_p , and the source spectrum $F(\omega)$, giving

$$\tilde{\phi} = F(\omega) \int_0^\infty \frac{k}{i\nu_1}\ J_o\ (kr)\ R_{pp}\ (\omega,k)\ r_p\ (\omega,k)\ \exp\ (i\ \nu_i\ z)\ dk \qquad (2.3)$$

The above equation involves an indefinite integral. In practice, the significant contribution to this integral is limited to a small range of the waveslowness, corresponding to the range of phase velocities for which arrivals at a particular distance exist. Rayleigh poles (caused by a singularities in the reflectivity function), lie on the real axis (for non-attenuating media), and therefore on the path of integration. However the waveslowness integration is usually terminated at a lower value of the waveslowness than that of these Rayleigh poles, and as the integration is typically performed by trapezoidal quadrature, it is limited to a finite section of the waveslowness domain. The transformation from the frequency domain into the time domain is normally performed by the fast Fourier transform. This also restricts the range of frequencies considered, so that the numerical integration is usually limited to a finite rectangular region within the ω-k plane.

The Thompson-Haskell matrix technique is formulated on the basis of flat homogeneous layers. In order to apply the reflectivity method, the spherical Earth model must be transformed into a model with flat homogeneous layers. An inhomogeneous layer can be approximated by a series of homogeneous layers having varying velocities, and it can be shown that

in the limit, this approaches the inhomogeneous case. To correct for the curvature of a spherical Earth model, an "Earth Flattening Approximation" (EFA) is used. This increases the velocity of the "flat Earth" model at a particular depth, to compensate for the curvature of the spherical model. EFA transformations have been discussed by several authors, including Hill (1972), Chapman (1973), and Muller (1977). Chapman (1973) has shown that although an exact EFA exists for the SH and acoustic cases, no exact EFA can be formulated for the P-SV wave system. Muller (1977) has appealed to geometric arguments to derive the most suitable EFA for the P-SV system.

Linear attenuation can easily be incorporated into the Reflectivity method by allowing the layer velocities to have a small imaginary component corresponding to the Q of the layer. The introduction of attenuation improves the general stability of the Reflectivity method by moving poles further away from the real axis path of integration. Kennett (1975) has discussed the effects of attenuation in the calculation of synthetic seismograms by the Reflectivity method. Significant changes in waveform character and amplitude are realized by the introduction of attenuation (especially low Q layers) into an Earth model. O'Neill and Hill (1979) have investigated the effects of causal absorption in the Reflectivity calculation, but found that dispersion was a relatively unimportant phenomenon in the calculation of upper mantle synthetic seismograms.

Several important extensions of the Reflectivity method have recently been made by Kind (1978,1979). A reformulation of the Thompson-Haskellmatrix method, allowing the source to be located within the reflective zone, has been given by Kind (1978), while the extension of the work of Harkrider (1964) to incorporate a dislocation point source of arbitary orientation into the Reflectivity algorithm has been given by Kind (1979). Some numerical refinements of the Reflectivity algorithm are also discussed by Kind (1979).

2.4 GENERALIZED RAY METHOD.

The theory of the Generalized Ray Method was pioneered by Cagniard (1939), and simplified by de Hoop (1960) and is often referred to as the Cagniard de Hoop method. The technique is a waveslowness method, as the frequency-time transform is evaluated first and the waveslowness transformation is achieved by an integration along a path in the complex ray parameter plane. The synthetic seismogram is computed in the time domain by a convolution procedure.

The method was first applied in exploration geophysics by Spencer (1960), and later utilized in refraction studies by Helmberger (1968) in the interpretation of a marine refraction survey conducted in the Bering Sea. The theory of the Generalized Ray Method has been discussed by many authors, including Cagniard, Dix, and Flynn (1962), Helmberger (1968), Longman (1970), Gilbert and Helmberger (1972), Johnson (1974), Wiggins and Helmberger (1974), and Pao and Gajewski (1977). For the case of two welded semi-infinite homogeneous half spaces, the problem of finding the displacement response of a point source can be solved analytically, (Bath, 1962; Cagniard et al., 1962). Although this serves to demonstrate the method, it is of little practical use, as in this solution the inverse transformation is achieved by analytical manipulations, and these manipulations become intractibly difficult in the case of more complicated models. Recourse must therefore be taken in numerical techniques for handling these more complicated models.

The waves emanating from an explosive source in a homogeneous medium can be theoretically decomposed into plane waves which travel simultaneously at all angles through the source point. Expressing this mathematically, the source function of an explosion at a depth z_o, transposed into the Laplace domain is

$$\phi(x,z,s) = s\int_{-\infty}^{\infty} S(\xi)\, \exp(s[i\xi x - \eta|z-z_o|])d\xi \qquad (2.4)$$

where s is the Laplace variable (complex frequency), S is a function describing the geometry of the source, and η is the vertical slowness, and

$$\eta^2 = \xi^2 + \alpha_i^{-2}$$

The above solution of the wave equation, represents a cylindrical wave with its axis parallel to the Y coordinate at a depth z_o, and having a wavefront expanding with a velocity α_i. When the component plane waves of the above expression impinge on an interface between two media, reflected/refracted P and S waves are generated.

In a multilayered medium, a ray typically undergoes a series of reflections and refractions. Denoting the product of all the relevant coefficients along the constructed generalized raypath as $E(\xi)$, the displacement can be expressed as

$$u(x,z,s) = s^2 \int_{-\infty}^{\infty} S(\xi)\, E(\xi) \exp\{s\, g(x,z,\xi)\}\, d\xi \qquad (2.6)$$

where

$g = i\xi x - \Sigma$ (vertical slowness) x (vertical transit distance)

The function g is seen to have the dimension of time, and if a change of variable is made, such that

$$-t = g(x,z,\xi) \qquad (2.7)$$

so that the inverse function $\xi = g(t)$ is explicitly determined, then the integral becomes equivalent to the Laplace transform of

$$S[\xi(t)]\; E[\xi(t)]\; \frac{d\xi}{dt} \qquad (2.8)$$

and the inverse Laplace transform can be performed by inspection. This is the essence of the Cagniard de Hoop method.

The expression

$$-t = g(x,z,\xi) = -i\xi x - \sum_i z_i \left(\xi^2 - \alpha_i^{-2}\right)^{\frac{1}{2}} \qquad (2.9)$$

(assuming that $\alpha_i > \alpha_{i-1}$, ie. that the velocities increase with depth), maps the ξ plane on to the complex t (time) plane. Branch cuts must be inserted in the ξ plane from the branch points $i\alpha_i^{-1}$, and these conventionally are parallel to the negative real ξ axis. The function $E(\xi)$ may also have simple poles on the imaginary ξ axis, corresponding to "Stoneley type" waves at the various interfaces, and to the Rayleigh wave at the free surface.

The inverse function $g^{-1}(t)$ is evaluated numerically, typically using a Taylor series expansion. If the integration contour of Equation 2.6 is included in a closed path of integration ABCM shown in Figure 2-3, this contour contains no singularities. The integration along the postive real axis may therefore be replaced by the integration along the path AMC, as the contribution along the infinite arc BC (at infinity) is neglible. The path AMC in the ξ domain transforms to the path A'M'C' in the time domain, and this path lies along the real time axis. Using this transformation, the integral of Equation 2.6 can be expressed as

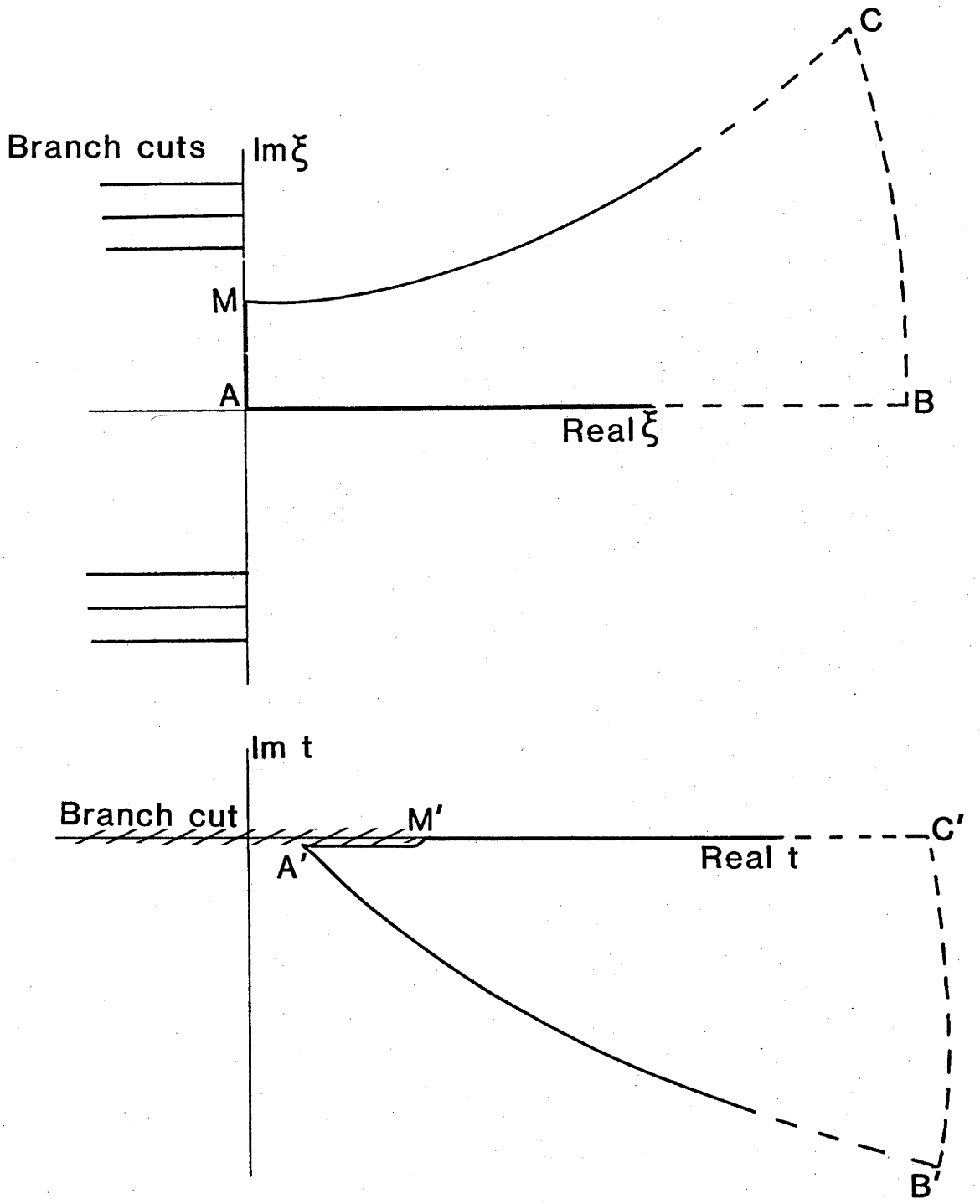

Figure 2.3

The transformation of the contour AMCB from the ξ plane into the time domain.

$$u(s) = \int_0^{t_a} \xi(t)\ E[\xi]\ \frac{d\xi}{dt}\ \exp(-st)dt \qquad (2.10)$$

and the inverse Laplace transformation is given by

$$u(t) = \xi(t)\ E[\xi(t)]\ \frac{d\xi}{dt}\ H(t-t_a) \qquad (2.11)$$

where this expression is evaluated along the contour as specified by the relation of Equation 2.9 .

2.5 WKBJ METHOD.

Wiggins and Madrid (1974) developed a method which empirically approximates the generalized ray theory method, and they called this method Quantitized Ray Theory. Later Wiggins (1976) obtained a similar method by an intuitive argument which he called Disc Ray theory. Chapman (1976a,b) placed the formulation of the general concept of both these methods on a firmer mathematical footing, and more recently Chapman (1978), and Dey Sarkar and Chapman (1978) have outlined the resulting method which they have called the WKBJ technique (which uses, but should not be confused with, the WKBJ technique for solving differential equations).

The WKBJ synthetic seismogram technique is a waveslowness method, in which the frequency-time transformation is performed analytically, and the waveslowness transformation is evaluated along the real axis, typically by trapezoidal quadrature. The intervals of this integration are chosen to be those ranges of the waveslowness which correspond to the ray parameter values for arrivals at the desired epicentral distance.

Following Dey Sarkar and Chapman (1978), the displacement can be expressed as

$$u(t,\Delta,r) = -r\ \frac{d^2}{dt^2} \int_0^{\infty} \{ \sum_{m=-\infty}^{\infty} (-1)^m\ \overset{\vee}{P}(t-P/r-2m\pi,\Delta) * \underset{\sim}{\hat{u}}(t,P,r) \} dp \qquad (2.12)$$

where $\overset{\vee}{P}(t,\Delta)$ is the inverse Fourier transform of $P(\omega,\Delta)$

$$P(t,\Delta) = \frac{1}{\pi} \int_0^{\infty} P_{\omega-\frac{1}{2}}\ (\cos\ \omega t)d\omega$$

$$\approx \frac{\lambda(t-\Delta)}{\pi(2\sin\Delta)^{\frac{1}{2}}}$$

$$\lambda = H(t)t^{-\frac{1}{2}}$$

$$\bar{\lambda} = H(-t)\ (-t)^{-\frac{1}{2}}$$

$$\Lambda(t) = \lambda(t) + i\bar{\lambda}(t)$$

Using this approximation, and considering only those rays which travel less than 180°, ie m=0, we obtain

$$\underset{\sim}{u}(t,\Delta,r) \approx \frac{r^{3/2}}{\pi(2\mathrm{Sin}\Delta)^{\frac{1}{2}}} \frac{d^2}{dt^2}\lambda(t)\int_0^\infty P^{\frac{1}{2}}\ \bar{\underset{\sim}{u}}(t-pr\Delta,p,r)dp \qquad (2.13)$$

where the overbar denotes a Hilbert transform.

Using the high frequency WKBJ approximation for $\bar{\underset{\sim}{u}}(\omega,P,r)$,

$$\bar{\underset{\sim}{u}}(\omega,P,r) \approx \frac{\hat{M}(\omega)\ C(P)\ \exp(i\omega\tau(p)\ )}{r_s^{\frac{1}{2}}\ r^{\frac{3}{2}}\ 4\pi\alpha_s^{\ 2}(\rho_s q_s \rho_r q_r)} \begin{pmatrix} P \\ q_r \end{pmatrix} \qquad (2.14)$$

where $M(\omega)$ is the source spectrum, C(p) is the product of relevant transmission and reflection coefficients. The subscripts s and r refer to source and receiver respectively, $\tau(p)$ is the integrated vertical slowness,

and $P = \dfrac{\xi\ \mathrm{Sin}\ i(\xi)}{r\alpha(\xi)}$ is the horizontal slowness,

and $q = \left(\dfrac{\xi^2}{r^2\alpha^2(\xi)} - P^2(\xi)\right)^{\frac{1}{2}}$ is the vertical slowness.

Using this approximation, and using a rectangular integration technique over those ranges of p for which $t \pm \delta t = pr\Delta + \tau(p)$, we obtain

$$u(t,\Delta,r) \approx -\frac{\ddot{M}(t)}{\pi(2r_s\mathrm{Sin}\Delta)^{\frac{1}{2}}} * \mathrm{Im}\ \left[\Lambda(t) * \sum_{t=\theta} \frac{p^{\frac{1}{2}}C(P)}{4\pi\alpha_s^{\ 2}(\rho_s q_s \rho_r q_r)^{\frac{1}{2}}} \begin{pmatrix} P \\ q_r \end{pmatrix} \frac{1}{|\theta'|}\ \right] \qquad (2.15)$$

In order to implement this formula for the generation of synthetic seismograms, some smoothing of the singularities must be introduced to avoid the numerical difficulties associated with singularities in the time series.

2.6 FULL WAVE THEORY.

The full wave synthetic seismogram technique was pioneered by Scholte (1956), and further developed by Phinney and Alexander (1966), Chapman and Phinney (1972), and Richards (1973). It performs an

integration in the waveslowness domain to transform back into the distance domain first, and allows the contour of this integration to be deformed away from the real waveslowness axis. The potential displacement for a P-SV wave emanating from an explosive source in a spherically symmetrical Earth can be expressed as

$$\underset{\sim}{u}(\omega,r) = \frac{1}{\rho^{\frac{1}{2}}} [\nabla\phi + \nabla \times (0,0 \frac{\partial\chi}{\partial\Delta})] + 0\left(\frac{|\underset{\sim}{u}|}{\omega}\right) \qquad (2.16)$$

where $\underset{\sim}{u}$ is the displacement vector, and ρ and ω are the density and frequency, respectively. The scalar potential functions ϕ and χ satisfy the Helmholtz type equations

$$\begin{aligned} \nabla^2\phi + \left(\frac{\omega}{\alpha}\right)^2 \phi &= K_s\, \delta(r-r_s) + 0\left(\frac{|\underset{\sim}{u}|}{\omega}\right) \\ \nabla^2\chi + \left(\frac{\omega}{\beta}\right)^2 \chi &= 0 + 0\left(\frac{|\underset{\sim}{u}|}{\omega}\right) \end{aligned} \qquad (2.17)$$

The solution of these Helmholtz equations is found by the application of the separation of variables technique. If the velocity is assumed to vary only with the radial coordinate (ie. a vertically inhomogeneous medium) the separated angular equations are easily solved, and the radial equation reduces to a Schroedinger-type equation,

$$\frac{\partial^2 R}{\partial r^2} + \frac{2}{r}\frac{\partial R}{\partial r} + [k^2 - \frac{n(n+1)}{r^2}] R = K_s\, \delta(r-r_s) \qquad (2.19)$$

In a homogeneous medium, the waveslowness k is independent of the radius, and this equation reduces to a Bessel equation, for which the two travelling wave solutions are the Hankel functions of the first and second kind.

Several different approaches have been taken to solving this equation in the case of a vertically inhomogeneous medium. The classic approach has been the use of the WKBJ approximation. However, this approximation is known to fail at the turning point of the differential equation, corresponding to the turning point of the seismic ray. It is at this point that the most important seismological phenomena occur, so the failure of the WKBJ approximation at the turning point is a serious limitation. In the vicinity of the turning point, the radial wave equation can be approximated by an Airy equation, although this leads to problems with the matching of the Airy solution (which is valid near the turning point) to the WKBJ solution (valid away from the turning point), Nayfeh

(1973).

An alternative approach to the solution of this differential equation has been developed by Langer (1951), and has been applied to the problem of the radial wave equation by Richards (1976). The Langer approximation, as it has become known, provides a uniformly convergent solution to the radial wave equation, and is asymptotically convergent to both the WKBJ and Airy solutions in their respective regions of applicability.

Richards (1976) used the Langer approximation to introduce the concept of generalized cosines, which extend the range of applicability of coefficients derived from plane wave theory (Knott and Zoeppritz equations). The generalized cosines are the normalized radial derivatives of the radial wave function, obtained using the Langer approximation, and these are substituted for the cosine function. The application of this approximation will be discussed in more detail in Chapter 6.

The displacement response can therefore be written as an integral over the raypath parameter p,

$$U_r = F_s \int p^{\frac{1}{2}} E(p) \exp[i\omega J(r,p)] \, dp \qquad (2.20)$$

where F_s incorporates source effects, E(p) is the product of all the relevant boundary conditions, and J(r,p) is the WKBJ phase delay function.

Both E(p) and J(r,p) can be calculated more accurately by employing the Langer approximation, as discussed by Choy (1977). Cormier and Richards (1977) extended the application of the Full Wave method to the case of a discontinuous increase in velocity.

CHAPTER 3

CENTRAL QUEENSLAND CRUSTAL REFRACTION SURVEY.

3.1 INTRODUCTION.

In early 1977, a medium range crustal refraction survey was conducted in the Bowen Basin region of eastern Central Queensland. The insert of Figure 3-1 shows the location of the survey area. The purpose of this survey, designated QHC, was to study the crustal structure of this region, utilizing, as seismic sources, the explosions detonated in the large open cut coal mines operating in the Bowen Basin. The refraction profile extends as a linear array of 450 km length, from Gladstone, in a west south-westerly direction to past Springsure.

During the preliminary analysis of this data, it became apparent that the survey would have to be extended in order to fill in gaps in the coverage caused by instrument failure, and also to achieve a closer station spacing. The survey was repeated in early 1978, this project being designated CQM.

3.2 AIMS OF THE SURVEY.

The major aims of the survey were:-

(1) to investigate the transistion of crustal structure from a coastal zone to a stable continental zone,

(2) to investigate the response of the crust to the sedimentary Bowen Basin structure,

(3) to compare the crustal structure derived from an east-west profile, with that obtained from an approximately north-south profile (Collins, (1978) ; Rynn, (in preparation)).

(4) to investigate the application of different types of theoretical seismograms to the interpretation of crustal refraction data,

(5) to perform a Time Term analysis in order to study the structure of the crust in this region, using the QHC and CQM data together with other crustal refraction data from the Bowen Basin region, and to investigate the anisotropy of the crust and uppermost mantle using this data.

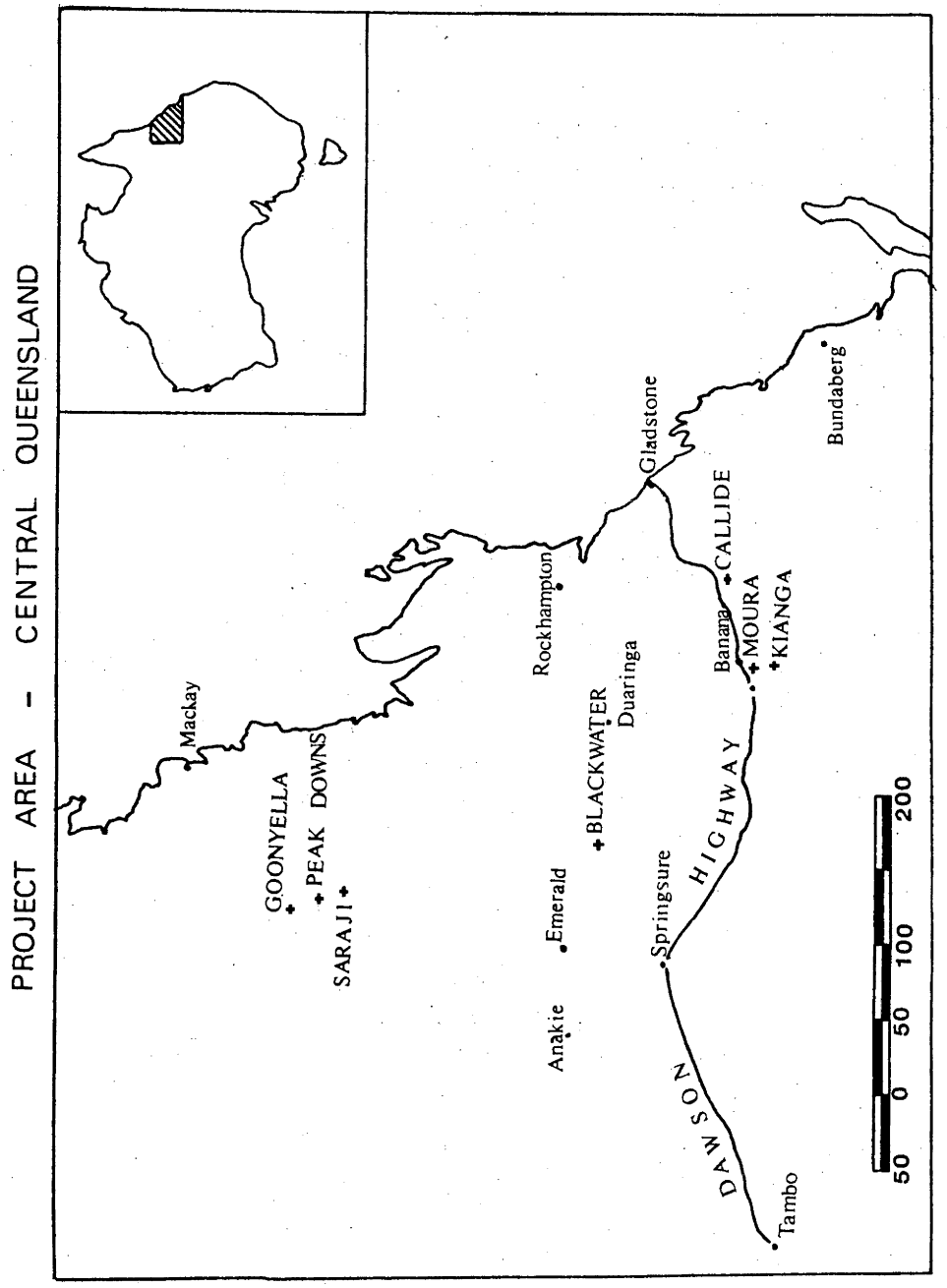

Figure 3.1

Central Queensland crustal refraction project survey area.

3.3 GEOLOGY.

Although the crustal refraction surveys were designed to investigate the broad crustal structure rather than the detailed geological structure, a broad outline of the geology and tectonic history of the survey area is necessary for an understanding of the interpretation of the seismic data. The geology of the area is discussed in greater detail in Paten and McDonagh, (1961); Dickens and Malone, (1973); and Malone (1974).

The region has four major geological provinces, shown in Figure 3.2. These are the Clermont Stable Block, the Eungella-Cracow Mobile Belt, the Bowen Basin, and the Great Artesian Basin.

3.3.1 The Clermont Stable Block.

The Clermont Stable Block is a Paleozoic stable tectonic unit, the southern extent of which comprises low grade metamorphic rocks and sedimentary basins which were deposited between the Ordivician and the upper Carboniferious periods.

3.3.2 Eungella-Cracow Mobile Belt.

The geologic history of this province has been complicated by the intense tectonic activity, which has severly metamorphosed most of the rock units. The rocks of this belt in the vicinity of Gladstone have been dated as Upper Permian (Webb, 1969). In the Middle Devonian, great thicknesses of volcanics and limestones were accumulated. This volcanic episode lasted into the Upper Devonian, with sedimentation continuing in the Yarrol Basin into the Lower Carboniferious, as a result of the regional downwarping.

Late in the Upper Permian, numerous acid intrusions were emplaced in the southern part of the Eungella-Cracow Mobile Belt, and this is thought to be associated with the uplift of the Mobile Belt.

3.3.3 Bowen Basin.

The Bowen Basin is a Permian to Triassic elongate basin trending in a north-northwesterly direction for over 900 km, between Taroom in the south and Collinsville in the north. The sediments of the basin are believed to be depositionally continuous with those of the Sydney Basin. However at approximately twenty five degrees south latitude the sediments plunge beneath the cover of the Great Artesian Basin. Attention will be restricted to the northern out-cropping portion of the basin. This section is wedged between the Clermont Stable Block to the west and the

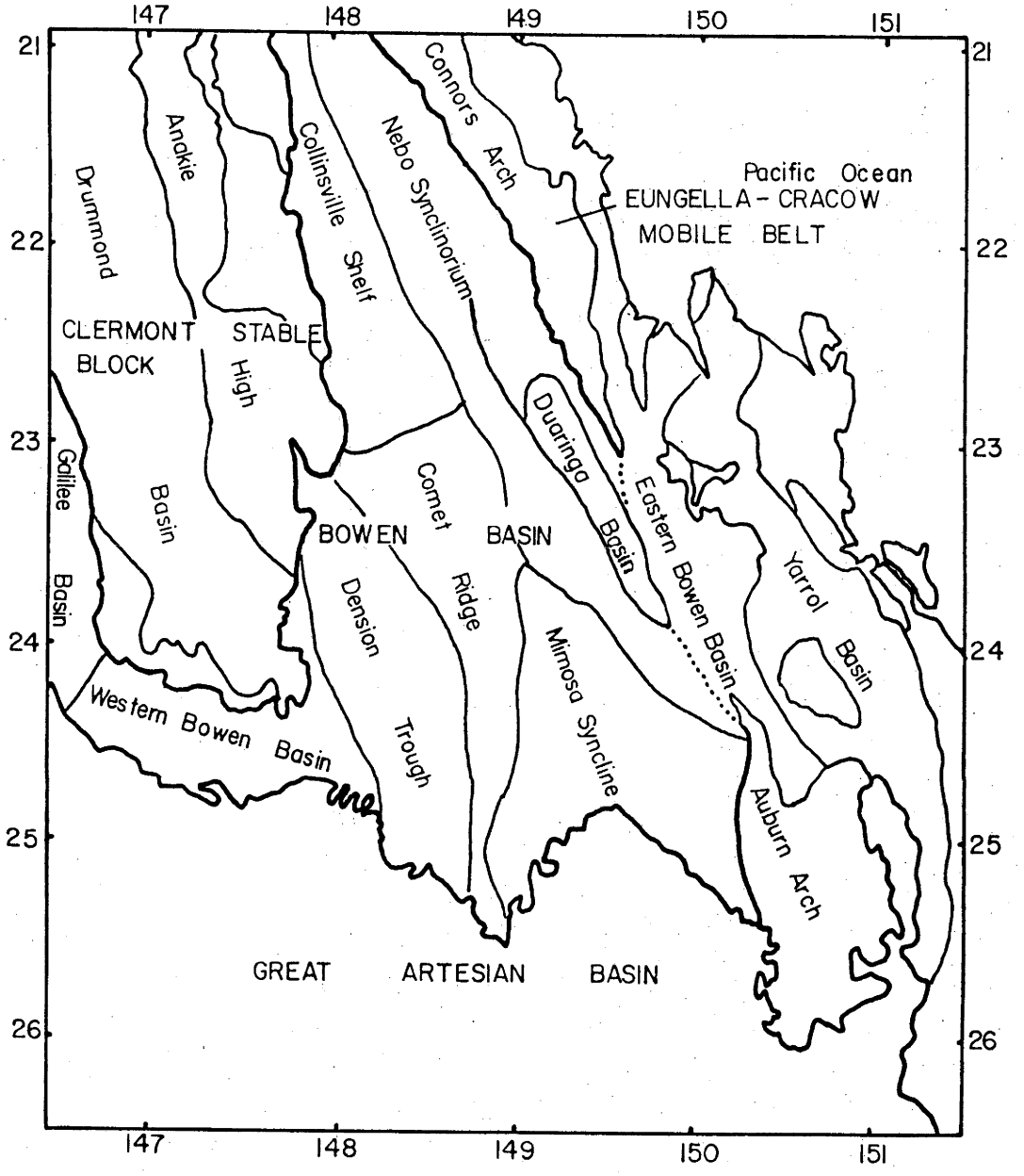

Figure 3.2

Geology of the Central Queensland region.

Eungella-Cracow Mobile Belt to the east, fanning out slightly towards the south.

Deposition commenced in the Bowen Basin during the early Lower Permian with terrestial sedimentation in the Denison Trough, and accumulation of considerable thicknesses of sediments, particularly in the Mimosa Syncline. Sedimentation in the Bowen Basin ceased in the Late Triassic with an episode of uplift and folding, including some erosion. The tectonic structure of the Basin is shown in Figure 3.2. The western margin is essentially the orginal deposition boundary, while the eastern margin of the present day trough is structural, being marked by the faulted, steeply folded and intruded rocks of the Eungella-Cracow Mobile Belt. The basin structure at the latitude of the seismic profiles, is dominated by the Mimosa Syncline, with lower amplitude tighter folding occuring to the west of the basin.

3.3.4 The Great Artesian Basin.

The deposition of the sediments of the Great Artesian Basin commenced in the early Jurassic , with the Precipice Sandstone. The sediments of the Surat Basin, (a sub-basin of the Great Artesian Basin), were unconformally deposited over the southern part of the Bowen Basin.

3.4 FIELD WORK AND DATA REDUCTION.

3.4.1 Introduction.

The two surveys involved in this project employed differing field techniques in the deployment of the portable seismic recorders. The first, QHC, deployed 26 instruments at approximately 25 kilometre spacing along a line roughly following the Dawson Highway, and these were left to run for a period of 31 days. This operation was similar to the technique used routinely by the Research School of Earth Sciences, to record earthquakes for upper mantle studies. In the CQM survey, a leap-frog technique was employed to install fifteen instruments at a station spacing of approximately 10 kilometres along the 450 kilometre survey line, while leaving fourteen recorders fixed as mine monitors and control stations for the duration of the survey. Although this involved constant field work throughout the two month duration of this survey, it proved to be the more successful operation.

3.4.2 Equipment.

Both the QHC and the CQM surveys employed essentially the same equipment to record the seismic signals. Six track and fourteen track analogue tape recorders and strip-chart shot recorders were used to record ground motion at varying distances from the explosions.

New six track recorders.

These seismic recorders (designated N6 recorders), are the latest version of the orginal 4 track recorders described by Muirhead and Simpson (1972). They were built at the Australian National University and employ a direct analogue recording on to magnetic tape. The six tracks of information comprise a radio time signal (VNG), two clock channels, and signal recorded at three gain levels, each separated by 24 dB. The signal is recorded on to 10.5 inch spools of 1/4 inch magnetic tape. The seismic recorder employs a low tape speed of 1/100 inch/second (2.54×10^{-3} m/s) so that continuous recording on one tape can extend over a period of two months. As a result of this low tape speed, tape skew across the recording head must be taken into consideration. This is achieved by recording the clock signal simultaneously on the top and bottom channels of the tape. On playback this tape skew can be determined and its effect removed.

The electronics of the recorder is in modular form, and comprises four exchangable printed circuit boards:- a radio receiver, a clock, an amplifier board, and a power supply board. A Mark Products L-4 vertical component seismometer, with a natural period of one second, is operated in a critically damped mode as the sensing element of the system. Ten of the N6 instruments were used in the two field surveys.

Fourteen track recorders

The 14 track seismic recorders, (designated H14), used in the survey, were modified University of Texas, Dallas instrumemts, in which the electronics had been reconstructed in line with that of the N6's. The recorder differs only in that there are twelve tracks of information recorded, (using a fourteen track head - hence the name), these being the radio, two clock channels, and three seismic components (vertical, radial, and transverse), each at three gain levels (high, medium, and low, as in the N6 recorders). A Mark Products L4-3D seismometer is used with this system.

Ocean Bottom Seismic Recorders.

Four Ocean Bottom Seismic Recorders (OBS) were used in the CQM survey, and these instruments are similar in most respects to the N6 recorders. The three major differences between these and the N6 recorders are the layout of the recorder and case, the smaller tape spool, and the use of an oil damped, gimbal mounted, Mark Products L-22 seismometer. The L-22 seismometer has a natural period of 0.5 seconds. The OBS's were deployed as normal land recorders.

Old Six Track Recorders

These instruments, designated M6, used as mine monitors in the QHC project, were proto-types of the N6 instruments. They employed identical electronics, but were housed in a wooden box. This was a major source of trouble, as they could not be made completely watertight, and water leaking into the instruments caused many failures. These recorders were connected to a L-22 Mark Products seismometer.

Hellige Shot Recorders.

Four Hellige strip-chart recorders were borrowed from the Bureau of Mineral Resources, for the purpose of recording the shot instant times of the source explosions. These chart recorders were connected to a seismometer (usually a Mark Products L-22), and to a VNG radio receiver which recorded both these signals along with an internal clock signal. As the seismometer was always placed in close proximity to the explosion, a sizable signal was generated by the seismometer, and this could be recorded directly, without amplification.

The time of the shot instant could be scaled from the strip-chart record, and allowance made for the distance of the shot instant seismometer from the explosion. In this way the shot instant could be measured with an accuracy of within 1/20 second.

3.4.3 Mine Operations.

The explosive used by the coal mines is ANFO, which is a mixture of ammonia nitrate and diesolene, and does not constitute a high energy explosive. The mixture is detonated using detonator caps, and these are connected via CORDTEX to an electrical detonator.

The explosions fall into two categories, overburden and coal shots.

The overburden shots are designed to break up the rock material overlying the coal seam so that it can be readily removed by dragline. The explosive is distributed in rows along the bench, usually with detonation delays between the rows. The explosion is therefore distributed in time over a period equal to the detonation delay between rows multiplied by the number of rows. A typical row may consist of 30 holes, each loaded with ANFO and interconnected with CORDTEX. The row delays are typically 25 milliseconds, although longer delays, or no delays, are occasionally used, depending on the nature of the desired explosion.

The purpose of the overburden explosion is to channel the maximum amount of energy into fracturing the rock. This is at variance with the object of a seismic explosion, which is to couple the explosion to the rock so as to maximize the production of seismic energy. In this respect the overburden explosions are poor seismic sources, as they are distributed explosions, not fully tamped, and are detonated in relatively incompetent rock over a delayed interval. However, the sheer size of these explosions compensates for this, a typical overburden shot containing of the order of 100 tonnes of explosive.

The coal shots are designed to fracture the coal seam, in order to facilitate loading and transportation. A smaller charge is distributed throughout the coal seam, and this is commonly detonated instantaneously. For this reason the coal shots more nearly approximate an ideal point source explosion.

3.4.4 Field Work.

The QHC survey occupied the period from the 27th March to the 23rd April, 1977, and the instruments were installed and left running unattended during this 4 week period. An analysis of the operation of the instruments is shown in Table 3-1. An important factor was the poor performance of the mine monitor instruments. The main reason for this was that the instruments used for these sites were the least reliable, being the M6 and OBS recorders. As previously noted, the M6 instruments became waterlogged, while the OBS's failed owing to a shorting fault in the side battery pack. The failure of these mine monitors meant that shot identifaction and estimation of the orgin times of an event became a problem.

As well as the portable seimic recorders, three Hellige Shot recorders were operated by the mine personnel, to determine shot times. This was not as successful as had been envisaged. A list of the shot

instant recorded shots is given in Table 3-3. Of the two Moura Mine shots recorded, one was before the installation of the majority of the line instruments, and the other after the pull-out of most of the instruments. No shot instant times were recorded from Saraji, Kianga, or Callide Mines during the QHC survey.

Within the main line of recorders, six of the twenty-three instruments failed (Table 3-1). The lack of data, and especially the lack of coverage at distances which were considered critical for the interpretation, led to the decision to return and reoccupy the refraction line in early 1978.

The second period of recording took place from the 19th January to the 21st March 1978. It was decided to reoccupy the same line, but the philosophy of the operation was different. Twenty nine seismic recorders were used, comprising ten N6's, four OBS's, and fifteen H14's. Of the N6 instruments, seven were deployed as mine monitors at the seven major open-cut coal mines, and three as control stations and tie points to the previous QHC line, occupying exactly the same sites as the stations QHC02, QHC09, and QHC16. The four OBS's were used in two separate experiments. The first was designed to aid the time term analysis, by placing the recorders on radial lines from the northern mines (Goonyella, Peak Downs, and Saraji), at approximately the same radius from these mines, on either side of Moura. The second experiment involved the deployment of the OBS instruments as a short refraction array to the east and west of the Moura and Kianga Mines, to determine the velocity structure of the Bowen Basin sediments directly beneath these mines.

The H14 instruments were used to record along the survey line at approximately a 10 km spacing. A leap-frog operation was employed to enable the 15 instruments to be installed at this spacing along the 450 km line. This involved continuous field work, the H14's being constantly moved west; however, the instrument success of this project warranted the extra field work. An analysis of the instrument performance for the CQM project is given in Table 3-2.

During this latter project, four Hellige recorders were used to record origin times of the explosions. The mine personnel proved to be most cooperative in this venture, and a total of 23 shots were timed at the four mines:- Moura, Kianga, Callide, and Goonyella. Table 3-3 gives the details of the timed shots.

3.4.5 Data Reduction.

The reduction of the vast amount of data collected by continuous recording analogue recorders, into a form in which it can be interpreted, is a time-consuming task. The final result of this processing is a selection of record sections, from which the various phases can be identified, and inverted into a crustal structure. The intervening step between the analogue tapes and the production of record sections is the digitization of the data and its storage on digital tapes.

The first step in the data reduction is the location of the shot points and receivers in the grid coordinates (Australian National Spheroid), and the conversion of these coordinates to geographical coordinates. This is done by a utility programme, of the type available at most geophysicial institutions.

The next procedure is the calculation of clock corrections of the seismic recorders. The internal clock of the recorder is normally set about 3 seconds slower than Universal Time (UT) on installation, and subsequently drifts relative to UT at a rate which would normally not exceed 3 seconds a month. The VNG radio time signal which is recorded allows the exact offset of the internal clock from UT to be determined. However, the radio signal is often not continuously received, because of atmospheric conditions, and as it is a short wave signal, its reception is generally better at night. The random drift of the clock during one day is typically very much less than one tenth of a second, so a determination of the clock offset each day enables the compilation of clock correction curves for the duration of the recording period.

The digitization of the analogue data is performed using a Datacraft 6024/4 computer interfaced with a ADC designed and built at RSES. The programmes for the digitization have been written by Dr. K. Muirhead, some of these having been further modified by the author. The digitization programme takes the ADC data, sorts and interpolates this to a constant sampling rate of 20 samples per second, and then packs this data on to a standard 9 track digital tape in a compact binary format. This data can then be retrieved from these digital tapes for the production of record sections.

3.5 INTERPRETATION.

The aim of refraction interpretation is the derivation of the simplest velocity model, which adequately explains the observed data. As previously mentioned, the interpretation inevitably involves some method of iterative improvement, and in the case of crustal refraction studies, the feedback for this improvement is provided either by some form of raytracing, or by synthetic seismograms. However, the first step in the interpretation procedure is the derivation of a suitable starting model.

3.5.1 Record Sections.

The presentation of record sections for crustal refraction profiles has been discussed by Giese et. al. (1977). As most of the profiles were split spread in nature, record sections were plotted in a split spread format, with those stations to the east of the shot point being plotted in the right-hand section. Following the usual conventions, the record sections have been reduced on a velocity of 6 km/s or 8 km/s, depending on whether the arrival the record section seeks to display is Pg or Pn, respectively. The record sections of explosions from Blackwater, Callide, Kianga, and Moura mines which display longitudinal wavegroups have been reduced on 6 km/s, while those of Goonyella, Peak Downs, and Saraji mines have been reduced on 8 km/s.

The transverse wavegroups have been displayed in record sections using a reducing velocity of 3.46 km/s ($6/\sqrt{3}$) for Sg, and 4.62 km/s ($8/\sqrt{3}$) for Sn wavegroups. Only the H14 instruments recorded horizontal component data, and the component and gain used in the S wave record sections was chosen as the one which best displayed the shear wave onset. The N6 and OBS instruments recorded no horizontal component data, while the horizontal components of the L4-3D seismometers were subject to a relatively greater number of failures, (these components of the L4-3D seismometer being more susceptible to damage during transport), and this accounts for the large variation in the quality of the S data in these record sections.

Shots from the Blackwater, Goonyella, Peak Downs, and Saraji mines are not amenable to conventional record section display, owing to the fan-like geometry of the shot and stations. A conventional record section, which plots traces as a function of the source-receiver distance, will have many of these traces overlying one another. For this reason, events from these mines have been plotted using a fan record section (Giese et.al. ,

1977), in which traces are plotted as a function of azimuth rather than distance. This has the distinct disadvantage that the apparent velocities of the wavegroups can not be read directly from the record sections; however, this format does make the identification of the various wavegroups possible.

3.5.2 Quality of the Data.

The relatively recent advent of digital processing and recording has greatly improved the quality of seismic data available for interpretation. The digital data of the present two surveys displays excellent reproducibility. Explosions from a mine, shot on different days and at slightly different locations within the mine, have been recorded at the same receiver, and can be superimposed "wiggle for wiggle". An example of this with shots recorded at CQM18 station is shown in Figure 3.3. This reproducibility is encouraging, as it not only establishes that the different explosions can, to the approximation required, be considered to be identical, but also demonstrates the fidelity of the recording and playback systems.

The frequency bandwidth of the present data is limited by the bandwidth of the combined recording and playback systems, this being dominated by the response of the seismometer at the lower end and by the digitizing frequency at the higher end of the spectrum. The response of the combined record and playback is discussed in detail in Appendix I. Several record sections were made with the traces deconvolved of the total system response; however, the results were, apart from the greatly enhanced and undoubtedly spurious low frequency component, visually identical to the unprocessed records. For this reason, no deconvolution procedure was applied to the traces of the record sections.

The dynamic range of the digitized data is limited by the dynamic range of the analogue recording stage, and subsequently by the digitization word length. The digital word size used is 12 bits, but as the signal is recorded and digitized at three gain levels, this imposes no limitation.

Timing accuracy of the digitized data is ultimately limited by the 20 Hz sampling frequency used, so that 0.05 seconds is the greatest temporal accuracy that can be achieved. In practice, other factors also contribute to the timing inaccuracy; such effects as variation of the tape skew and errors in the computer's interpretation of the clock and radio signal pulse break can increase the maximum timing error to 1/10 of a

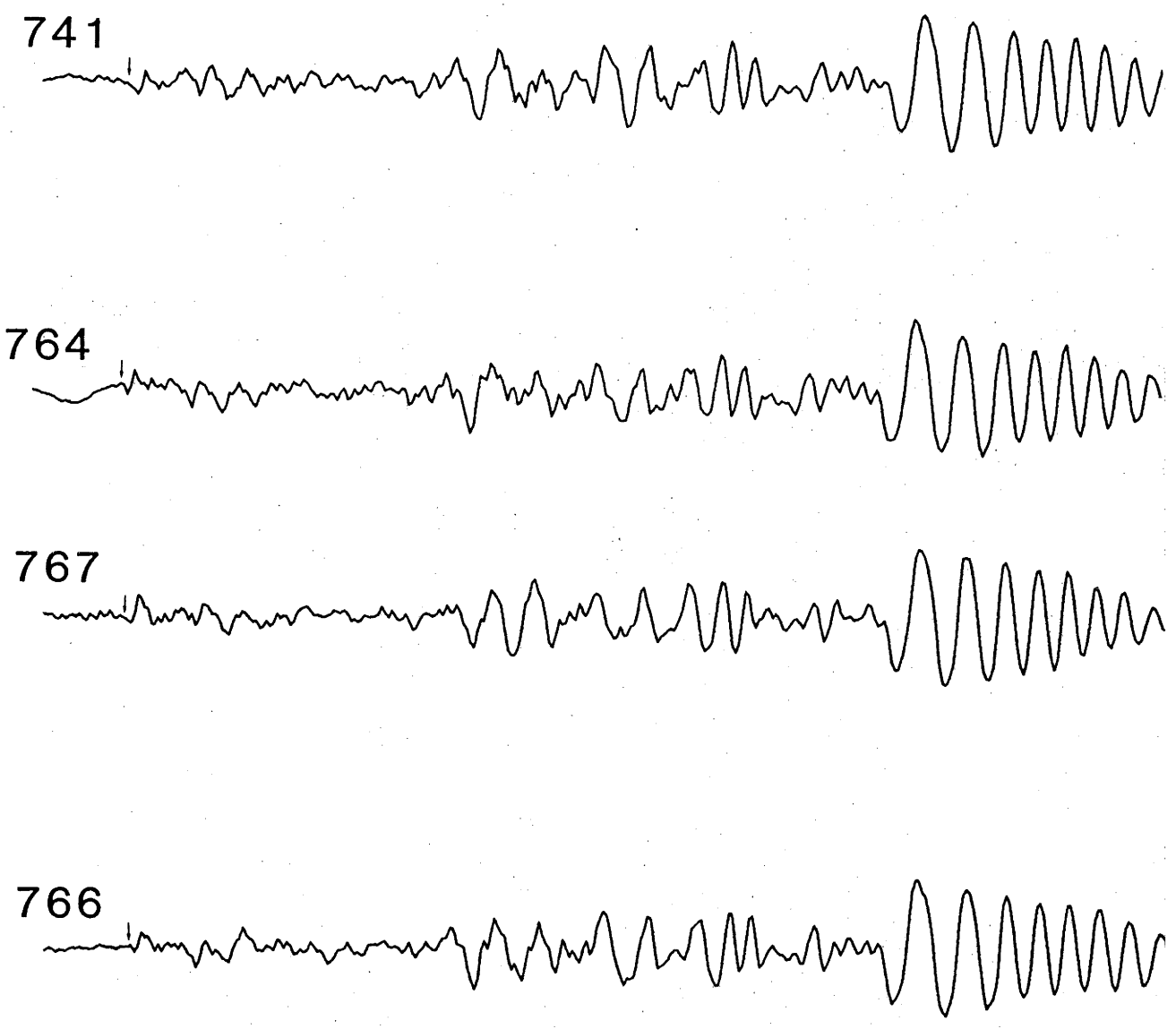

Figure 3.3

A comparison of records from station CQM18 of different explosions from the Kianga mine; see Fig. 3-42 for a superposition of these traces. All traces are scaled at 1 cm/s and have been recorded approximately 18 km from the explosion.

second. Most records, however, are better than this.

3.5.3 Description of the Principal Wavegroups.

The seismic onsets of record sections are conventionally catalogued into separate wavegroups by the process of group correlation. This correlation is one of the first and most important stages in the interpretation of seismic data. Because there exists no completely objective technique for performing this correlation, the experience of the interpreter, together with his biases, is introduced at an early stage. The correlation of any wavegroup when it is a first arrival is relatively straight-forward; however, there is greater difficulty, and hence greater subjectivity, when correlating arrivals of later onsets, which are masked in the coda of earlier arrivals.

Giese (1977) discusses some of the problems associated with the correlation process. The distinction is made here between phase correlation and group correlation (often called phase correlation, in a broader sense). As demonstrated by Giese et al.,(1977), using data from a lithospheric profile in Europe, the Pn wavegroup comprises several phases, each phase having a marginally higher phase velocity and a marginally greater intercept time, so that these phases successively become the first arrival within the wavegroup over a range of distances. Refraction studies, however, rarely maintain the station density necessary to resolve these separate phases within the wavegroup.

Several crustal wavegroups have conventionally maintained standard nomenclature. However, there exists a diversity of nomenclature for many other crustal phases. For this reason, and because some new nomenclature will be introduced, a brief description of the main wavegroups together with the nomenclature used in this study is given in Table 3-4.

3.5.4 Generalized Pg and Pn Velocities.

In conjunction with a time term analysis to be discussed in chapter 4, the Pg and Pn onset times and distances from four crustal refraction surveys in the Bowen Basin have been digitized. A plot of the reduced travel time distance graph (hodograph) for the Pg onsets is shown in Figure 4-3. This displays a considerable amount of scatter, as the readings are from widely varying structural zones within the survey region. The thickness of the Bowen Basin sediments beneath the receiver and shot affects the intercept time of the Pg arrivals, while any slope on the

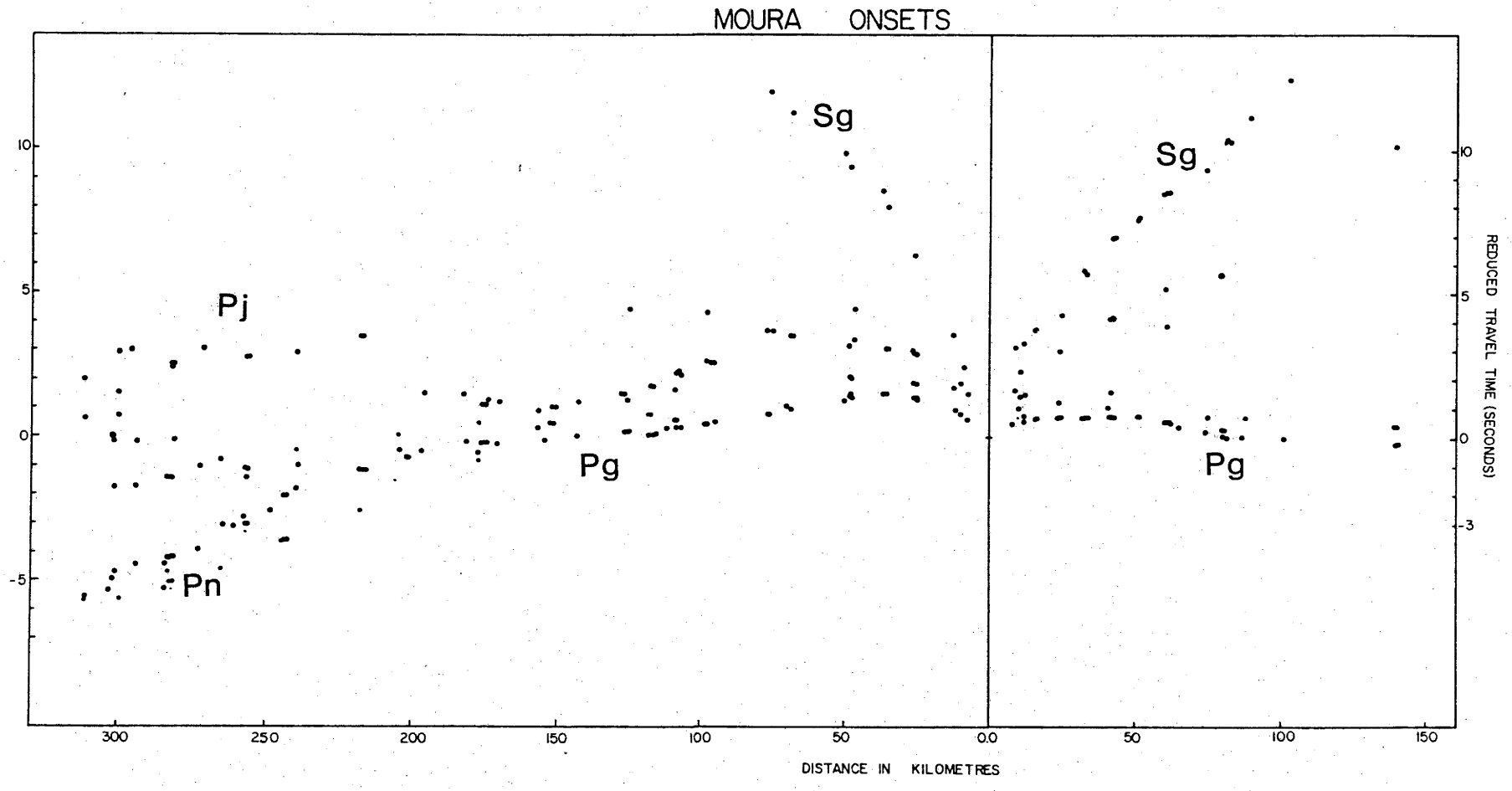

Figure 3.4

Hodograph of P wave onsets from the Moura explosions recorded to the east (right) and west (left) of the mine. The major wavegroups have been labelled.

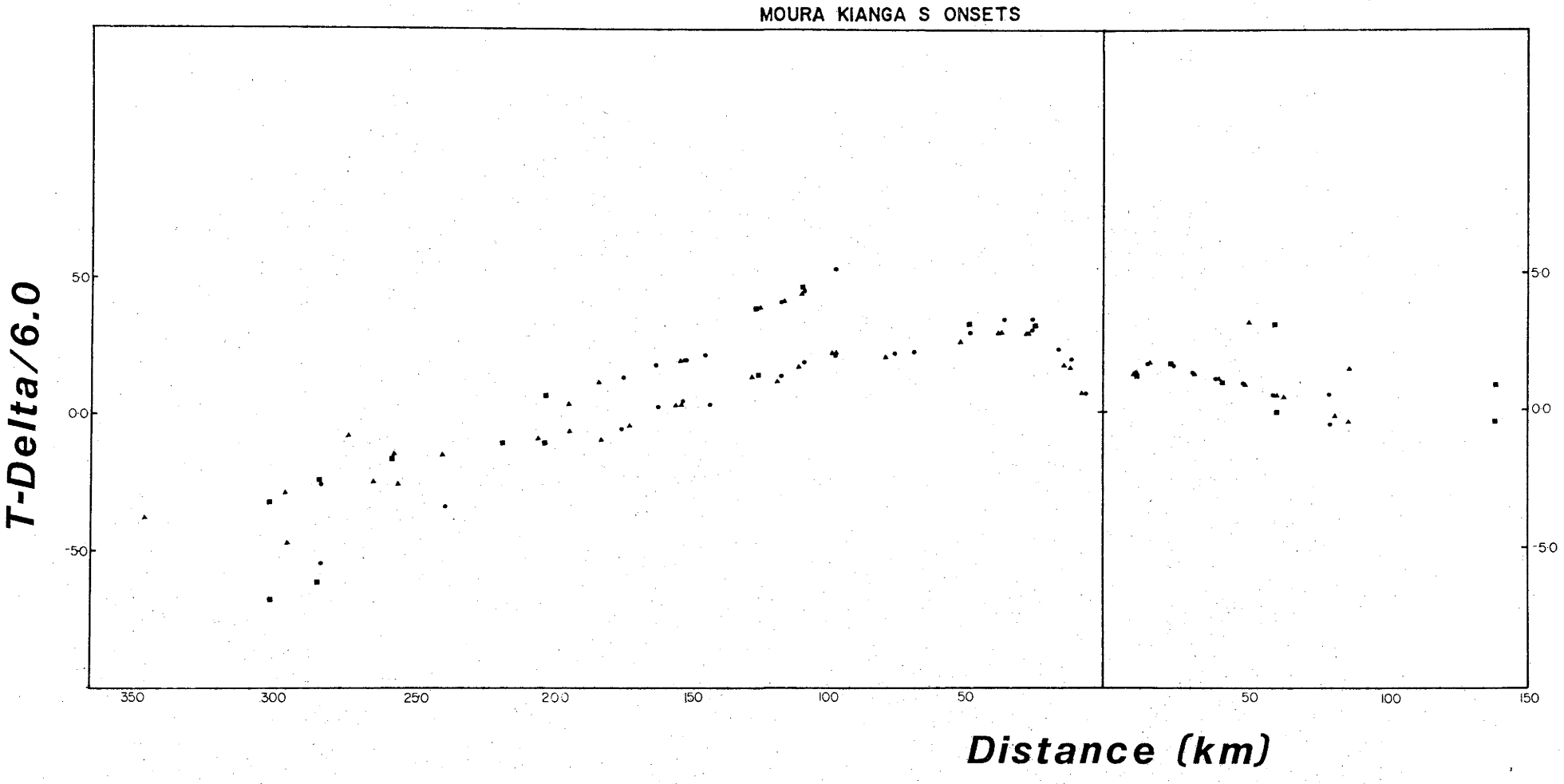

Figure 3.5

Hodograph of S wave onsets from Moura/Kianga explosions, as for Fig. 3.4.

basement will perturb the apparent velocity of the wave group. The latter is thought to have a relatively small effect, and tends to statistically average out, while the former is considered responsible for the large amount of scatter. A least squares analysis of this data gives an average velocity for the Pg wavegroup in the Bowen Basin region of 6.37 km/s, with an intercept time of 1.08 seconds. The 6.37 km/s average velocity, obtained from this large body of data, constrains the upper crustal velocity in this region to around 6.3 km/s, but does not preclude the possibility of a velocity gradient in the basement. However, the intercept time, arrived at by the least squares analysis of all the data, is less useful, owing to the differing structure of the upper crust sampled over the region.

A similar hodogram of Pn onsets is shown in Figure 4-2. Once again the considerable scatter can be attributed to the variability of the crustal structure over the eastern Central Queensland region. The least squares analysis of these data gives an average Pn apparent velocity of 7.70 km/s, with a corresponding intercept of 5.25 seconds. This compares with a sub-Moho velocity given by Collins (1978) of 8.1 km/s. As with the Pg, the intercept time is thought to have no great significance owing to the changing structure of the crust sampled.

3.5.5 Description of the Moura and Kianga Record Sections.

Four Moura and one Kianga composite medium range P-wave record sections are shown in Figures 3-6 to 3-10. Each of these record sections comprises records from several different overburden explosions at the respective mines. The individual events used for each record section are listed in Table 3-1, and the origin times and locations of these events are listed in Table 3-2. Both sets of record sections show arrivals in the distance range 0 to 320 km to the west, and 0 to 150 km to the east of the Moura-Kianga mines.

The main wavegroups are shown in Figure 3-4. Between 0 and 170 km, the Pg wavegroup is the first arrival, with a pronounced delay in the arrivals immediately to the west of Moura. These delayed arrivals have a relatively smaller Pg amplitude as is best seen in Figure 3-7. This delay is attributed to the thick section of low velocity basin sediments of the Mimosa Syncline. The amplitude of the Pg wavegroup diminishes with increasing distance away from the shot point, both out to the Pg-Pn cross-over distance, at 175 km to the west, and to the extremity of the record section to the east. Beyond the cross-over distance to the west of

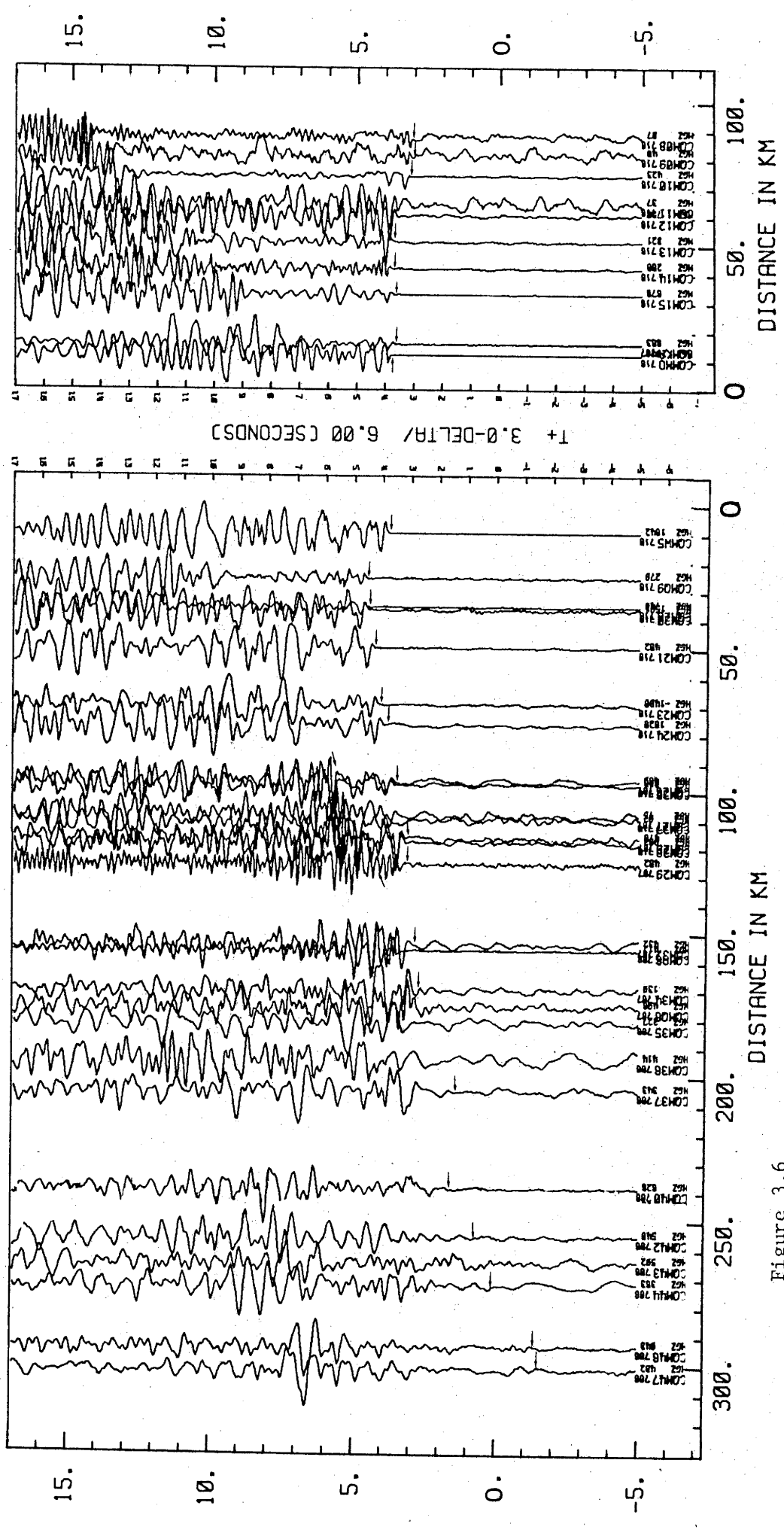

Figure 3.6

Composite vertical component P-wave record section of Moura explosions (MO-1P) Record section trace normalized.

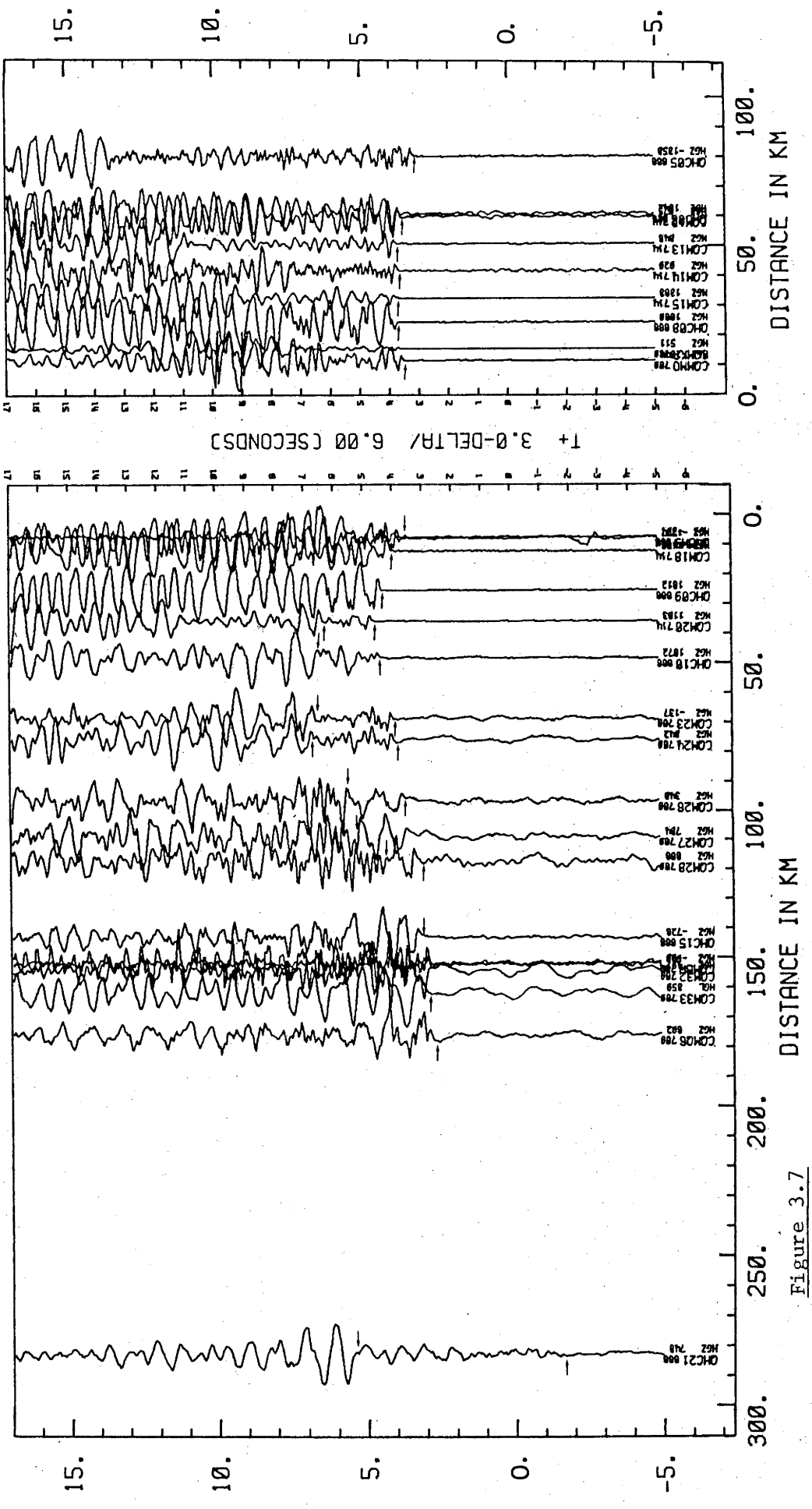

Figure 3.7

Composite vertical component P-wave record section of Moura explosion, (MO-2P).

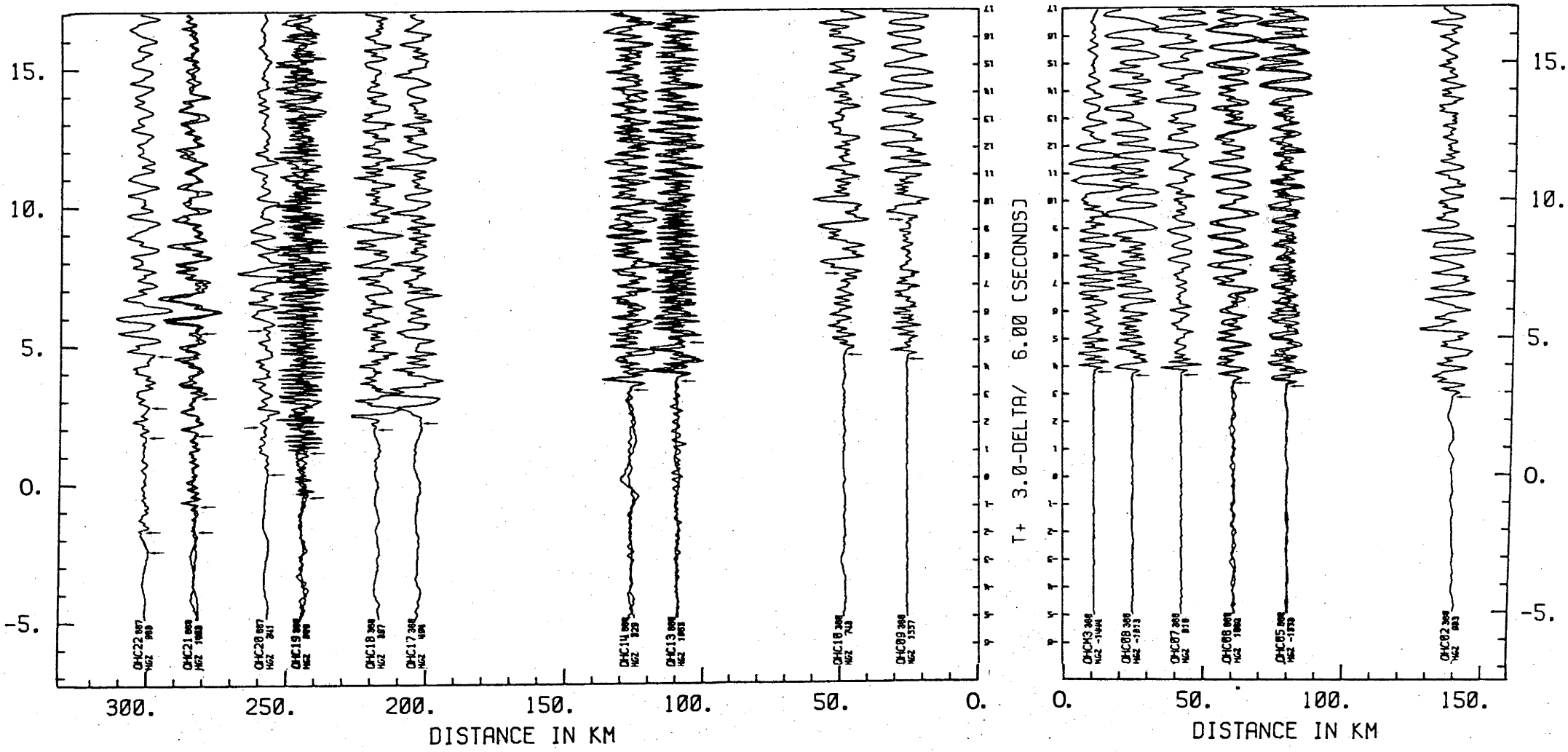

Figure 3.8

Composite vertical component P-wave record section of Moura explosions, (MO-3P).

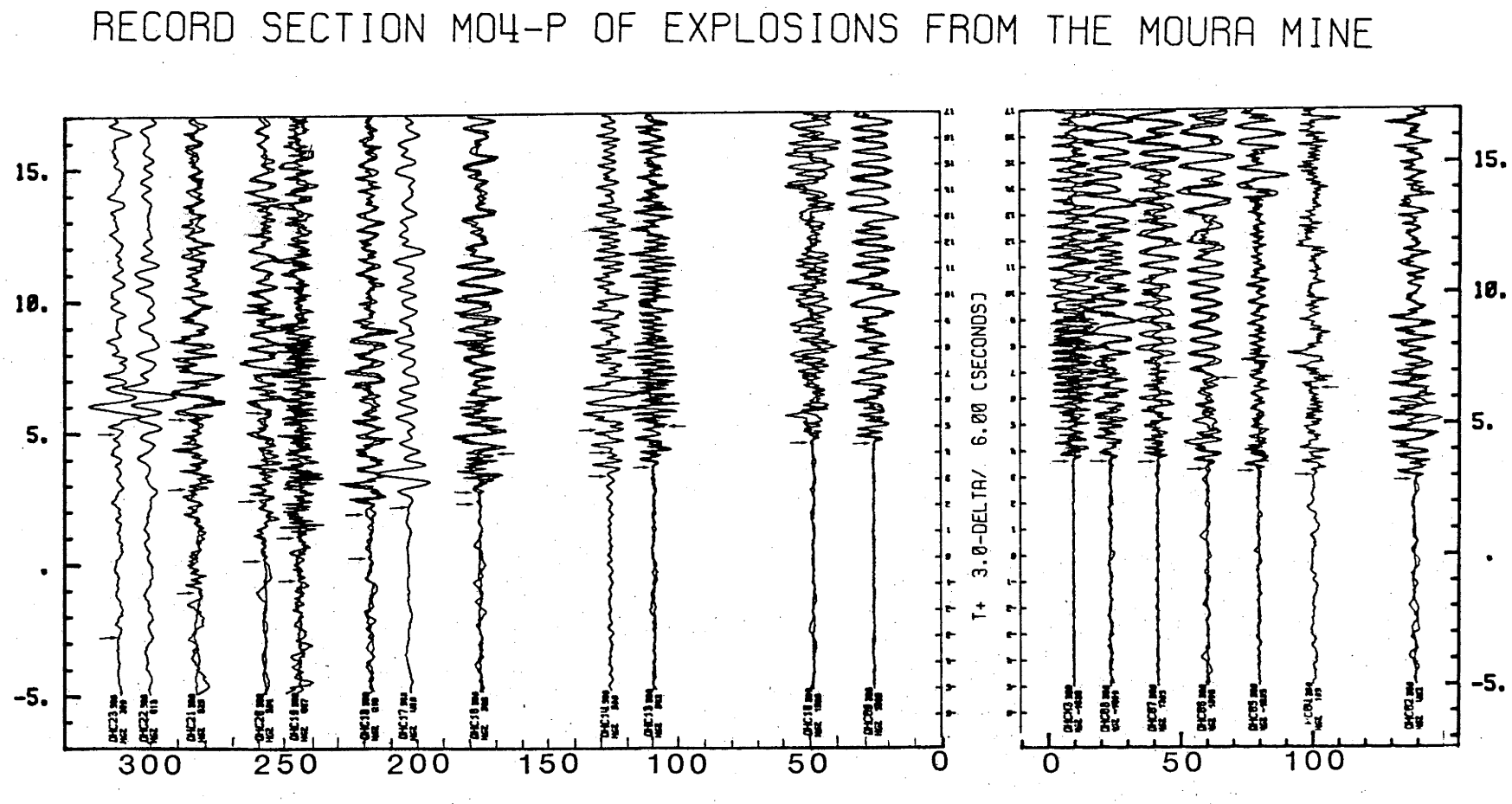

Figure 3.9

Composite vertical component P-wave record section of Moura explosions, (MO-4P).

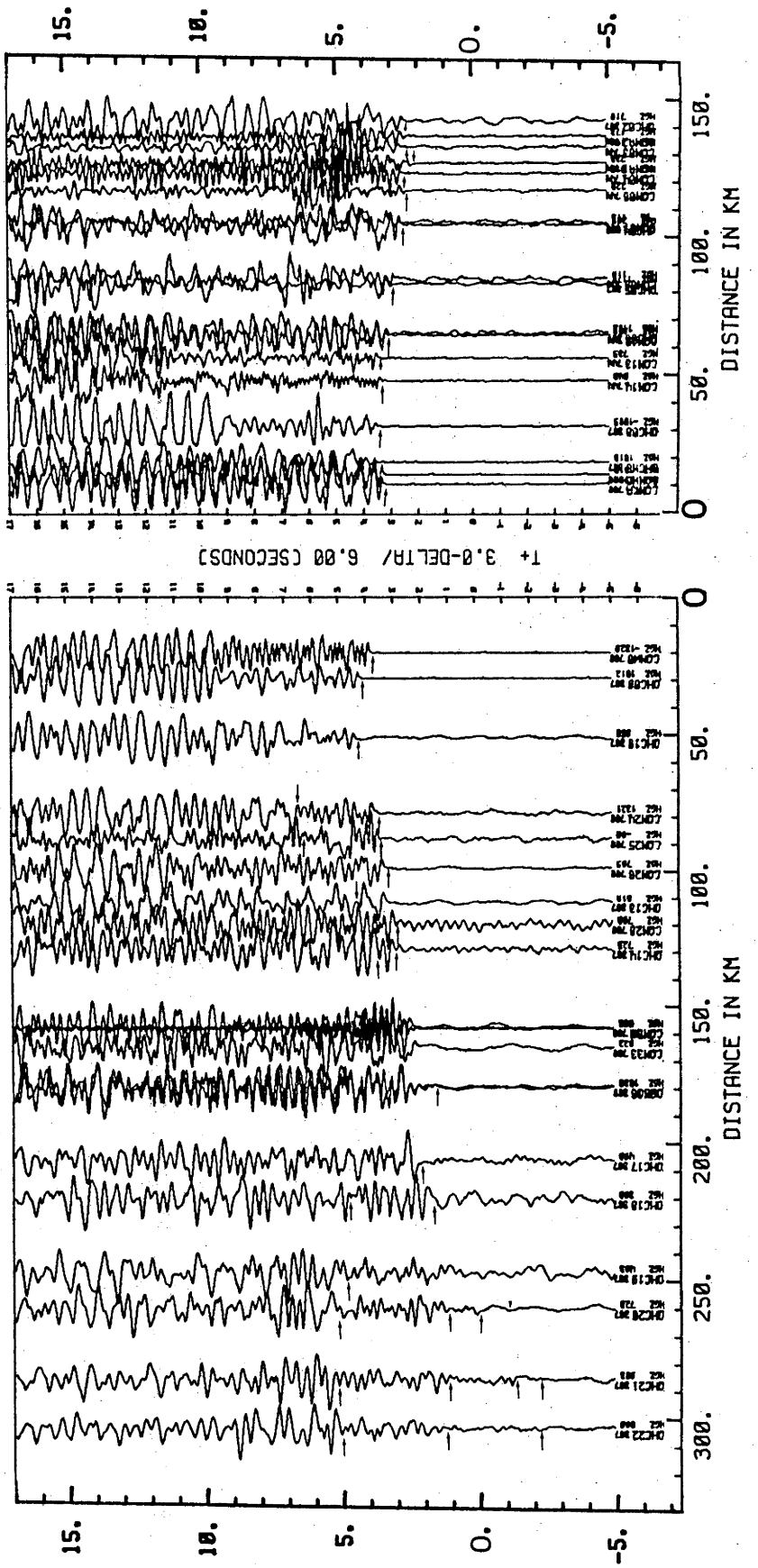

Figure 3.10

Composite vertical component P-wave record section of Kianga explosions, (KA-1P).

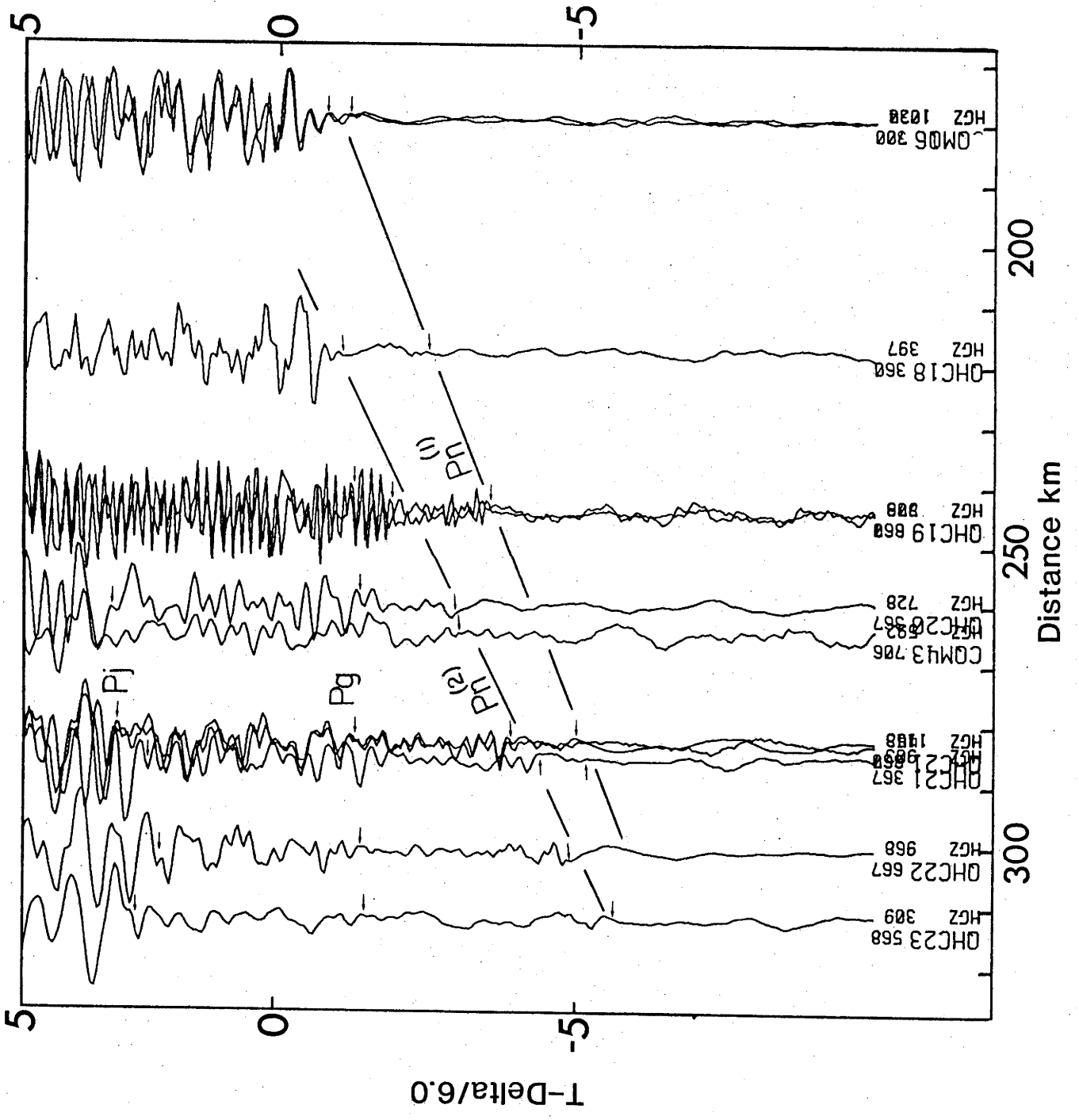

Figure 3.11

Composite vertical component P-wave record section of Moura and Kianga explosions, showing the nature of the $P_n^{(1)}$, $P_n^{(2)}$, and P_j arrivals.

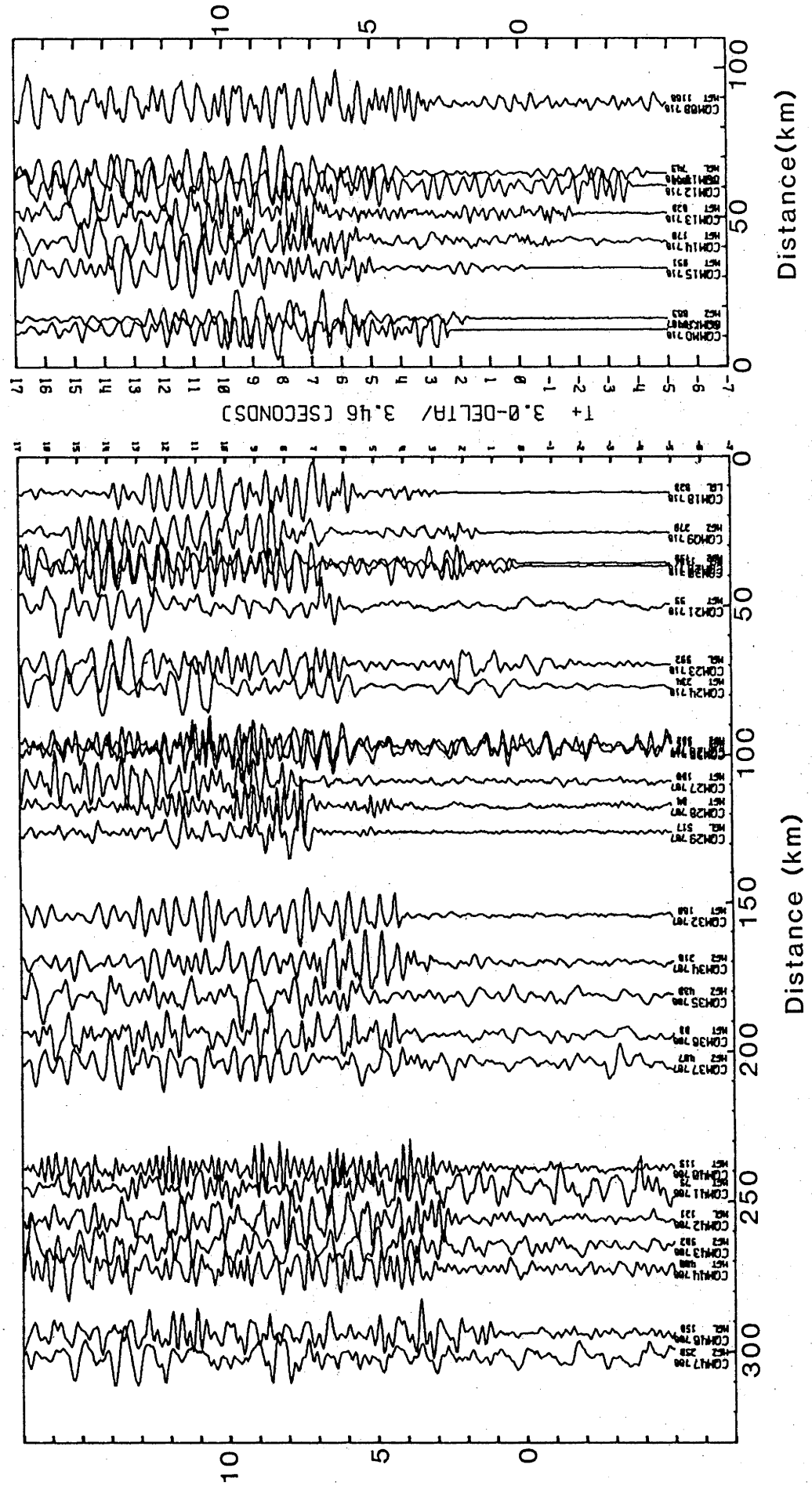

Figure 3.12

Composite S-wave record section of Moura explosions, (M0-1S)

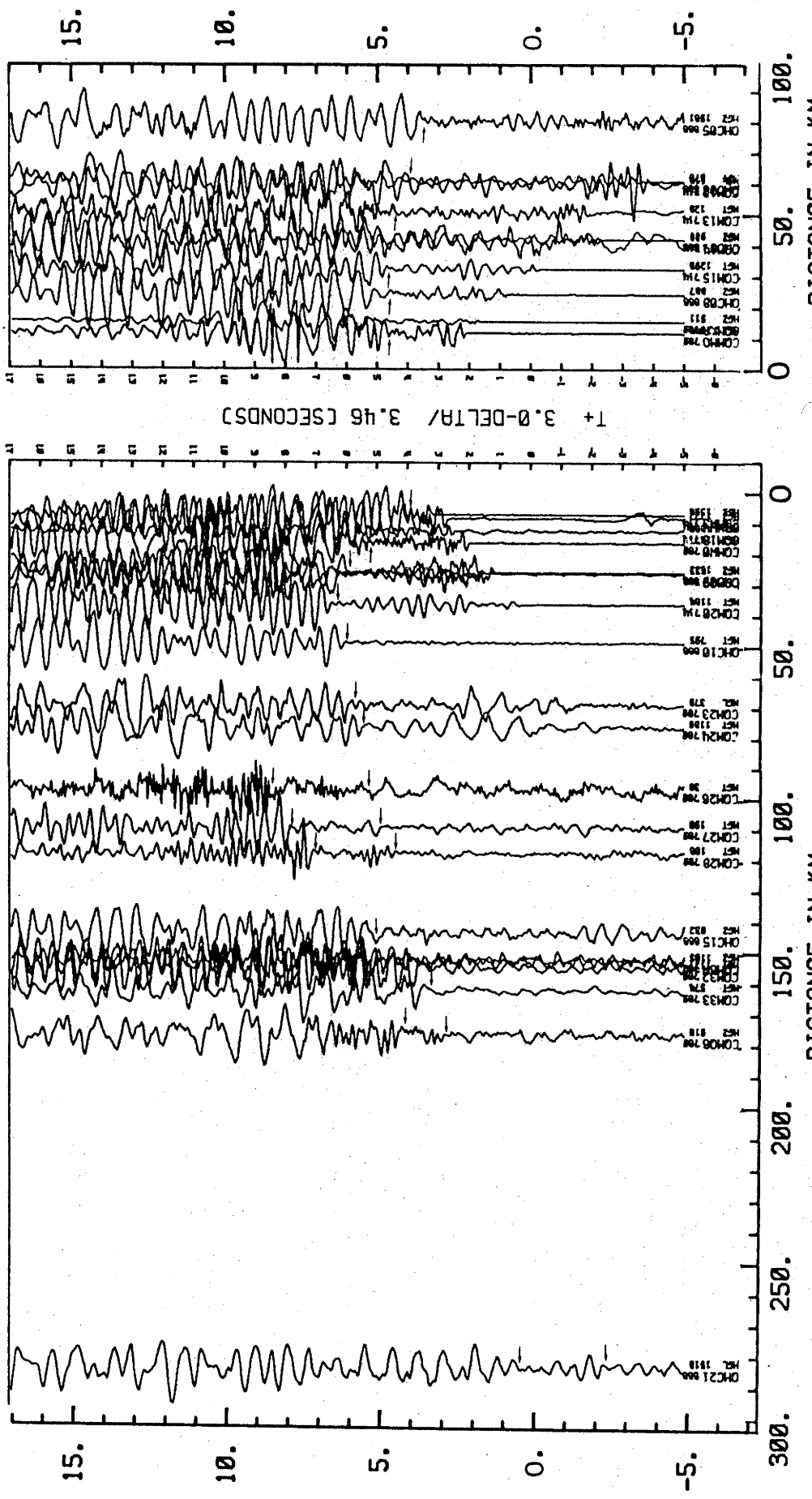

Figure 3.13

Composite S-wave record section of Moura explosions, (MO-2S).

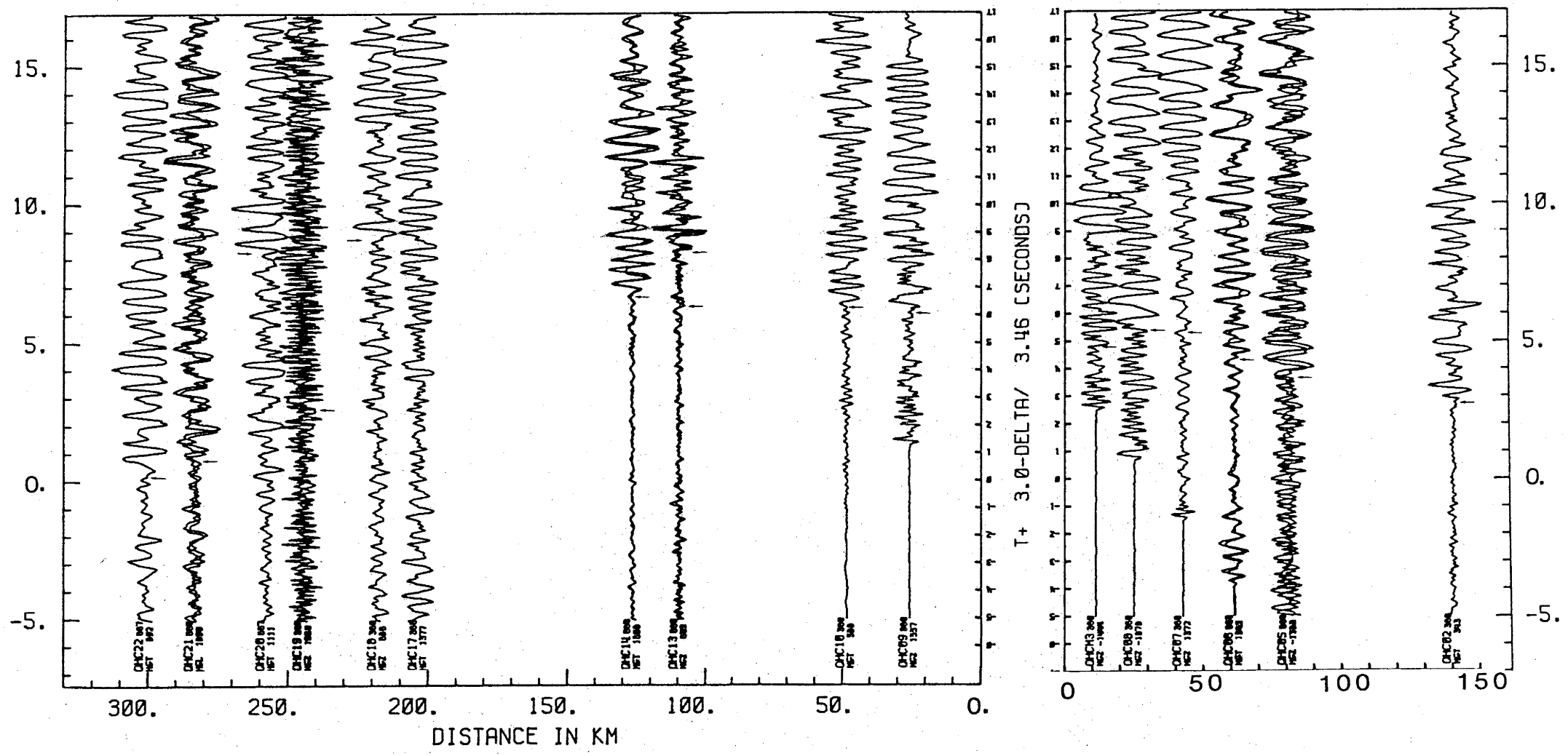

Figure 3.14

Composite S-wave record section of Moura explosions, (MO-3S).

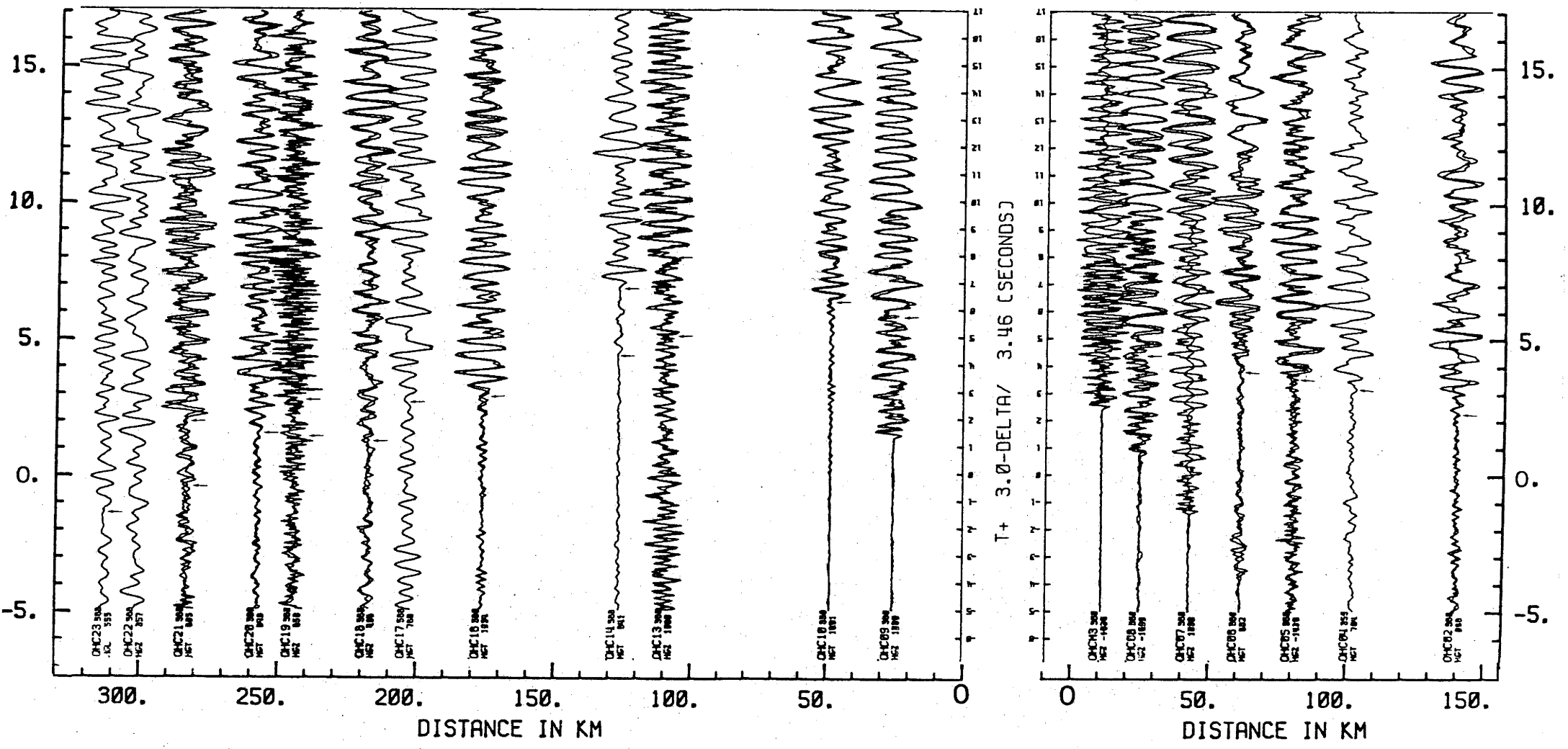

Figure 3.15

Composite S-wave record section of Moura explosions, (MO-4S).

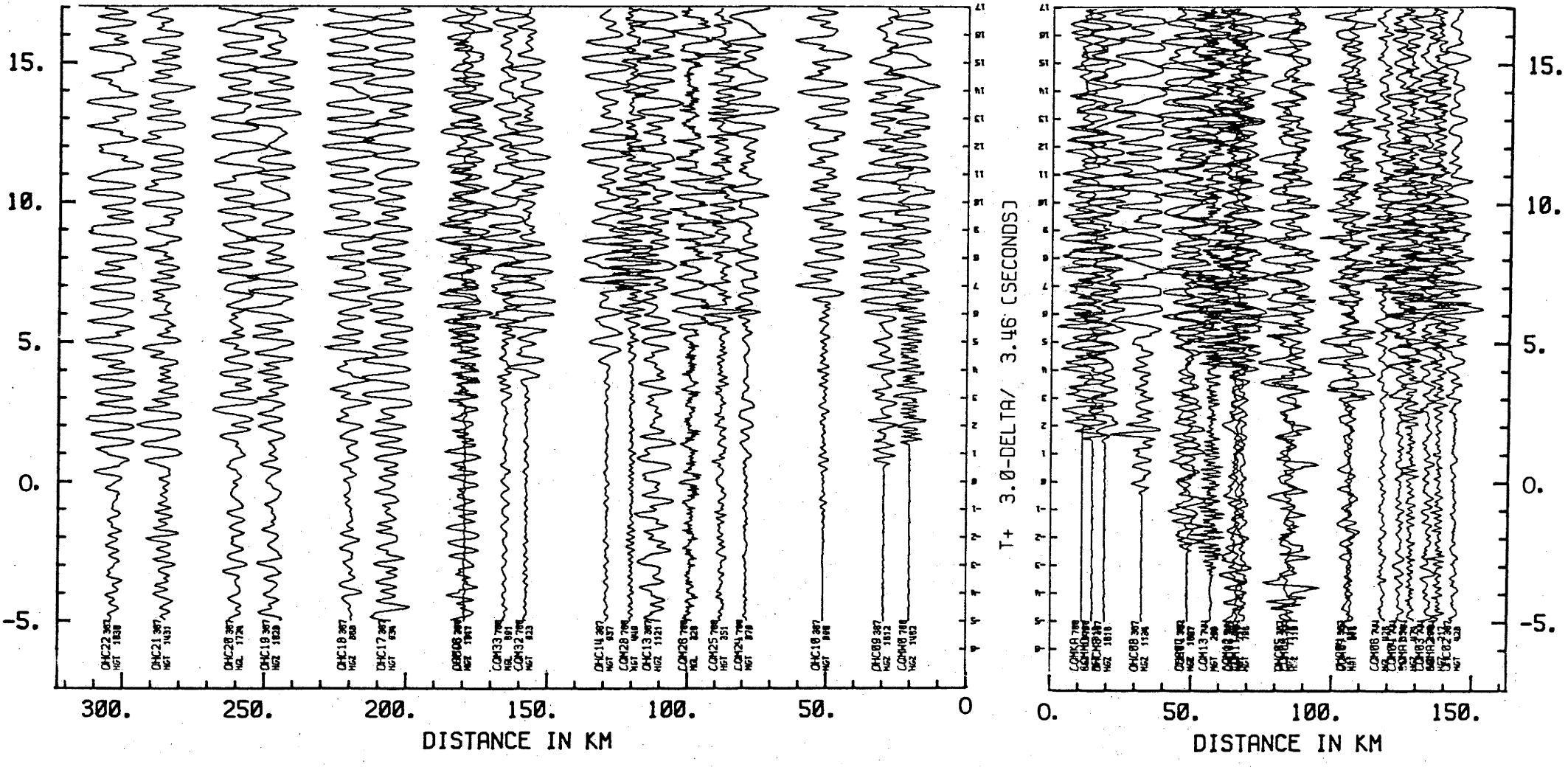

Figure 3.16

Composite S-wave record section of Kianga explosions, (KA-1S).

the mines, the Pg onsets are observed as later arrivals to the extremity of the record section. Between the distances of 50 and 70 kilometres to the east, the Pg travel time displays a pronounced kink to earlier times at distances greater than 70 km (Figure 3-6).

Prominent large arrivals of the Pm cusp[1] are observed between the distances of 90 and 140 kilometres to the west of the Moura-Kianga mines, but no corresponding Pm cusp is observed to the east of these shot points.

The Pn onsets of the Moura-Kianga record sections are low amplitude signals, and have a double onset nature, as shown in the onset plot of Figure 3-4, and the record section of Figure 3-11. The first group of onsets will be denoted $Pn^{(1)}$ and the second, which arrives approximately 0.5 seconds later $Pn^{(2)}$. $Pn^{(1)}$ is not well defined; its weak nature makes it difficult to detect, and it was initially thought that $Pn^{(2)}$ was the sub-Moho refracted arrival. However, the data from QHC19 (Figure 3-8), clearly shows the $Pn^{(1)}$ arrival from two different events. Careful re-checking of the clock corrections and station location of this recorder has indicated that this data can not be dismissed. The apparent velocity of the $Pn^{(1)}$ given on the basis of the detectable onsets of this wavegroup from the Moura/Kianga events, and constrained by the location of the Pm cusp is 7.937 ± 0.017 km/s, with an intercept time of 6.340 ± 0.052 seconds. The onsets of the $Pn^{(2)}$ are more widely scattered, with a linear regression of these data giving an apparent velocity of 8.432 ± 0.057 km/s and an intercept time of 9.494 ± 0.213 seconds.

The Pj wavegroup, clearly observed in Figure 3-11, shows large amplitude onsets and has an apparent velocity similar to that of the Pg wavegroup and an intercept time of around 5.3 seconds, although both of these quantities are not well constrained owing to the limited distance over which the wavegroup is observed, and the emergent nature of its onset. The wavegroup becomes less pronounced at smaller distances, becoming undetectable at distances less than 200 kilometres.

Composite record sections, displaying the S wavegroups from the Moura and Kianga mine overburden explosions, are shown in Figures 3-12 to 3-16. Two transverse wavegroups can be identified on the S record sections, these being the Sg and Sn groups. As with the Pn wave group, the Sn arrivals are relatively weak; however, an increase in the amplitude of these onsets is observed at a distance which corresponds to the Sn-Sm cusp. The Sm arrivals away from this cusp, cannot be clearly identified within the coda. An apparent velocity of 3.72 km/s is obtained for the Sg

1 See Table 3-4 page 97.

wavegroup, accounting for the delayed arrivals within the Bowen Basin. The apparent velocity of the Sn wavegroup is poorly constrained at about 4.4 km/s. No double onset character of this Sn wave has been observed, although this finer detail may quite possibly be lost in the ambient noise of the P coda.

3.5.6 Description of the Callide Record Sections.

An onset plot of Callide events (Fig. 3-17) shows a similar form to that of the Moura and Kianga plot (Fig. 3-4). Three composite P-wave record sections of Callide Mine explosions Figures 3-18 to 3-20, have been constructed from the events listed in Table 3-3. All three sections are split spread in nature, with a short section of profile extending eastwards for 50 km to the coast near Gladstone, and a longer profile running for up to 370 km west from the Callide mine.

To the east of the Callide mine, the Pg wavegroup has an apparent velocity of 6.06 km/s, and an intercept time of 0.1 seconds. To the west, a group of arrivals is observed over a distance of 40 km, with an apparent velocity of 5.11 km/s, and an approximately zero intercept time. This group is succeeded by a Pg wavegroup with an apparent velocity of 6.46 km/s and an intercept time of 0.45 seconds. As with the Moura and Kianga record sections, the thick sediments of the Mimosa Syncline produce a time delay in the arrivals of the Pg wave group between the distances of 65 and 235 km west of the Callide mine.

The Pn wavegroup, displayed in the record section of Figure 3-17, has much stronger onsets than observed in the Moura-Kianga record sections. The apparent velocity of the Pn wavegroup is 7.987 ± 0.160 km/s, and the $Pn^{(1)}$ intercept time is 7.202 ± 0.073 seconds, which is significantly larger than the intercept of the Pn wavegroup measured from the Moura-Kianga record sections. Another notable difference is the absence of any strong arrivals corresponding to the Pm cusp. The Pj phase has a smaller amplitude, and higher characteristic frequency in this Callide record section, (Fig. 3-17), and is not observed in the other two Callide record sections. A strong onset occurs in the record section of Figure 3-18 at around 250 km west of the source, and at a reduced travel time of seven seconds. However, this phase is only coherent over a few traces (of the order of 20 km).

There is evidence of a kink in the onsets of the Pg wavegroup to the east of Callide, with onsets at distances greater than 20 km east of the source arriving around 0.25 seconds earlier. The actual location of

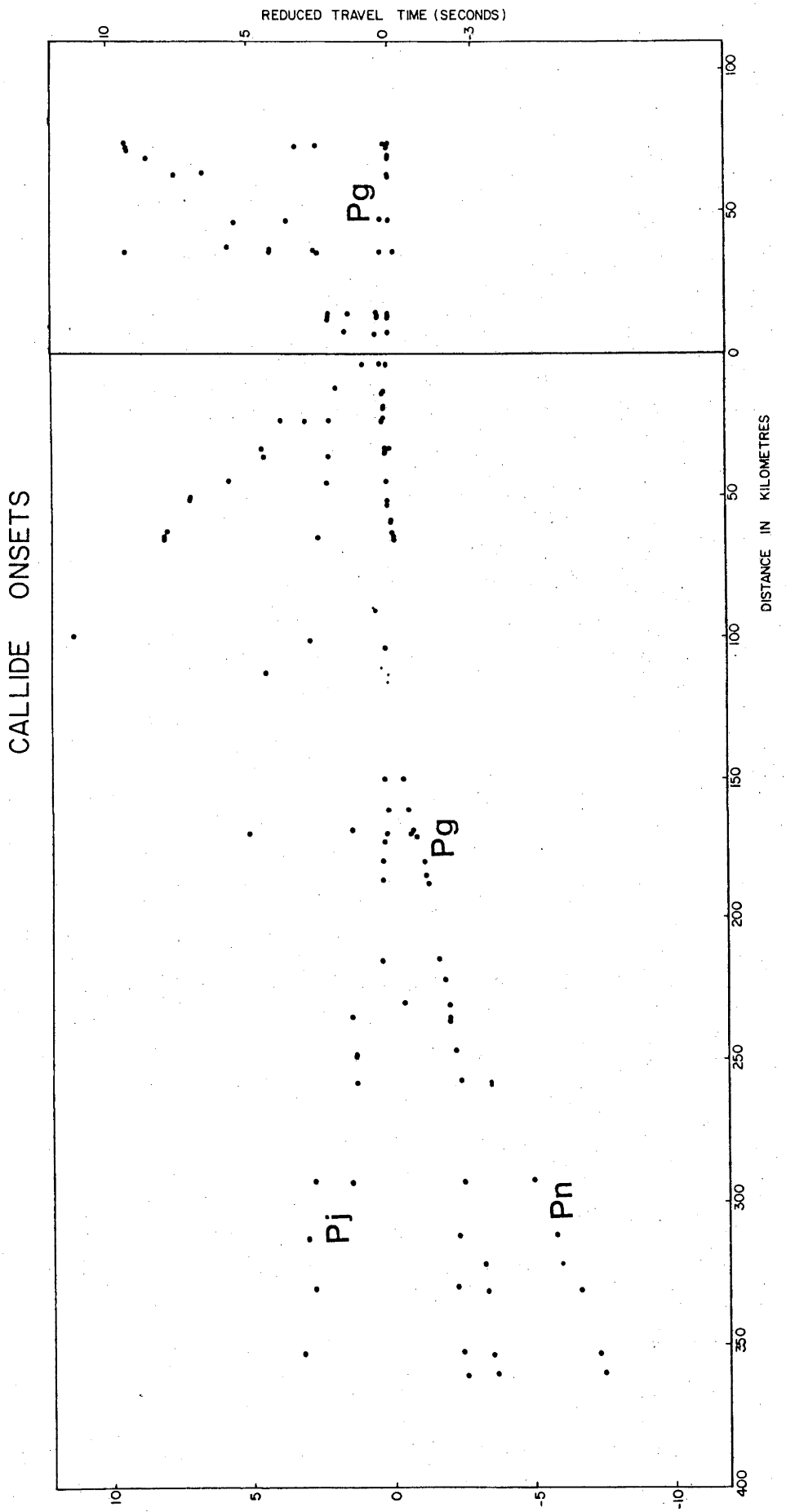

Figure 3.17

Hodograph of onsets recorded from Callide explosions, (as for Fig. 3.4).

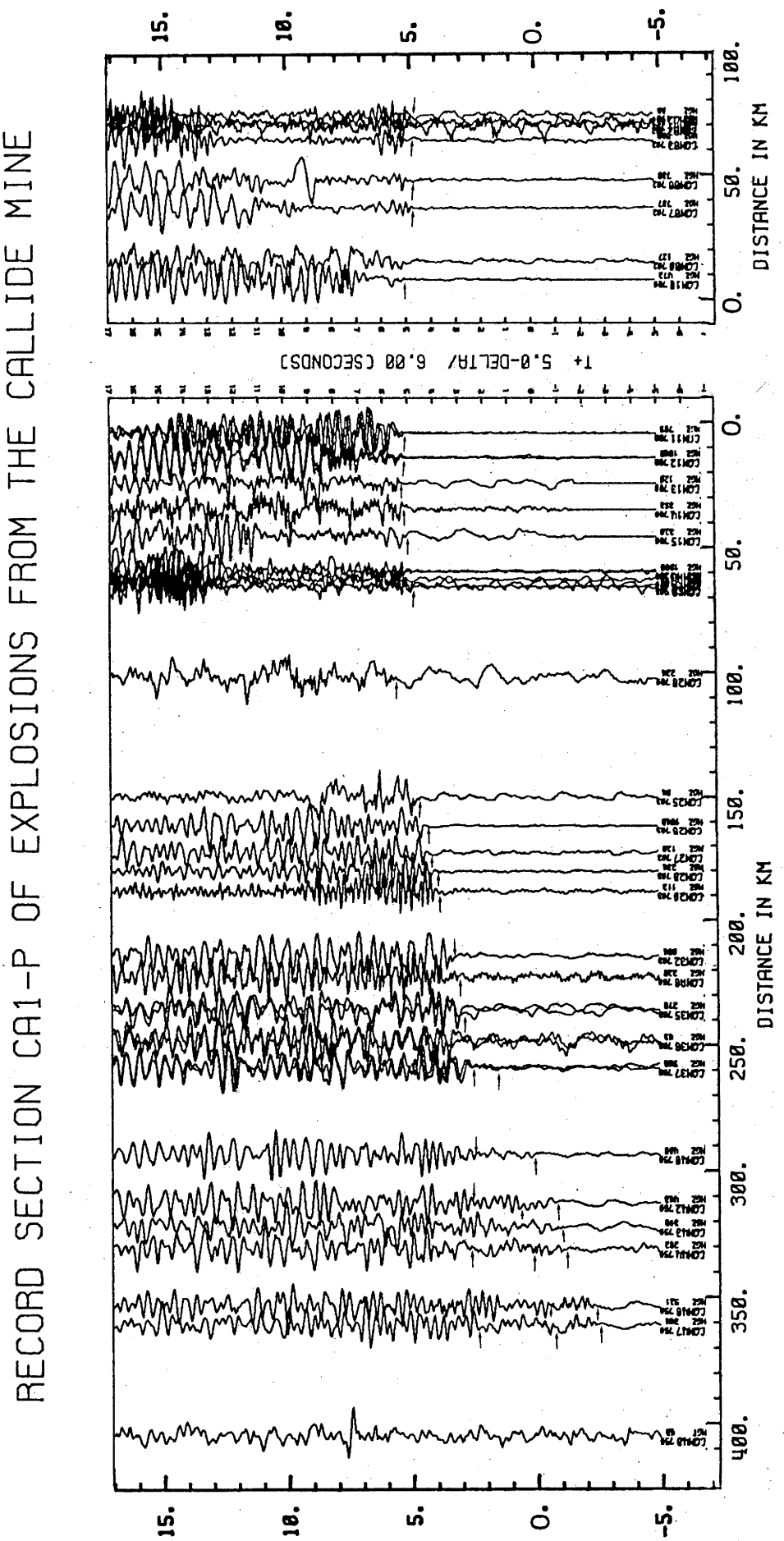

Figure 3.18

Composite vertical component P-wave record section of Callide explosions, (CA-1P).

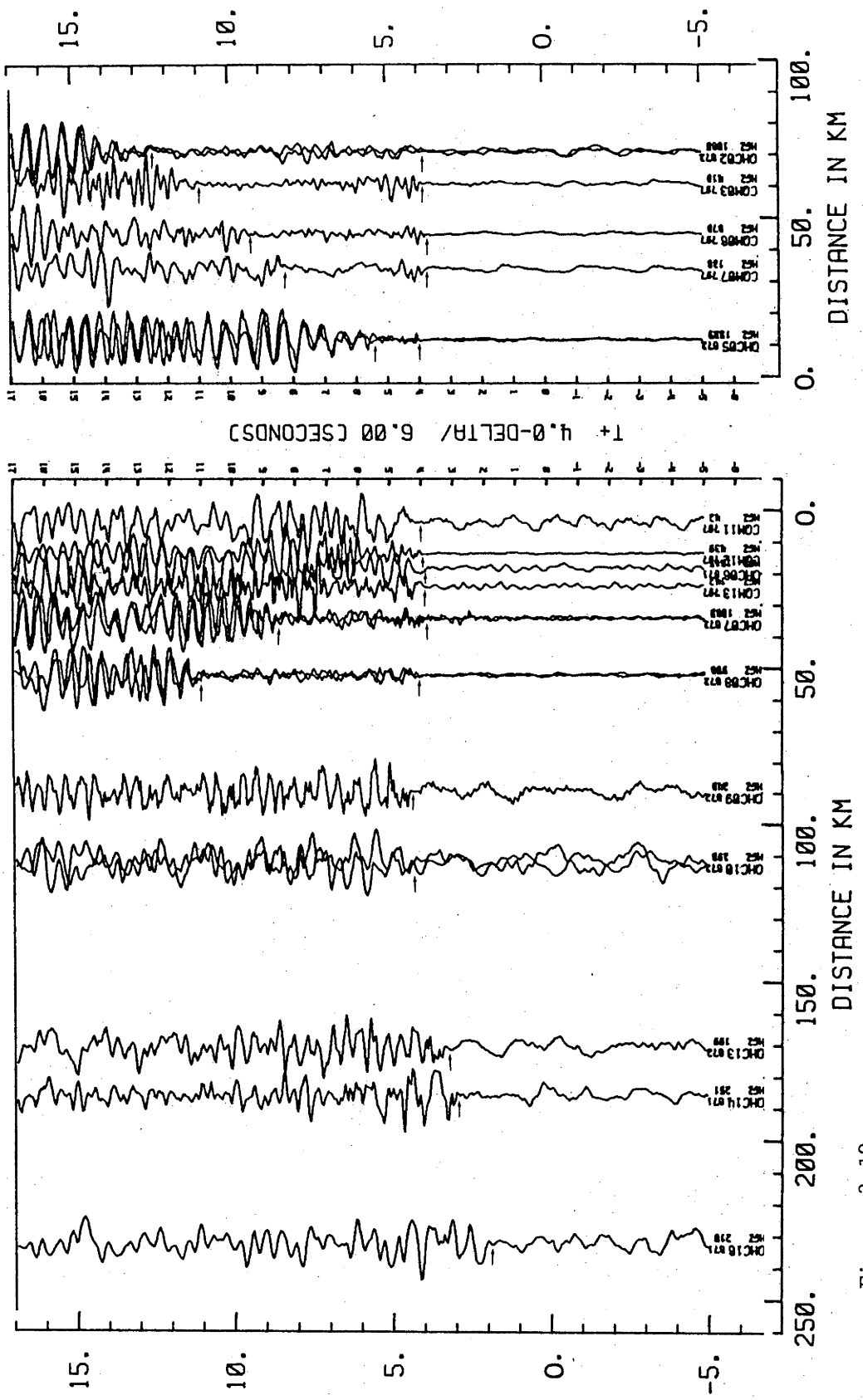

Figure 3.19

Composite vertical component P-wave record section of Callide explosions, (CA-2P).

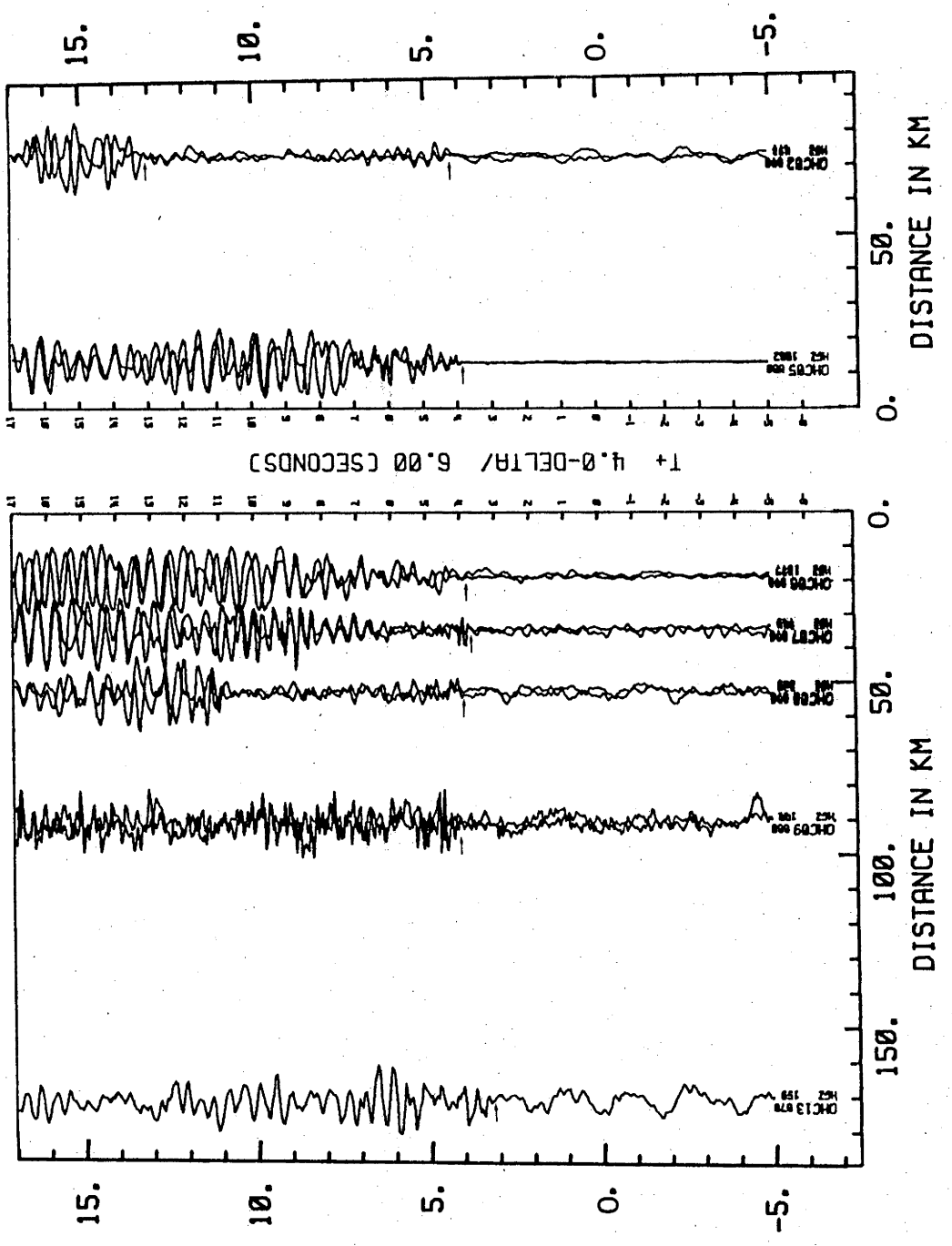

Figure 3.20

Composite vertical component P-wave record section of Callide explosions, (CA-3P).

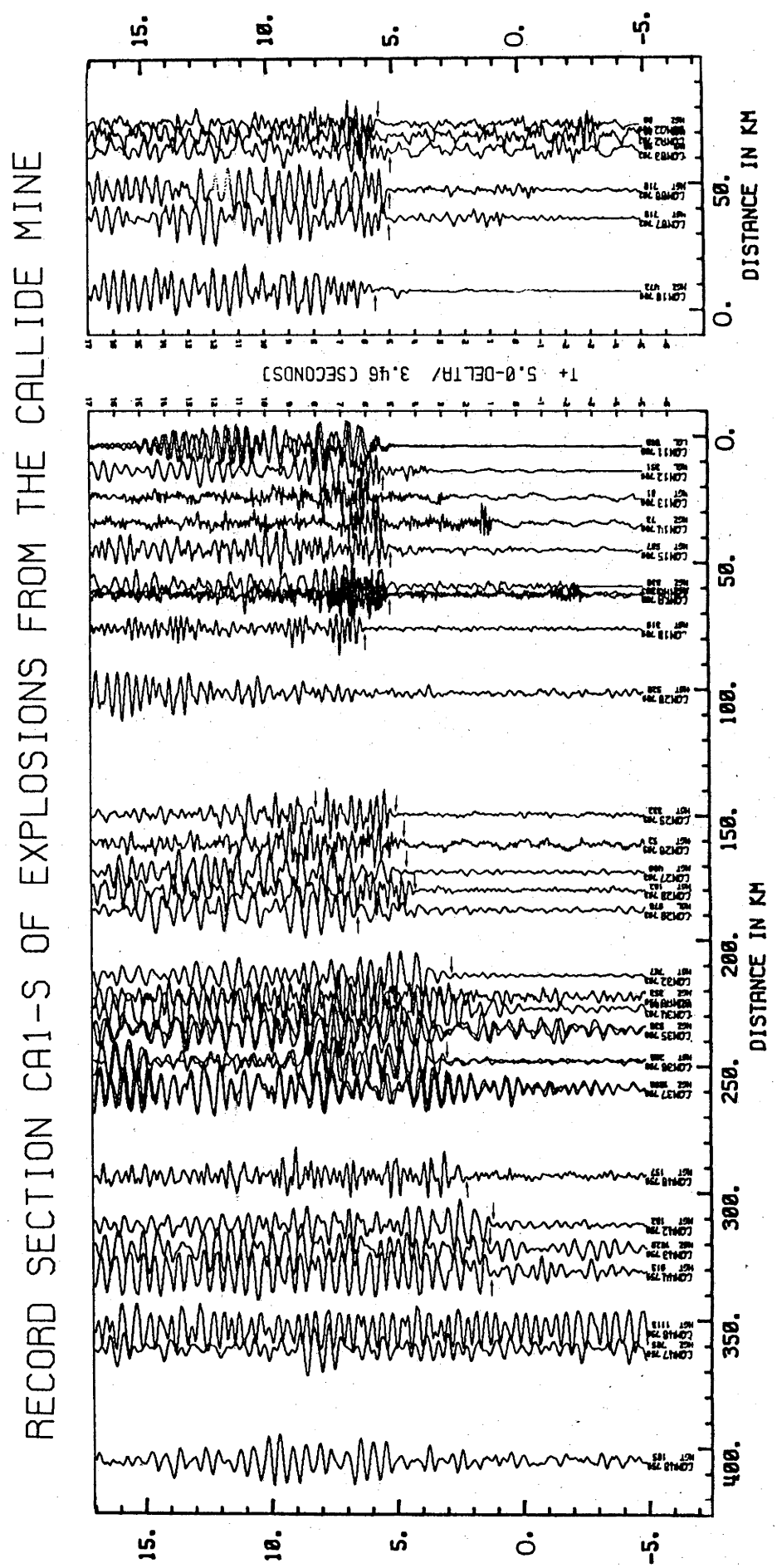

Figure 3.21

Composite S-wave record section of Callide explosions, (CA-1S).

this kink has been displaced 20 km to the east in the Callide record sections, relative to its position in the Moura and Kianga sections, and a smaller offset in the Callide section is observed.

A shear wave record section of Callide events is given in Figure 3-21. Strong Sg onsets occur west of the Callide mine to a distance of around 65 km, where this wavegroup is delayed by around 1.5 seconds by the sediments of the Mimosa Syncline. The Sg onset at site COM20 (Figure 3-21) has a considerably smaller amplitude than the Sg onsets on the traces to either side. Beyond the Mimosa syncline, the onsets of this wavegroup are relatively clear out to a distance of 330 km, beyond which the signal strength of the shear wave onsets deteriorates markedly. In the distance range 150 to 190 km, relatively larger amplitude onsets of the Sm/Sn cusp are observed, but at larger distances, neither the Sm or the Sn onsets are clearly identifiable. The apparent velocity of the Sg wavegroup is 3.76 km/s.

3.5.7 Interpretation of the Moura, Kianga and Callide. record sections.

The first and most obvious feature of all record sections from these mines is the pronounced delay caused by the thick section of low velocity sediments of the Bowen Basin, particularly in the vicinity of the Mimosa Syncline, (see Fig. 3-4 and 3-17). As the structure of the basin varies along the profile, the delay caused by the Bowen Basin sediments must be removed to enable interpretation of the lower crustal structure. To calculate this delay, two complementary approaches have been employed.

The Pg onsets outside the region of the Bowen Basin were interpolated back through the delayed range, with an apparent velocity of 6.37 km/s, obtained from the generalized analysis. Subtracting this postulated onset time in the absence of the Bowen Basin from the observed onsets gives the time delay of the sediments shown in Figures 3-22 and 3-23. Using an average basin velocity of 4.35 km/s obtained from the short refraction array, this delay time can be inverted to give the structure of the basin. The results of this inversion are also shown in Figures 3-22 and 3-23, and agree well with the general shape of the basin obtained from geological considerations (Dickens and Malone, 1973). However, in using this technique, a small error in the measurement of the onset time will result in a relatively large error in the resultant basin depth, so that the derived structure cannot be considered to give the exact depths.

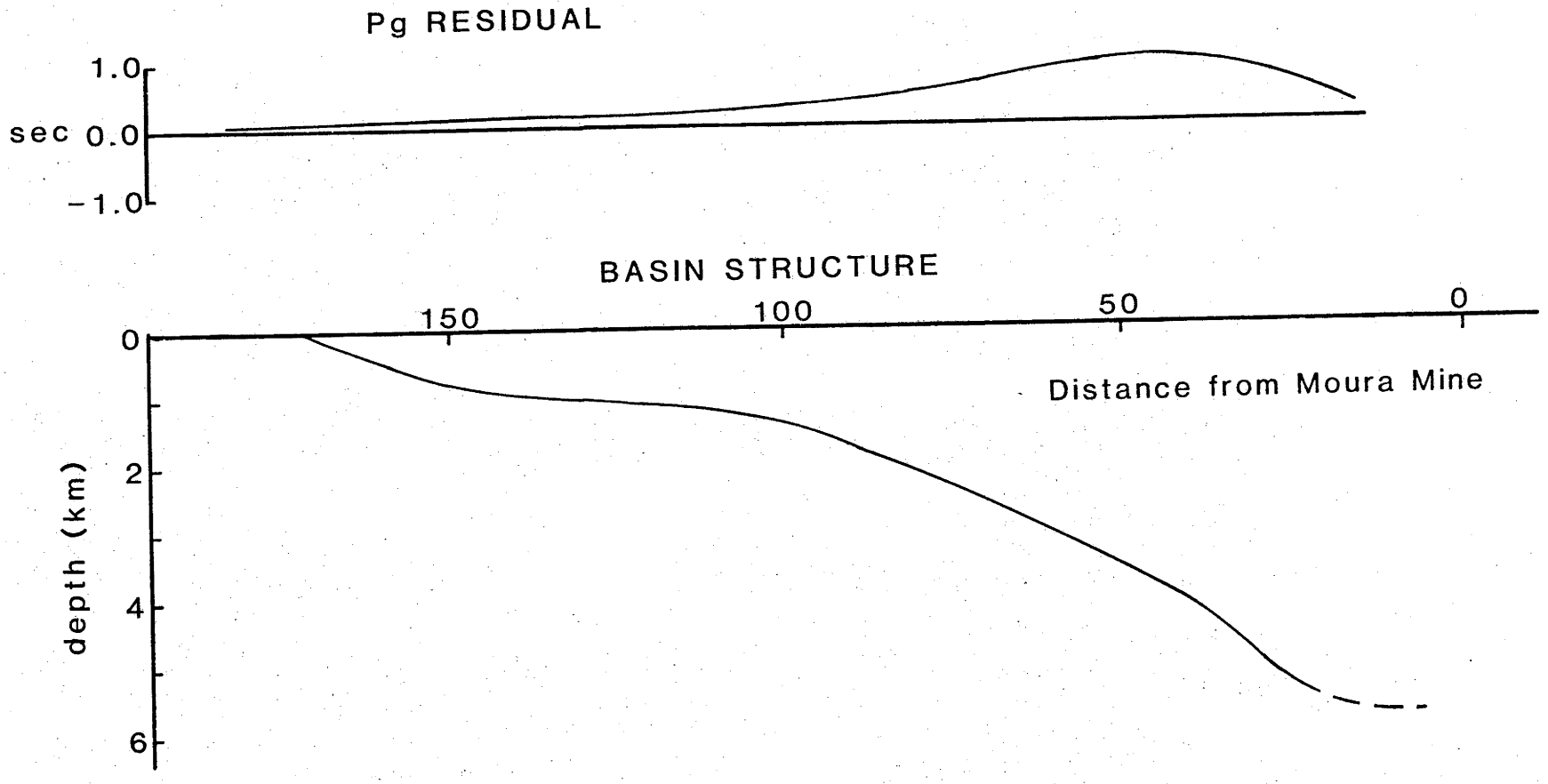

Figure 3-22.

Pg residuals from Moura records, and the inverted Bowen Basin structure.

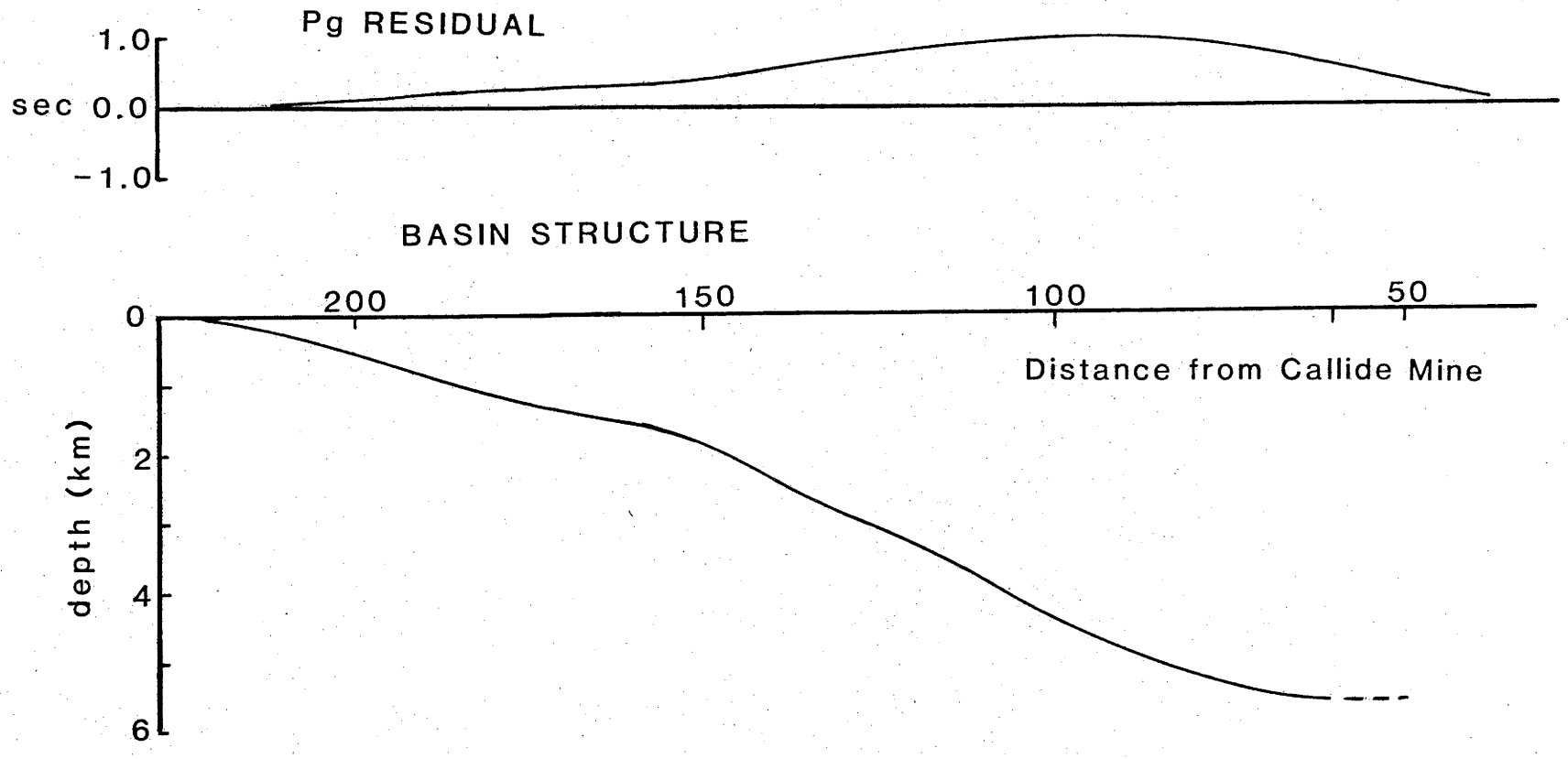

Figure 3-23
Pg residuals from Callide records, and the inverted Bowen Basin structure.

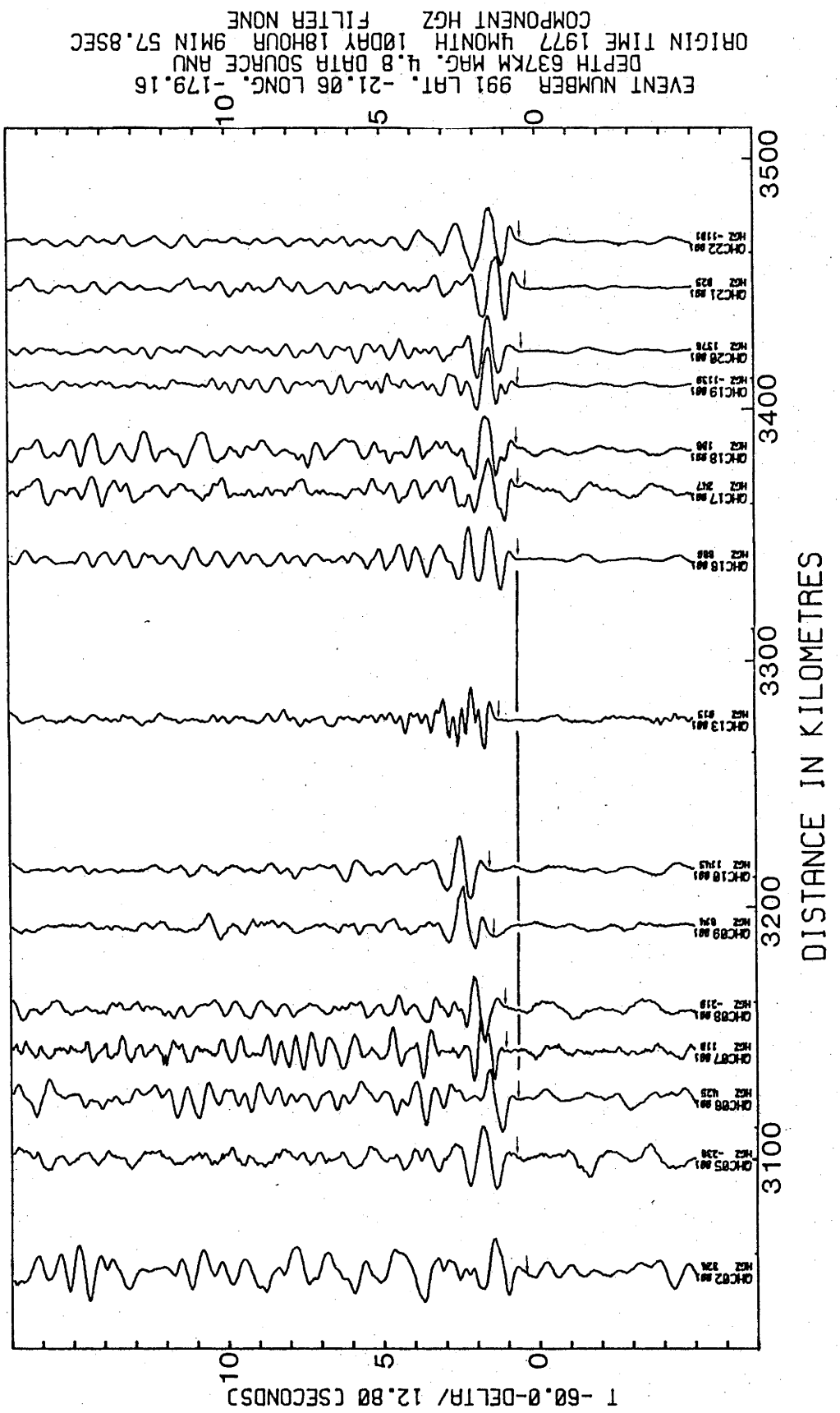

Figure 3.24

Residuals from a teleseismic event recorded across the Bowen Basin.

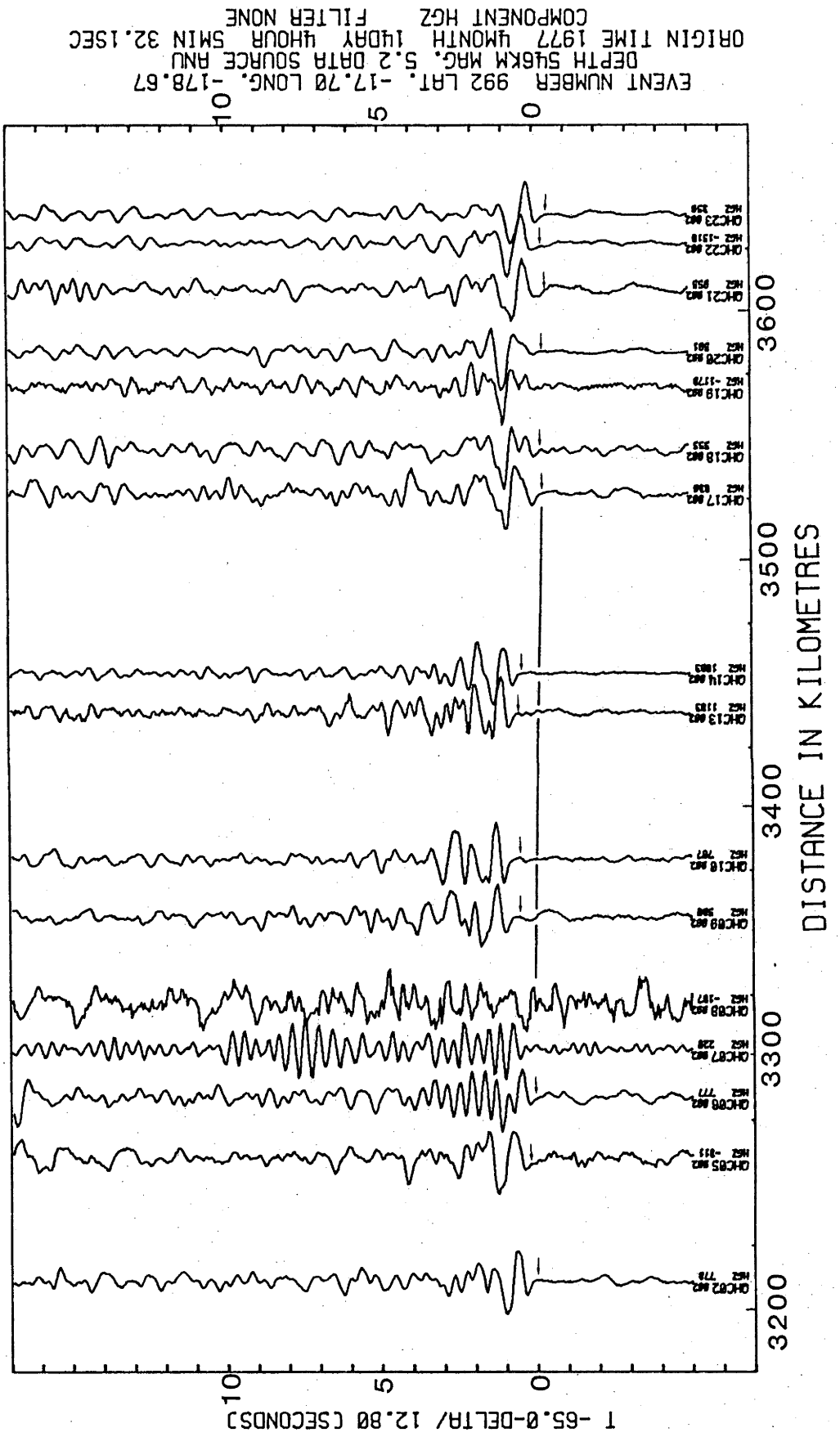

Figure 3.25

Residuals from a teleseismic event recorded across the Bowen Basin.

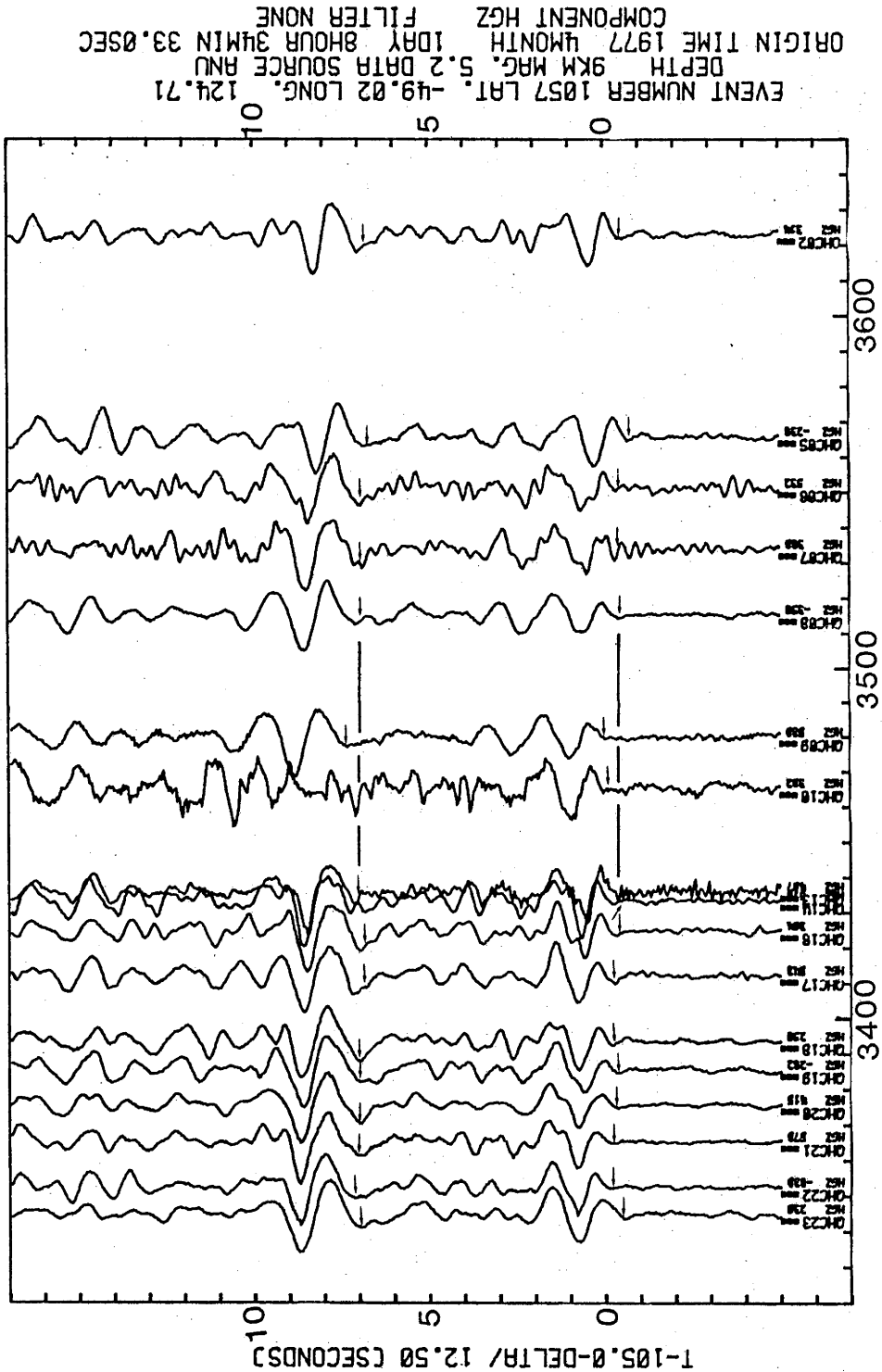

Figure 3.26

Residuals from a teleseismic event recorded across the Bowen Basin. The first onset is P, while the later one is pP, which displays the same residual pattern.

However, the relative errors of the onsets could be expected to be better than the absolute errors, so that the overall shape of the basin would be more reliable than the calculated depths. The major features of the Bowen Basin are the pronounced deepening near the eastern margin, corresponding to the Mimosa Syncline and the shelf-like structure of the western extent of the basin.

The second approach uses the residuals of teleseismic events which arrive with a high apparent velocities. Care must be taken to ensure that a single branch of the travel time curve is observed at all stations along the profile. The record sections obtained from the recording of four earthquakes from various regions are shown in Figures 3-24 to 3-26; the arrival times are indicated by an arrow. All four record sections display the onset delay due to the Bowen Basin, with the largest delay occuring at the stations QHC09 and QHC10 (corresponding to the deepest portion of the basin.) Event 1057 (Figure 3-26) also displays clear pP onsets, which follow the P onsets, and which exhibit the same residual pattern. The residual delays of the teleseimic events are smaller than those associated with the Pg wavegroup, as the rays travel in a more nearly vertical raypath through the sediments. However, an analysis of the residuals associated with these events gives a similar result to the analysis based on the Pg delays.

A model has been constructed on the basis of raytracing, for the Moura-Kianga and Callide P wave data, (stripped of the Bowen Basin sediments). The apparent velocities and intercept times have been inverted (Dobrin, 1960), and this model has been iteratively adjusted to fit the onset times. In comparing this model with the onset plots, it must be borne in mind that the seismic waves from the Moura-Kianga explosions will travel through the section of low velocity sediments before reaching the basement, and this will cause an intercept delay of the observed times relative to the stripped model times.

This model, together with the corresponding travel time-distance graph is shown in Figures 3-27 and 3-28. Spherical Earth layers with no lateral variation have been assumed in producing this Earth model, and this assumption is totally inadequate in regions as structurally complex as the Tasman Geosyncline region of eastern Australia. For this reason, a Snell's Law raytracing programme (SEISRAY, developed by Mr C. Collins of the BMR) which calculates reflection times and distances in a laterally varying structure, has been used to model the structure of the crust along this

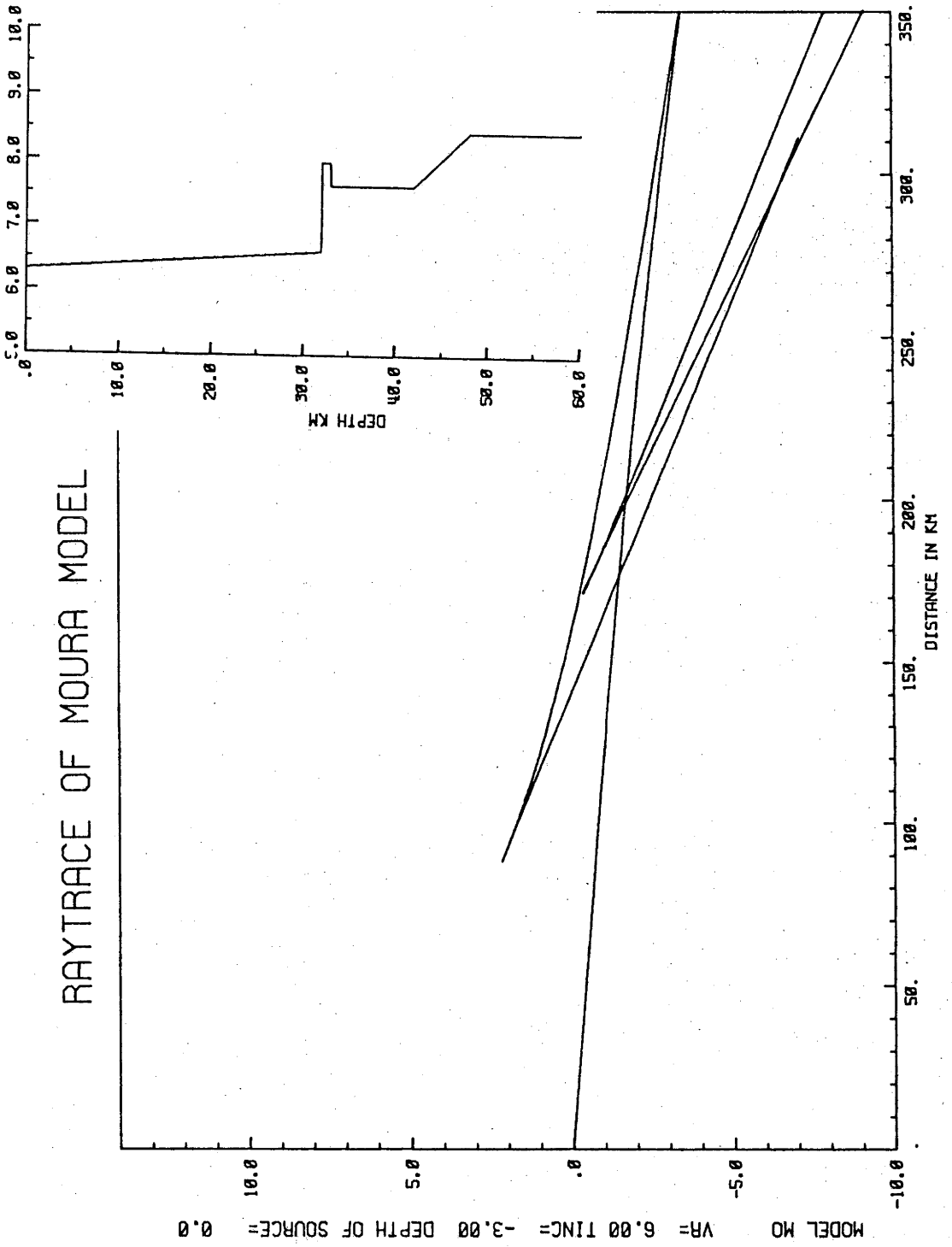

Figure 3.27

A raytracing travel time distance curve of the derived crustal model from the Moura mine data, (stripped of the Bowen Basin).

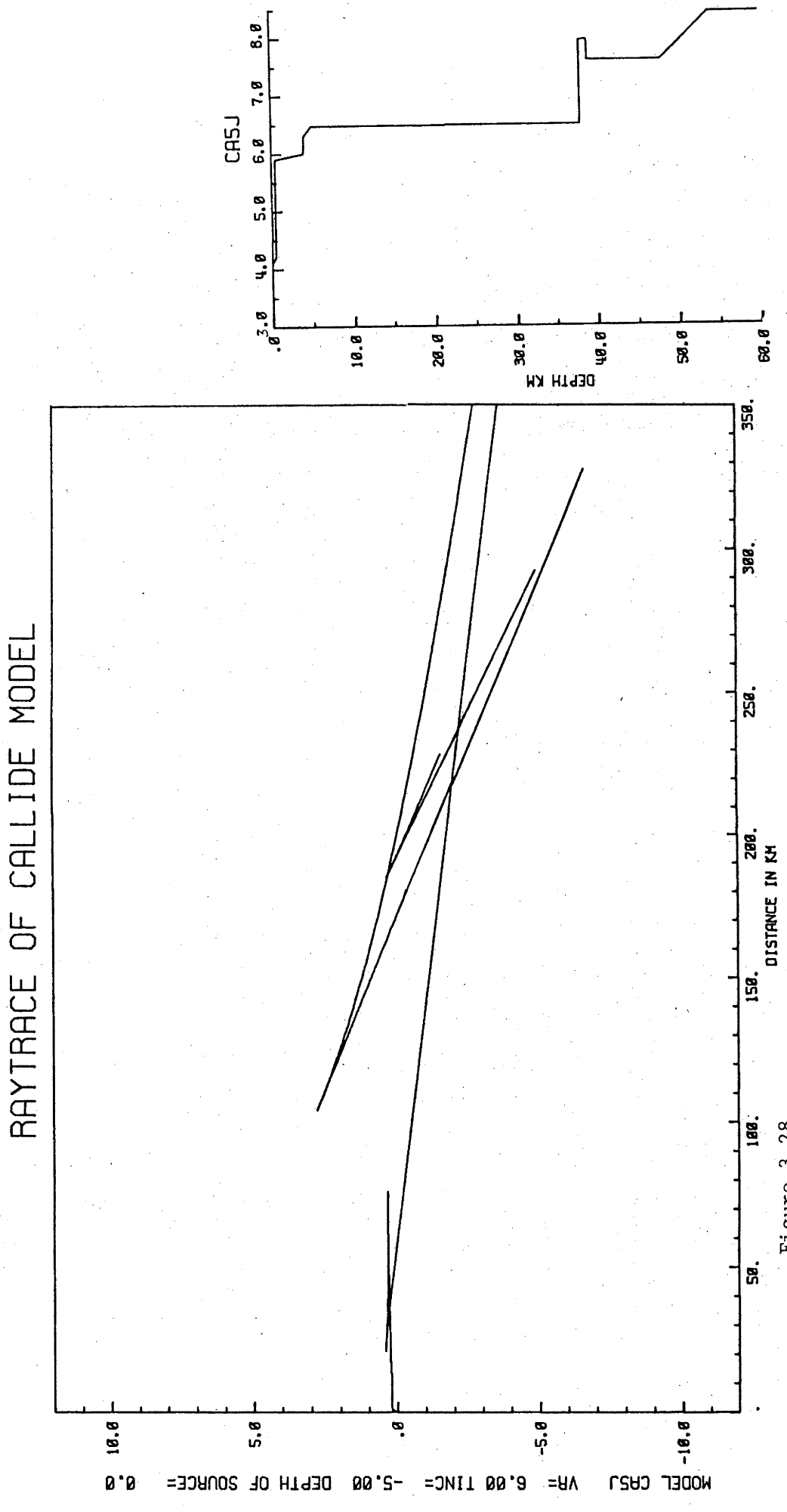

Figure 3.28

A raytracing travel time distance curve of the derived crustal mode from the Callide mine data, as for Fig. 3.27.

profile in greater detail. The model, derived by trial and error, is shown in Figures 3-29 and 3-30. While the SEISRAY[1] programme allows lateral variation of structure, it assumes layers having a homogeneous velocity, unlike a similar programme, described by Wills et al.,(1978).

The sediments of the Bowen Basin have been modelled by a layer having a velocity of 4.2 km/s, and a structure derived from the analyses of the Pg and teleseismic delays. Beneath this, a thin layer with a velocity of 5.9 km/s has been incorporated, to explain the arrivals with a corresponding apparent velocity which are observed for 40 km west of Callide. No evidence for this refractor is observed in the record sections of the Moura/Kianga explosions, but this may be due to the complicating effects of the Bowen Basin. Therefore a layer having this velocity has been modelled to underlie the sediments of the Bowen Basin, and could correspond to the Permian sequence, thought to underlie the Bowen Basin series. Beneath this layer, the upper crustal rocks have been modelled with a velocity of 6.3 km/s, changing to 6.4 km/s at a depth of 8 km, to infer a slight velocity gradient.

The form of the Mohorovicic discontinuity has been indicated by the results of the time term analysis (Chapter 4). This includes the substantial increase in depth of the Moho towards the eastern end of the section, and the relatively constant Moho depth in the western end of the profile. As the SEISRAY programme only calculates reflected arrivals, the refraction branches of the arrival time curve must be drawn in as being asymptotic to the reflected onsets, and with the appropriate apparent velocity.

The delay in the Pg caused by the Bowen Basin sediments is clearly seen, and the results indicate strong onset on the upward deflection of this delayed region, and very weak Pg arrivals in the distance range around 90 km west of Callide. At larger distances the onsets are refracted, so that they are not accounted for by the SEISRAY programme. The group of arrivals which occur above the Pg onsets around the distance range of 60 km west of Callide, corresponds to rays which have travelled along the 5.8 km/s layer, and then have been refracted to the surface by the lower velocity sediments. Both traces of QHC09 in Figures 3-19 and 3-20 show a relatively strong arrival following the Pg onset, which is thought to correspond to this SEISRAY onset.

The strong Pm-Pn cusp is clearly indicated by the SEISRAY plot. The onsets show that while the structure of the upper crustal layers

1 See C Collins' unpublished BMR report on SEISRAY programme.

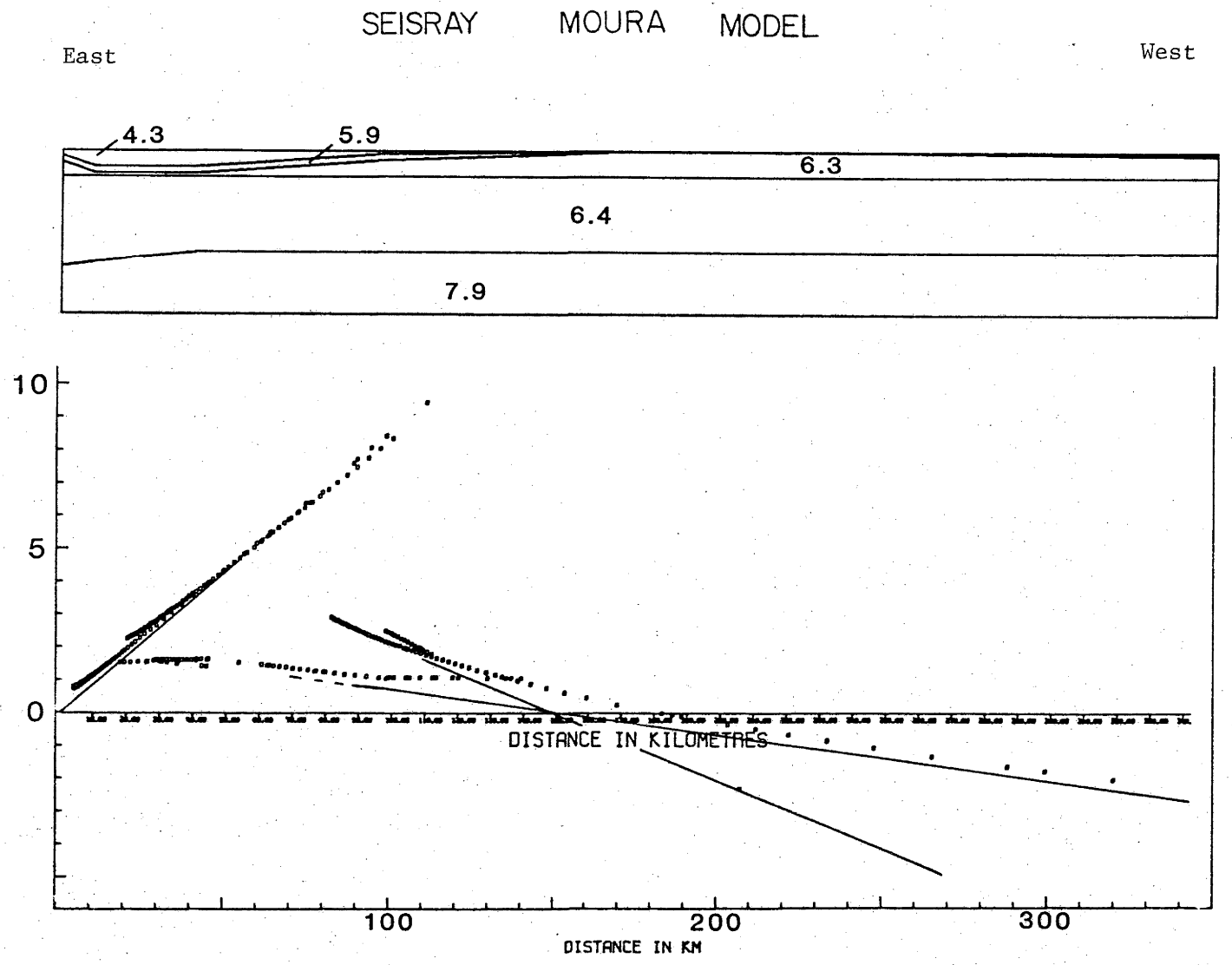

Figure 3.29

A SEISRAY travel time distance plot for the Moura model.

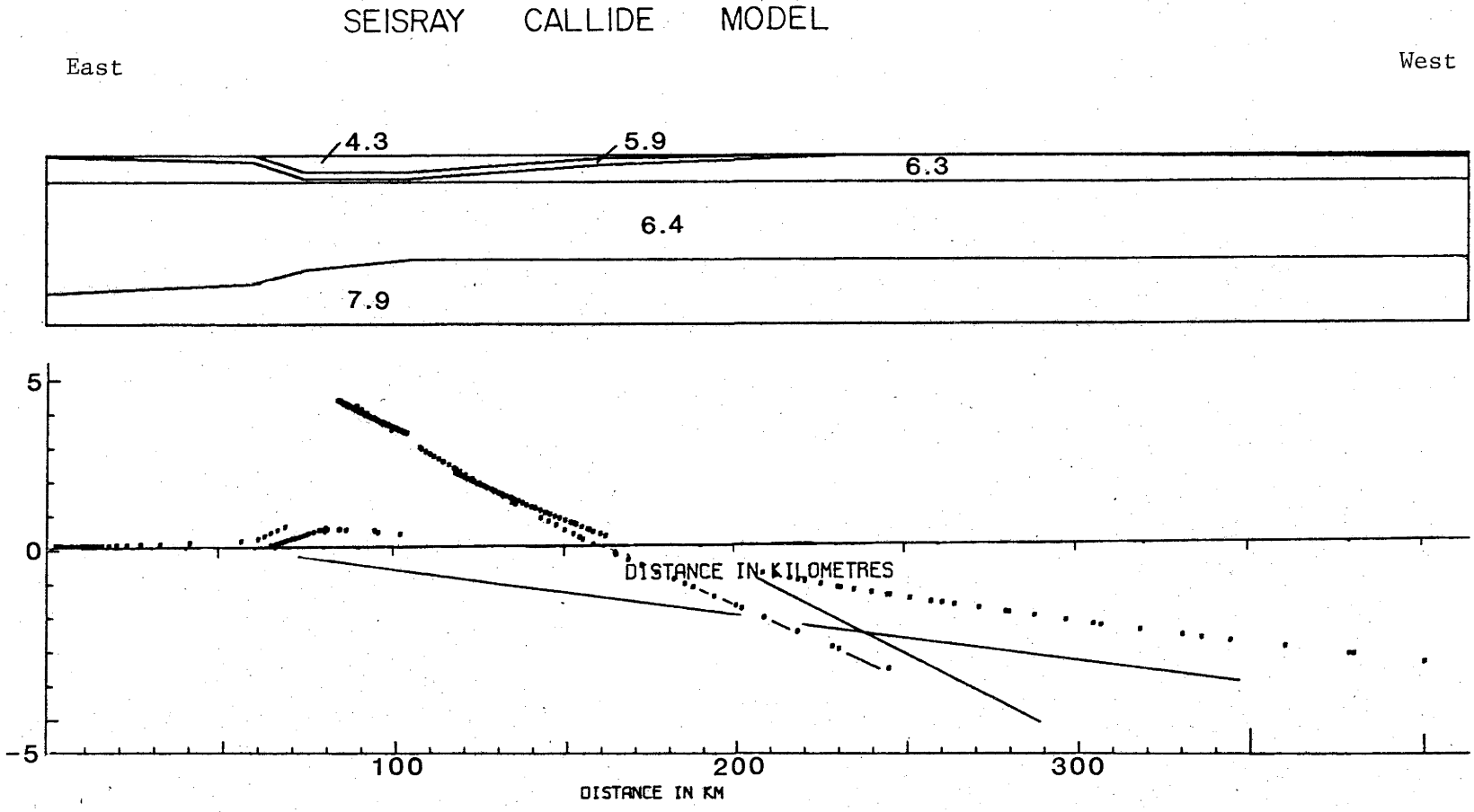

Figure 3.30

A SEISRAY travel time distance plot for the Callide model.

does not significantly change the form of this retrograde branch for the Moura/Kianga record sections, the slope on the Moho together with this upper crustal structure disrupts the Pm branch observed from Callide explosions. As no clear Pn/Pm cusp is observed from the Callide shots, this is attributed to the structure of the Moho beneath Moura.

The comparatively low amplitude of the Pn arrivals from Moura/Kianga explosions, relative to the smaller (in terms of weight of explosive) Callide explosions may be explained by the defocusing effect of the steeply dipping (14°) edge of the Bowen Basin beneath the Moura/Kianga mines.

A major limitation of the data gathered from the QHC and CQM profiles is that, due to the fixed geometry of the coal mines, these refraction profiles were not reversed. Cunningham (1974) developed an interpretation technique for use with single-ended refraction profiles. The difference in intercept times for the Pn phase recorded from the Moura and Callide mines can be used together with the apparent velocities, to solve for the true refractor velocity, and the refractor dip. In applying this method, allowance must be made for the variation in thickness of the sedimentary section along the profile. The accuracy of this method depends on the accuracy with which the difference in the two nearly equal intercept times can be determined. The uncertainty of necessary corrections to these intercepts, arising from the delay of the sedimentary section, made this technique inappropriate for determining the Moho structure. It was felt that the Moho structure was more accurately determined from the time term analysis of Chapter 4. Pre-empting the results of the time term analysis, the crustal thickness in the western end of the profile, as interpreted from the delay times, is relatively constant, so that the apparent velocities of 7.96 km/s obtained from both the Moura/Kianga and Callide record section are thought to reflect the true velocity of the sub-Moho mantle.

3.5.8 Description of the Blackwater record sections.

Two composite fan record sections of Blackwater events are shown in Figures 3-31 and 3-32. The Pg wavegroup is the dominant first arrival across the record section. Relatively large onsets are observed on traces CQM20, CQM21, CQM25, and CQM26 of Figure 3-32 and these correspond to the Pm - Pn cusp. These onsets are also observed in Figure 3-31, however the traces at larger distances (smaller azimuth) are unfortunately poorly recorded, owing to the ambient noise of the Moura and Kianga mine

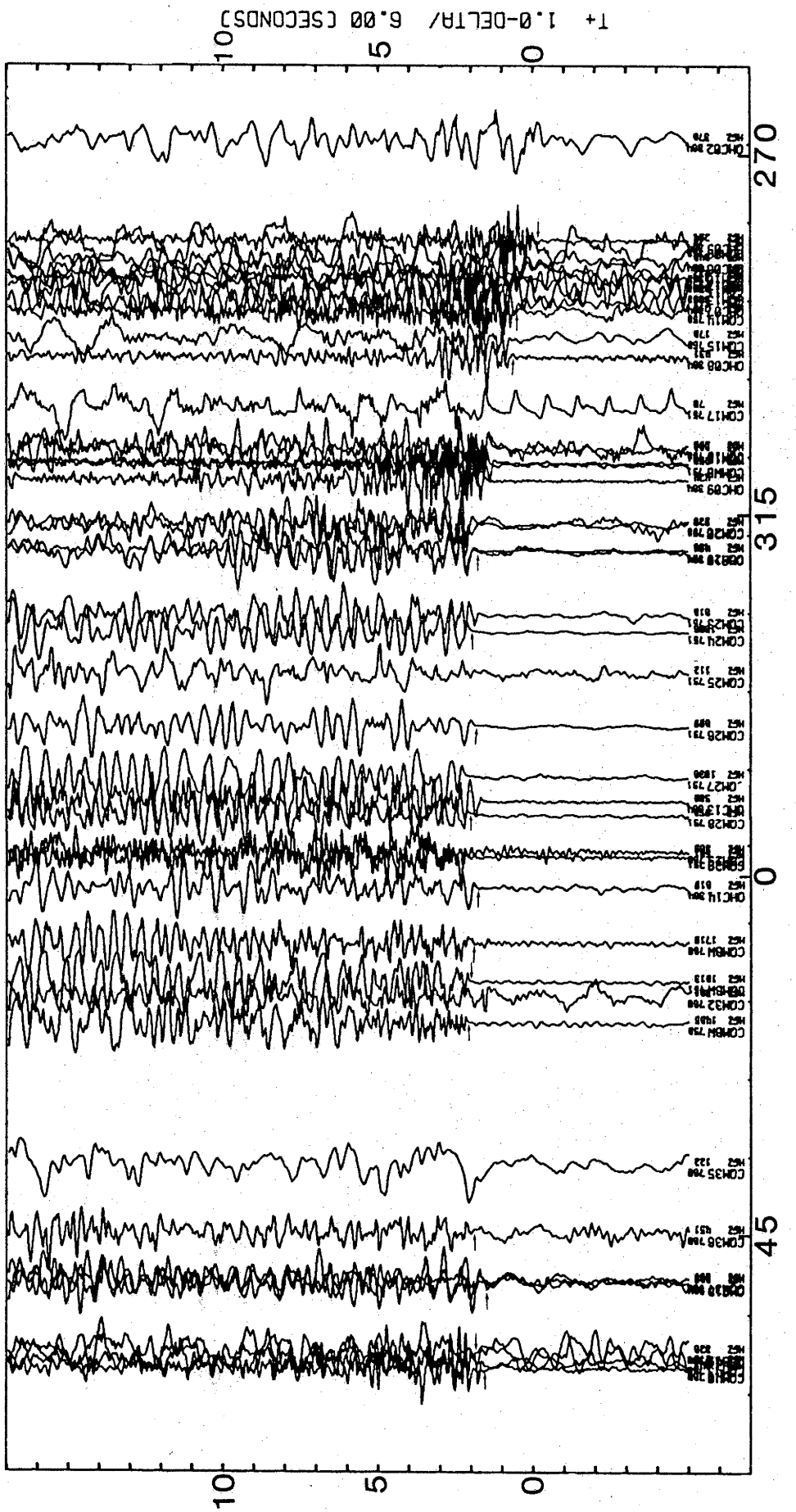

Figure 3.31

Composite vertical component P-wave fan record section of Blackwater mine explosions, (BW-1P). Fan radius = 150 km

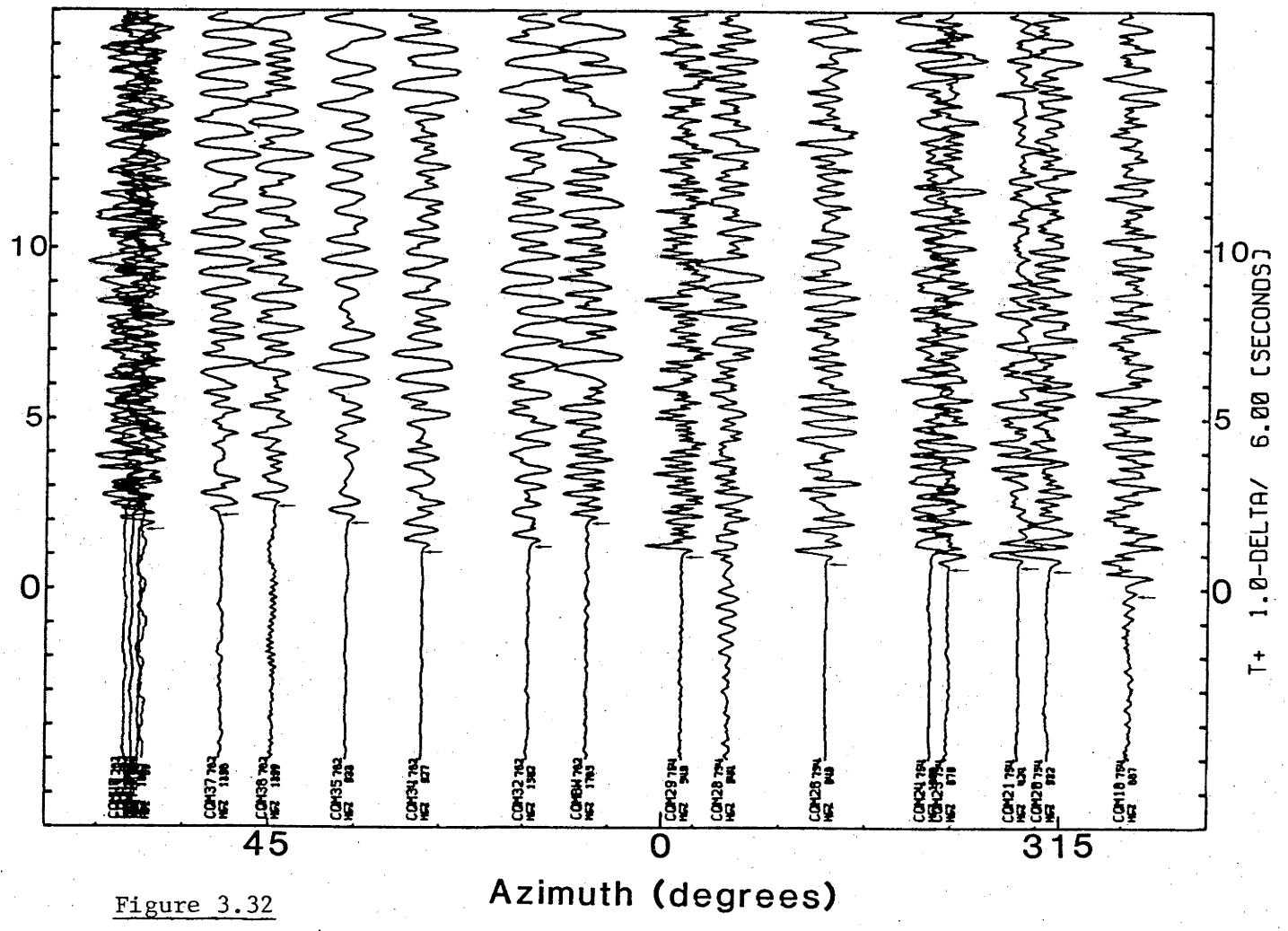

Figure 3.32

Composite vertical component P-wave fan record section of Blackwater mine explosions, (BW-2P). (Fan radius = 150 km)

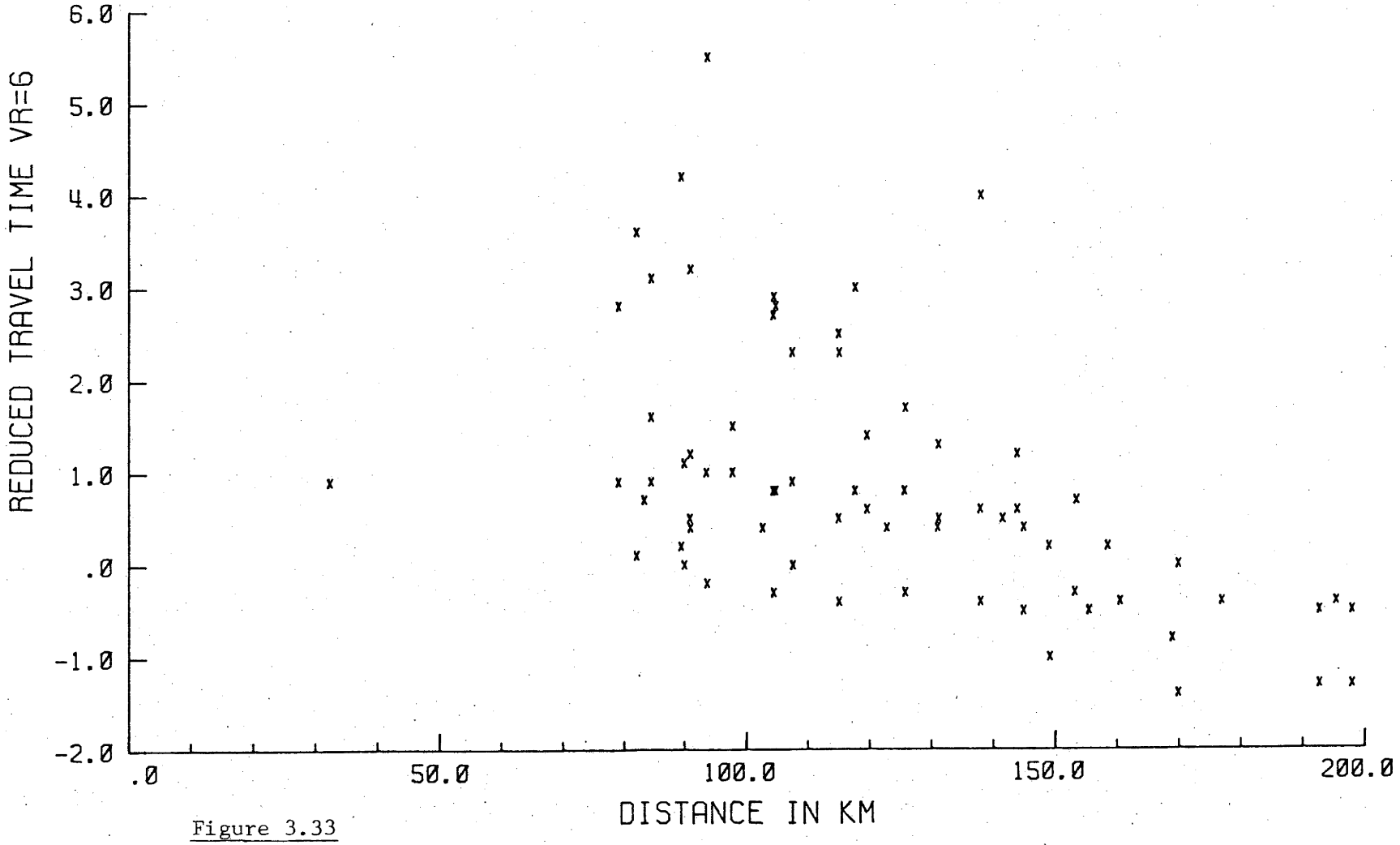

Figure 3.33

A hodograph of onsets from Blackwater explosions, demonstrating the scatter caused by the changing structure of the Bowen Basin along the profile.

operations. The greatest distance at which Blackwater shots were recorded was around 200 km. On the basis of the data from the Moura and Kianga mines, the Pn wavegroup would have been expected to become the first arrival at this distance. The trace from QHC02 in Figure 3-31 has a small onset before the larger Pg arrival, which could be interpreted as a Pn onset. However, the signal to noise ratio is less than one. Other onsets which may correspond to Pn arrivals can be seen in the noiser records at the larger azimuths.

Shear wave records from the Blackwater shots were particularly poorly recorded, so that the S wave records from Blackwater mine will not be considered.

3.5.9 Interpretation of the Blackwater record sections.

Figure 3-33 shows a hodogram of the onsets of the Blackwater events. The variability of these onsets is due to the changing structure of the Bowen Basin along the profile and this cannot satisfactorily be analysed using either the fan record section or the hodograph. The most suitable method for analysing this structure is the time term method, and the application of this method is discussed in Chapter 4.

3.5.10 Description of the Northern Mines record sections.

The three mines, Goonyella, Peak Downs, and Saraji, are collectively referred to as the northern mines, as all three mines lie approximately 300 km north of the profile. The record sections from these mines have been plotted as fan sections, and are shown in Figures 3-34 to 3-36. Events from the Saraji mine produced extremely poor records, with very low signal to noise ratio. Why Saraji shots should have produced such poor record sections is not understood, as the P wave arrivals from the other two northern mines, which are further to the north, were relatively clear, and the Saraji mine detonated similar sized overburden explosions. The record sections of the Saraji events have not been included in the figures.

A fan record section of the Peak Downs event is shown in Figure 3-36. Small but evident Pn onsets are observed at a reduced travel time of around 6 seconds. The generally large Pg onsets arrive with a reduced travel time of between 8 and 9 seconds, although these are more scattered, as can be seeen in the hodograph, Figure 3-38. The third wavegroup is observed only at distances greater than 270 km, and corresponds to the Pj

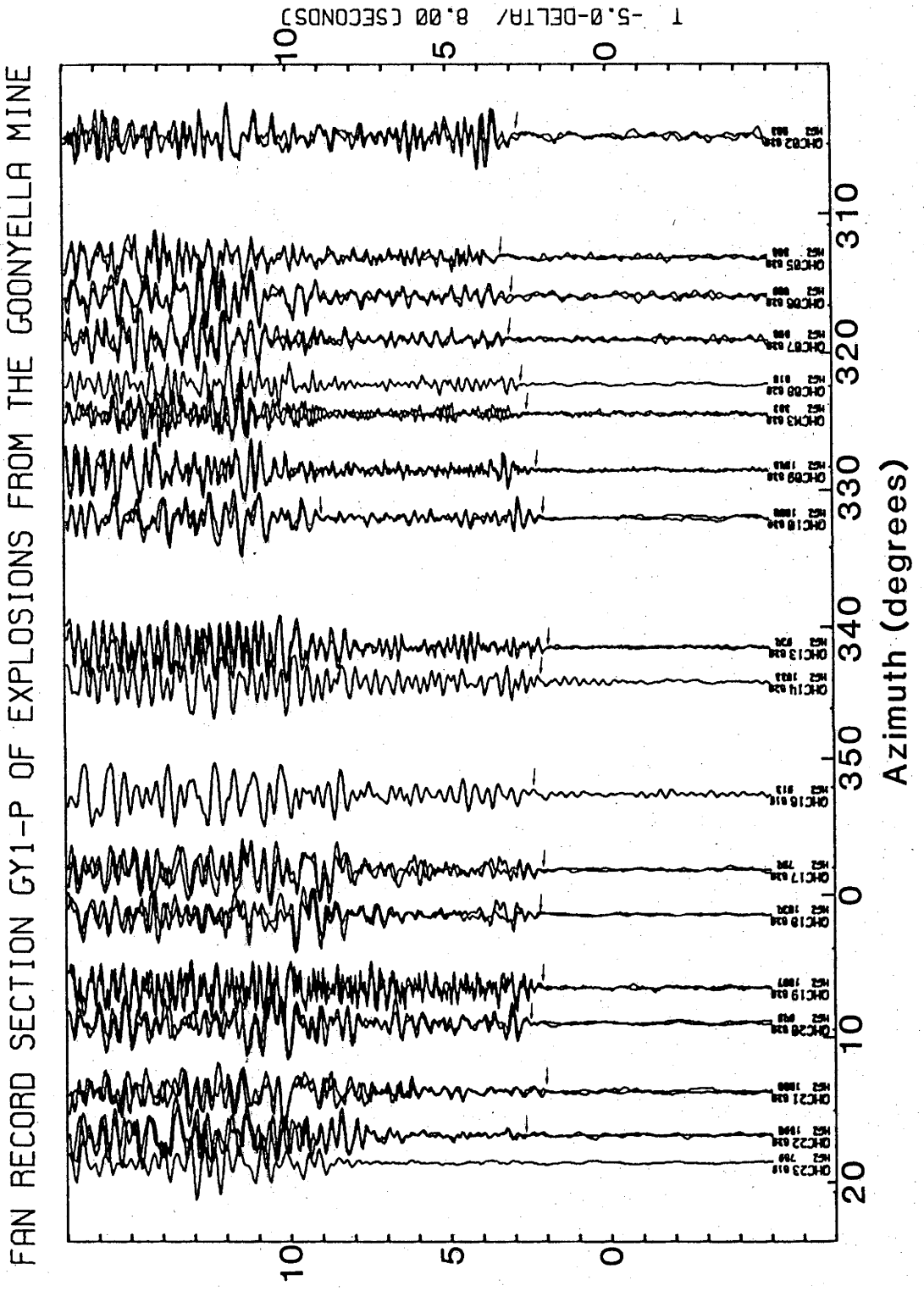

Figure 3.34

Composite vertical component P-wave fan record section of Goonyella explosions, (GY-1P). Fan radius = 250 km

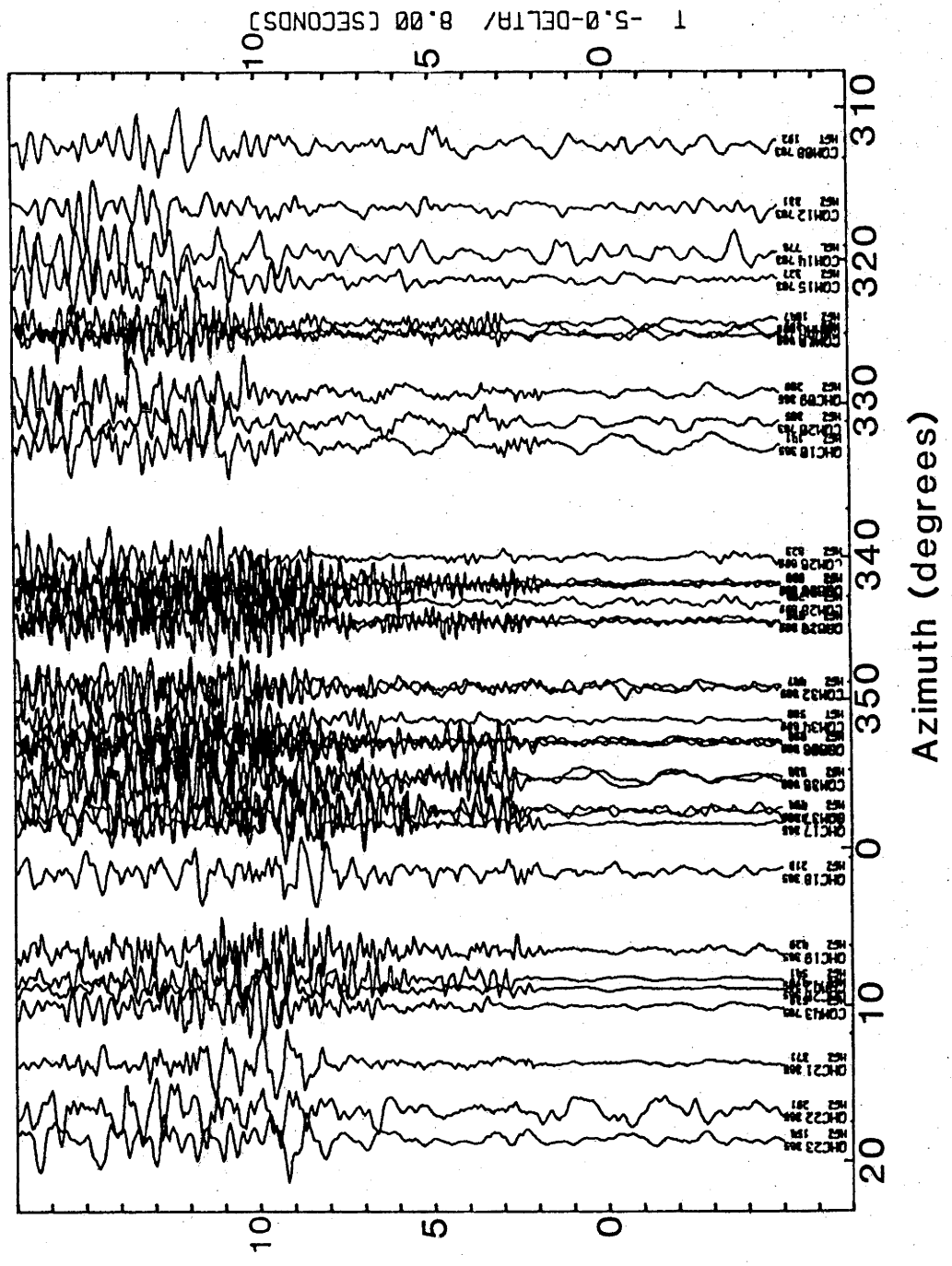

Figure 3.35

Composite vertical component P-wave fan record section of Goonyella explosions, (GY-2P). Fan radius = 250 km

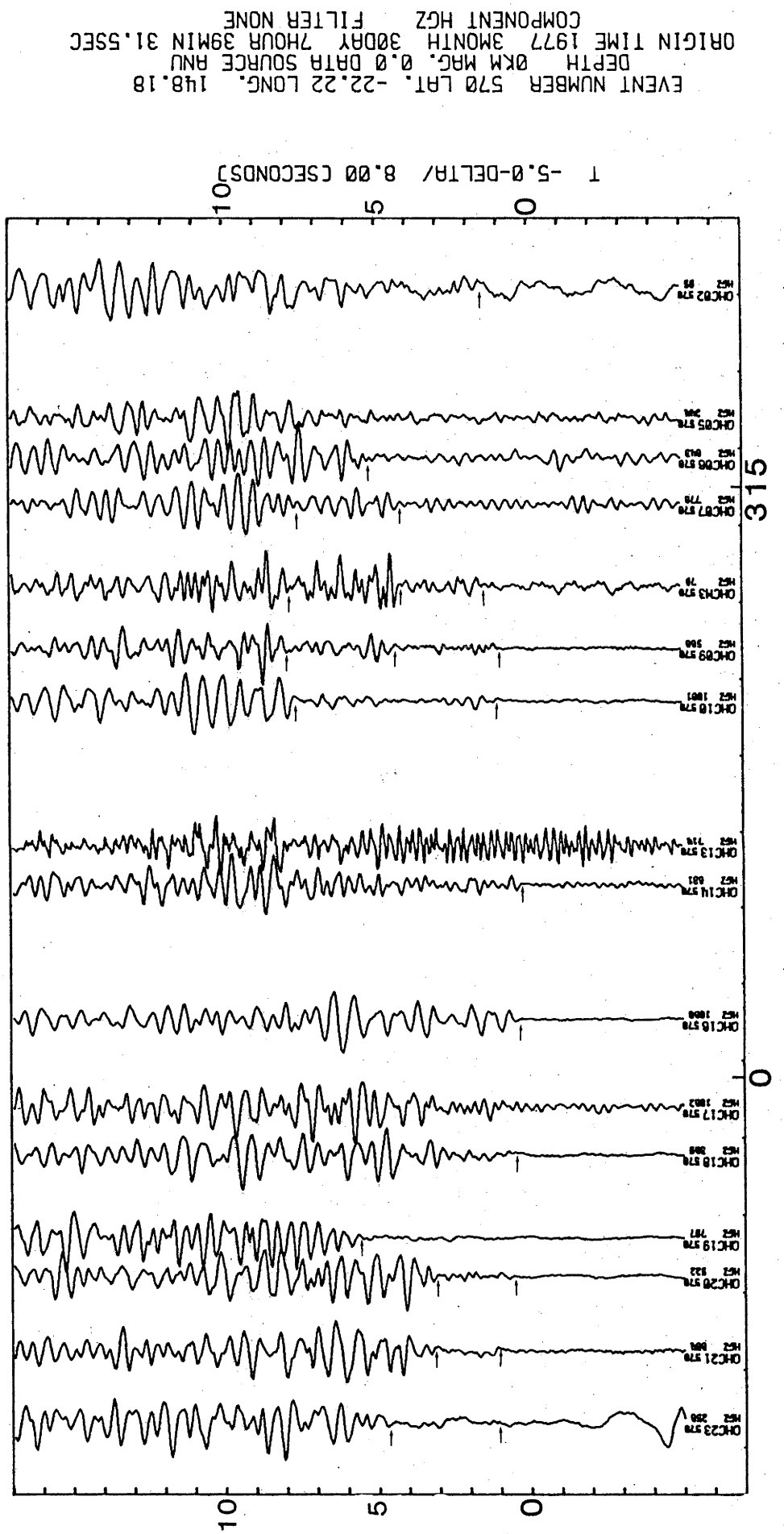

Figure 3.36

Composite vertical component P-wave fan record section of Peak Downs explosions, (PD-1P). Fan radius = 250 km

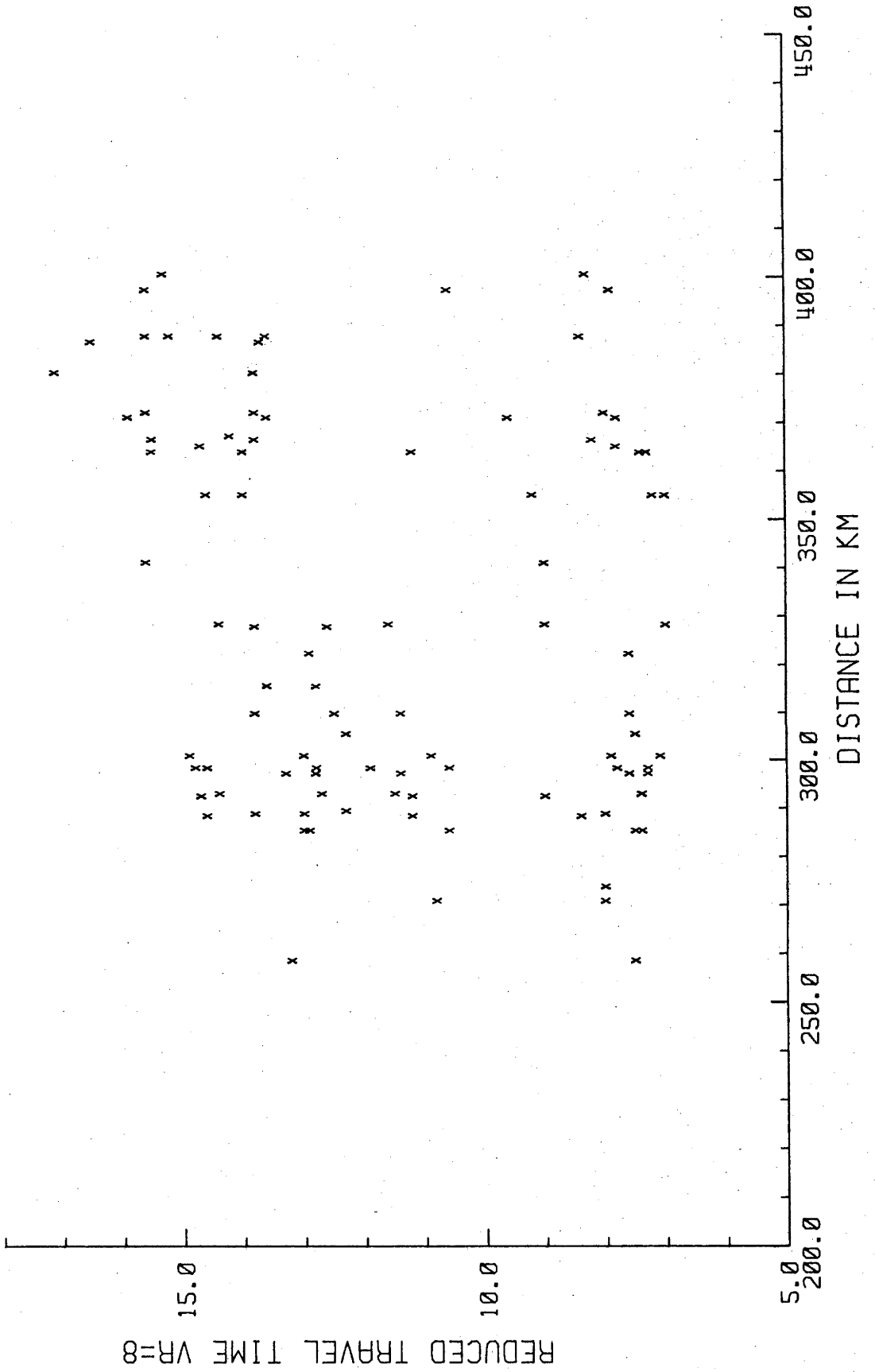

Figure 3.37

A hodograph of arrivals from Goonyella explosions.

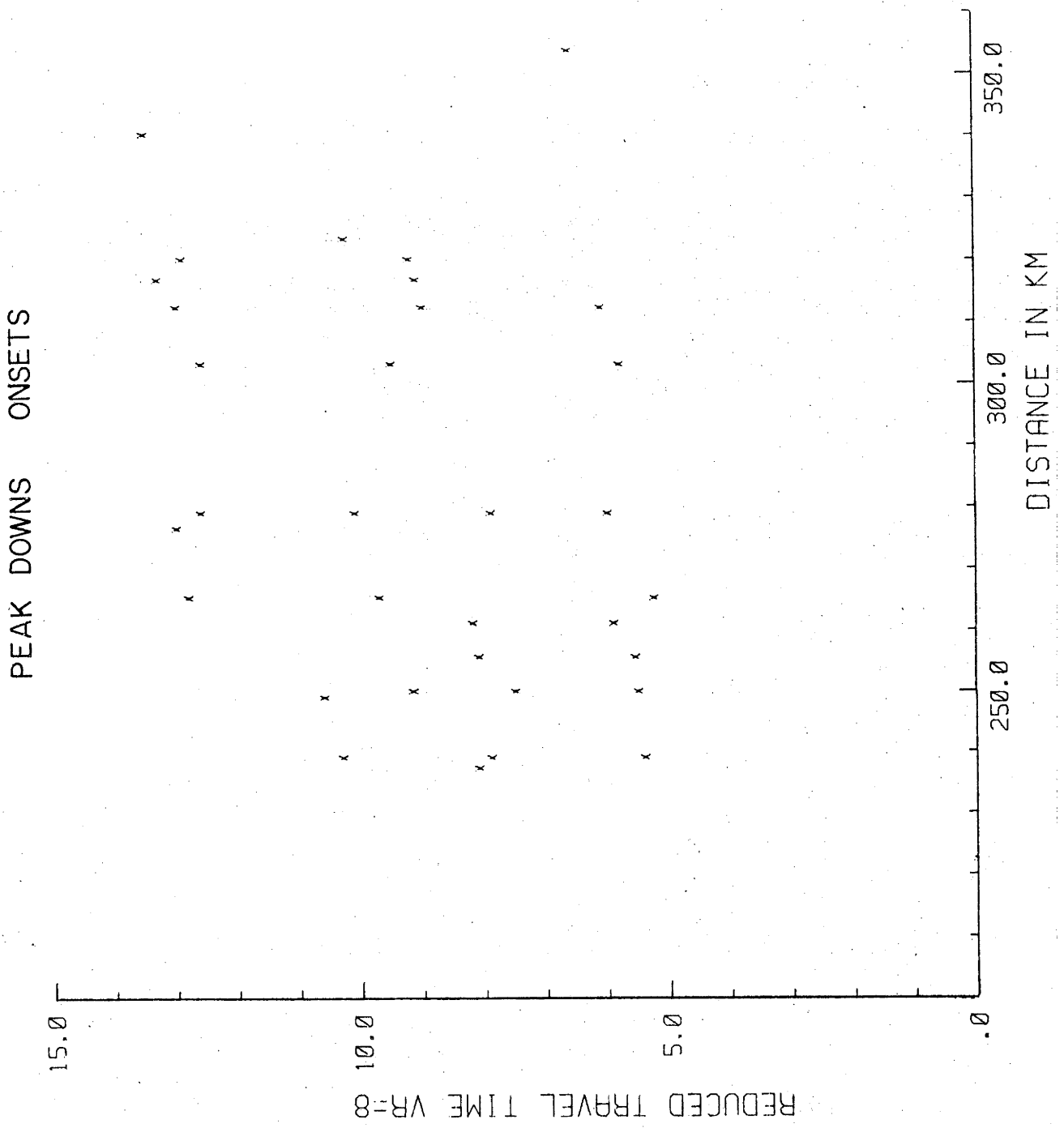

Figure 3.38

A hodograph of arrivals from Peak Downs explosions.

wavegroup observed in the Moura, Kianga, and Callide record sections, although it does not possess the obvious low frequency character observed in the Moura/Kianga sections.

Two composite record sections of the Goonyella overburden explosions are shown in Figures 3-34 and 3-35. The Pn onsets possess low amplitudes, but have clear arrivals which do not have the double onset character observed in the Moura/Kianga sections. The hodograph shows a greater amount of scatter in the Goonyella onsets than is observed in the Peak Downs records, owing to the larger distance range over which the Goonyellla onsets were observed.

The Pg onsets from the Gonnyella mine are less prominent than those from Peak Downs. The hodograph shows that the Pg onsets have considerable scatter, and merge into the Pj onsets. This is a reflection of the difficulty in accurately reading the onset times for these weaker arrivals.

3.5.11 Interpretation of the northern mines.

As discussed in relation to the interpretation of the Blackwater record sections, there are difficulties in applying conventional interpretation techniques to fan profiles. The Pn onsets from the Peak Downs record section have an apparent velocity of 7.4 km/s (as measured from the hodograph of Fig. 3-38). However, this is not an indication of the real sub-Moho velocity, but rather points to the change in the structure of the crust along the profile. This is also reflected in the observed scatter of the wavegroups seen in Figures 3-37 and 3-38. No interpretation of these onsets has been performed, other than the time term method analysis of Chapter 4. However, the comparsion of the observed onsets with those predicted by the model of Collins (1978) provides insight into the varation of the crustal structure.

3.5.12 A Short Refraction Profile near the Moura-Kianga Mines.

A short refraction profile was deployed in an east-west direction, along the Gibhi Road (Figure 3-39), running between the Moura and Kianga mines. The purpose of this profile was to define the velocity of the basin sediments and to detect any near-vertical deep crustal reflections; in particular, reflections from the Moho. It was thought that there was a good chance of recording these reflections with this profile, because of the size of the source explosions, and the success of the BMR reflection group, in obtaining deep crustal reflections in the sedimentary basins (Dr. J.

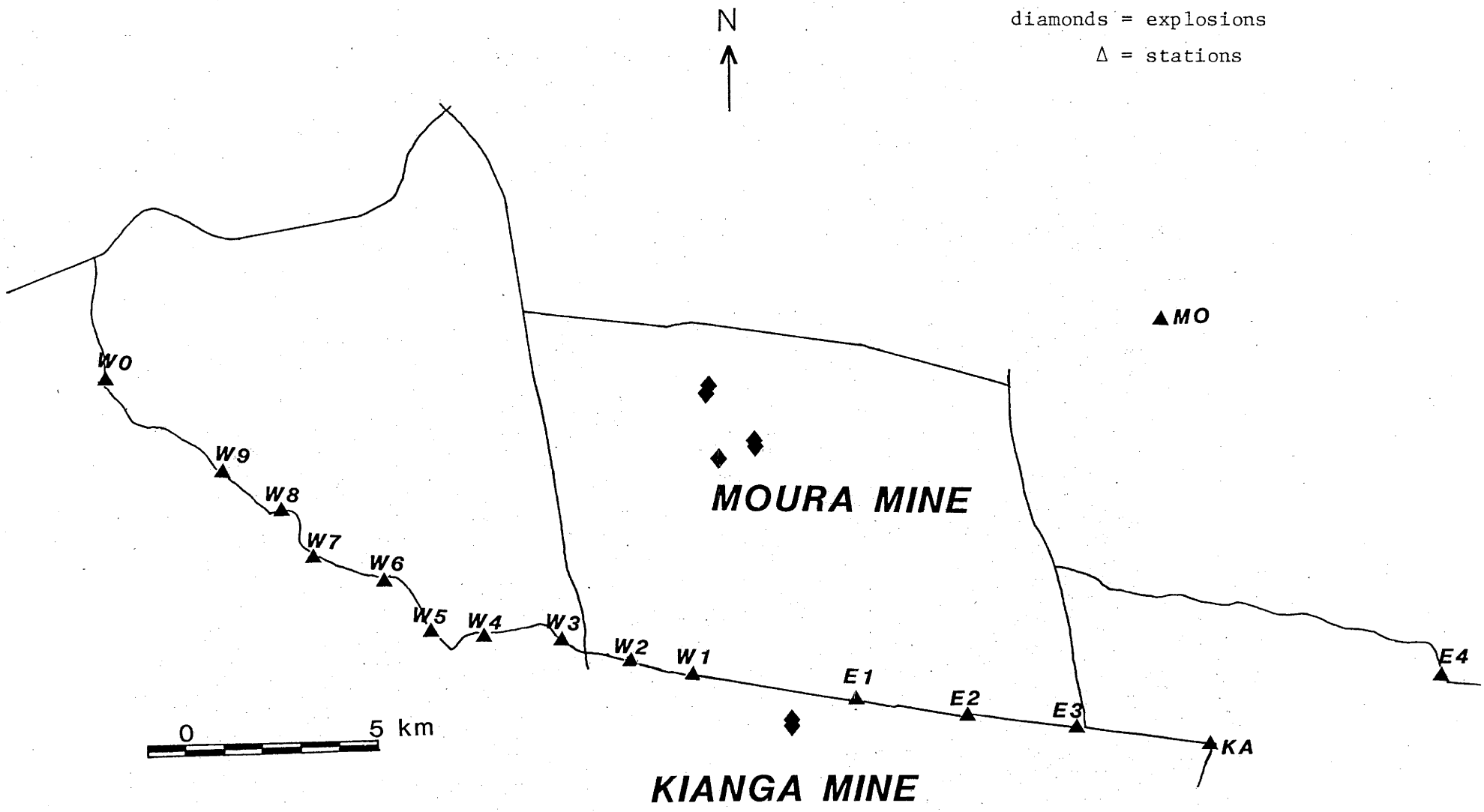

Figure 3.39

A plan of the short refraction profile near the Moura and Kianga mines.

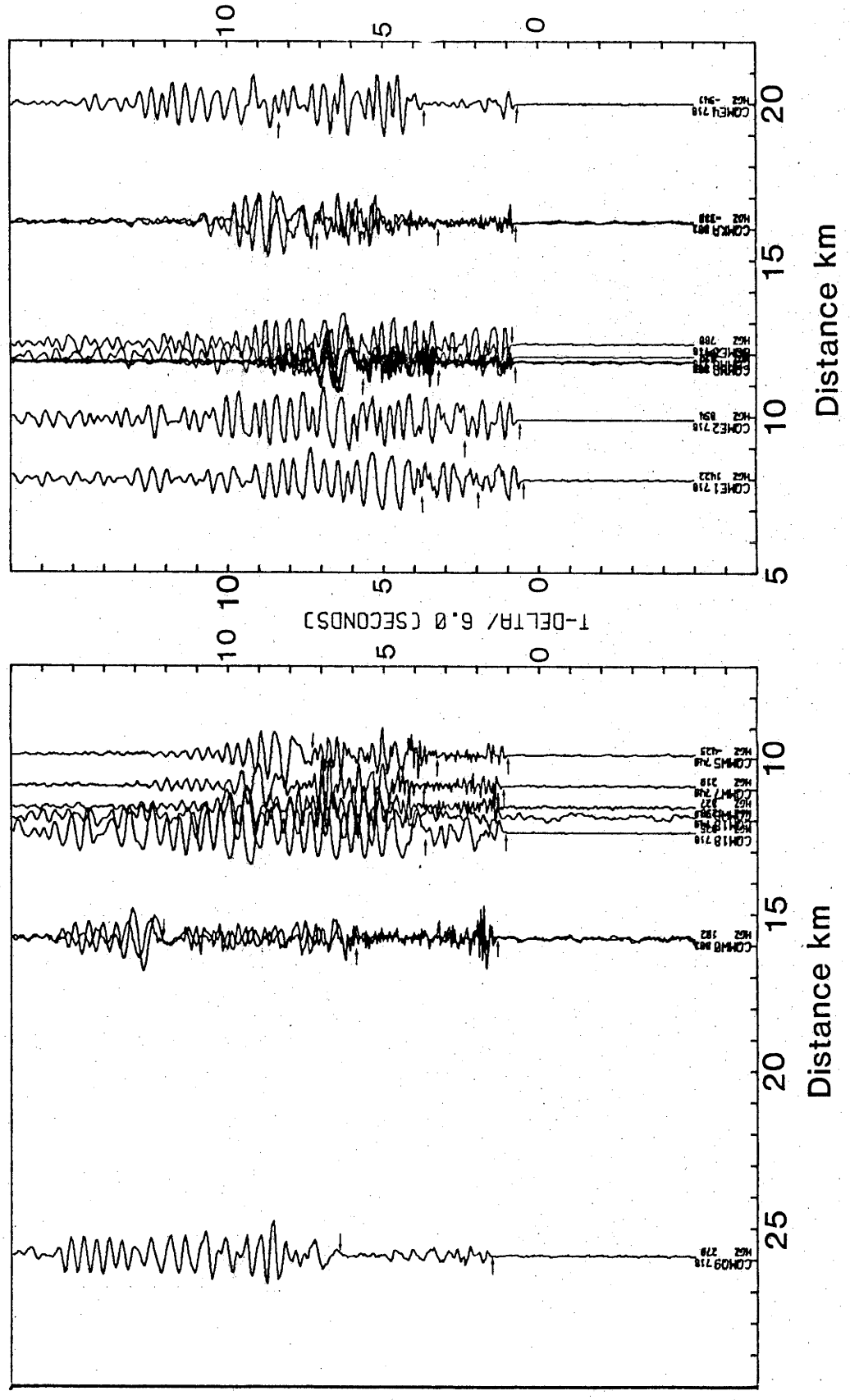

Figure 3.40

Composite vertical component record section of Moura explosions recorded on the short basin refraction profile, (MO-5).

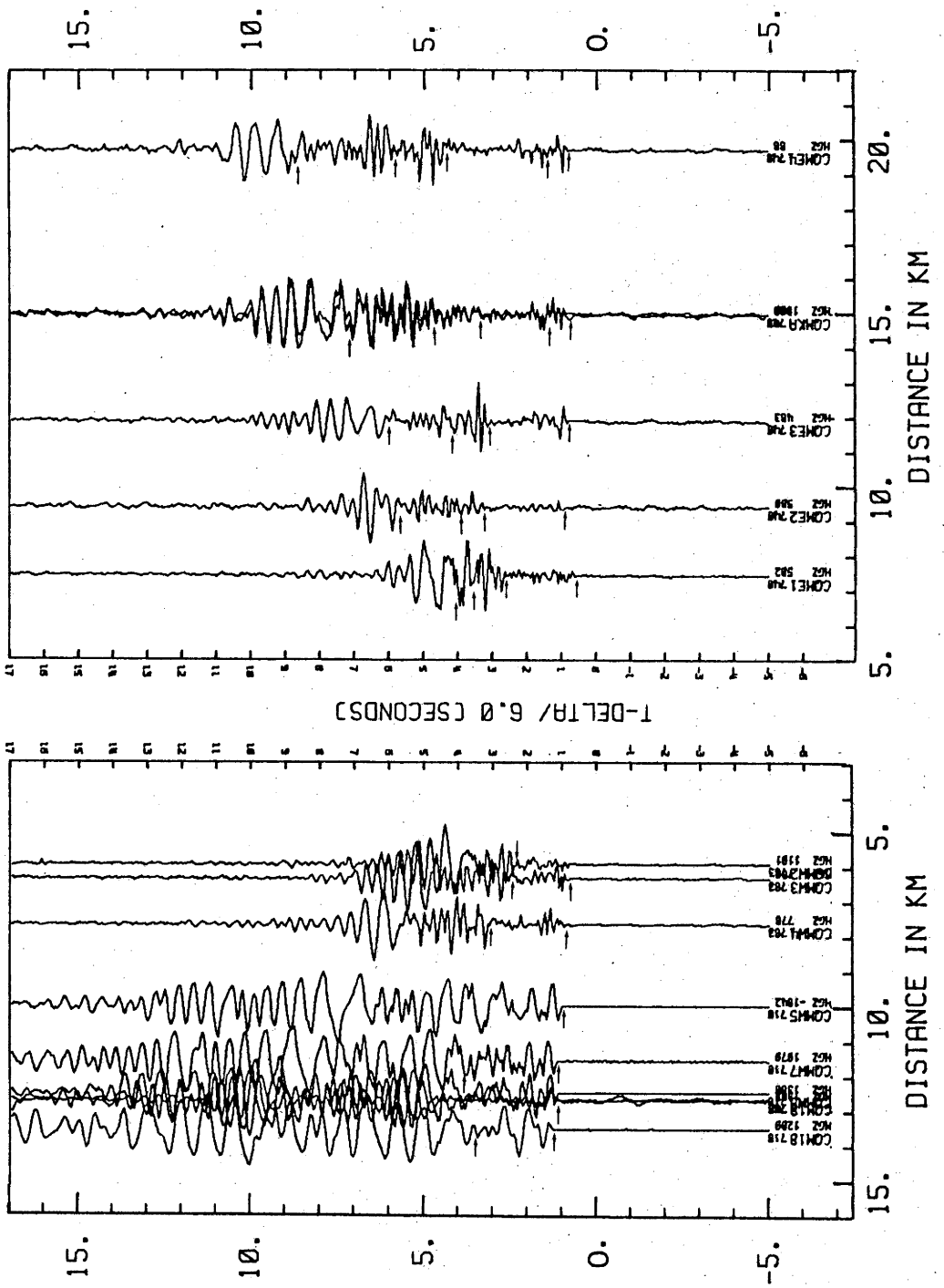

Figure 3.41

Composite vertical component record section of Moura explosions recorded on the short basin refraction profile, (MO-6).

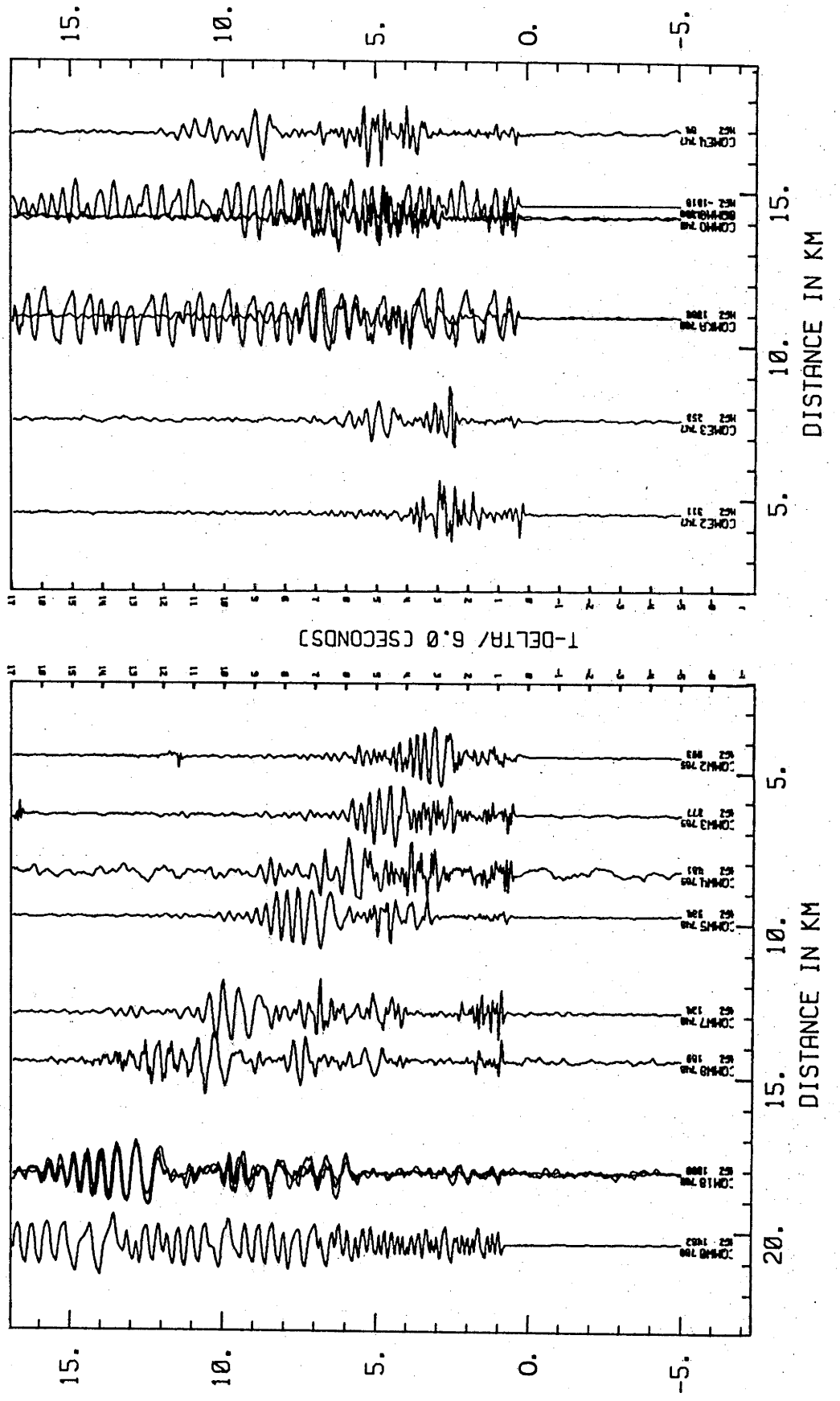

Figure 3.42

Composite vertical component record section of Kianga explosions recorded on the short basin refraction profile, (KA-2).

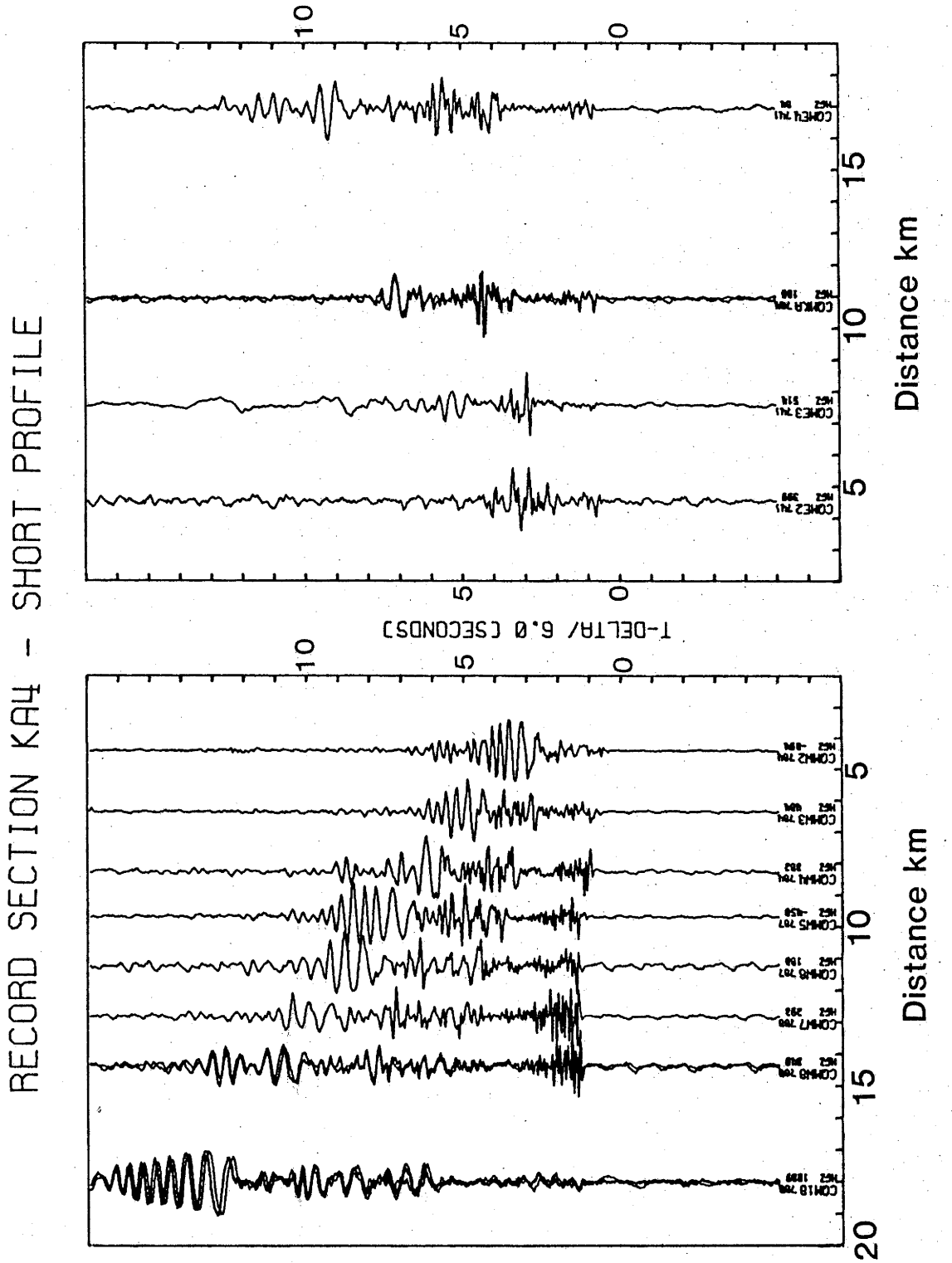

Figure 3-43

Composite vertical component record section of Kianga explosions recorded on the short basin refraction profile, (KA-4).

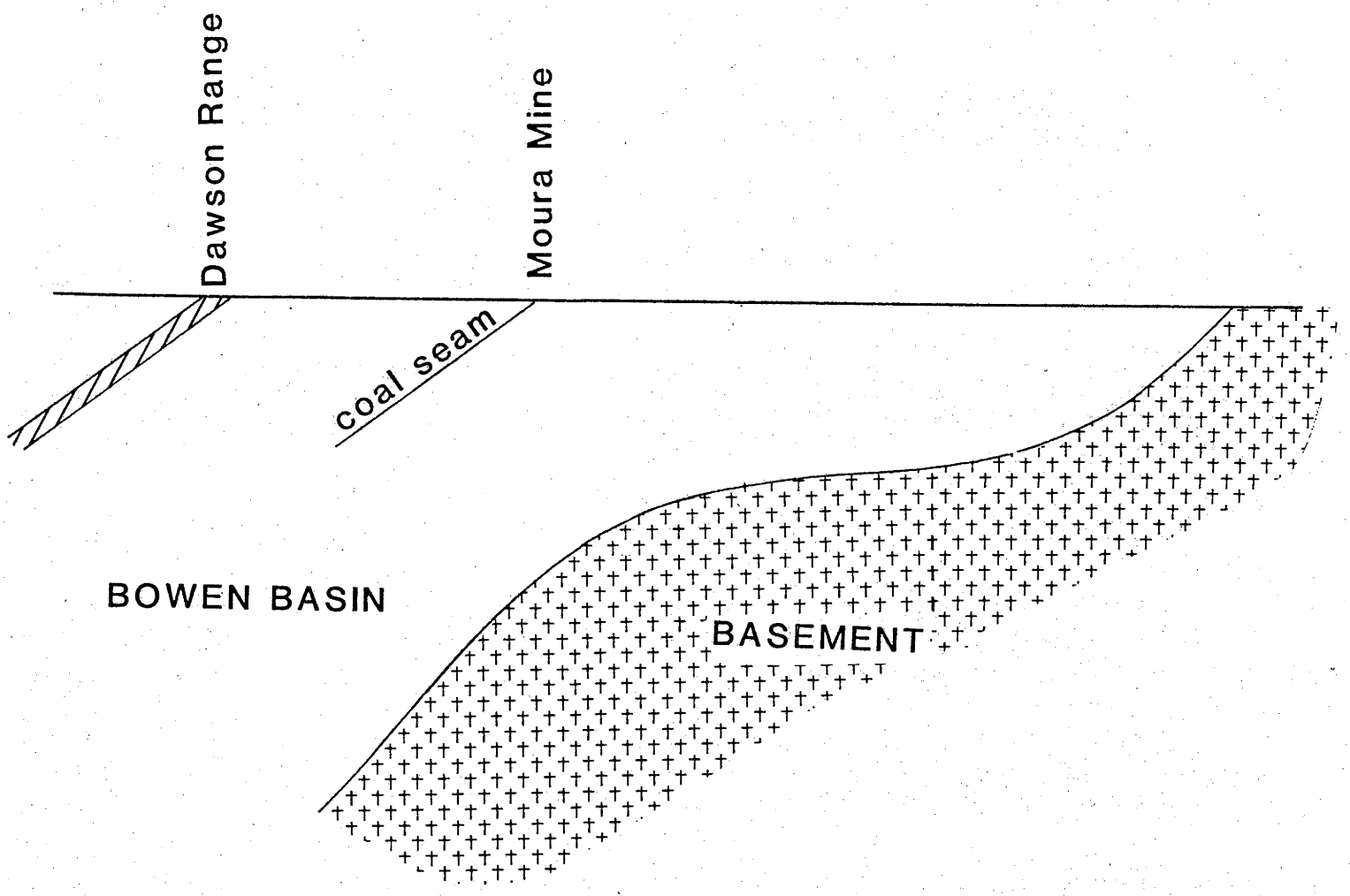

Figure 3.44

Schematic diagram showing the structure of the eastern edge of the Bowen Basin, after Dicken and Malone (1973).

Moss, personal communication).

Ten stations were occupied to the west of the mines, at a spacing of two kilometres, these being CQMW1 to CQMW0 at approximately 2 and 20 kilometres respectively. To the east, four sites were occupied, (the permanently located mine monitor CQMM0 was incorporated into this array) at a spacing of four kilometres out to a distance of about 18 kilometres; (the exact distances depend on the location of the explosion within these mines.) Figure 3-39 shows the location of the recorders and the explosions which were used as sources in this experiment. A leap frog technique was also used with this smaller profile to deploy the four OBS recorders among the 14 sites.

Four composite record sections have been compiled from this experiment, two each from Moura and Kianga mine explosions, (Figures 3-40 to 3-43). Two longitudinal wavegroups are observed on these record sections, these being Ps and Pg. The Ps wave is the first observed arrival out to a distance of approximately 12 km, where it is succeeded as a first arrival by the Pg wavegroup. The apparent velocity of the Pg wavegroup will be discussed in relation to profiles of greater length, where more control on the apparent velocity is obtained. Table 3-5 gives apparent velocities of the Ps wavegroup from these record sections. The variability of these apparent velocities is thought to be due to variations in the local geological structure of the eastern edge of the Bowen Basin. The observed Ps velocities to the west of the mines are consistently lower than those to the east. The explanation of this is two-fold. Firstly, those rays travelling to the east are penetrating older, and therefore more consolidated, sedimentary rocks of the basin with a correspondingly higher seismic velocity than that sampled by the rays travelling to the east; and secondly, rays travelling west from the explosion will have a portion of their raypath within the coal seam, with its very low velocity, as the coal seam dips at approximately 14° to the west near these mines. The difference in velocity between eastward and westward travelling rays suggests that the velocity in the sedimentary section increases with depth, according to the age of the sediments, with the average P velocity near the surface being 4.1 km/s, increasing to 4.5 km/s in the basal beds of the Bowen Basin.

The record section displays well developed Ss and Sg wavegroups. The origin of the shear wave at the explosions may be due to the geometry of the detonation - as the overburden explosions are detonated adjacent to

the high wall of the pit - or may be due to the mode conversion at interfaces near the source. The genesis of the shear waves in the case of the coal shots can only be attributed to the mode conversion of the P wave at or near the explosion. The most probable interface for this is the large velocity contrast that occurs at the coal/bedrock boundary.

The Ss apparent velocities are also tabulated in Table 3-4. As with Ps, the observed Ss apparent velocities are substantially higher to the east of these mines than to the west, and the shear velocity is inferred to increase from 1.9 km/s at the top to 2.2 km/s towards the base of the sediments.

Figure 3-43 displays the emergence and development of the surface wave train in the sediments to the west of these mines, in the deeper section of the basin. The surface wave is seen to diverge from the Ss wavegroup at CQMW2, with a lower group velocity. The surface wavegroup velocities are tabulated in Table 3-4, and, within the error of measurement, all have a zero intercept time. CQM18 instrument (an H14 with a 1 Hz. seismometer) has recorded the dispersed character of the surface wave far better than the OBS recorders. Beyond CQM18, the surface wave degenerates quite markedly, and at the next recorder to the west (CQM20), the surface wave has been completely disrupted. This disruption is attributed to the more competent layer of the Clematis Sandstone (Mimosa Group) which outcrops between these two sites, forming the Dawson Range. To the east of the Moura-Kianga mines the surface waves are less well developed, because of the wedging out of the Bowen Basin sediments in this direction.

The traces of the recorders CQMW2 and CQMW3 of Figure 3-42 display the sharp onset of the air wave which arrives after the surface wave. However, a careful study has revealed no coherent arrivals that could be attributed to deep crustal reflections. The clean character of the coal shots (as opposed to the complex and ongoing coda of the overburden explosions) suggests that an experiment using a reflection survey type array may be warranted to detect the presence of any near vertical crustal reflections. As can be seen, in the case of the coal shots, the noise level, recorded at a distance of about two kilometres from the explosion, has dropped to almost the pre-onset value seven seconds after the first arrival, and as any Moho reflections would be expected to arrive around 11 seconds after the explosion, any Moho reflections of significant energy which exist, should be observable.

Figure 3-44 gives an idealized and expanded vertical section of the eastern edge of the Bowen Basin near the Moura/Kianga mines. The observed features of the record sections are in accord with this structural interpretation. However, the complicated geological structure and the limited number of shot points have precluded any detailed inversion of this data. The observed variation of the basin sediment velocities indicates that the problem cannot be simplified to a two dimensional approach, as the various shot points range over a distance of 12 km, in a line roughly perpendicular to the refraction profile.

3.5.13 $t^2 - x^2$ analysis of Pm onsets.

$t^2 - x^2$ analyses of retrograde branches provide very useful control for velocity modelling. Giese (1978) discusses in detail the theory of this method. The simplifying assumptions that the overburden above the reflecting horizon can be approximated by a constant velocity layer, and that the interface is horizontal, (or some allowance made for this structure of the overburden, as discussed in the wide angle reflection technique of Bamford, 1978).

Given these simplifying assumptions, the slope q and the intercept I of a linear regression of the t^2-x^2 data, are related to the mean velocity c of the overburden above the reflecting interface, and the depth z of this interface, by the relations

$$q = \frac{1}{c^2}$$

$$I = \frac{2z}{c^2}$$

A t^2-x^2 graph of the onsets of the Pm phase read from the record sections of Moura/Kianga mines overburden explosion is shown in Figure 3-45. The linear regression of these data gives c = 6.29 km/s, and z = 32.3 km. The point at which the depth z to the reflector is applicable is offset to the midpoint between the shot-point and the receiver, i.e. around 50 km west of the Moura mine. The average velocity includes the effects of the lower velocity sediments of the Bowen Basin, through which the Pm rays must pass.

A similar analysis was not possible for the Callide Pm onsets, as no large amplitude Pm onsets were clearly recorded. Collins' (1978) model for the crustal structure of the Bowen Basin between the Goonyella and Moura mines has a small ($\sim$0.7°) southward dip on the Moho. The average crustal velocity of this model is 6.32 km/s, with the model displaying a

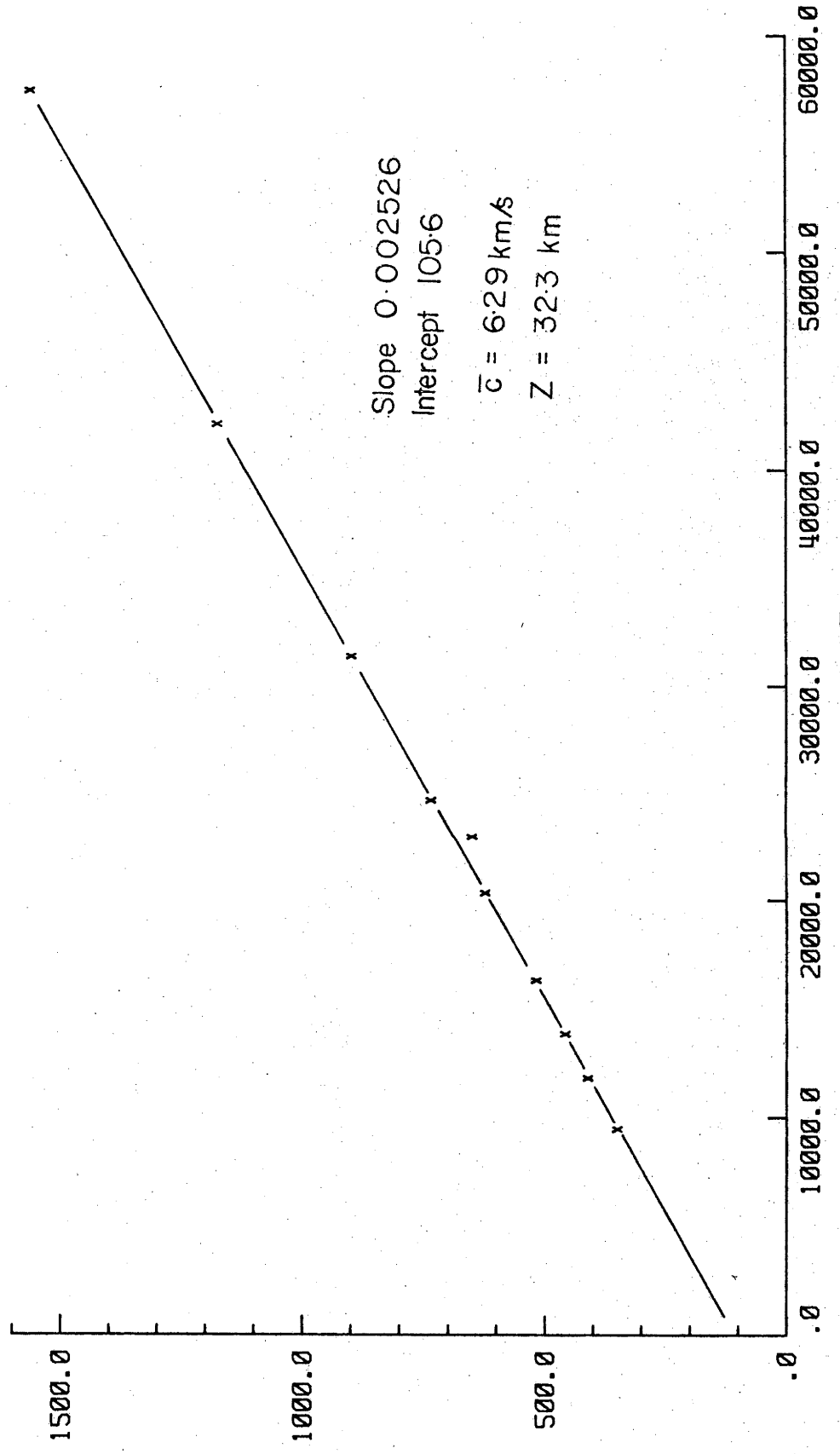

Figure 3.45

$t^2 - x^2$ analysis of the P_m onset recorded to the west from the Moura and Kianga mines.

relatively constant geometry along the profile. The average crustal velocity agrees relatively well with the value obtained from the Moura/Kianga Pm t^2-x^2 analysis.

The apparent velocity of the Pg wavegroup from the Moura/Kianga mines is 6.34 km/s, suggesting that there can be no significant increase of velocity with depth in the crust, in order to maintain the average crustal velocity at 6.29 km/s.

3.5.14 τ-p analysis.

The τ-p velocity inversion technique was employed to obtain constraints on the errors in the velocity model. A τ-p curve of Moura P-wave arrivals was constructed using the graphical technique of Bessonova et al.,(1976) for the first arrivals, and the measured apparent velocities and intercepts of later branches. A τ-p inversion programme, (written by Dr. I. Reid) using the algorithm presented by Kennett (1976) was employed to derive the velocity bounds shown in Figure 3-45. Estimating the error in τ is a subjective process, and for any reasonable estimate, the derived extremal bounds on the velocity model were thought to be unreasonably large. This was particularly so in the range of greater depths. It was felt that although the errors in the velocity could not be determined, the uncertainty in velocity models derived by raytracing methods were far less than the extremal bounds would indicate.

Tatel et al.,(1955) sternly admonished crustal refraction seismologists for not placing error bounds on their derived velocity models; but the fact that this practice continues today is an indication of the inherent difficulty of obtaining any realistic error bounds for a model. The measurement of apparent velocity is relatively straight-forward, and therefore the error component in the velocity (solely the velocity component) is considered relatively minor. However the depth associated with a particular apparent velocity is a product of the interpretation, and this inevitably is where the greatest uncertainty lies. The form of retrograde branches of the refraction curve helps to constrain the depth of the associated velocity feature; however, depth constraint on those portions of the velocity profile for prograde branches is less certain.

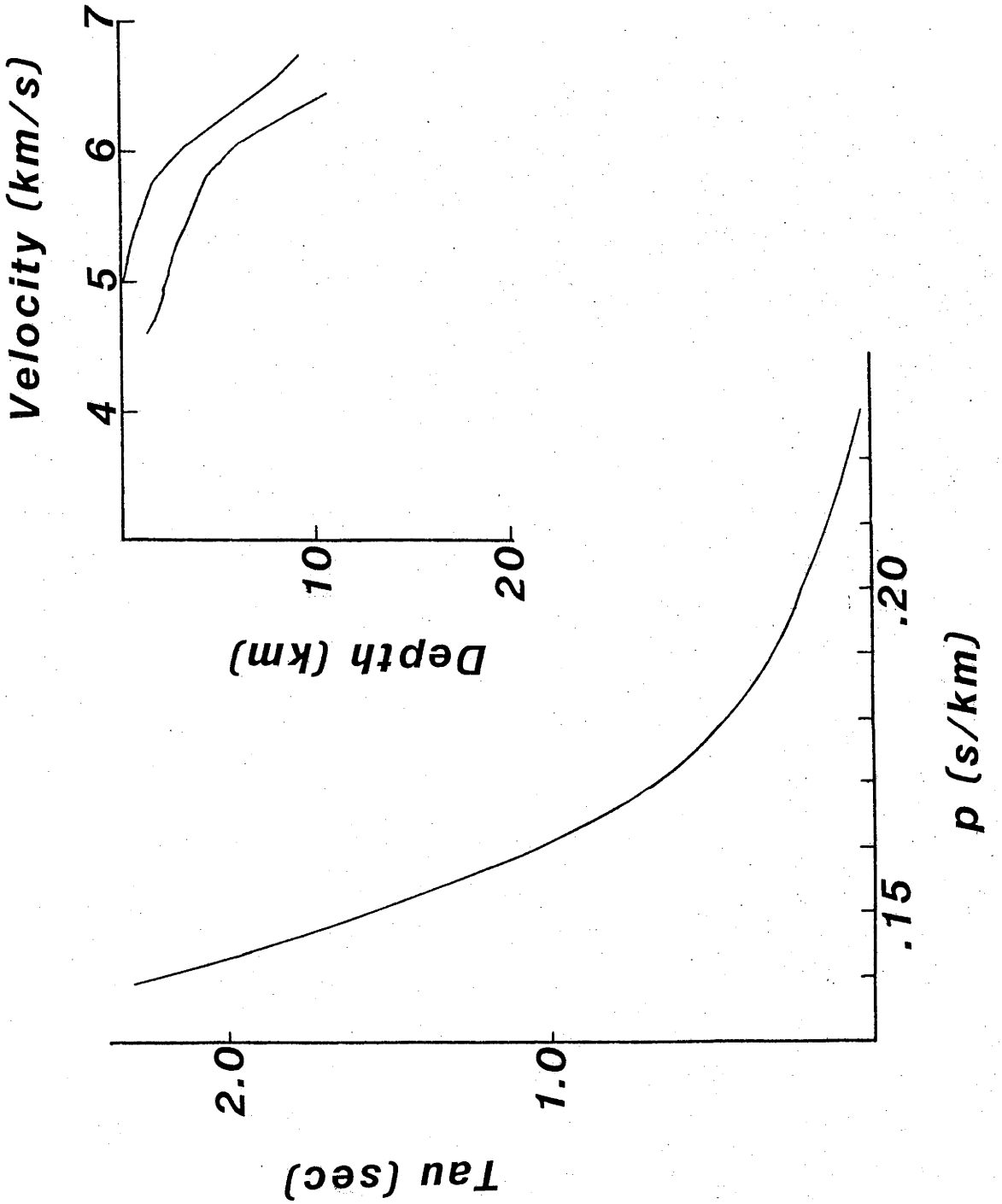

Figure 3.46

τ-p plot of the P_g arrivals recorded to the east of Moura, and the inverted velocity depth profile.

3.6 COMPARISON OF CENTRAL QUEENSLAND MODEL WITH OTHER CRUSTAL PROFILES.

Figure 3-47 displays the range of crustal models derived from Australian seismic surveys. There exists a wide range of structures, with no clear systematic variation. Most of the models have an intermediate crustal discontinuity, corresponding to the conventional idea of a Conrad discontinuity; the exceptions to this are the Maralinga surveys, and the two Central Queensland refraction surveys. The depth of the Mohorovicic discontinuity in the Australian surveys ranges from in excess of 50 km to less than 30 km, with Pn velocities ranging from 7.79 km/s to in excess of 8.3 km/s in the older cratonic regions of Western Australia.

Cleary (1973) suggested that there was an increase of Pg (P^*) velocities from east to west in the Australian continent. The data from the present survey indicate a Pg velocity of 6.37 km/s, comparable with that found in the shield regions of Western Australia. Collins' (1978) model also has a crustal velocity of 6.39 km/s. However, his model possesses a lower crustal layer with an intermediate velocity of 7.07 km/s at the base of the crust, with the thickness this layer being of around 7 km. No evidence for this layer of intermediate velocity has been observed in the present survey, which runs approximately east-west in the same region.

The Pn velocity of 7.96 km/s measured from the data of the present east-west survey, contrasts with Collins' Pn velocity of 8.10 km/s measured in an approximately north-south direction. Evidence for Pn anisotropy from both these data is investigated in Chapter 4.

Synthetic seismograms have been used in Chapter 5 to investigate the nature of the Pn wavegroups observed in the present survey. With the exception of Finlayson et al.,1979, the other Australian crustal models have been derived without the benefit of synthetic seismograms modelling. The relatively complicated structure below the Moho which has been postulated from the present data has not been modelled in any other Australian crustal interpretation. Finlayson et al.,(1979), using synthetic seismograms, have proposed that the Mohorovicic discontinuity in the Lachlan Fold Belt of SE Australia is a simple second order type discontinuity. However, evidence for a stronger arrival occurring one to two seconds after the Pn onset is observed in the data analysied by Collins (1978) - see for example the traces in the distance range 240 to 300 km of Fig. 4a of Collins (1978). It is tentatively suggested that this inter-leaving of

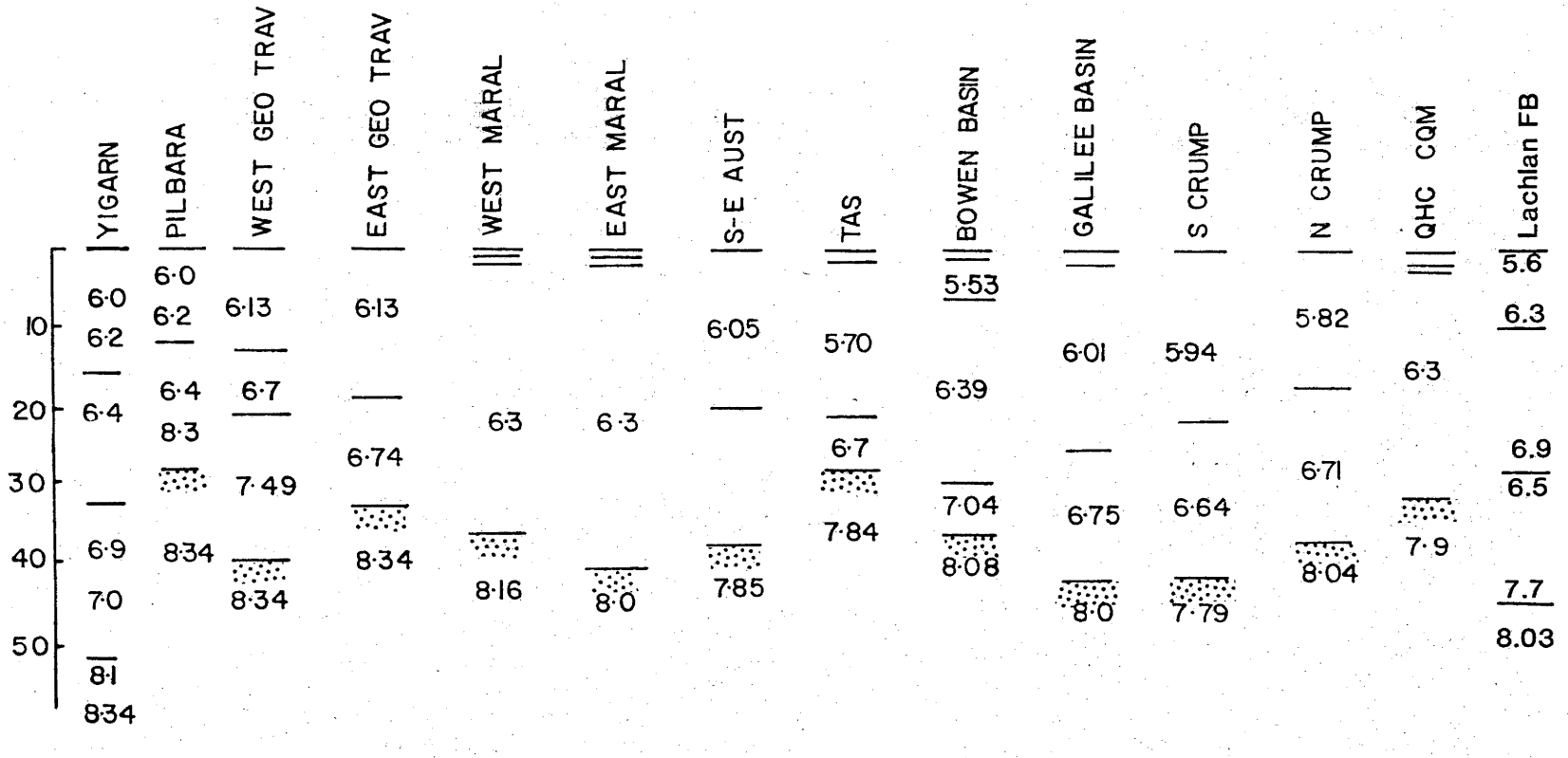

Figure 3-47.

A comparison of Australian Crustal models, after Dooley, (1976).

high and low velocity layers near the Moho may be associated with crustal graben type structures, although this idea certainly needs further examination.

It is currently thought that the lower crust is composed of rocks of a granodioritic composition in a granulite facies. Velocity increases and discontinuities within the crust can be explained in terms of advancing metamorphic fronts, (see Mueller, 1978), and the vertical location of these fronts would vary considerably as a consequence of changes in the thermal profile in the crust. There is current controvesy over the question of whether water exists in a free form in the lower crust, (see Padovani and Carter, 1977; and Lee and Holdaway, 1977). A noticeable feature of the majority of the Australian crustal models is the absence of low velocity zones. Both the presence of water and the transformation of quartz from the alpha to beta structure (Van der Molen, 1979) could be responsible for low velocity zones within the crust, and further careful studies in regions possessing less complicated surface geology than Central Queensland will be required to elucidate this point.

TABLE 3-1

STATION	LAT. deg.	LONG. deg.	HT m.	INSTR	COMMENT*
QHC01	-23.4472	151.9154	5	H4	Too noisy for use
QHC02	-23.8694	151.1333	40	H7	
QHC03	-23.9729	150.9683	58	N6	No data
QHC04	-24.0629	150.8210	80	H3	Severe clock problems
QHC05	-24.2260	150.6952	222	N10	
QHC06	-24.2405	150.4584	175	H5	
QHC07	-24.3224	150.2771	178	N6	
QHC08	-24.4254	150.1115	138	N7	Pulled out by police for 3 days
QHC08	-24.4265	150.1091	138	N7	
QHC09	-24.6156	149.7896	115	N4	
QHC10	-24.6390	149.5633	153	H9	
QHC12	-24.6113	149.1647	261	H6	Only 6 days of data
QHC13	-24.6089	148.9633	356	N5	
QHC14	-24.5451	148.7999	278	H1	
QHC15	-24.4582	148.6421	220	N3	Only 3 days of data
QHC16	-24.3741	148.3291	259	H8	
QHC17	-24.3610	148.0619	320	H11	
QHC18	-24.4687	147.9029	365	H10	
QHC19	-24.4135	147.6439	335	N9	
QHC20	-24.4448	147.5104	390	H13	
QHC21	-24.4203	147.2599	322	H2	
QHC22	-24.4572	147.0795	359	H14	
QHC23	-24.4762	146.9649	365	H12	
QHCM1	-21.7353	147.7287	260	002	Only 8 days of data
QHCM3	-24.5421	150.0406	160	001	
QHCM5	-24.7005	150.0703	150	M03	Only 3 days of data

* No comment implies that the instrument ran successfully.

TABLE 3-2

STATION	LAT. deg.	LONG. deg.	HT m.	INSTR	COMMENT
CQM02	-23.8691	151.1331	4	H01	Tape stopped, no data
CQM03	-23.9087	151.0333	80	H12	
CQM04	-23.9783	150.9725	60	H13	Clock stopped
CQM06	-23.9999	150.9111	120	H14	
CQM07	-24.0627	150.8206	80	H01	
CQM08	-24.1472	150.7203	330	H09	
CQM09	-24.2221	150.7027	530	H04	
CQM10	-24.3207	150.6842	240	H07	No radio
CQM11	-24.3253	150.5738	260	H03	
CQM12	-24.2824	150.4860	180	H10	No L component
CQM13	-24.2983	150.3763	170	H02	No L component
CQM14	-24.3299	150.2735	180	H11	No radio
CQM15	-24.3727	150.1730	180	H01	No radio
CQM16	-24.4255	150.1102	130	H08	Clock stopped
CQM17	-24.4966	149.9897	13	H03	Z component only
CQM18	-24.6066	149.9277	120	H15	
CQM19	-24.6151	149.7890	120	H13	Tape problems
CQM20	-24.6836	149.6907	150	H12	
CQM21	-24.6389	149.5586	150	H07	
CQM22	-24.6452	149.4573	170	H04	Seismic problems
CQM23	-24.6422	149.3643	140	H14	
CQM24	-24.6000	149.2944	190	H05	No L component
CQM25	-24.6131	149.1987	180	H06	No L component
CQM26	-24.6454	149.0874	320	H10	No L component
CQM27	-24.6088	148.9666	360	H11	No radio
CQM28	-24.5804	148.8852	320	H01	No L component
CQM29	-24.5504	148.8006	280	H02	
CQM30	-24.4956	148.7280	250	H15	Seismic trouble
CQM31	-24.4574	148.6417	220	H03	Tape stopped
CQM32	-24.4525	148.5322	220	H08	
CQM33	-24.4146	148.4652	236	H12	Tape stopped half way
CQM34	-24.3270	148.3978	250	H07	

CQM35	-24.2432	148.3179	247	H06	
CQM36	-24.2079	148.1958	366	H05	
CQM37	-24.1854	148.0920	396	H14	
CQM38	-24.1572	147.9854	366	H04	Medium Gain Z only
CQM39	-24.1545	147.8711	304	H13	Tape stopped
CQM40	-24.1732	147.7518	274	H10	
CQM41	-24.2567	147.6701	274	H01	No L component
CQM42	-24.3037	147.5564	304	H09	
CQM43	-24.3273	147.4630	304	H11	
CQM44	-24.3888	147.3772	366	H03	
CQM45	-24.4207	147.2671	320	H12	Tape stopped
CQM46	-24.4670	147.1580	344	H08	
CQM47	-24.4572	147.0813	366	H15Z	component only
CQM48	-24.5402	146.6520	475	H02	No L component
CQMA1	-23.6934	150.6297	20	004	
CQMA2	-23.7966	150.9639	40	001	
CQMA3	-24.1846	150.4151	160	002	Tape problems
CQMA4	-23.8737	150.3398	150	003	
CQMA5	-24.5999	148.5102	230	001	
CQMA6	-24.8788	148.5295	310	003	
CQMA7	-24.6696	149.2871	160	004	Tape stopped
CQMA8	-24.8907	149.2917	210	002	
CQME1	-24.7082	150.0803	170	002	
CQME2	-24.7116	150.1079	150	001	
CQME3	-24.7143	150.1380	160	003	
CQME4	-24.7025	150.2301	210	004	
CQMW1	-24.7025	150.0414	140	002	
CQMW2	-24.6994	150.0218	140	004	
CQMW3	-24.6936	150.0036	140	001	
CQMW4	-24.6925	149.9844	120	003	
CQMW5	-24.6933	149.9697	110	004	
CQMW6	-24.6795	149.9580	110	002	
CQMW7	-24.6735	149.9437	110	003	
CQMW8	-24.6624	149.9319	110	001	
CQMW9	-24.6542	149.9159	110	002	
CQMW0	-24.6304	149.8858	110	001	
CQMM0	-24.6168	150.1565	200	N09	Tape stopped for a period
CQMKA	-24.7190	150.1710	220	N05	

CQMBW	-23.9682	148.7367	270	N08	
CQMPD	-22.1347	148.1592	210	N04	No radio
CQMSJ	-22.4537	148.3518	200	N03	
CQMGY	-21.9297	147.9344	250	N07	Pulled out for a period
CQMCA	-24.2901	150.7190	270	N02	High gain Z not working
CQMQ2	-23.8691	151.1331	40	N10	No radio
CQMQ9	-24.6146	149.7894	120	N01	No radio
CQMQ6	-24.3751	148.3293	244	N06	

TABLE 3-3

EVENT	YR	MN	DY	HR	MN	SEC	LAT.	LONG.	MINE
359	77	4	7	1	24	32.69	-24.6322	150.0423	Moura OB
360	77	4	15	23	48	26.60	-24.6434	150.0442	Moura OB
364	77	4	20	4	42	51.22	-23.7947	148.8607	Blackwater OB
365	77	4	2	1	12	7.32	-21.7614	147.9736	Goonyella OB
367	77	4	5	23	1	45.39	-24.7120	150.0621	Kianga OB
568	77	4	2	0	52	15.25	-24.6340	150.0421	Moura OB
570	77	3	30	7	39	31.53	-22.2207	148.1773	Peak Downs OB
619	77	3	31	4	42	58.36	-21.7869	147.9804	Goonyella OB
620	77	4	16	1	2	51.70	-21.7839	147.9800	Goonyella OB
666	77	3	29	1	41	29.10	-24.6366	150.0415	Moura OB
667	77	4	22	2	16	28.02	-24.6412	150.0444	Moura OB
668	77	3	30	4	58	23.61	-24.3241	150.6218	Callide shot
669	77	4	1	21	44	20.90	-24.3241	150.6218	Callide shot
670	77	4	6	1	59	.34	-24.3241	150.6136	Callide shot
671	77	4	13	2	0	40.38	-24.3261	150.6132	Callide shot
672	77	4	15	5	9	40.89	-24.3259	150.6127	Callide shot
699	78	3	6	6	59	3.31	-21.7438	147.9734	Goonyella OB
700	78	3	3	4	13	14.26	-24.7167	150.0629	Kianga OB
703	78	2	16	5	30	17.75	-21.7570	147.9726	Goonyella OB
704	78	2	25	0	51	31.00	-21.7592	147.9733	Goonyella OB
705	78	3	9	6	37	47.58	-21.7286	147.9689	Goonyella OB
706	78	3	12	1	47	38.34	-24.6482	150.0541	Moura OB
707	78	3	7	3	47	40.00	-24.6383	150.0435	Moura OB
708	78	3	8	4	53	7.00	-22.4421	148.3013	Saraji OB
709	78	3	3	1	54	16.37	-24.6403	150.0433	Moura OB
710	78	2	24	1	55	47.88	-24.6464	150.0542	Moura OB
711	78	2	17	1	52	29.54	-24.3259	150.6127	Callide shot
714	78	2	18	1	53	1.81	-24.6419	150.0431	Moura OB
715	78	2	17	6	32	10.64	-24.6269	150.0418	Moura CS
716	78	2	14	3	50	8.12	-24.6448	150.0429	Moura OB
733	78	2	14	3	53	37.79	-22.2045	148.1510	Peak Downs OB
734	78	2	22	6	6	10.00	-22.3033	148.2085	Peak Downs OB
735	78	2	22	6	13	54.19	-22.4369	148.2987	Saraji OB

TABLE 3-3 continued.

EVENT	YR	MN	DY	HR	MN	SEC	LAT.	LONG.	MINE
736	78	2	8	8	41	33.37	-22.2910	148.2066	Peak Downs OB
737	78	3	7	7	21	21.75	-22.2025	148.1457	Peak Downs OB
738	78	3	9	5	57	31.00	-22.2606	148.1889	Peak Downs OB
739	78	3	13	7	46	55.59	-22.2988	148.2226	Peak Downs OB
740	78	2	15	3	49	45.51	-24.6498	150.0440	Moura CS
741	78	2	15	3	58	29.91	-24.7123	150.0631	Kianga CS
744	78	2	8	22	14	11.21	-24.7208	150.0594	Kianga OB
745	78	2	13	4	2	3.18	-24.6501	150.0440	Kianga CS
746	78	2	13	4	2	21.79	-24.6351	150.0551	Moura CS
747	78	2	14	4	2	57.03	-24.7123	150.0631	Kianga CS
748	78	2	27	3	55	36.13	-24.7123	150.0631	Kianga CS
749	78	2	27	3	58	19.62	-24.6329	150.0417	Moura CS
750	78	2	10	1	55	42.00	-22.4019	148.2891	Saraji OB
751	78	2	24	4	9	28.79	-23.7393	148.8068	Blackwater OB
753	78	2	17	4	7	4.50	-23.6821	148.7973	Blackwater CS
754	78	2	22	4	19	54.12	-23.7384	148.8066	Blackwater OB
758	78	2	16	3	51	39.70	-23.7599	148.8229	Blackwater CS
759	78	3	14	2	1	18.91	-24.3105	150.6361	Callide shot
760	78	3	9	4	15	7.32	-23.6826	148.7970	Blackwater CS
763	78	2	16	3	59	52.46	-24.6497	150.0440	Moura CS
764	78	2	16	4	0	50.94	-24.7123	150.0631	Kianga CS
765	78	2	17	3	57	20.86	-24.7123	150.0631	Kianga CS
766	78	2	20	3	57	59.66	-24.7123	150.0631	Kianga CS
767	78	2	23	1	32	17.64	-24.7123	150.0631	Kianga CS
768	78	2	24	11	7	19.61	-24.6502	150.0440	Moura CS
769	78	2	15	22	56	33.68	-24.3259	150.6127	Callide shot
792	78	2	8	4	41	34.06	-24.3259	150.6127	Callide shot
793	78	3	7	4	36	25.33	-24.3105	150.6361	Callide shot
795	78	2	6	3	57	44.77	-24.6491	150.0440	Moura CS
796	78	2	7	4	2	13.60	-24.6351	150.0551	Moura CS
797	78	2	9	23	50	28.54	-24.3259	150.6127	Callide shot
798	78	2	8	8	44	46.00	-24.6351	150.0551	Moura CS
799	78	2	9	4	2	30.69	-24.7123	150.0631	Kianga CS
800	78	2	10	3	43	36.63	-24.6485	150.0441	Moura CS
801	78	3	2	4	3	27.43	-24.6327	150.0417	Moura CS
802	78	3	6	3	46	29.51	-24.6323	150.0417	Moura CS

Table 3.4

Symbol	Velocity Range km/s	Distance Range km	Nature of Wave
COMPRESSIONAL WAVES			
Ps	$V_p \leq 5.5$	0 - 20	Travels in sedimentary section relatively large amplitude.
Pg	$6.0 \leq V_p \leq 6.5$	20 - 350	Crustal wavegroup.
Pn	$7.8 \leq V_p \leq 8.1$	100 - 350	Refracted in uppermost mantle.
Pm	~ 7.8	80 - 160	Super-critically reflected from Moho.
Pj	~ 6.5	200 - 300	Low frequency character, arrives ~ 2 sec after Pg.
SHEAR WAVES			
Ss	$2.2 \leq V_s < 3.4$	0 - 20	Travels in sedimentary section.
Sg	$3.2 \leq V_s \leq 3.8$	20 - 250	Crustal shear wave.
Sm	~ 4.6	80 - 150	Super-critically reflected from Moho.
Sn	~ 4.6	120 - 300?	Refracted in uppermost mantle.

Table 3.5 Apparent Velocities of P_s and S_s wavegroups.

Record Section	P_s		S_s	
	East	West	East	West
MO5	4.28	4.01	2.21	1.94
MO6	4.8	4.36	2.21	1.96
KA2	4.7	4.08	2.29	1.98
KA4	-	4.28	2.11	1.71

CHAPTER 4

A TIME TERM ANALYSIS OF THE CENTRAL QUEENSLAND REFRACTION DATA.

4.1 INTRODUCTION.

The need to generalize the interpretation of crustal and upper mantle refraction profiles so as to include data from different surveys, has promoted the development of an analysis technique referred to as the time term method. This method provides a unified approach to the analysis of all the refraction data within a region, as demonstrated by Bamford (1973a) using the West German quarry blast data. In this way the method ties together what otherwise would be spacially isolated and unrelated interpretations of the crustal structure, so that an overview of the crust is obtained.

The time term method also allows more structurally complicated models than the plane layered models which have been historically and are commonly utilized in crustal refraction interpretation. Models incorporating curved interfaces, lateral velocity variations, and anisotropy can be handled by the time term method, whereas their consideration poses difficulties in other interpretation techniques. The time term method therefore allows the development of integrated models, which are capable of more closely approaching the actual complexity of the Earth. In this respect, the method is particularly useful in the understanding of the crust.

The time term method was first introduced by Scheidegger & Willmore (1957), and applied to crustal refraction interpretation by Willmore and Bancroft (1960). A later modification by Raitt et al., (1969) extended the method to encompass anisotropic velocity variation within the refracting layer, and Raitt et al. also introduced the idea of a regional delay time function. Subsequently, Bamford (1973b) stressed the importance of iteratively correcting the delay time function for an initial assumption that the refracting interface is horizontal. Bamford (1977) also developed the MOZAIC time term method.

4.2 THEORY OF THE TIME TERM METHOD

An introduction to the fundamental principles and the theory of the time term method is given by Willmore and Bancroft (1960), and more

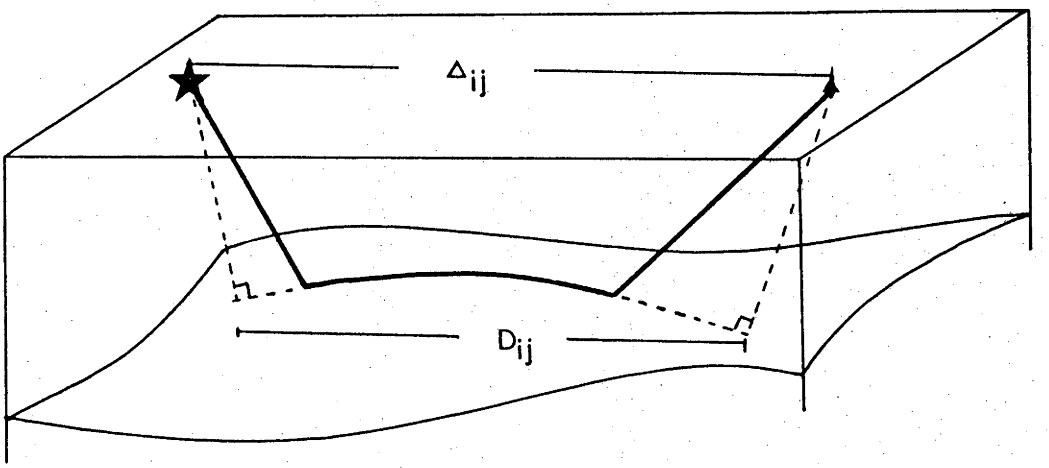

$$t_{ij} = a_i + a_j + D_{ij}/V$$

Figure 4.1

Schematic diagram of refracted ray travelling between shot point and receiver, showing quantities Δ_{ij} and D_{ij}.

recently by Bamford (1973a). The technique allows the regional mapping of the depth of a velocity discontinuity from the seismic refraction data.

4.2.1 Simple time term method.

The travel time, T_{ij} , of a seismic ray between a shot point and a receiver can be approximated by a theoretical travel time t_{ij} , which in turn can be decomposed into three independent terms,

$$t_{ij} = a_i + a_j + D_{ij}/V \qquad (4.1)$$

The a_i and a_j represent the time terms or delay times of the shot and receiver points respectively, while the D_{ij} is the distance between the feet of the perpendiculars dropped from the shot and receiver locations to the lines drawn tangentially through the points of refraction (see Figure 4-1). V is the refractor velocity, which can be taken as a constant, or be described by a function which incorporates anisotropic velocity variation, or some variation of the refracting velocity with spacial coordinates.

The time terms correspond to the time delay introduced by the presence of the overburden above the refracting surface, and are given by

$$a = \int_0^H \frac{(V^2 - v^2(z))^{\frac{1}{2}}}{Vv(z)}\, dz \qquad (4.2)$$

where V is the refractor velocity at the point of refraction, v(z) is the overburden velocity as a function of depth, and H is the depth to the refractor at the point of refraction. As already noted, V may be allowed to vary as a function of azimuth (giving anisotropy), or as a function of position within the survey area. Backus (1965) derived an expansion of the velocity of a weakly anisotropic material in terms of azimuth, and the generalized elastic constants of the material.

$$V = V_0 + A \sin 2\phi + B \cos 2\phi + C \sin 4\phi + E \cos 4\phi \qquad (4.3)$$

This has been extended by Crampin (1977) to include both types of quasi-shear waves which exist in an anistropic medium.

If the refractor velocity V is taken to be azimuthally dependent, then the anisotropic variation in the refractor velocity can be expressed as $V = V_m + \delta V$, where V is the anisotropic velocity, V_m is the mean

velocity, and δV is the deviatoric velocity. Because the shot point and receiver time terms are functions of V (Equ. 4.2), they are azimuthally dependent, and this dependence is undesirable. Taking a Taylor series expansion of Equation 4-1 about V_m, and neglecting second and higher order terms in the small quantity δV, we get

$$t_{ij} = a_i(V_m) + a_j(V_m) + \frac{D_{ij}}{V_m^2} + \left(\frac{\partial a_i}{\partial V} + \frac{\partial a_j}{\partial V} - \frac{D_{ij}}{V^2} \right) \delta V \qquad (4.4)$$

Noting that, (Willmore and Bancroft, 1966),

$$\frac{\partial a}{\partial V} = \frac{F}{V_2} \qquad (4.5)$$

where F is the horizontal offset distance between the shot or receiver point and the point of refraction (the half critical distance), we obtain

$$t_{ij} = a_i(V_m) + a_j(V_m) + \frac{D_{ij}}{V^2} + (F_i + F_j - D_{ij}) \frac{\delta V}{V^2} \qquad (4.6)$$

In the simple time term, described by Willmore and Bancroft (1960), and later by Willmore (1969), each receiver and shot point has an associated time term. Equation (4.1) can then be formulated as a matrix equation where t_{ij} is replaced by T_{ij}. Assumptions must be made regarding the distance D_{ij}. If the refracting interface is horizontal then D equals Δ_{ij}, the distance between the shot and receiver. However, if there is any topography on the refractor interface, then the D_{ij} will deviate from Δ_{ij}. The usual initial assumption is that D_{ij} equals Δ_{ij}, but this approximation is discussed more throughly later in this chapter.

Provided that the receivers record more than one shot the formulated matrix equation can be solved in a least squares sense, thereby giving the delay times at the receiver and shot points. However, this process is unsatisfactory for several reasons. As the a_i and a_j are assumed to be completely independent, the least squares algorithm can add some time increment to the a_i, while subtracting it from the corresponding a_j and still maintain a solution to the matrix equation. In practice this adjustment occurs, and often produces unrealistic time terms. The second point which argues against this simple approach is that, on physical grounds, it would be expected that the actual delay times would vary as some smooth function of position. However this simple algorithm,

with independent time terms, often produces an erratic spacial varation in the delay times. The solution to this latter problem involves the introduction of a delay time surface (Raitt et al., 1969).

4.2.2 Delay Time Function Method

This modification of the time term method, first introduced by Raitt et al., (1969), abandons the assumption of independent delay times. In practice, some degree of continuity would be expected between the depth of the refracting surface and the overburden velocity between adjacent stations or shot points, and hence in the delay times. Instead of using independent time terms for each shot point and receiver location, a delay time function is defined throughout the survey area as a smoothly varying function of coordinates, which has the value of the time term at any point. This constrains the delay time surface, and hence the time terms, to be a smooth function of coordinates, and thereby removes the two objections to the simple time term approach.

The function commonly used to define the delay time surface is a combination of a polynomial and a double Fourier series. There exists some flexibility with regard to the order of the polynomial and Fourier series used, as discussed by Raitt et al., (1969), as well as Whitten (1969). Given a rectangular coordinate system (x,y) defined throughout the survey region, the delay function $\tau(x,y)$ can be expressed as, (Raitt et al., 1969),

$$\tau(x,y) = p_0 + p_1 x + p_2 y + p_3 x^2 + p_4 y^2 + p_5 xy + \ldots\ldots$$
$$+ \sum_{n=1}^{N} \sum_{m=1}^{N} \{b_{nm} \sin(nUx) \sin(mVy) + c_{nm} \sin(nUx) \cos(mVy) + d_{nm} \cos(nUx) \sin(mVy) + e_{nm} \cos(nUx) \cos(mVy)\} \quad (4.7)$$

where p_k are the coefficients of the polynomial and N is the order of the Fourier series, U and V are scaling factors, and b_{nm}, c_{nm}, d_{nm}, e_{nm} are the double Fourier coefficients.

The number of unknown parameters introduced to specify the delay time surface, with P and N the order of the polynomial and Fourier series respectively, is

$$\frac{(1+P)(2+P)}{2} + 4N^2$$

Four additional parameters are needed to specify a weakly anisotropic variation in the refractor velocity (equation 4.3). Raitt et al. give the expression for the formulation of the matrix equation for the delay time surface, including an anisotropic refractor velocity.

The introduction of a delay time surface substantially reduces the number of unknown parameters in the least squares formulation, and therefore in the size of the matrix which must be inverted. However, in practice, the $4N^2$ term in equation (4.8) becomes dominantly large if a double Fourier series of order greater than four is required. This imposes a limitation on the resolution that can be obtained using this delay time function method.

4.2.3 An Iterative Correction to the Time Term Method

As previously noted, the assumption that D_{ij} is equal to the shot receiver distance Δ_{ij} is incorrect if the refracting surface is not planar and horizontal. Bamford (1973b) pointed out that the initial assumption that $D_{ij} = \Delta_{ij}$ can be iteratively corrected utilizing the information on the topograpy of the refracting surface obtained from the delay time function. This correction must be applied if the final analysis is to truly reflect the actual structure.

Given $\tau^q(x,y)$, where the superscript refers to the q th iteration of the time term procedure, then a more accurate approximation for D_{ij} can be derived. Allowing $\hat{z}$ to be a unit vector in the direction from the source to the receiver, then the slope of the refractor at the point of refraction in this direction (see figure 4-2) is

$$\text{Tan}\ (\phi) = \hat{z} \cdot \nabla \tau(x,y)$$

The angular deviation of the path of the refracted ray from the horizontal, denoted by δ, is given to a first approximation by

$$\delta = \arctan \left\{ \frac{h_i \text{Cos}\ \phi_i - h_j \text{Cos}\ \phi_j}{\Delta_{ij} - h_i \text{Sin}\ \phi_i - h_j \text{Sin}\ \phi_j} \right\}$$

If the average overburden velocity $\bar{c}$ of the material above the refracting interface is known, the depth h, to the point of refraction for either the shot or receiver point is

$$h_k = \frac{a_k \bar{c}}{\text{Cos}\ \theta_k} \qquad \text{where } k = i \text{ or } j \qquad (4.11)$$

where a is the time term, ie $\tau^q(x,y)$, and c is known, but θ is undetermined. From the geometry

$$\delta = \frac{\pi}{2} - \phi - \theta_2 \qquad (4.12)$$

where θ_2 is the angle of refraction, and Snell's Law relates this to the angle of incidence, θ

$$\frac{\text{Sin } \theta}{\text{Sin } \theta_2} = \frac{c_1}{V} \tag{4.13}$$

Using the approximation for δ, a better approximation for θ_1 can be derived, and in turn this can be used to improve the approximation for δ. This iterative stage is found in practice to be very stable, with two or three iterations producing a convergence.

Once a satisfactory (q+1)th approximation to the h and θ has been obtained, the topographic dependent distances D_{ij}, F_i, F_j can be calculated,

$$D_{ij} = \sqrt{(H_i \text{ Cos } \phi_i - h_j \text{ Cos } \phi_j)^2 + (\Delta_{ij} - h_i \text{ Sin } \phi_i - h_j \text{ Sin } \phi_j)^2}$$

$$F_i = h_i \text{ Sin } \phi_i \tag{4.14}$$

$$F_j = h_j \text{ Sin } \phi_j$$

and these can be substituted into equation 4.6, and the least squares analysis repeated to give the (q+1) th solution of the delay time surface.

The iteration of this kind is important for two reasons. Firstly, an incorrect value of the distance D_{ij} may distort the delay time surface and give an unrealistic determination of the geometry and depth of the refracting surface. Secondly, the D_{ij} and the offset distances F_i and F_j have a direct influence on the determination of the anisotropic velocity variation. As can be seen from equation (4.4), if these distances are incorrect, the time terms, and therefore the delay time suface, are dependent on the azimuth of the observations.

4.3 THE DATA

This study utilizes data from four crustal refraction surveys in eastern Central Queensland. The surveys include one performed by the Bureau of Mineral Resources (BMR), and three surveys performed by the Research School of Earth Sciences (RSES). The survey area, shown in Figure 3-1, is approximately 500 km square centred roughly 100 km west of Rockhampton, and its regional geology and tectonic setting has been discussed in Chapter 3.

The data for the time term analysis were either taken from

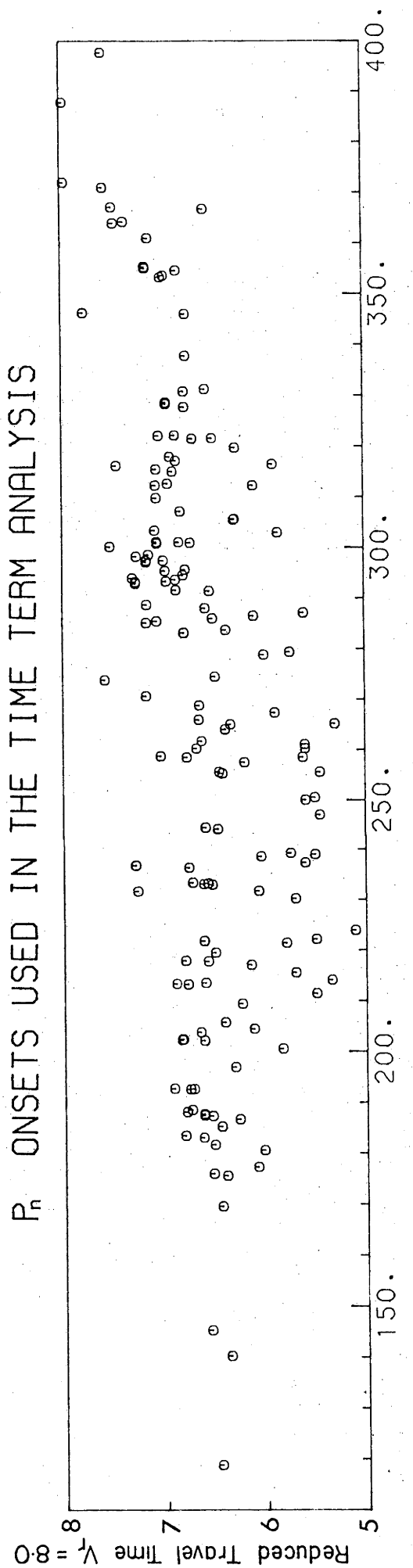

Figure 4.2

P_n data for time term analysis.

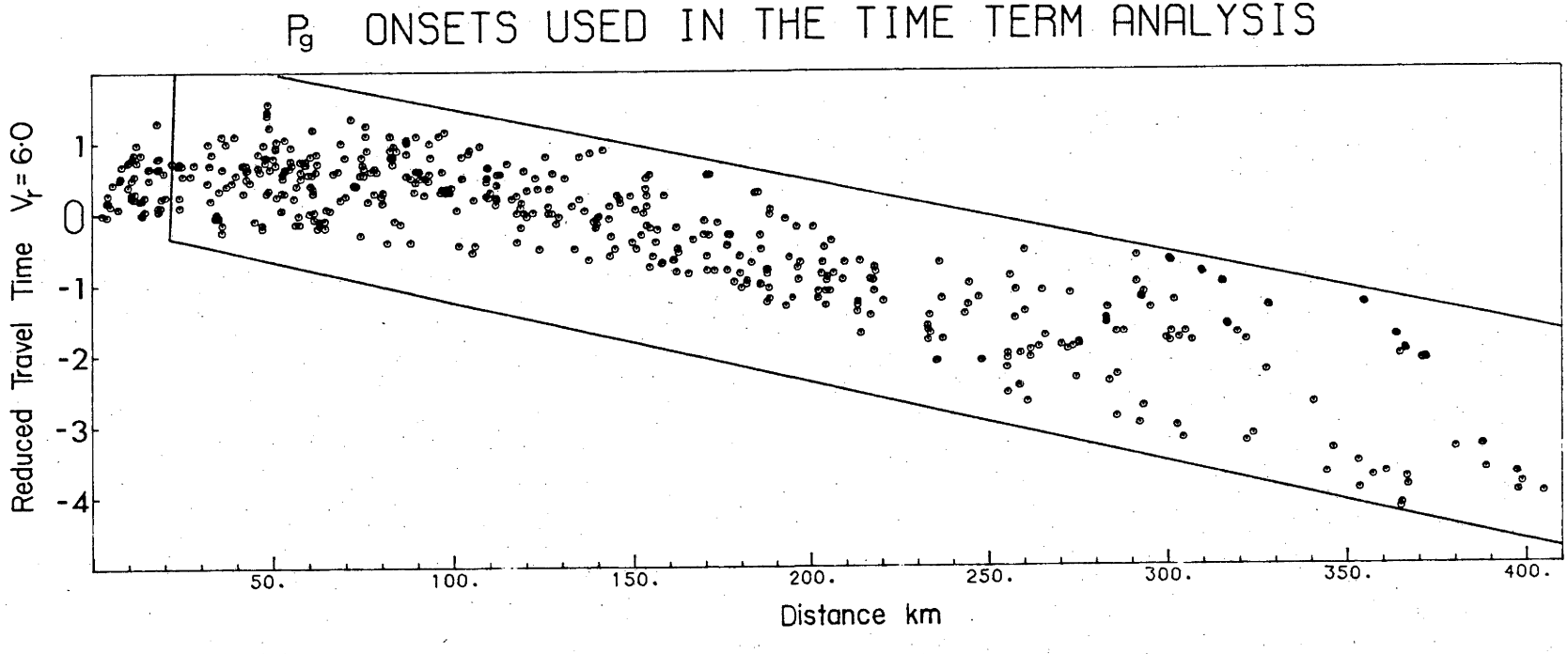

Figure 4.3

P_g data for time term analyses, showing the selective window used to cull the data. Note the greater dispersion of the data beyond 250 km, reflecting greater difficulty in detecting the P_g onset.

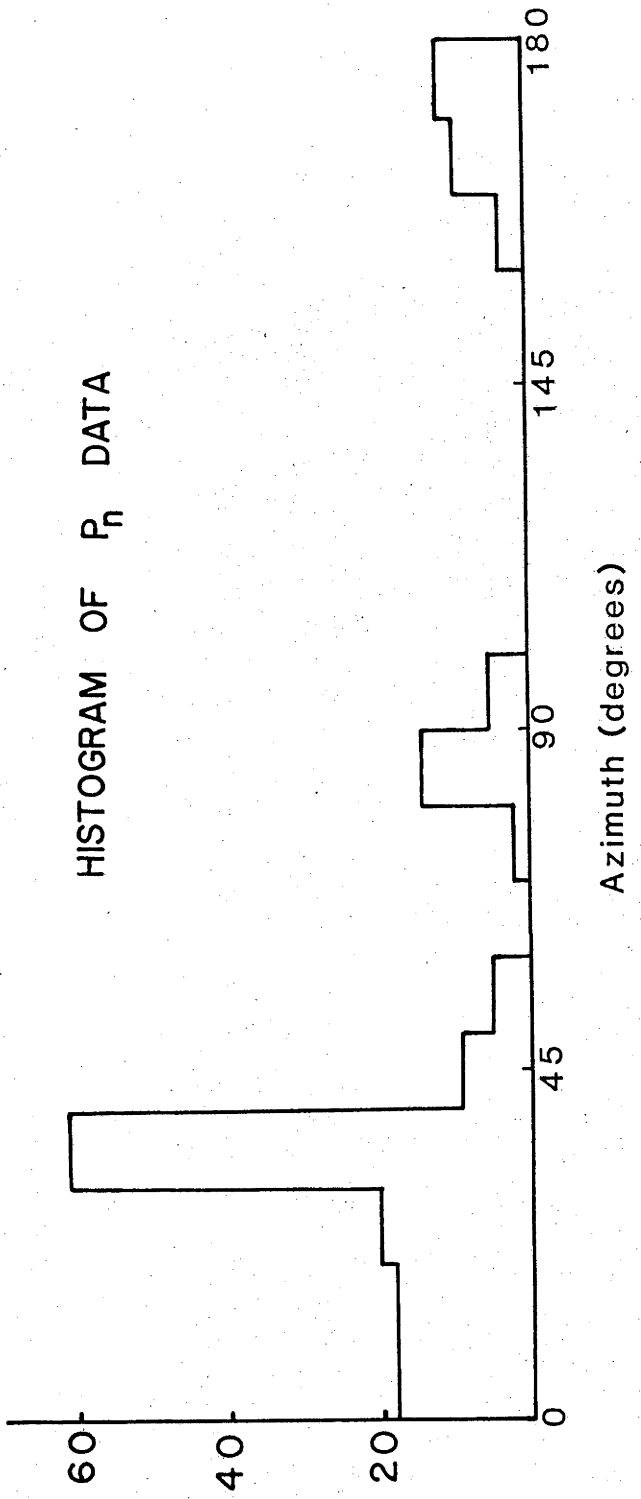

Figure 4.4

Histogram of azimuths sampled by (a) P_n data.

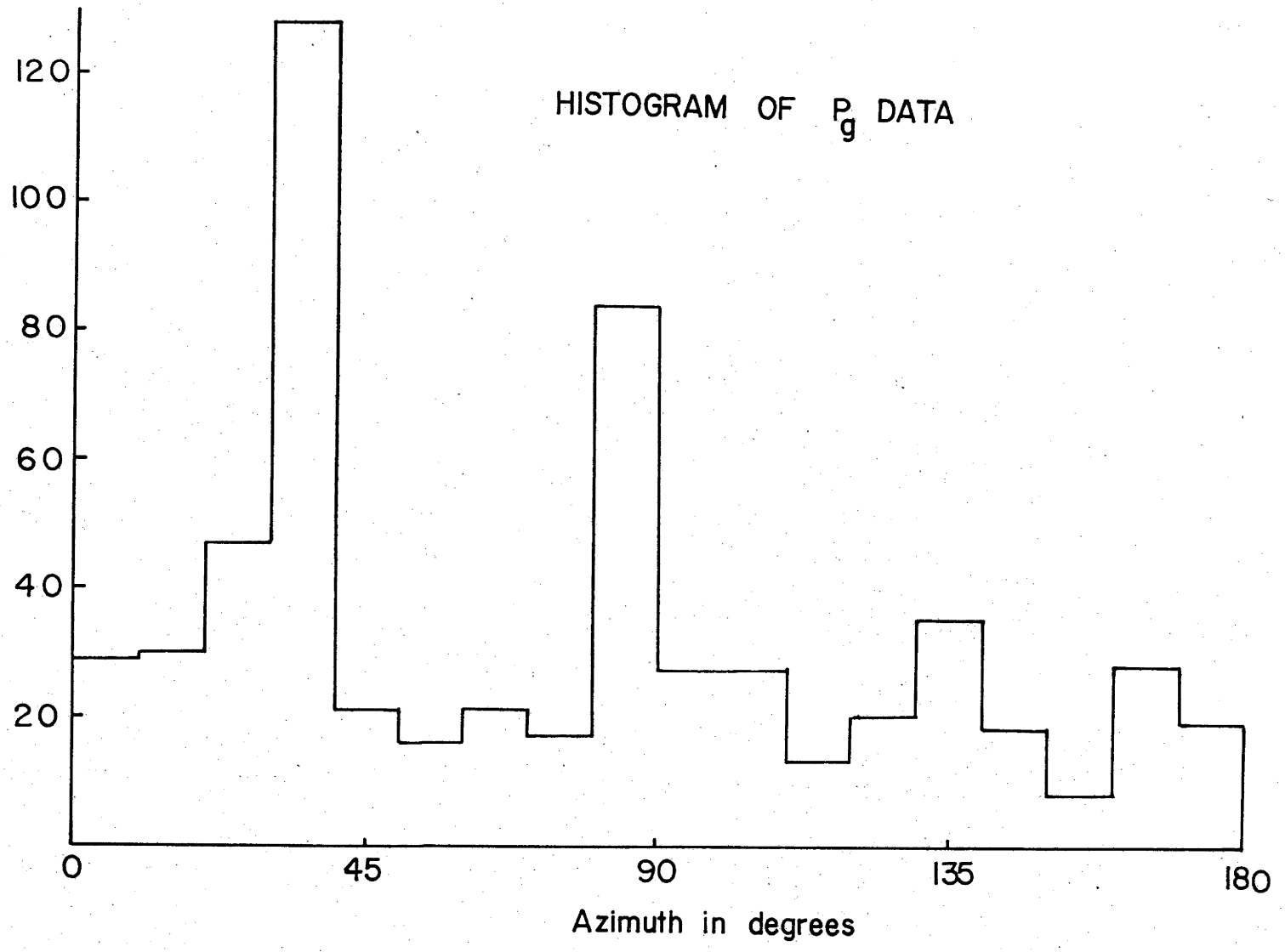

Figure 4.4

Histogram of azimuths sampled by (b) P_g data.

tabulated readings of the onset times in the case of the BMR survey (Connelly and Collins, 1973), or read directly from record sections (in the case of the other three RSES surveys). Positive identification of onsets of particular phases becomes a problem with some of the weaker arrivals of the Pn wave group beyond 200 km, and also with the Pg phase beyond the cross-over distance with Pn. Plots of the time versus distance, and average velocity versus distance were used to cull unreasonable data (ie incorrectly identified wave groups etc.), and to establish the consistency of the data. In accordance with common practice, a selective window has been applied to the data to remove spurious values. The respective windows for the travel-time distance plots are shown superimposed over the data in Figures 4-2 and 4-3. Figure 4-2 and 4-3 show the t-Δ plots for the combined Pn and Pg data respectively. A least squares analysis of these data has been discussed in Chapter 3.

A histogram of the azimuths sampled by the combined data is shown in Figure 4-4. The azimuthal distribution of the data is important for the analysis of the anisotropic variation of the refractor velocity. Unless the data evenly sample all azimuths, the resolution with which the anisotropic velocity variation can be detected is degraded. The azimuthal distribution of the Pg data is relatively even, despite the T shaped geometry of shot points and receivers shown in Figure 4-5. Fan spreads which result from the shots at the Blackwater, Goonyella, and Peak Downs mines have tended to even this distribution. However, the Pn data have a distinctly bi-modal distribution due to the geometry of the surveys. As the Pn observations only exist at distances beyond the critical distance, the range of azimuth over which they are observed is limited.

4.4 ANALYSIS OF THE Pn DATA.

Using the delay time method previously discussed, several different types of delay time surfaces were fitted to the Pn data. Table 4-1 details the statistics of these various fits. The total number of data prohibits the use of a high order polynomial or double Fourier series in the representation of the delay time surface. It must also be borne in mind that the data only constrain the delay time surface in the vicinity of the shot points or receiver stations, and little significance can be attached to the extraploated values of the delay times away from these points. For the delay time surface, both a linear and quadratic polynomial function of

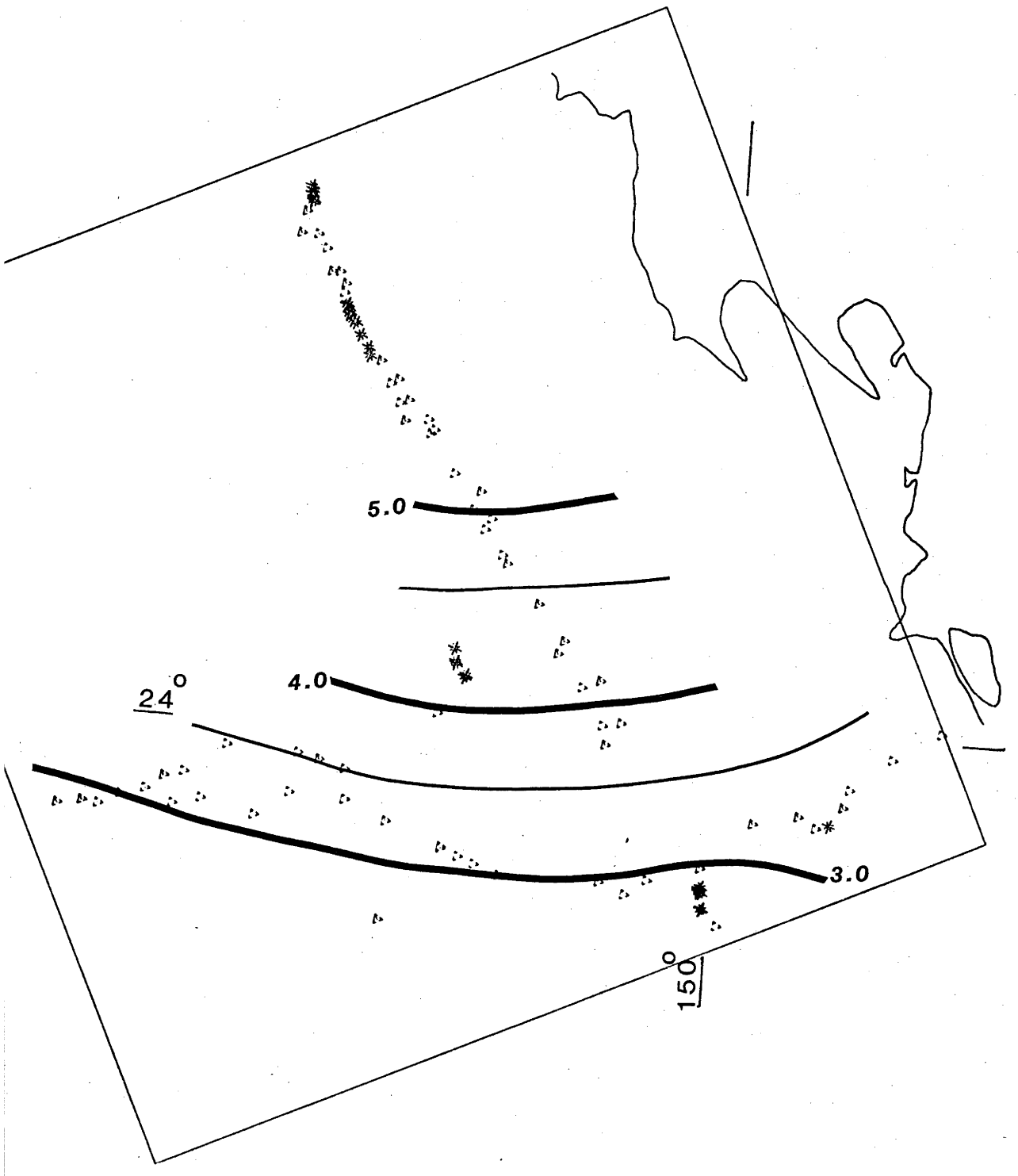

Figure 4.5

Quadratic delay time surface of P_n analysis, Fourier order 2.

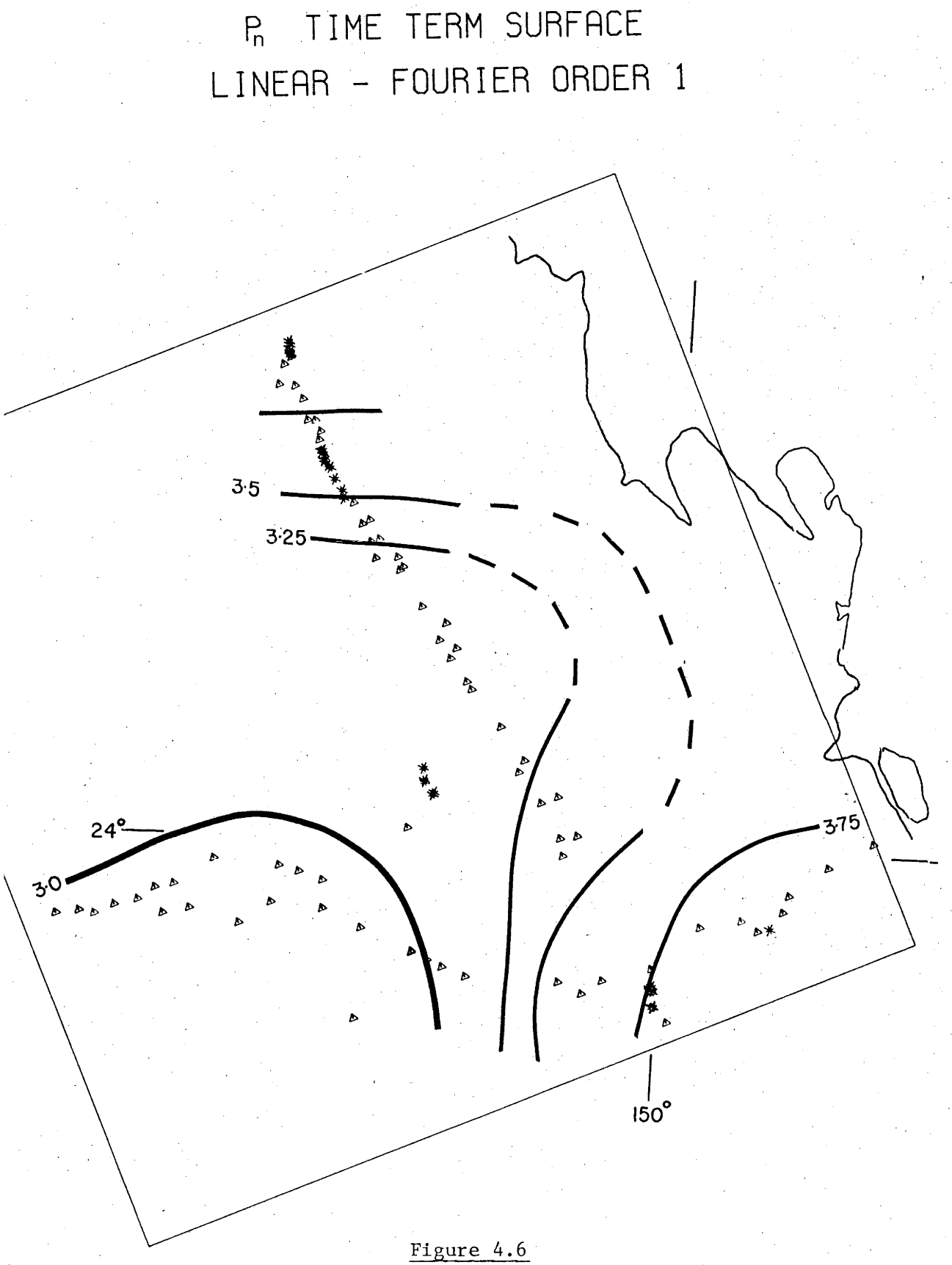

Figure 4.6

Linear delay time surface of P_n analysis, Fourier order 1.

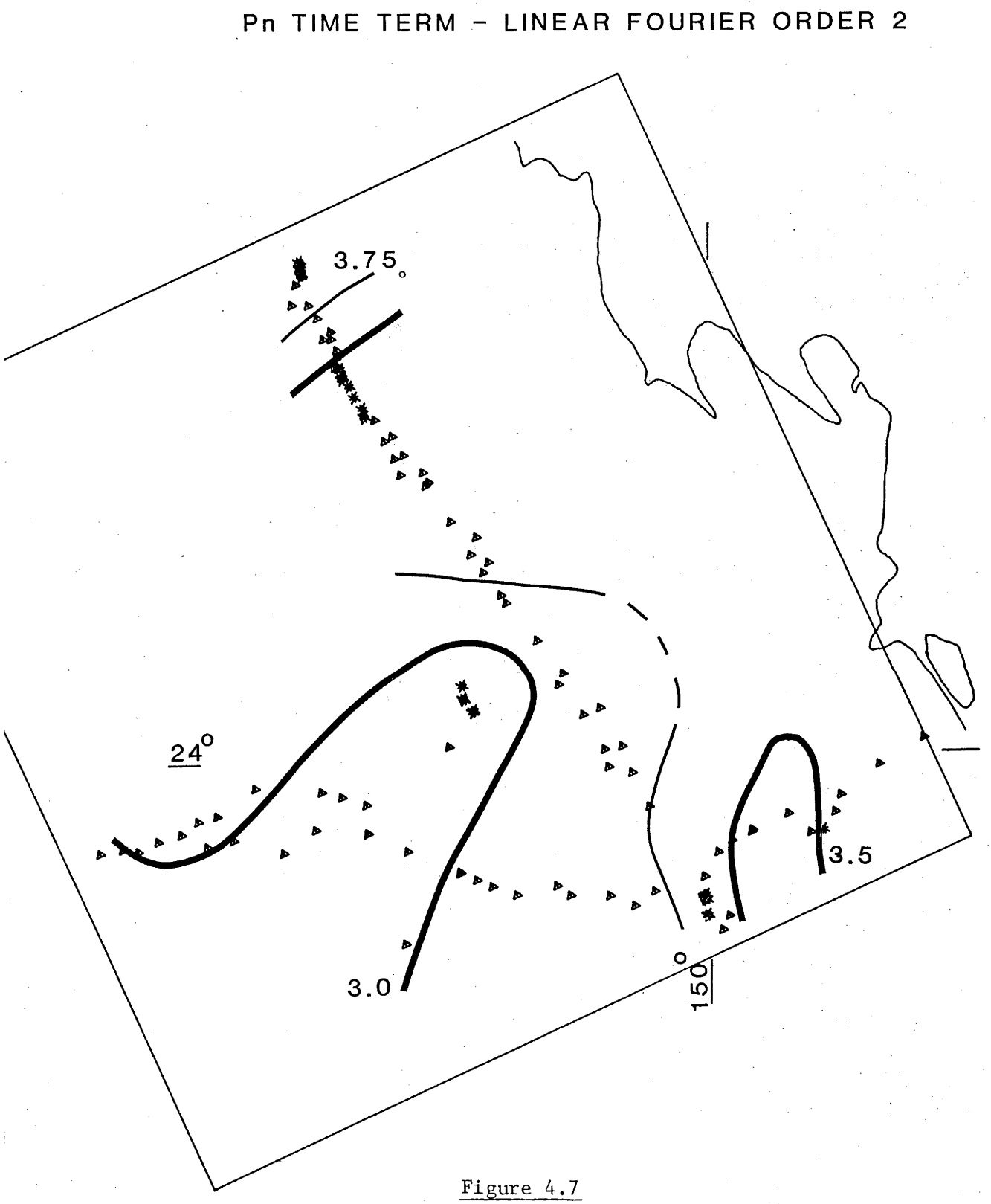

Figure 4.7

Linear delay time surface of P_n analysis, Fourier order 2.

position were used, but it was found that the quadratic form of the delay time function produced results which had a dominant saddle structure, and unreasonable time terms, as shown in Figure 4-5. The instability of the quadratic solution can be seen in the variation of the delay time surface between the solutions of differing Fourier order. The T shaped geometry of the profiles is thought to be responsible for such instability, as the linear polynomial surfaces do not display this instability. For this reason the quadratic solutions have not been considered further.

The low order linear delay time surfaces have several common features, (Figures 4-6 and 4-7), although the exact form of the delay time surface varies between these solutions. While confidence can not be placed in the finer details of the time terms, these common features are thought to be reliable. There is a significant increase in the delay times towards the south-eastern corner of the survey area, typically from 3 seconds around Moura, to 3.5 seconds or greater for the stations towards the coast near Gladstone. The delay time function decreases to the west of Moura, to a value of around 2 seconds beneath Springsure. Between Moura and the Peak Downs mines, a relatively constant value of the delay time along the axis of the Bowen Basin is indicated, with an increase north of the Peak Downs mine towards the Goonyella mine.

The increase of the delay times east of Moura is unexpected as it would normally be expected that the crustal thickness would decrease towards the continental margin. The increased thickness may represent the "root" of the Tasman Geosyncline, (Schneiber, 1974). The gravity map of Australia, (BMR), shows a linear positive free air anomaly running sub-parallel to the coast in this region around Gladstone. The increased thickness of the crust indicated by the time term analysis would be expected to cause a negative free air anomaly. The gravity data do not support the increasing crustal thickness. However, the linear positive gravity anomaly may be related to the older and denser rocks of the Cracow-Eungella Mobile Belt near the surface being juxaposed beside those of the Bowen Basin, and masking the smaller gravity effect of the deepening Moho. The whole gravity picture is undoubtedly complicated by the proximity of the coast. The Bouguer gravity map also indicates a similar positive anomaly running sub-parallel to the coast, so this gravity anomaly is therefore unrelated to the relatively minor topography of this region.

The increase in the delay times observed to the north of the Peak Downs mine suggests a thickening of the crust in this direction. The

refraction profile runs approximately parallel to the coast, so this thickening is not associated with the increasing thickness towards the coast. Both the Goonyella and Peak Downs mines lie close to the western margin of the Bowen Basin in this northern section, and the basin terminates to the north of the Goonyella mine. The increase in crustal thickness could therefore be associated with the crustal response of the transistion from the Bowen Basin to the Clermont Stable Block. A time term analysis of the data from the CRUMP survey (Finlayson 1968) has indicated a Moho depth exceeding 40 km in the Cape York region to the north of the present survey area. Shirley (1979) estimated on the basis of gravity data that the crustal thickness is greater than 40 km in the region to the north of Goonyella, stating that "the area is isostatically compensated and the crustal thickness reaches 43 km". Collins (1978) derived a crustal model from the data of the BMR refraction profile running between Moura and Goonyella Mines, and in this model the Moho dips at around 3 degrees towards the south, and has a depth of approximately 35 km beneath the Saraji mine. It can therefore be inferred that the crust must thicken rapidly north of the Saraji mine, as predicted by the time term analysis of the Pn data.

The increases in the delay time function both to the south-east and the north of the survey area are interpreted as resulting from a thickening of the crust. The alternative explanation of a decrease in the average crustal velocity is not tenable, as these areas do not correspond to regions of thickening sedimentary basins in which the greater section of low velocity sediment could significantly lower the average crustal velocity.

The application of the iterative improvement of the linear first order Pn delay times surface is shown in Figure 4-8. This delay time surface displays the same general characteristics as the original delay time surface.

Unfortunately, the azimuthal distribution of the Pn data do not constrain the anisotropic variation of the velocity in the uppermost mantle. The distinctly bi-modal azimuthal distribution of the data, the uncertainity of the finer detail of the structural variation, and the statistics of the fits all indicate that little significance can be placed in the determination of the Pn anisotropy. This is in spite of the fact that an apparent velocity of 8.1 km/s was measured from the north-south profiles, while apparent velocities of 7.9 km/s were measured along the

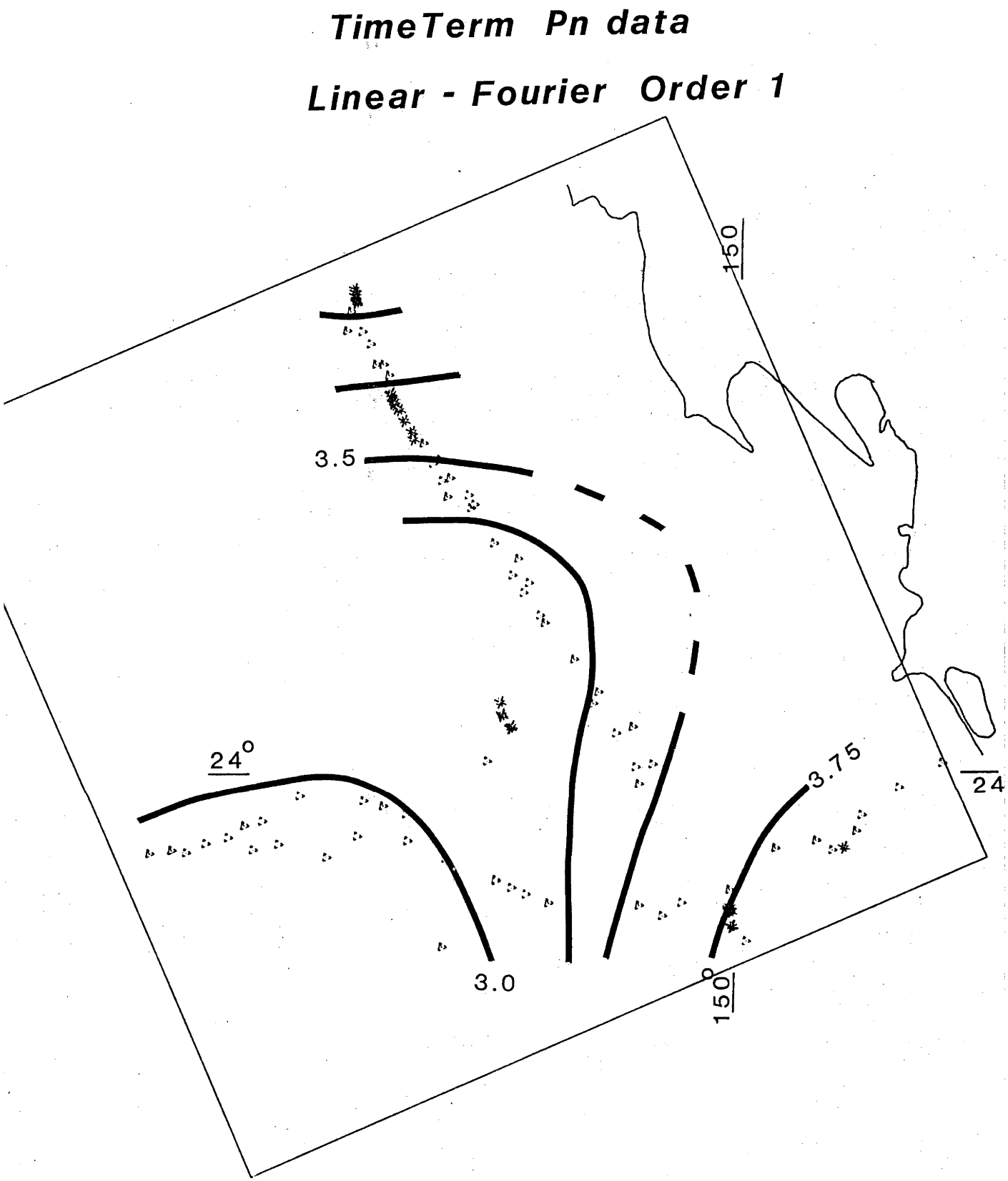

Figure 4.8

Linear delay time surface for P_n analysis, Fourier order 1. This surface has undergone iterative improvement.

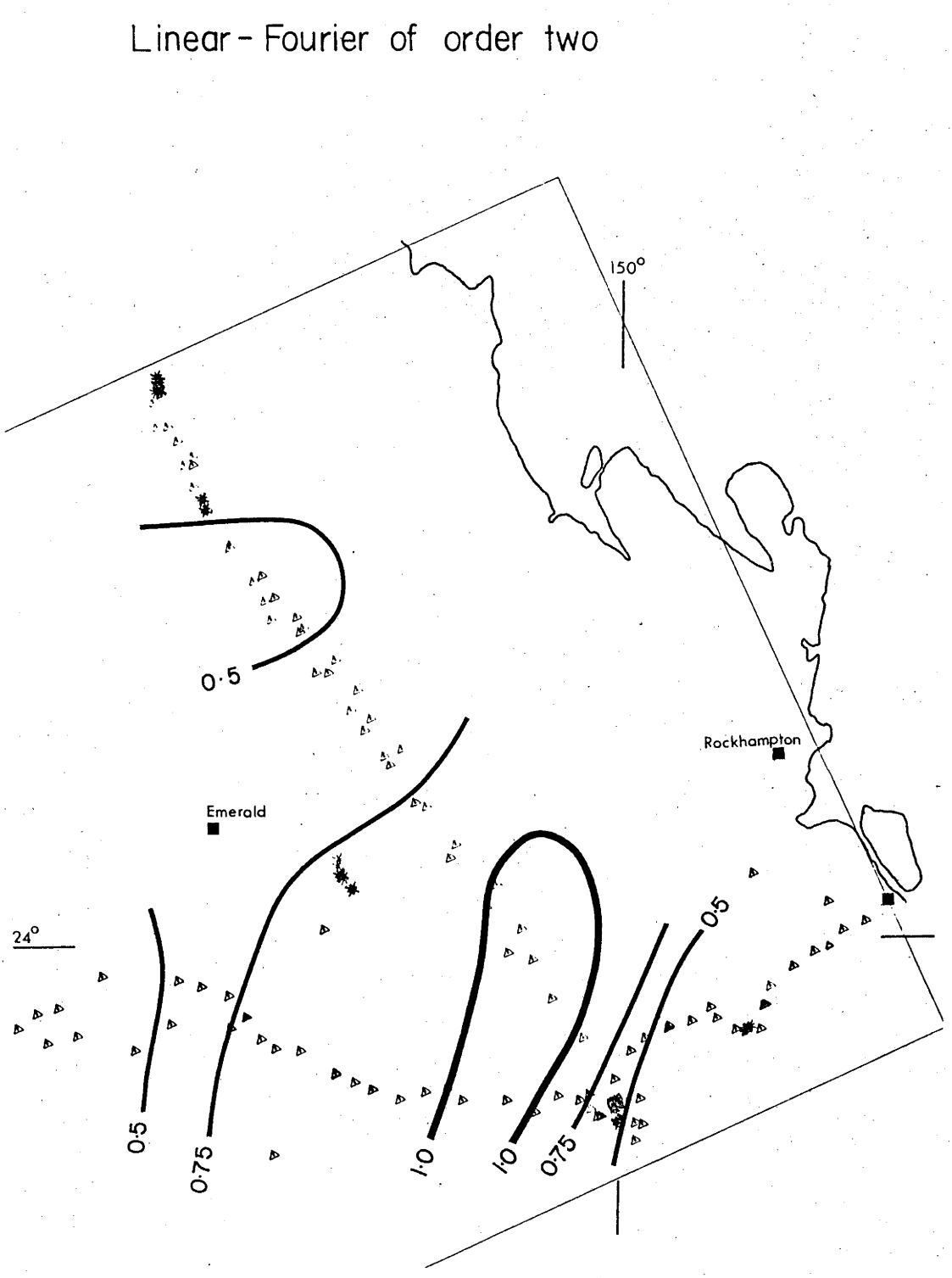

Figure 4.9

Linear delay time surface for Pg analysis, Fourier order 2.

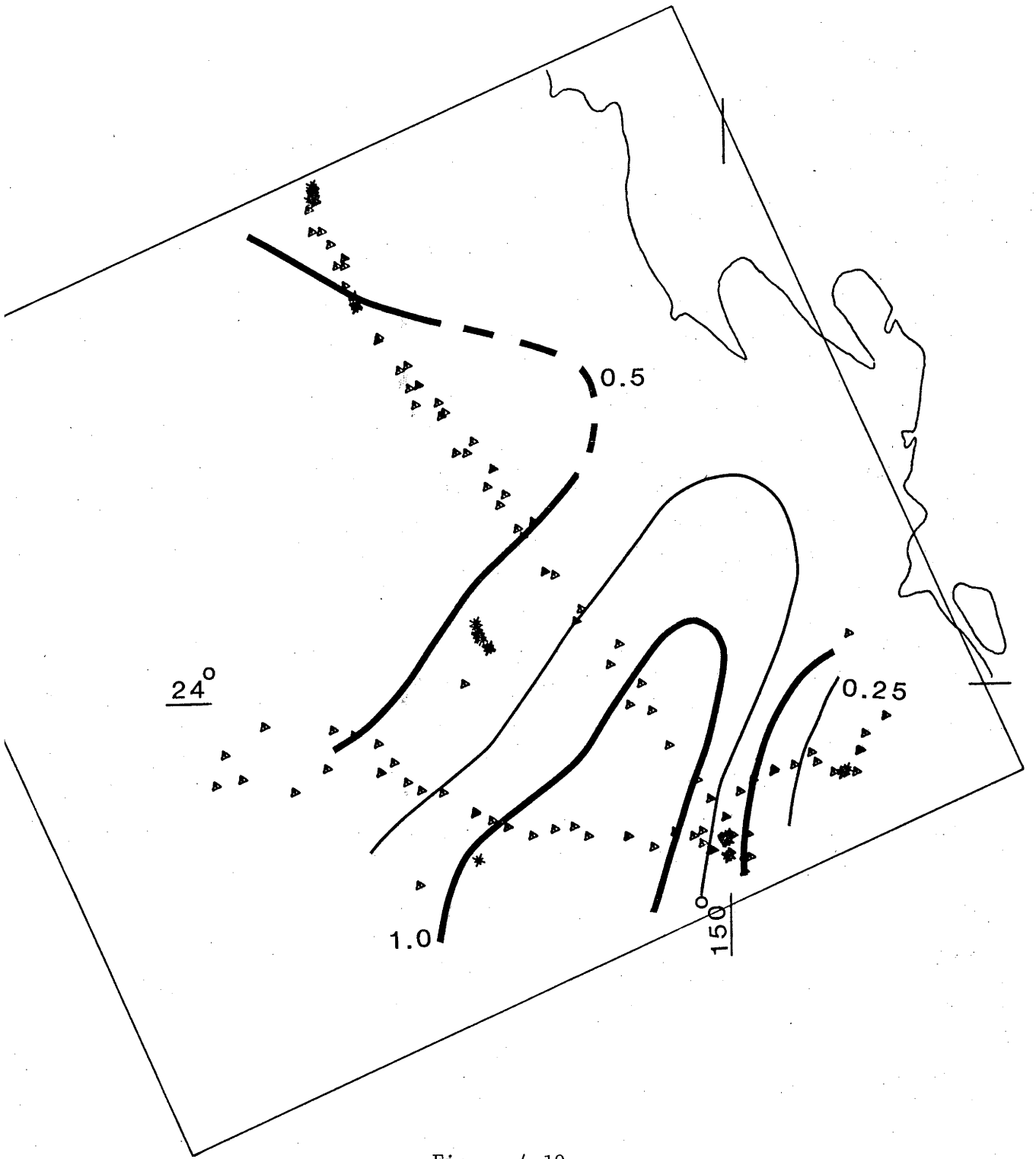

Figure 4.10

Linear delay time surface for P_g analysis, Fourier order 3.

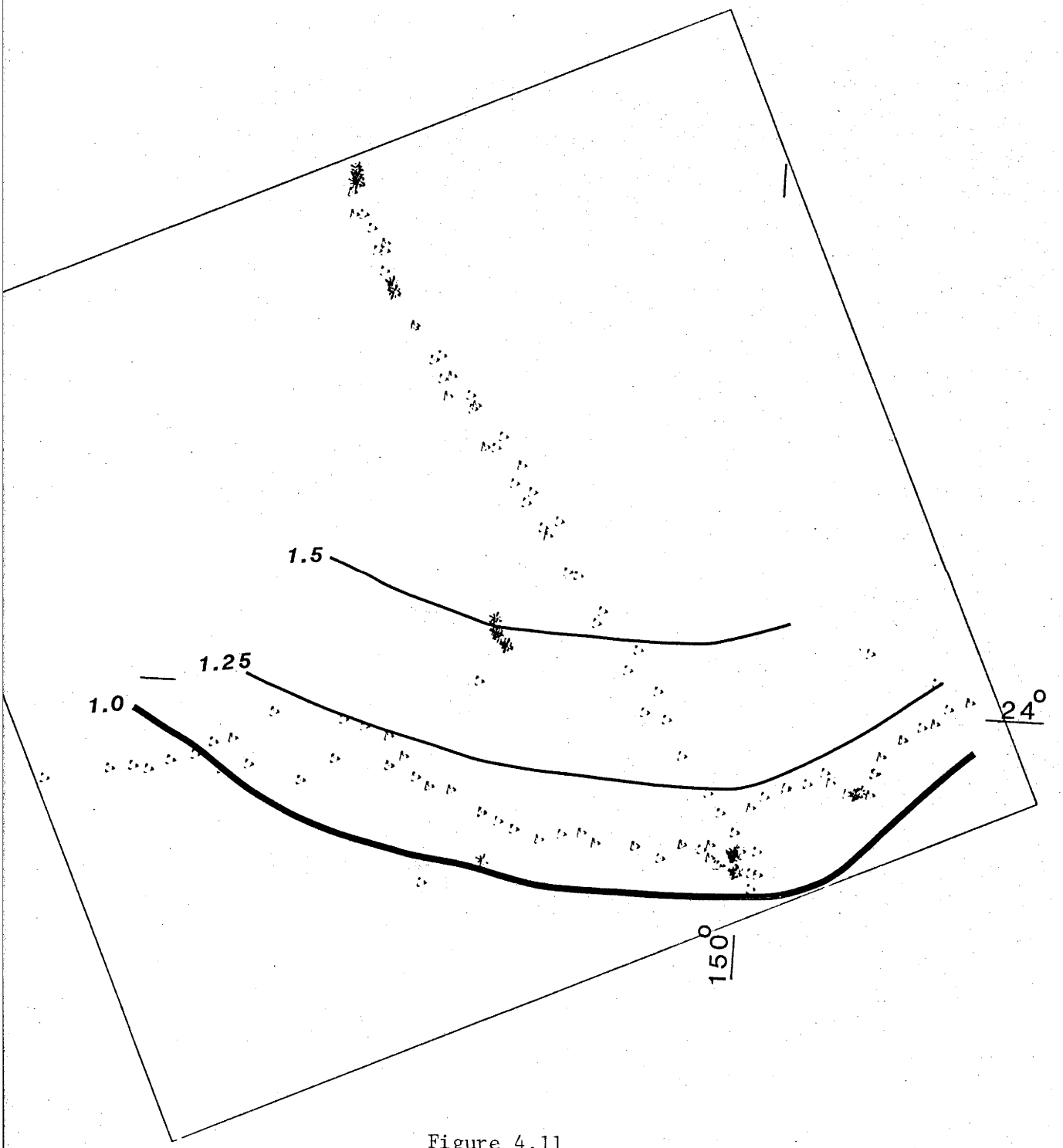

Figure 4.11

Quadratic delay time surface for P_g analysis, Fourier order 2.

east-west profile. Unless the structure of the crust is more fully determined, there is little hope of proving the existence of upper mantle anisotropy. The determinations of the anisotropy in the ocean basins have shown that the anisotropy can be conclusively measured in regions of simple crustal structure, but analysis of the present data has indicated that extremely careful experimental design, with a far greater number of recording sites, would be necessary to enable anisotropy to be unequivocally determined in the more complex continental crust. No consideration has been given to the effects of vertical variations in the overburden velocity, or lateral variations in the refractor velocity, as both these aspects would further complicate the interpretation.

4.5 ANALYSIS OF THE Pg DATA.

All the delay time surfaces derived from the time term analysis of the Pg data show a pronounced increase in the delay times west of Moura, corresponding to the deep section of the Mimosa Syncline. The linear polynomial surfaces derived using both the Fourier orders two and three (Figures 4-9 and 4-10) show a relatively consistent result. However, while the quadratic solution (Figure 4-11) shows similar general trends, its structure is more smoothed than that of the linear solutions. The maximium value of the delay time function in the vicinity of the Mimosa Syncline for the quadratic surface is 0.75 seconds, compared to over 1.0 second for the linear functions. The quadratic solution also has the basin structure distributed over a greater area, and the delay time of 0.75 seconds of the quadratic surface given in the vicinity of Springsure contradicts the known geology of this area, as well as the measured residuals of the Pg and the teleseismic events, which indicate a thinning of the sediments of the Bowen Basin on to the Springsure Shelf in this region. For reasons similar to those discussed in relation to the Pn analysis, the quadratic solutions have been considered unreliable.

The linear solutions show a marked increase in the delay time to the west of Moura, corresponding to the Mimosa Syncline. The short refraction profile around the Moura Mine has indicated an average velocity of the sedimentary section of 4.3 km/s. The conversion factor for the delay time to depth is around 5 km/s. This gives a thickness of the sedimentary section to the west of Moura in excess of 5 km which agrees with the postulated geological section of Dickens & Malone (1973). In the regions away from the Bowen Basin, the delay times are generally less than

0.3 seconds. Both the second and third order Fourier solutions Figures 4-9 and 4-10, of the linear polynomial delay time surfaces indicate a deepening of the basin from Peak Downs to Goonyella. This is in contrast to the geological mapping, which indicates a thinning of the basin towards its western margin in this direction.

The greater azimuthal coverage of the Pg data has allowed more control on the accurate determination of the anisotropy. No significant (<1%) horizontal anisotropy has been detected in the basement by the time term analysis of the Pg data. It would seem unlikely that there would be any widespread anisotropy in the "basement" rocks of the region, as these rocks do not contain any strongly anisotropic mineral, and it is unlikely that a regional mechanism could preferentially align the slightly anisotropic minerals, such as pyroxene, over the whole survey region.

4.6 CONCLUSIONS.

The time term analysis of the Pn data illustrates the difficulty of conducting an experiment on complex continental crust which can successfully measure the velocity anisotropy of the uppermost mantle. Bamford et al., (1979) analysed data from Britain, eastern, and western United States, and detected a small but significant anisotropy beneath eastern United States. Bamford (1973, 1976) had earlier found significant anisotropy beneath central Europe. The measurement of the uppermost mantle anisotropy in the eastern Australian region would have provided an interesting comparison. However, Whitcombe and Maguire (1979) demonstrated that if the refractor is not planar, the effects of structural complications can be absorbed into the time terms. A very simple crustal structure (as in the oceanic surveys) would be required to ensure that the effects of the anisotropy are not masked by structural variations. The Pg analysis shows relatively good agreement with the known geology. The most significant point raised by the time term analysis is the thickening of the crust towards the coast from Moura. This thickening has been interpreted as being the "root" of the Tasman Geosyncline. Finlayson et al., (1979) have found crustal thicknesses of up to 50 km in the Lachlan Fold Belt in a southern region of the Tasman Geosyncline in south-eastern NSW. It is therefore possible that the crustal thickness along the axis of the Tasman Geosyncline is significantly greater than the average Australian crustal thickness, (Dooley, 1976, Cleary, 1973). Wellman (1979) has discussed the implications of the isostatic compensation of the thicker crust beneath the

southern highlands of southeastern NSW, and favors a crustal underplating mechanism to explain this thickening.

Table 4.1

Wavegroup	Linear or Quadratic	Polynominal Order	Variance	Degrees of Free	Wt.Variance	Red.Chi Square	% Anis.
PN	L	0	0.113	128	0.098	0.66	2.1
PN	L	1	0.097	124	0.080	0.54	1.6
PN	L	2	0.091	112	0.081	0.55	4.7
PN	L	3	0.095	92	0.082	0.55	3.6
PN	Q	2	0.151	56	0.117	0.88	2.3
PG	L	0	0.156	456	0.146	1.48	1.1
PG	L	1	0.118	452	0.120	1.21	1.4
PG	L	2	0.096	400	0.095	0.981	1.7
PG	L	3	0.092	380	0.091	0.943	1.3
PG	Q	2	0.169	397	0.161	1.66	1.1

CHAPTER 5

SYNTHETIC SEISMOGRAMS APPLIED TO THE CENTRAL QUEENSLAND SURVEY.

5.1 INTRODUCTION.

The profile of the seismic survey conducted in Central Queensland extended over a region of relatively complicated crustal structure, and this structure has significantly affected the travel times and amplitudes of the recorded wave groups. Therefore, the modelling of the record sections along the whole length of this profile, using synthetic seismogram techniques which assume a laterally homogeneous structure, has not been possible. However, the time term analysis indicated a relatively constant crustal structure in the western extent of the profiles from the Moura/Kianga and Callide mines. Consequently, synthetic seismogram modelling will be restricted to the data obtained from the explosions within the above mentioned mines, recorded in this western region. The aspects to which the synthetic seismogram modelling will be specifically directed are the nature of the Pn wavegroup, and the origin of the Pj wavegroup. In the case of the Pg wavegroup, the assumption of spherical or planar homogeneous layers has been violated too severely to enable useful constraints to be obtained.

5.2 COMPARISON OF SYNTHETIC SEISMOGRAM TECHNIQUES.

Before applying synthetic seismograms to the modelling of crustal and uppermost mantle seismic phases, it is desirable to investigate the behaviour of the various techniques using simple velocity models. This will give some insight into the differences between the methods, as well as demonstrating the effect of changes in the velocity structure on the resultant seismograms. Because all synthetic seismogram techniques are primarily concerned with the interaction of seismic waves and velocity discontinuities, four particularly simple velocity models (Fig. 5-1) have been chosen. These are all variations of a velocity discontinuity, for which the ray theory is well understood. Model A is a classical first order discontinuous increase in velocity between two homogeneous layers. In model B, slight velocity gradients have been introduced above and below the discontinuity. Models C and D both possess second order type discontinuities, with a rapid increase in velocity occurring over a small

Figure 5.1

Spherical Earch velocity models A, B, C, and D, used in comparing synthetic seismogram methods. Number of layers refers to partitioning of each model in those synthetic seismogram methods using an Earth flattening transformation.

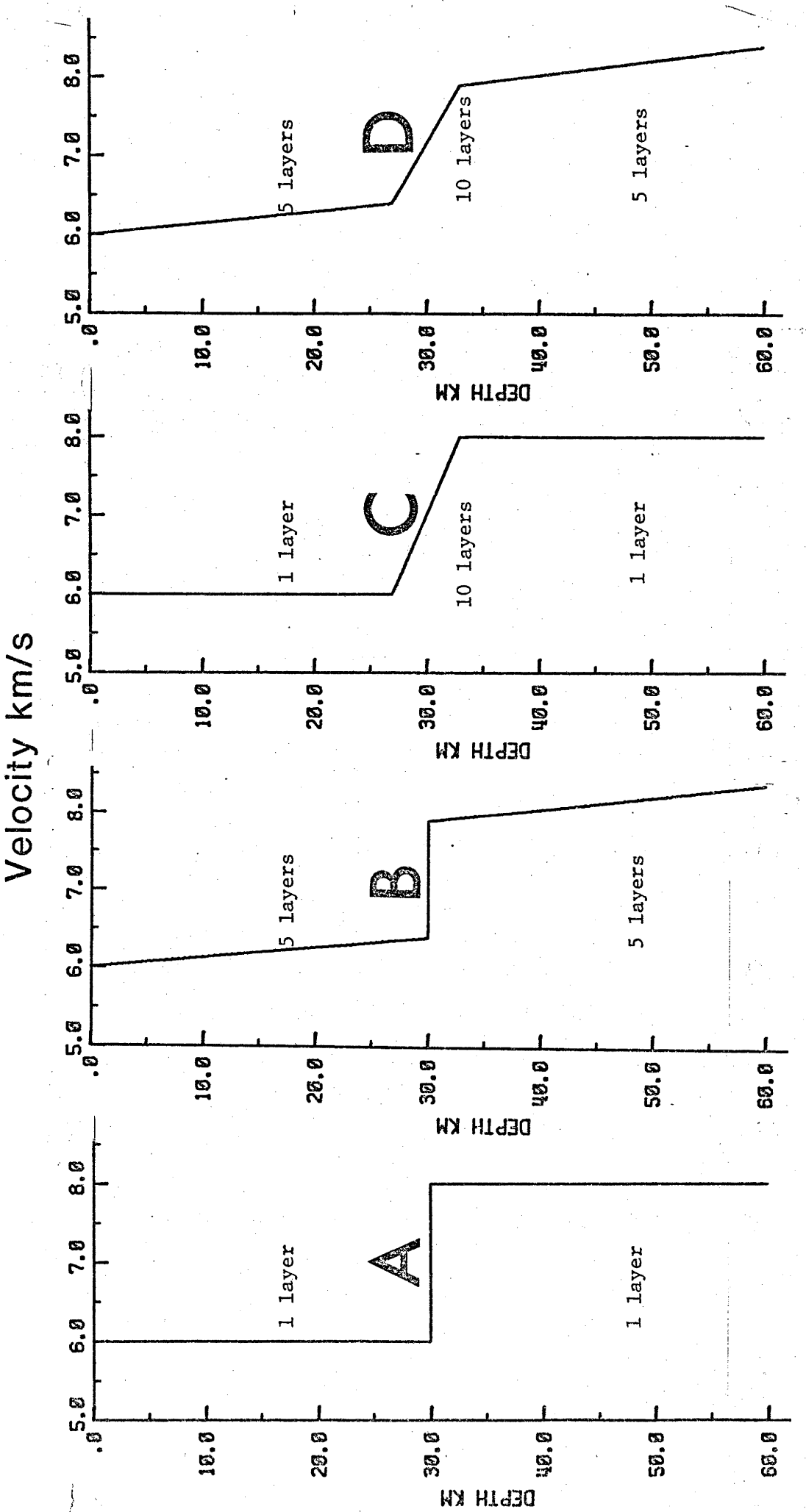
Velocity km/s
A
1 Layer
1 Layer
B
5 Layers
5 Layers
C
1 Layer
10 Layers
1 Layer
D
5 Layers
10 Layers
5 Layers
DEPTH KM
5.0
6.0
7.0
8.0
.0
10.0
20.0
30.0
40.0
50.0
60.0

Figure 5.2
Travel time distance curves of velocity models A,B,C, and D.

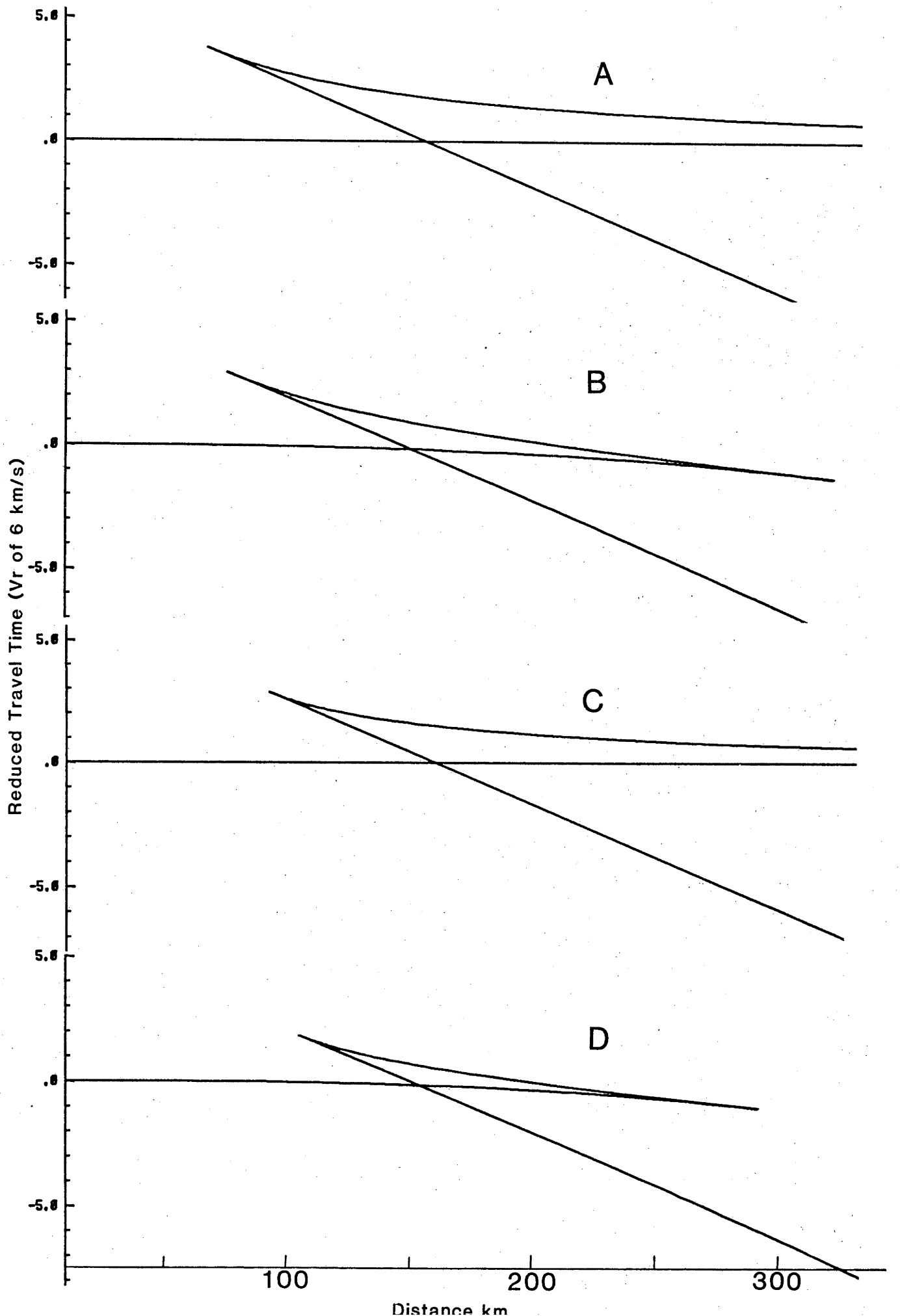

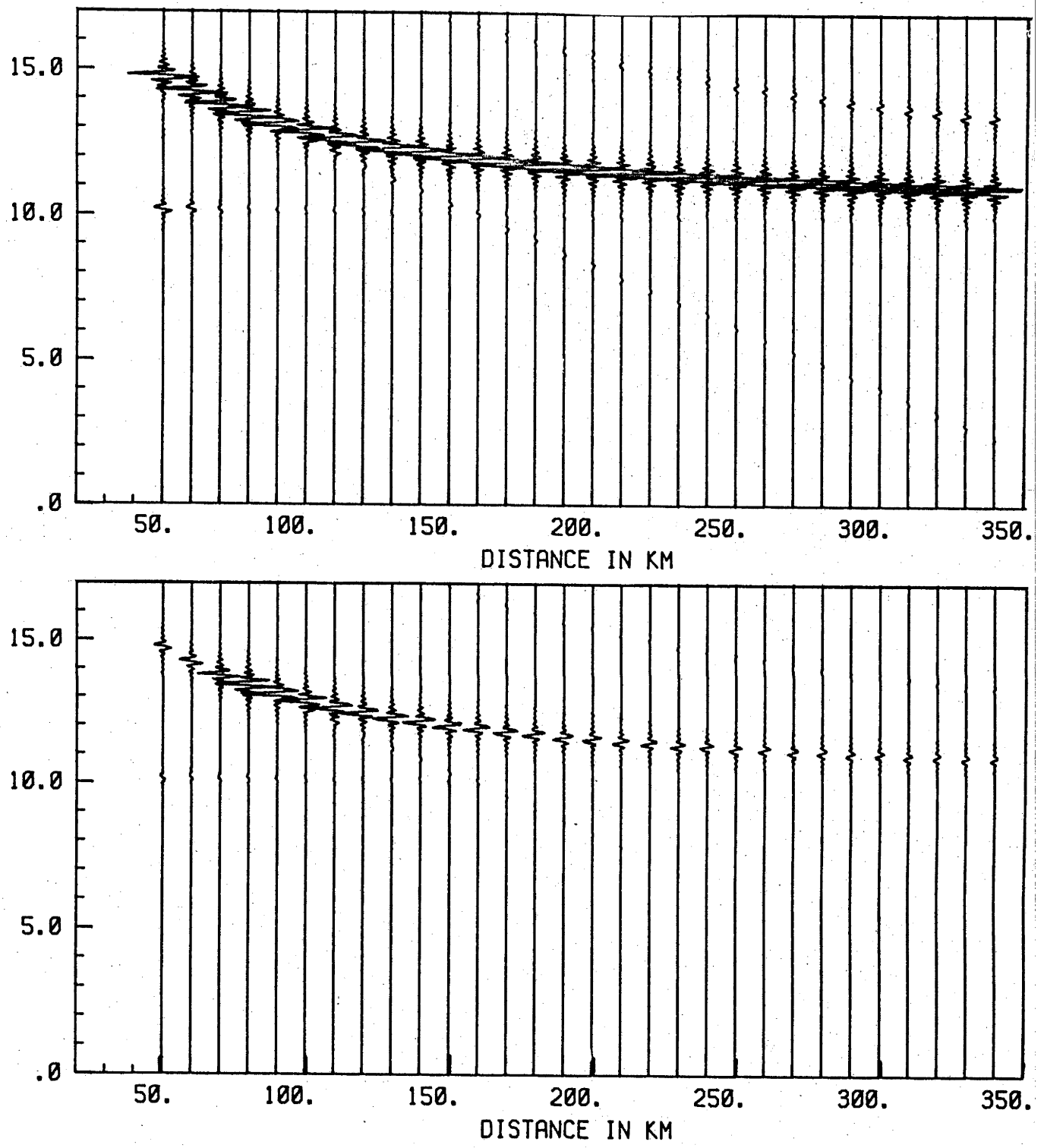

Figure 5.3

Reflectivity synthetic seismogram of model A. On this, and later synthetic seismogram figures, the vertical axis is reduced travel time, (Vr = 6 km/s) relative to an arbitary origin time. The top section is trace normalized, while the bottom section shows relative amplitudes.

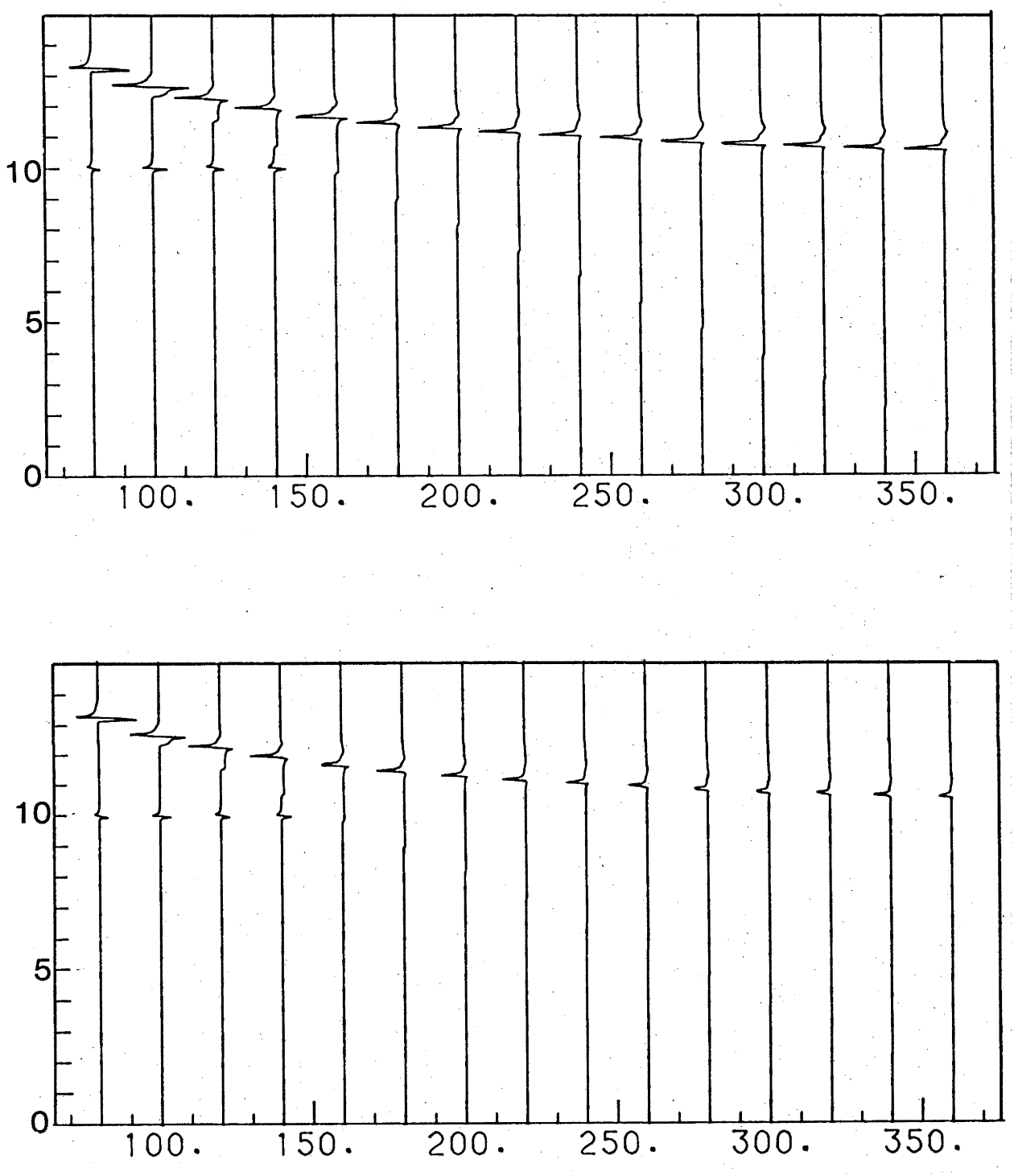

Figure 5.4

Generalized Ray theory synthetic seismogram of model A.

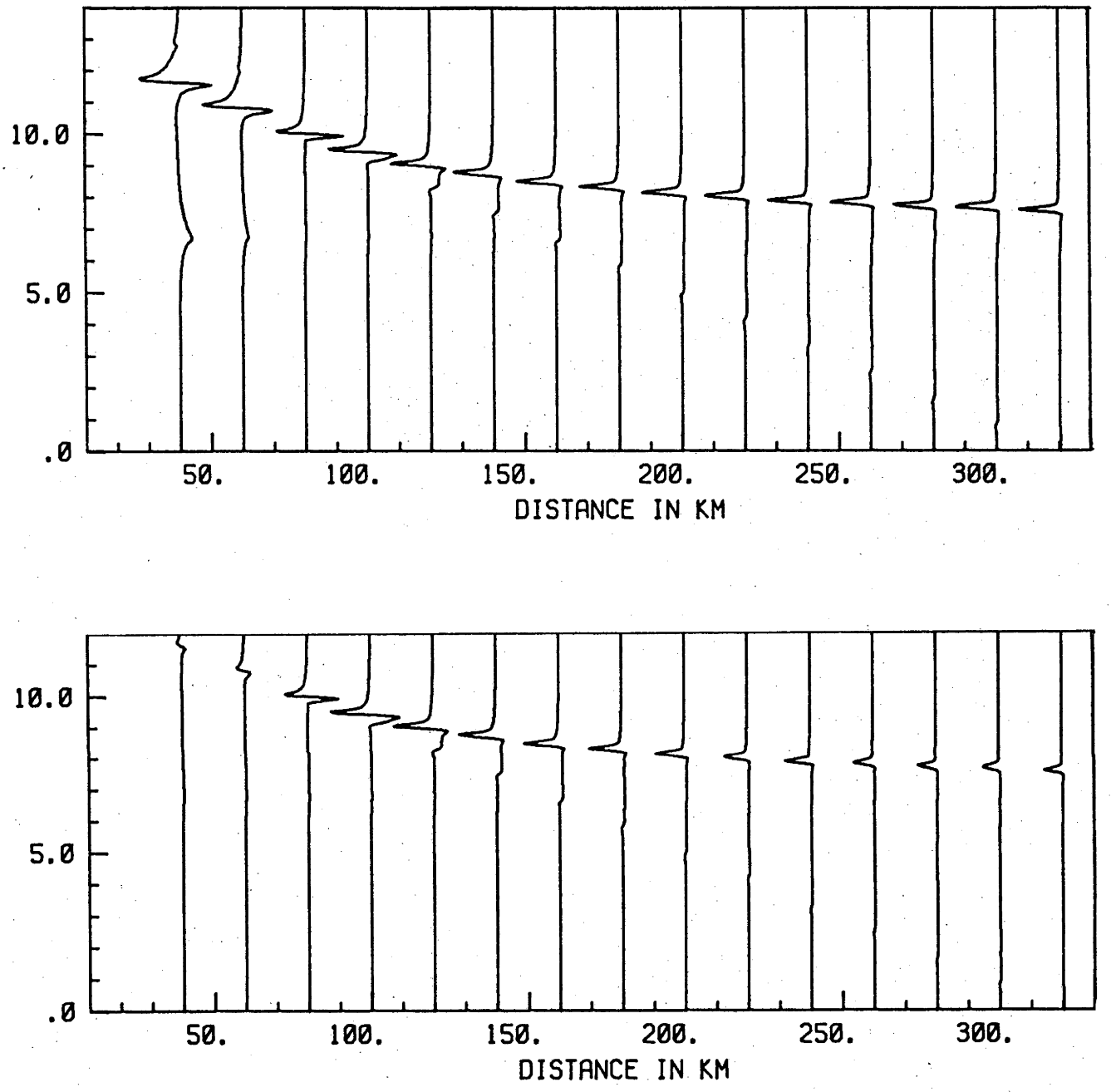

Figure 5.5

WKBJ synthetic seismogram of model A.

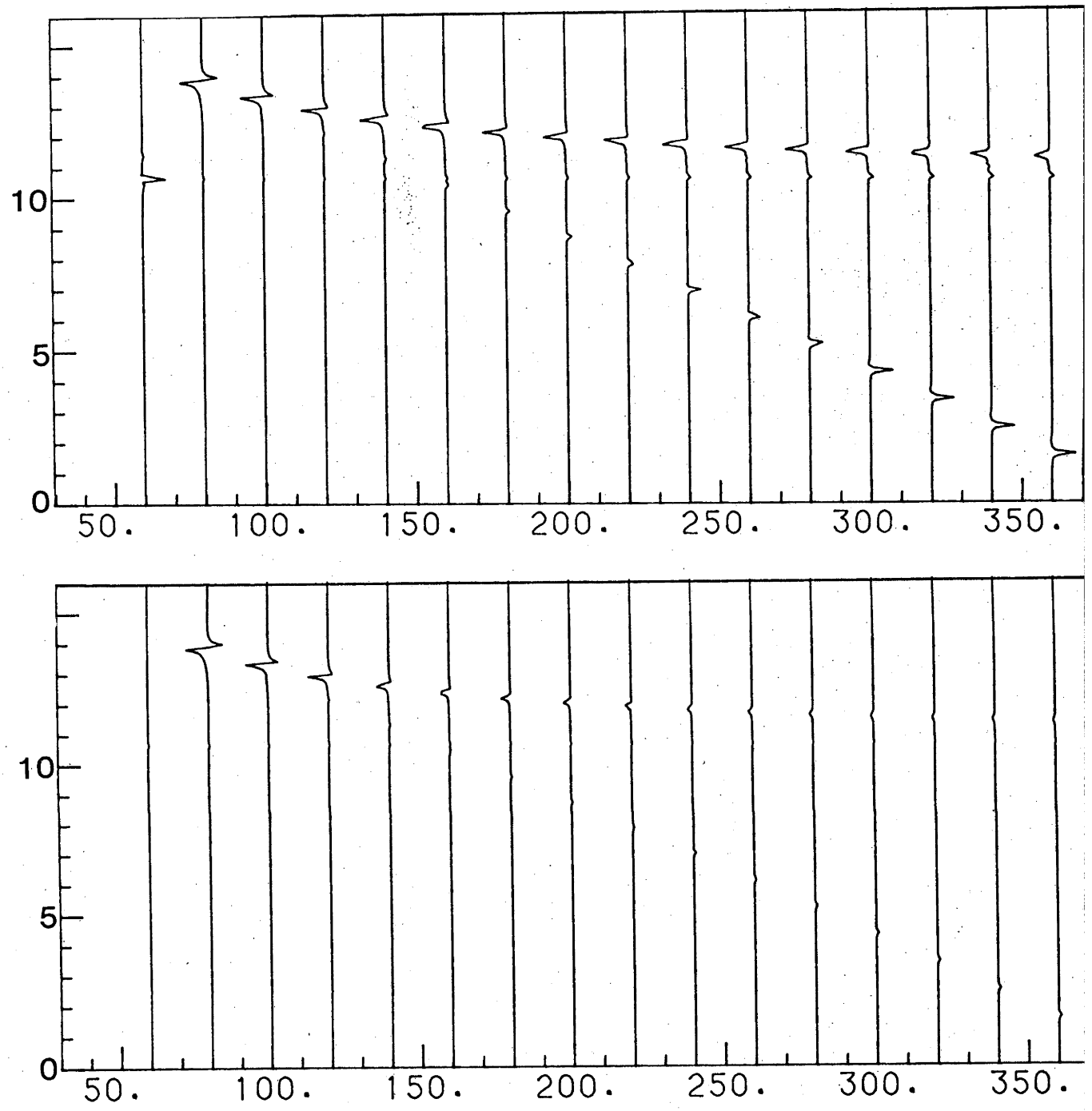

Figure 5.6

Full Wave synthetic seismogram of model A.

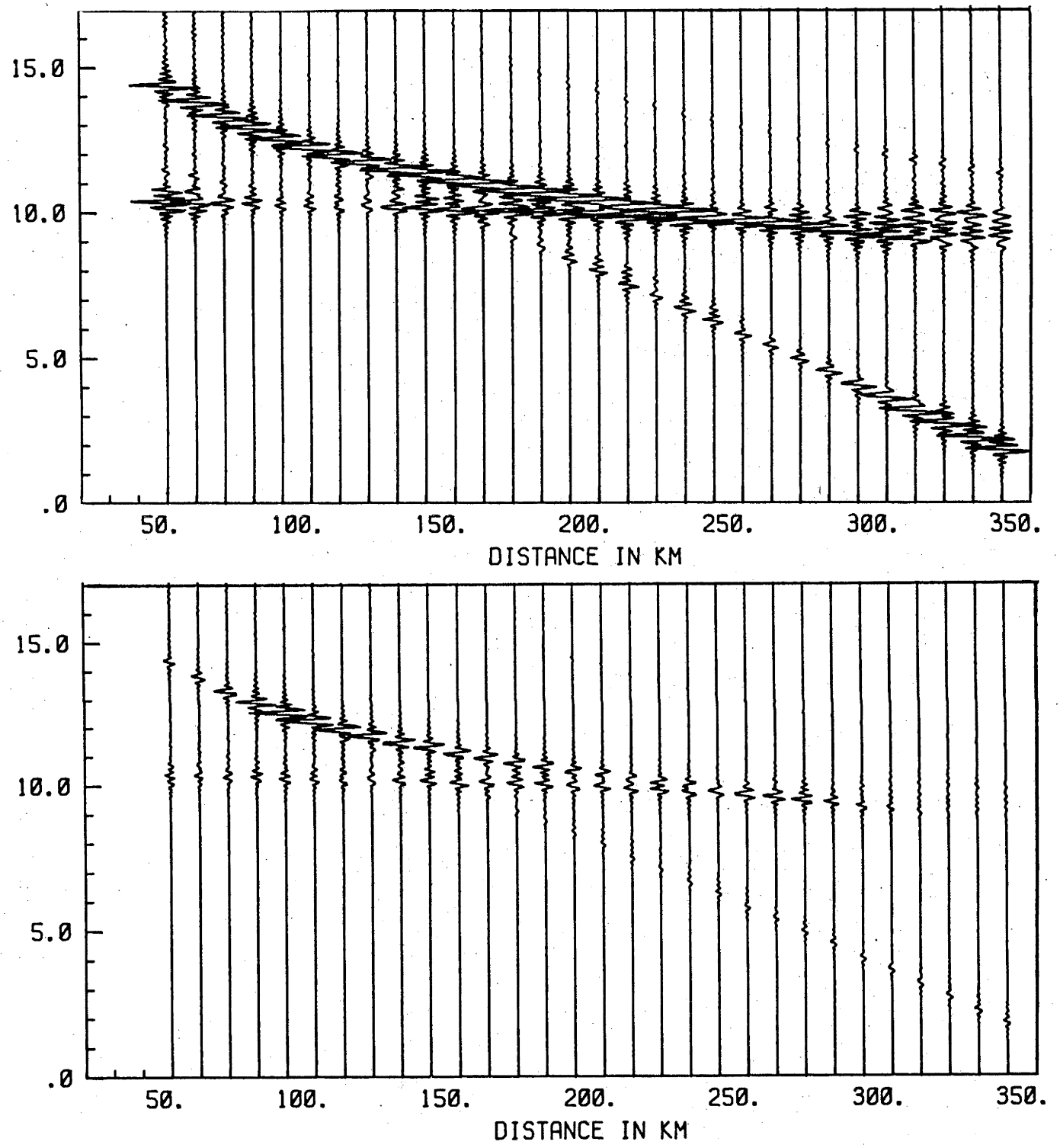

Figure 5.7

Reflectivity synthetic seismogram of model B.

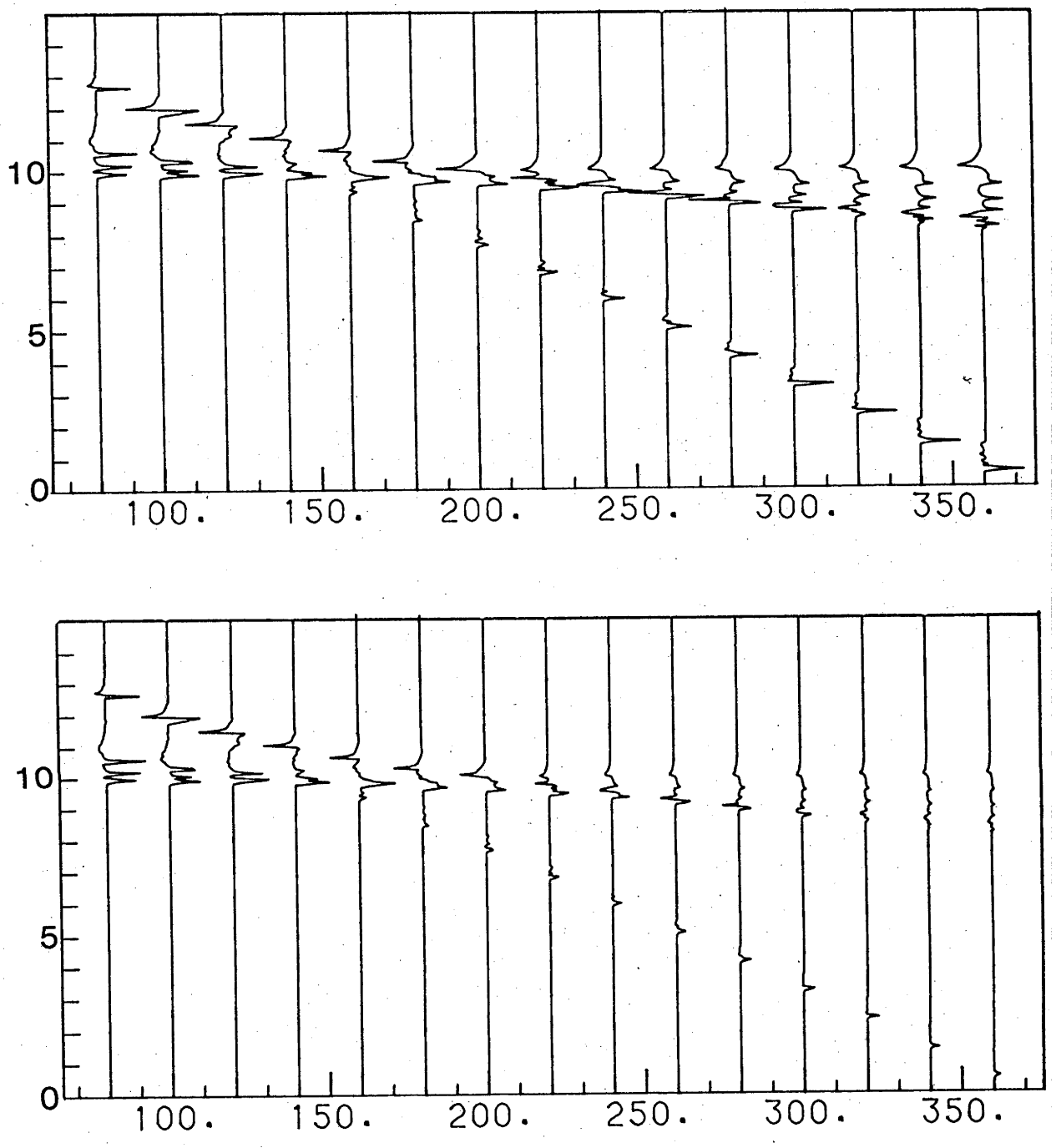

Figure 5.8

Generalized Ray theory synthetic seismogram of model B.

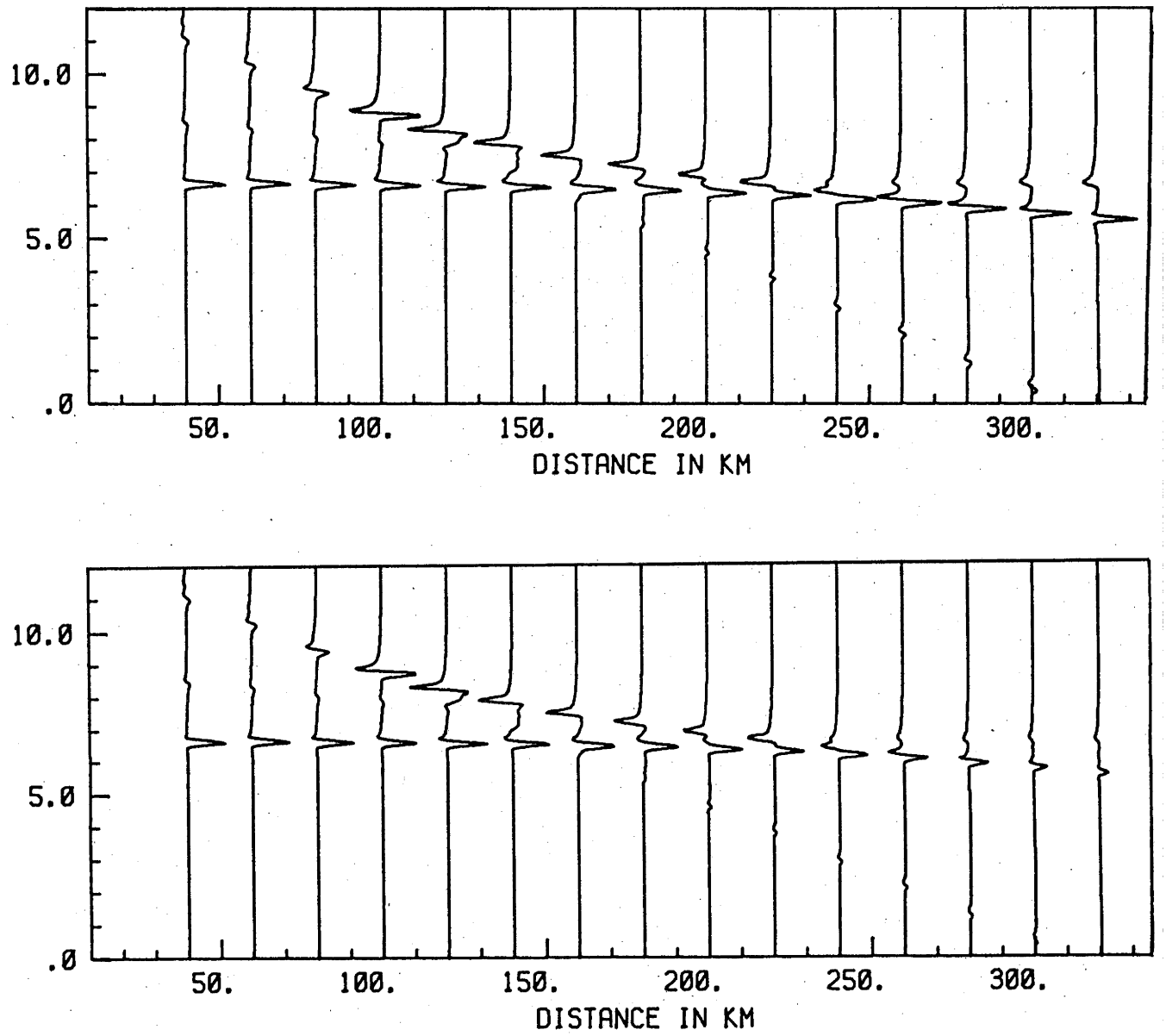

Figure 5.9

WKBJ synthetic seismogram of model B.

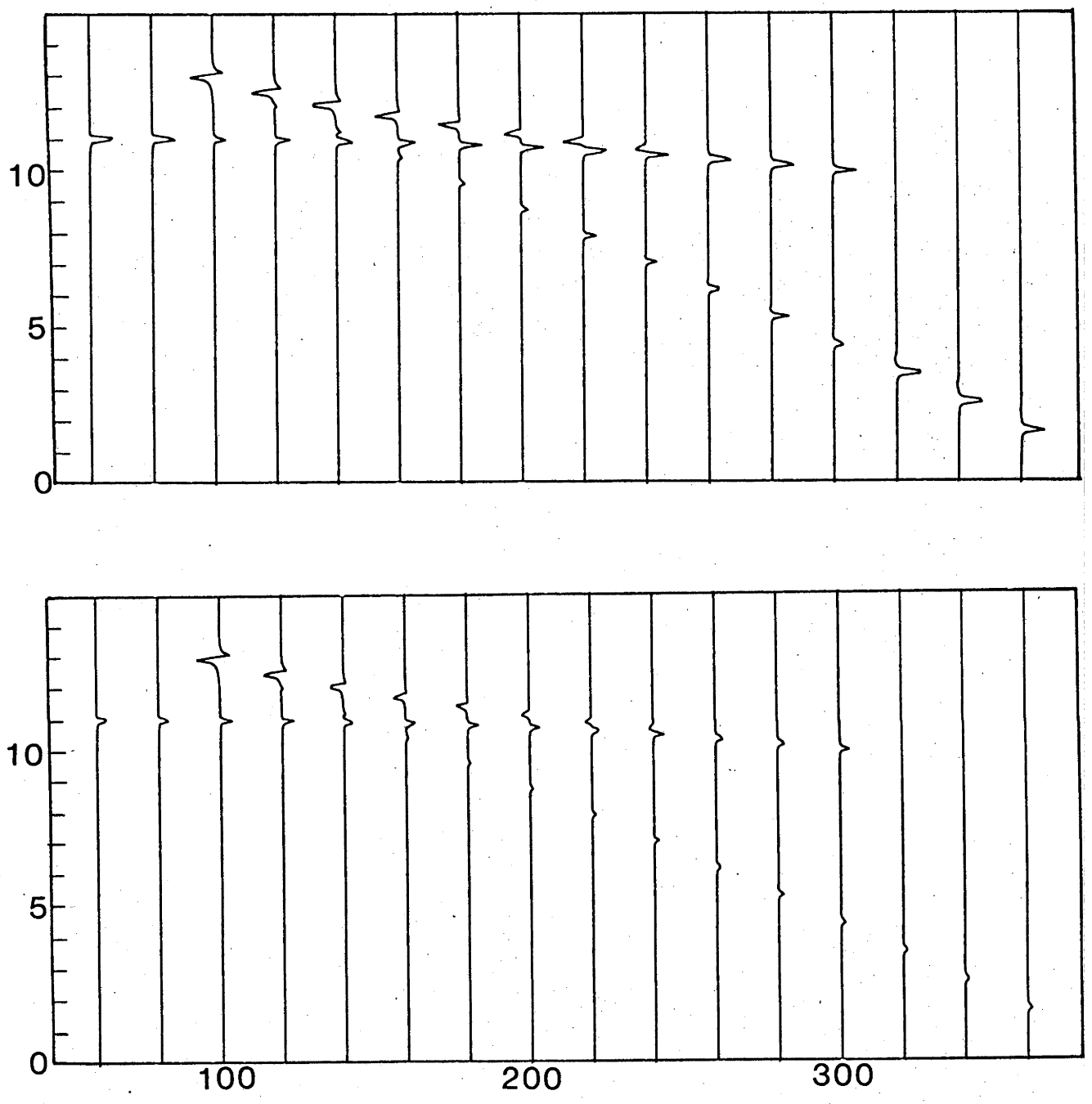

Figure 5.10

Full Wave synthetic seismogram of model B.

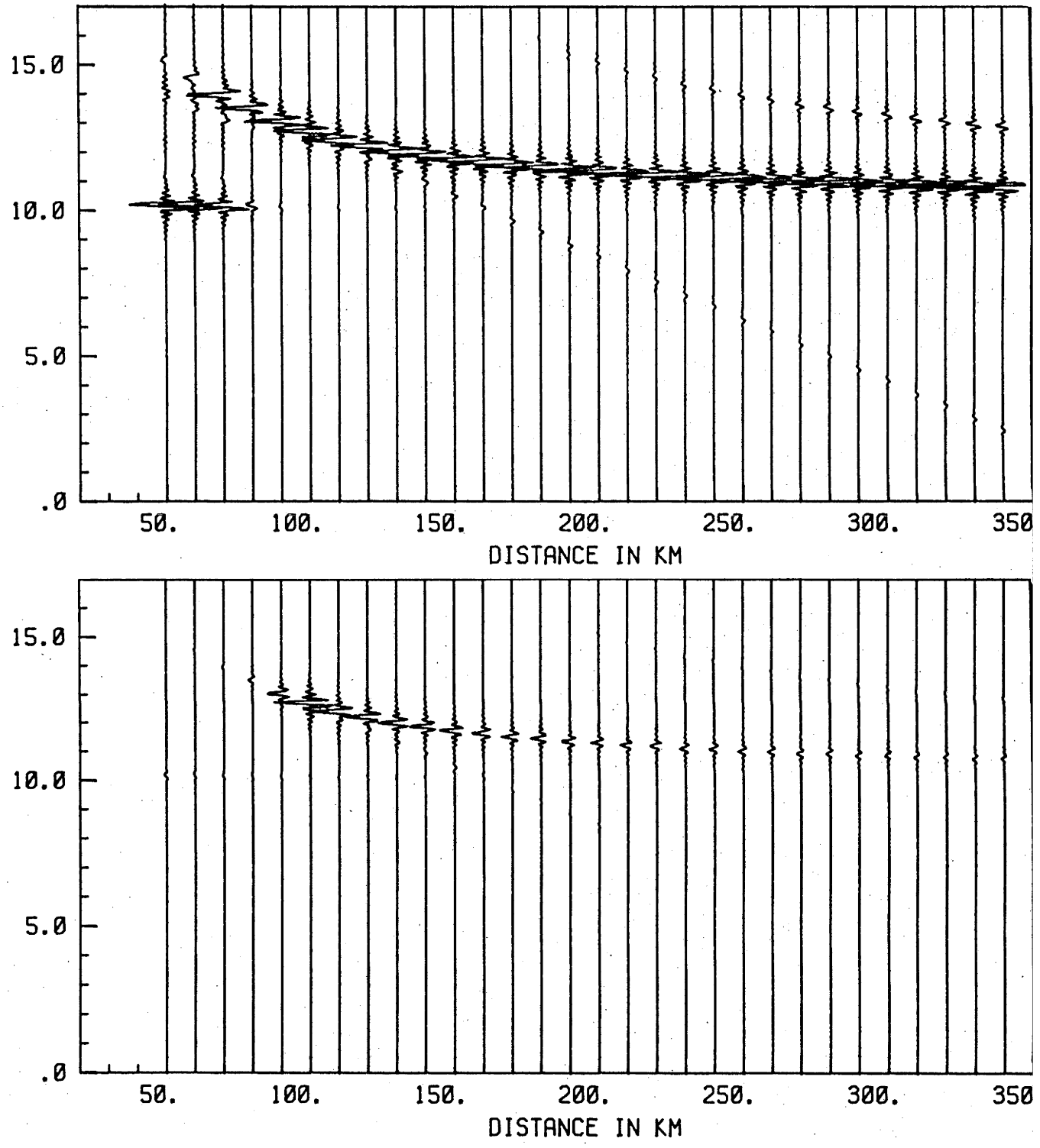

Figure 5.11

Reflectivity synthetic seismogram of model C.

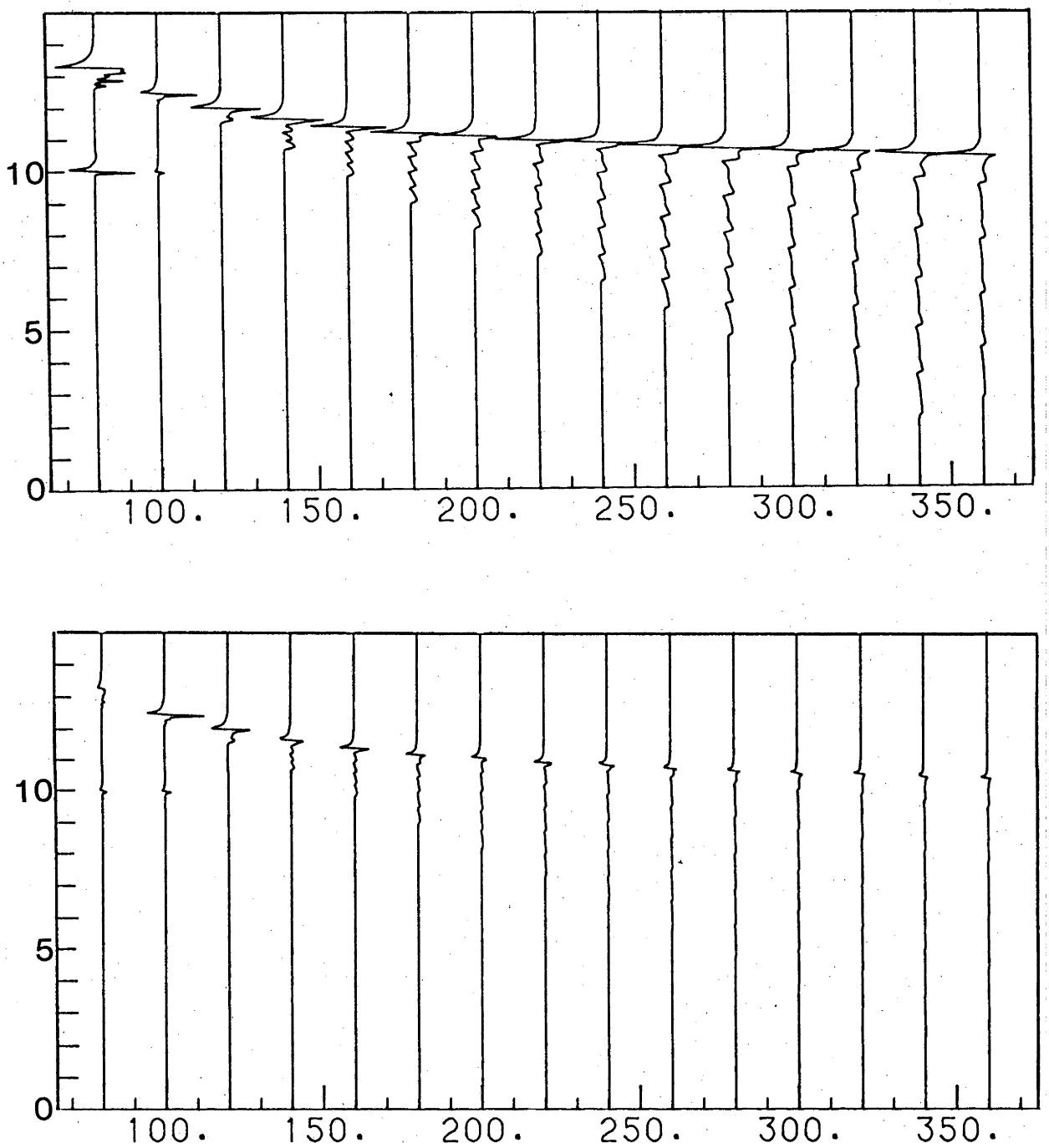

Figure 5.12

Generalized Ray theory synthetic seismogram of model C.

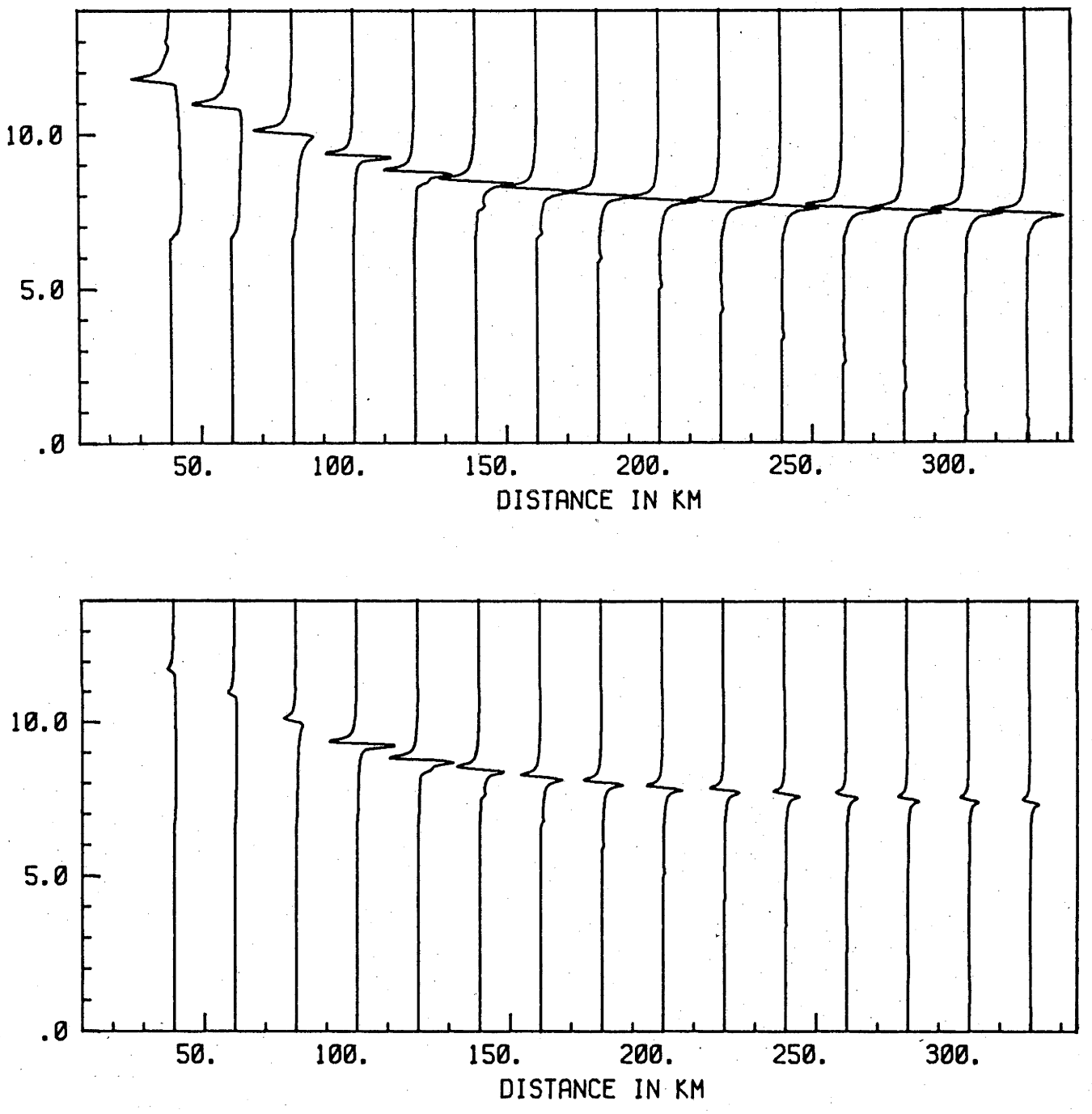

Figure 5.13

WKBJ synthetic seismogram of model C.

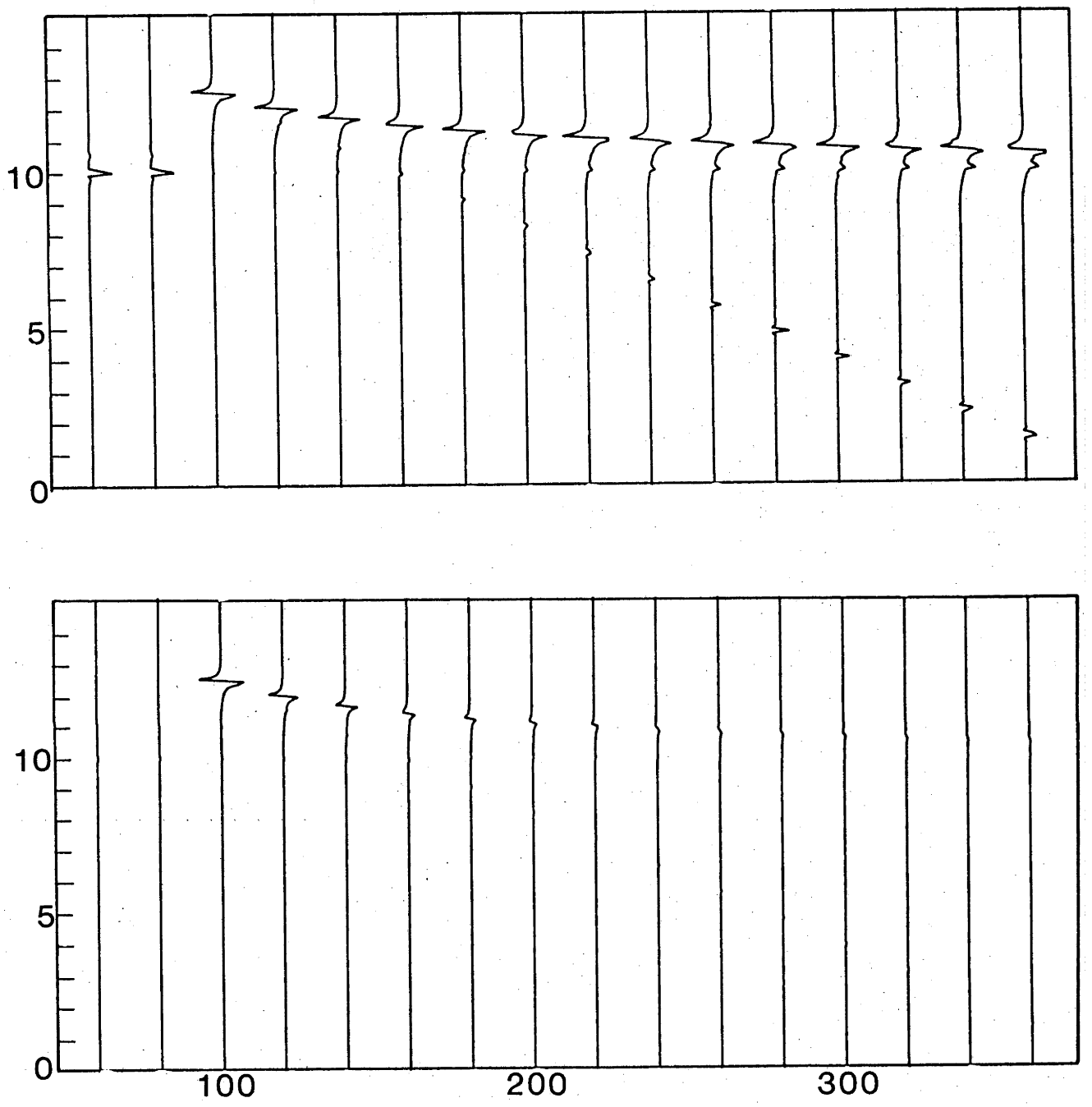

Figure 5.14

Full Wave synthetic seismogram of model C.

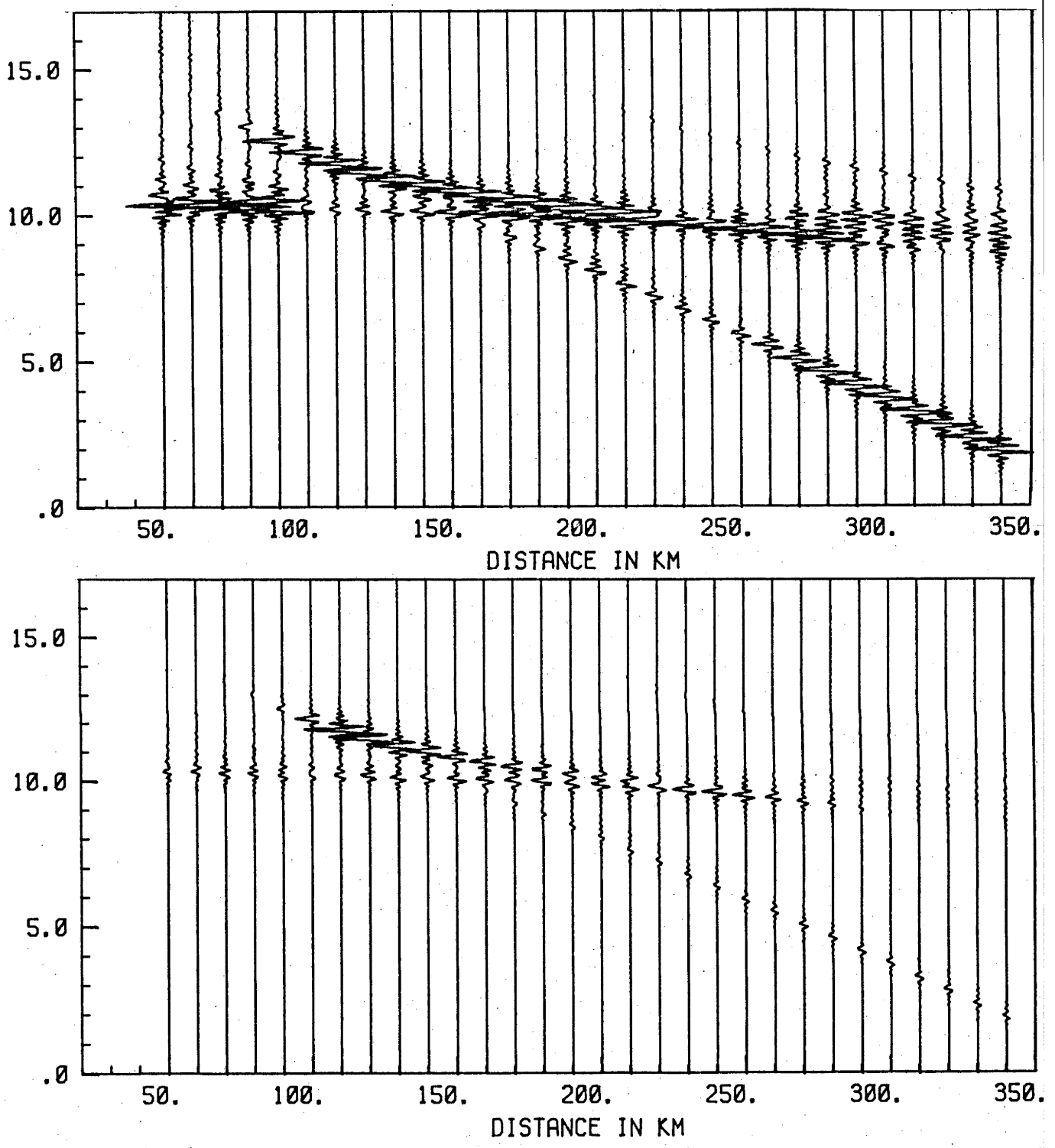

Figure 5.15

Reflectivity synthetic seismogram of model D.

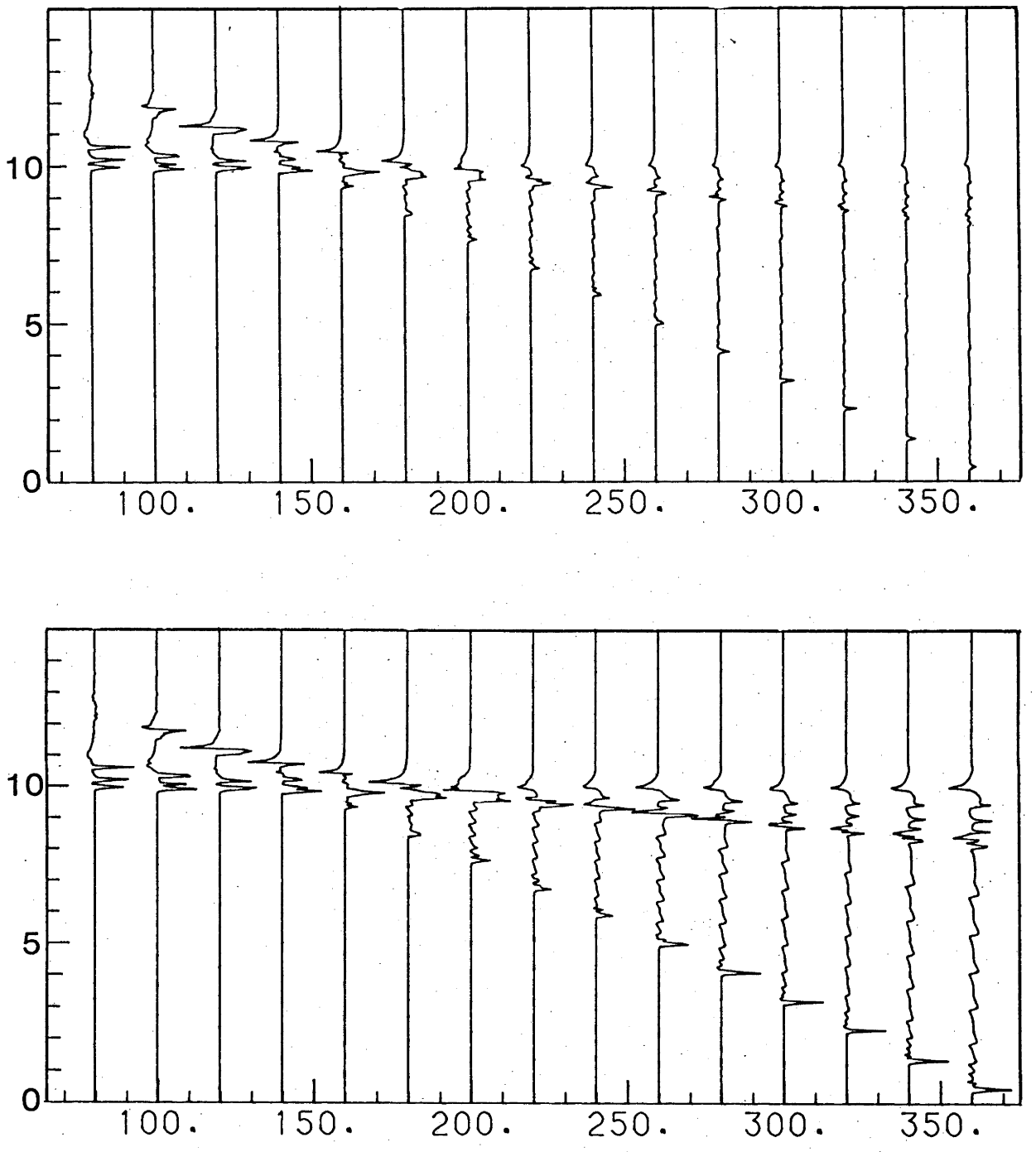

Figure 5.16

Generalized Ray theory synthetic seismogram of model D.

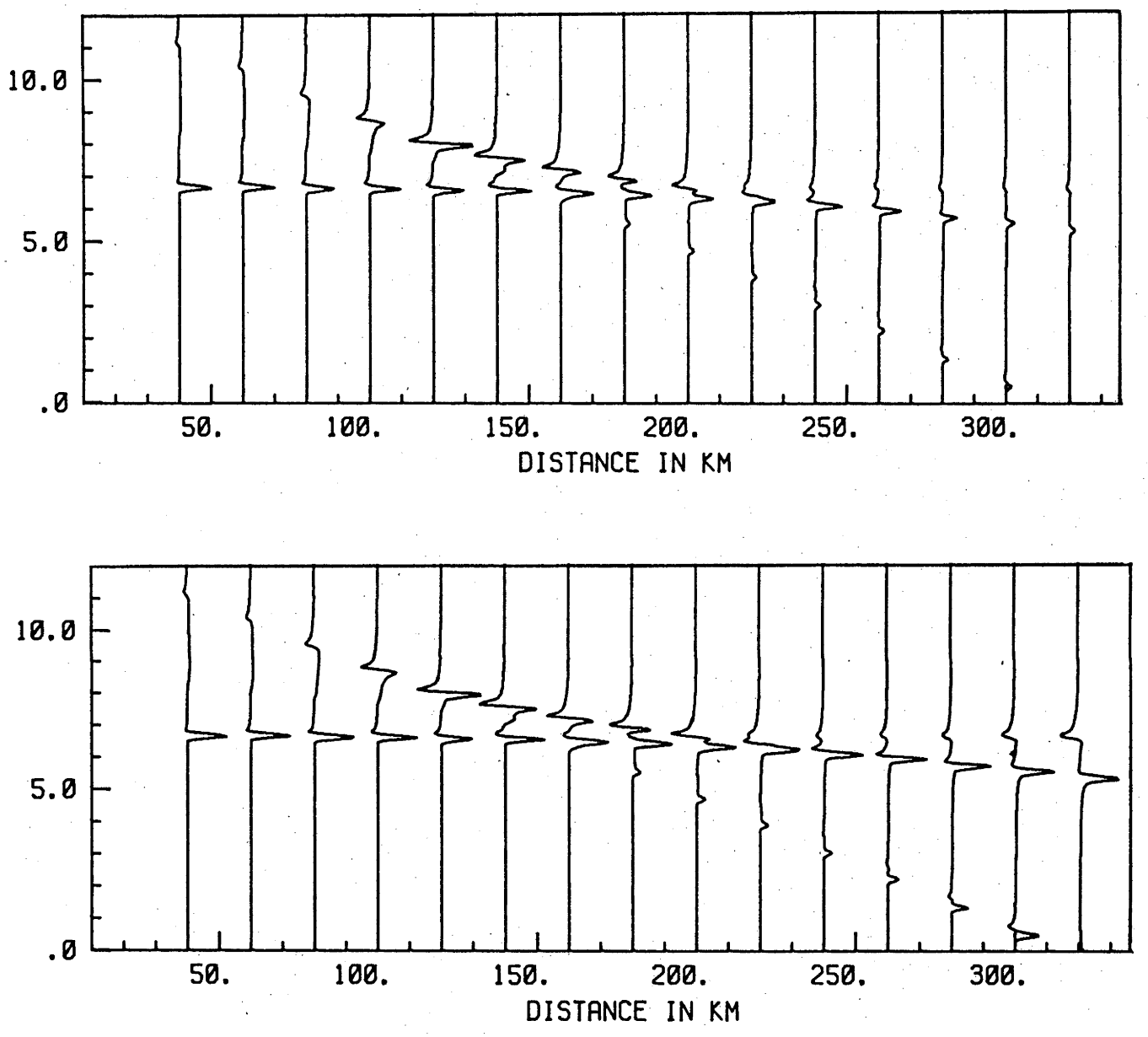

Figure 5.17

WKBJ synthetic seismogram of model D.

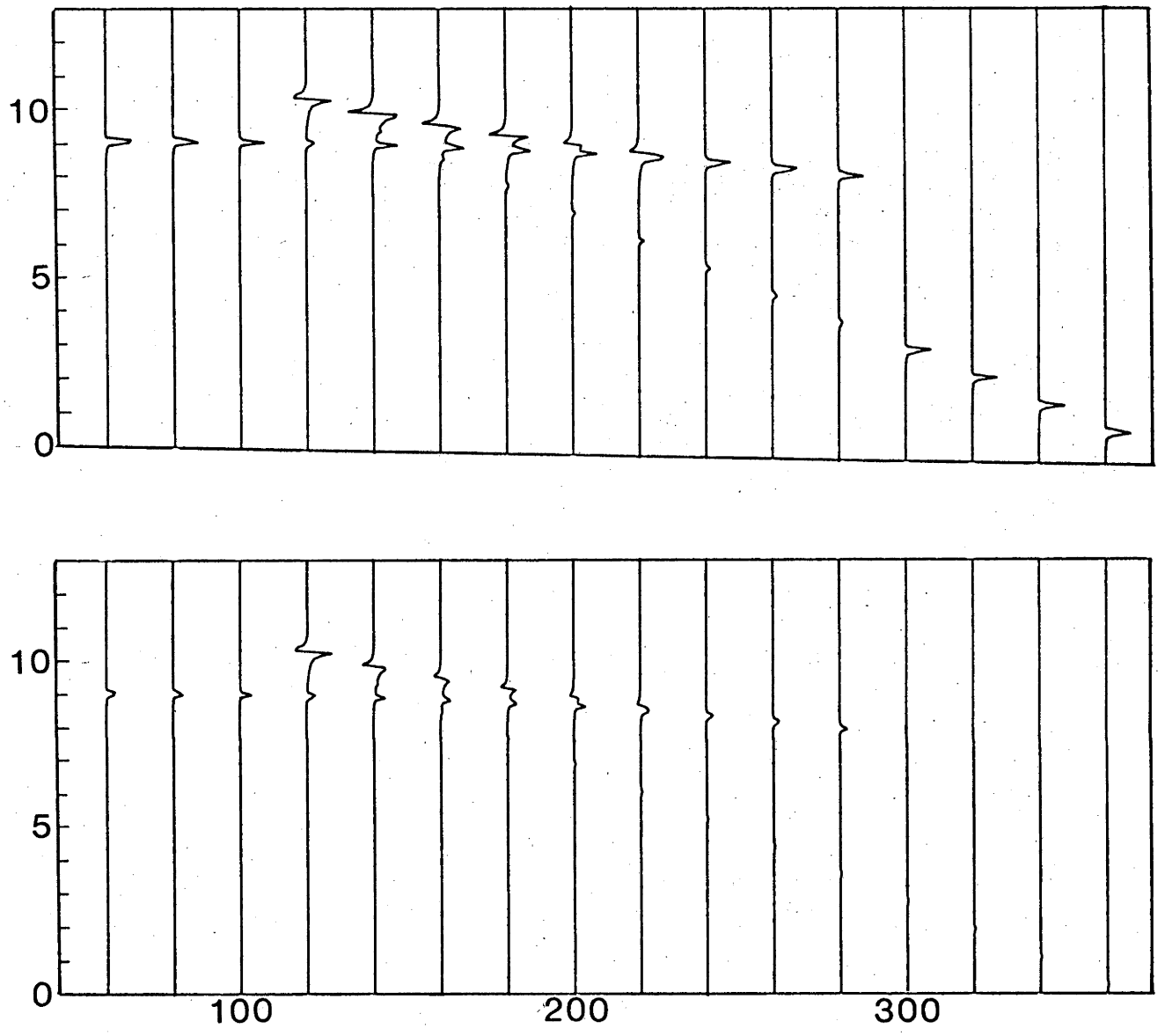

Figure 5.18

Full Wave synthetic seismogram of model D.

range of depth. (Classically, a second order discontinuity referred to a change in the gradient, but throughout this thesis, the above definition will apply.) Model C is similar to model A in that it has homogeneous layers above and below, while in model D slight gradients, similar to those in model B, have been introduced. The travel-time distance curves for these four velocity profiles are shown in Fig. 5-2.

Chapter 2 described the algorithms of the four synthetic seismogram techniques which will be used in the present study. Synthetic seismograms generated by these four different methods, using the four velocity models (A,B,C and D) are shown in Figures 5-3 to 5-18.

A comparison of the synthetic seismograms of velocity model A, produced by the four methods (Figs 5-3 to 5-6), shows that the retrograde Pm branch dominates. The "ringiness" of the Reflectivity synthetic seismograms has resulted from an attempt to obtain an impulse response (corresponding to the results of the other three methods). In practice, this output would be convolved with a relatively smooth source function, removing this "ringy" character. Both the Pm P_m branches have relatively weak arrivals, and multiples of the Pg and Pn wavegroups can be seen following the Pm arrivals. The multiples are implicitly incorporated into the Reflectivity technique. They are not calculated by any of the other three methods of Figures 5-4 to 5-6, because they have not been explicitly nominated in the "ray sum". The maximum amplitude of the Pm wavegroup in the Reflectivity synthetic seismogram is seen to be at a distance of around 80 km.

The Generalized Ray theory synthetic seismogram (Fig. 5-4) shows the dominance of the Pm branch, with very weak Pg and Pn branches. Only the primary interactions have been calculated for this and all the other Generalized Ray theory synthetics in this chapter. The Pn onset is seen to separate from the Pm wave at around 100 km, and thereafter to diminish. This section also clearly demonstrates the characteristic change in phase of the Pm cusp from a first order discontinuity, which was lost in the "ringy" nature of Fig. 5-3. The WKBJ synthetic seismogram (Fig. 5-5) is very similar to the Generalized Ray theory section. The maximum amplitude of the Pm is near 100 km, compared with 80 km for the Reflectivity method. The Full Wave theory synthetic seismogram (Fig. 5-6) shows some differences in comparison with the previous three methods. The most noticeable is the more rapid decrease in amplitude of the Pm branch at distances less than 100 km, and the relatively greater energy of the Pn onsets at larger

distances. At 80 km, where the Reflectivity method produces the maximum Pm energy, the Full Wave synthetic indicates a Pm/Pn cusp comparable to that of the small Pg onset.

The different appearance of the waveforms obtained by using the various synthetic techniques may be attributed to several factors. In all cases, a wide bandwidth (delta function) source was employed; however, each synthetic method uses a different approach in the derivation of the trace's time series. Of more importance are the intrinsic differences in the amplitudes, which are best seen in the lower (relatively amplitude) sections of the figures. The Full Wave synthetic shows a marked decrease in the amplitude of the Pg/Pm branch at distances beyond 200 km, but this may be a relative effect caused by this method predicting greater energy in the Pm cusp around 100 km epicentral distance. In comparison, the WKBJ synthetic has a slow decay of energy on the P_n/Pm branch.

All four synthetic seismograms predict small amplitudes for the Pg branch derived from model A in the distance range 80 to 200 km; however the Generalized Ray theory generates comparatively larger arrivals in this range. This may be attributed to the effects of the earth flattening transformation which introduces an artifical velocity gradient, and therefore necessitates partitioning into fictitious homogeneous layers which are artifacts of the EFA. The Reflectivity method also introduces the same artifical partitioning, but the incorporation of all multiple rays in the ray summation of the Reflectivity method, as opposed to the calculation of only the primary rays (a subjective decision) in the case of the Generalized Ray theory method, has produced a Pg amplitude in the Reflectivity seismogram similar to that produced by the spherical earth synthetic seismogram techniques.

The synthetic seismograms of model B are shown in Figures 5-7 to 5-10. In this case, the problem of representation of the model for calculation of the synthetic seismogram arises. Both the Reflectivity and the Generalized Ray methods require the model to be partitioned into homogeneous layers. In a region of vertical velocity gradient, this partitioning involves deciding the number of layers into which the gradient should be partitioned. While increasing the number of layers increases the accuracy, it also invariably increases the computation time. The WKBJ and Full Wave theory methods on the other hand, accommodate vertically inhomogeneous layers. The introduction of velocity gradients above and below the Moho serves to dramatically increase the Pg and Pn wavegroup amplitudes. This model also demonstrates the difference between the methods in a situation where the refraction branches terminate in an extremal cusp, as shown in Fig 5-2b.

The Reflectivity method synthetic seismogram demonstrates the large increase in amplitude of the Pg and Pn arrivals (Fig. 5-7). As would be expected, the Pm branch has a similar behaviour to that seen in Fig. 5-3. The Generalized Ray theory synthetic seismogram shows a dissociation of the elementary refraction branches arising from the partitioning of the velocity gradient into homogeneous layers. The thickness of this partitioning, chosen for the region above and below the Moho in models B and D, was 5 km, and the seismogram indicates that a finer partitioning should have been used above the discontinuity. The Pg onset at the smaller distances is seen to be composed of three prominent "reflections" from the artifical partitioned layers, and at the extremal Pg-Pm cusp, the ray contributions do not constructively converge. A finer partitioning above the Moho would remove this problem, but at the expense of greater computation time. The amplitudes on the Pg-Pm extremal cusp are seen to decrease rapidly beyond 300 km, corresponding to the termination of the ray theoretical arrivals of the inhomogeneous model.

The WKBJ synthetic seismogram technique accommodates an inhomogeneous model, and so does not suffer from the problem of the dissociation of arrivals. The Pg arrivals are relatively large, and decrease slowly around the critical point, from 250 to 350 km. The maximum amplitude of the Pm-Pn cusp is located around 110 km, compared with 100 km

for the Generalized Ray theory. Amplitudes of the Pn arrivals are also noticeably smaller than in both the Generalized Ray theory and the Reflectivity sections. The Full Wave synthetic seismogram shows a similar form, with slightly larger Pn onsets, and a maximum Pm cusp amplitude at about 100 km distance.

Model C incorporates homogeneous layers above and below a second order velocity discontinuity. As with model A, the amplitudes of the Pg and Pn arrivals are small, and the Pm onsets dominate the record sections. Comparing the Reflectivity synthetic (Fig. 5-11) with Fig. 5-3, it is seen that distributing the velocity increase over 6 km has moved the maximium amplitude on the Pm branch out from 80 km to 110 km. Fig. 5-12 of the Generalized Ray theory shows a similar amplitude distribution, with the layer partitioning in the transition zone generating arrivals in the time between the Pn and Pm onsets. The proximal cusp at 80 km is seen to be suffering slight dissociation on the leading edge, owing to this layer partitioning. A feature of the second order discontinuity is that the changing phase of the Pm arrival through the cusp is not as marked as in the case of a first order discontinuity.

The WKBJ synthetic seismogram (Fig. 5-13) has a similar amplitude character to that of Fig. 5-12. The Full Wave synthetic seismogram clearly indicates the dominance of the Pm branch, and this has its maximum amplitude around 100 km.

Model D possesses velocity gradients above and below the second order transition zone. The Reflectivity synthetic seismogram (Fig. 5-15) displays stronger Pn and Pg arrivals, as well as the two cusps - the proximal Pm/Pn cusp and the extremal Pg/Pm cusp. This synthetic seismogram shows more clearly than does Fig. 5-7 the synthetic behaviour beyond these critical points. At distances less than the proximal cusp, the waveform is seen to decrease in amplitude, maintaining its shape. Beyond the extremal cusp, the waveform disintegrates into a lower amplitude, relatively emergent waveform.

The Generalized Ray method synthetic seismogram of model D shows the combined effects of the layer partitioning discussed in relation to Figs. 5-8 and 5-12. In this case, the arrivals beyond the ray theoretical cusps are seen to be composed of the dissociated constituent pulses from the partitioned layering. The WKBJ synthetic seismogram (Fig. 5-17) shows that the amplitudes on the Pm branch decay slowly through the ray theoretical critical points. An onset is seen emerging from above the Pm cusp beyond

200 km, and this corresponds to a ray travelling horizontally with an apparent velocity of 6 km/s. Fig. 5-18 shows the Full Wave synthetic seismogram, which displays a similar character, but has a more rapid decrease in the amplitude of the Pm branch beyond the ray theoretical cusp.

An important aspect of the application of synthetic seismograms to the interpretation of refraction surveys is the relative ease or difficulty of applying the methods. The Reflectivity method has been found the easiest of these four methods to apply, as it requires few critical decisions for a successful execution of the programme. However, the Reflectivity method also requires the greatest amount of computation (and hence expense), the computation time of this method being typically one to two orders of magnitude greater than that of the fastest methods. The three other methods are of the "ray sum" type, and consequently require some specification of the ray/wave path, (cf. the Reflectivity method which automatically incorporates all possible ray paths). These methods therefore involve decisions regarding which rays/waves will be included in the generation of the synthetic seismogram. Both the Generalized Ray method and the WKBJ method need significant amounts of input to specify particular rays and to set up necessary parameters for an execution. The Full Wave method requires a far greater quantity of input for this purpose, as the contours of integration in the complex ray parameter plane must also be specified. A degree of experience is necessary to correctly specify these contours, and resort has often been had to a trial and error procedure to obtain the correct contour. This is both expensive and time consuming. The Full Wave theory synthetic seismogram method was therefore found to be the most difficult of these four methods to apply.

5.3 THE APPLICATION OF SYNTHETIC SEISMOGRAM MODELLING TO SELECTED PROFILES.

For the purpose of modelling using synthetic seismograms, the velocity model CQEW was constructed from the knowledge of the crustal structure in the western extent of the profile. The multiple nature of the refracted sub-Moho arrivals has been observed in other refraction surveys, notably the European studies, (see Giese et al. 1978). In these surveys the velocity structure has been commonly modelled in terms of interleaved high and low velocity layers. A similar structure was invoked to explain $Pn^{(1)}$ and $Pn^{(2)}$ arrivals observed in the Central Queensland survey. The retrograde reflections from the velocity increase around 45 km depth were

CQEW

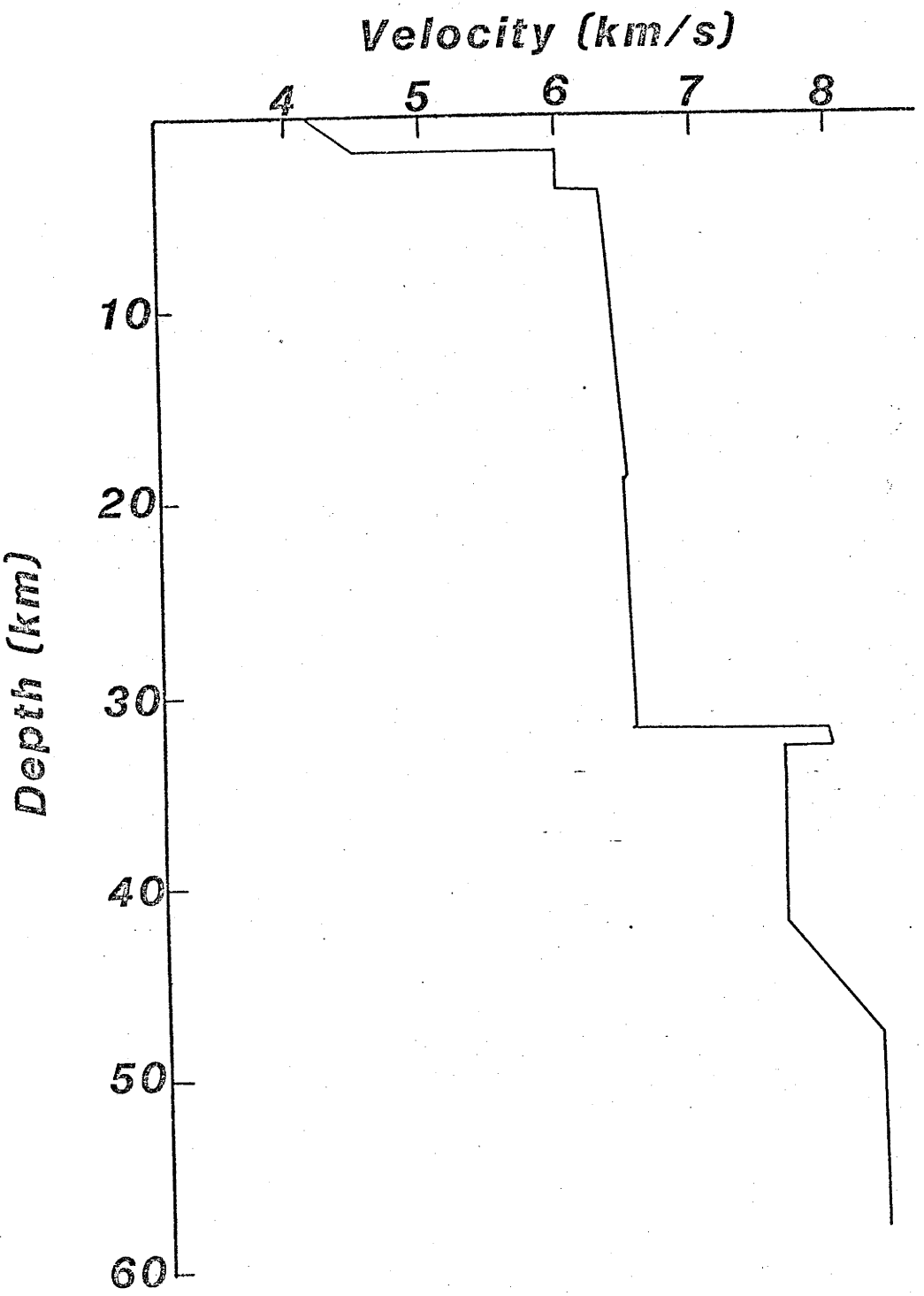

Figure 5.19

The CQEW velocity model.

too weak to be reconciled with a first order velocity discontinuity. A second-order type discontinuity was therefore employed to distribute the retrograde energy further away from the cusp. The velocities above and below this uppermost mantle low velocity zone were obtained from the apparent velocities of the $Pn^{(1)}$ and $Pn^{(2)}$ wavegroups, but the velocity within this low velocity zone is not constrained, apart from the fact that the velocity depth interval must produce the observed offset in intercept times between the $Pn^{(1)}$ and $Pn^{(2)}$ wavegroups.

Figure 5-19 displays the proposed model of the uppermost mantle structure. A synthetic seismogram of this velocity model, calculated by the WKBJ method, is displayed in Figure 5-20. The Pm amplitudes are dominantly large in the distance range 100 to 150 km, with the maximum amplitude around 110 km. The Pn arrival cross-over from the Pg wavegroup is around 180 km distance, with the Pn arrivals being relatively weak in comparison with the stronger second arrivals. The amplitude of this second arrival diminishes with distance, and beyond 350 km, the first arrival ($Pn^{(1)}$) is larger than the later arrivals.

In Figure 5-21, the synthetic seismogram of this velocity model calculated by the Reflectivity method is displayed. As with the WKBJ synthetic, the maximum amplitude of the Pm is around 110 km; however, there are substantial differences in the amplitude of the Pn phase. Beyond the Pg-Pn cross-over at around 180 km, the Pn arrival has a significant amplitude, but this diminishes with increasing distance, and beyond 250 km, the $Pn^{(2)}$ phase possesses the larger amplitude. This is in greater agreement with the data, (e.g. see Figure 3-11), for which the $Pn^{(1)}$ amplitudes are notably larger than $Pn^{(2)}$. The relatively large Pn arrivals displayed by both synthetic seismogram methods in the distance range around 200 km are not well corroborated by the data, which have small Pn onsets around this distance range. These larger Pn amplitudes in the synthetic seismograms are the product of the velocity gradient in the uppermost mantle layer (32 km, 7.94 km/s - 33 km, 7.98 km/s), which was incorporated into the model to terminate the projection of the $Pn^{(1)}$ arrivals to larger distances and to increase their amplitude in the synthetic seismograms. The small low velocity zone in the lower crust was designed to lower the Pg amplitudes beyond the crossover distance.

The Pj phase, observed in the western extent of the Moura/Kianga and Callide record sections, possesses a dominantly low frequency character. Initial attempts to model this wavegroup in terms of a crustal low

Table 5.1

CQEW Velocity Model

Depth (km)	Velocity (km/s)
0	4.1
2	4.5
2	6.0
4	6.0
4	6.3
19	6.49
19	6.44
32	6.49
32	7.94
33	7.98
33	7.6
42	7.6
48	8.3
60	8.3

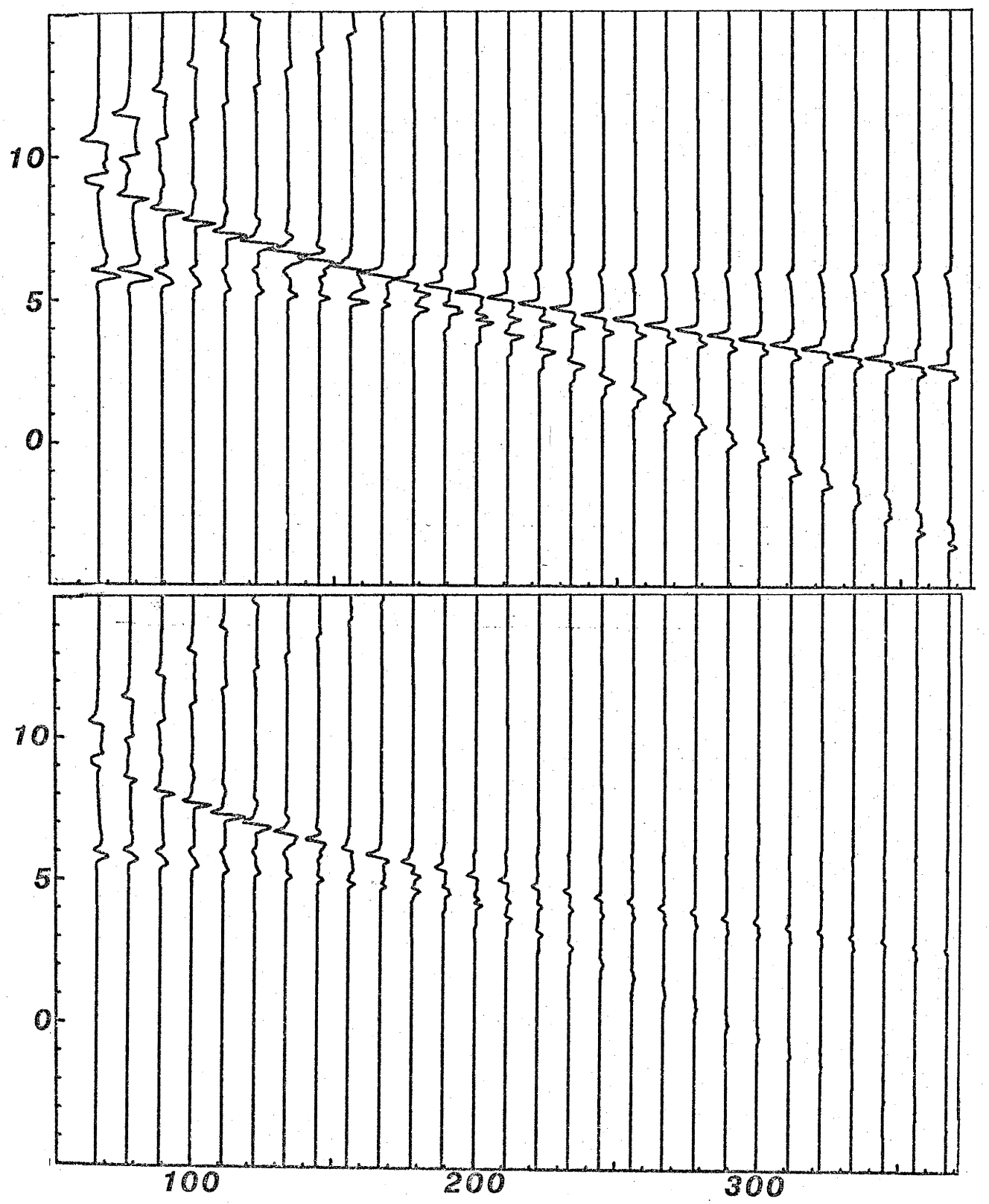

Figure 5.20

The WKBJ synthetic seismogram of the CQEW velocity model.

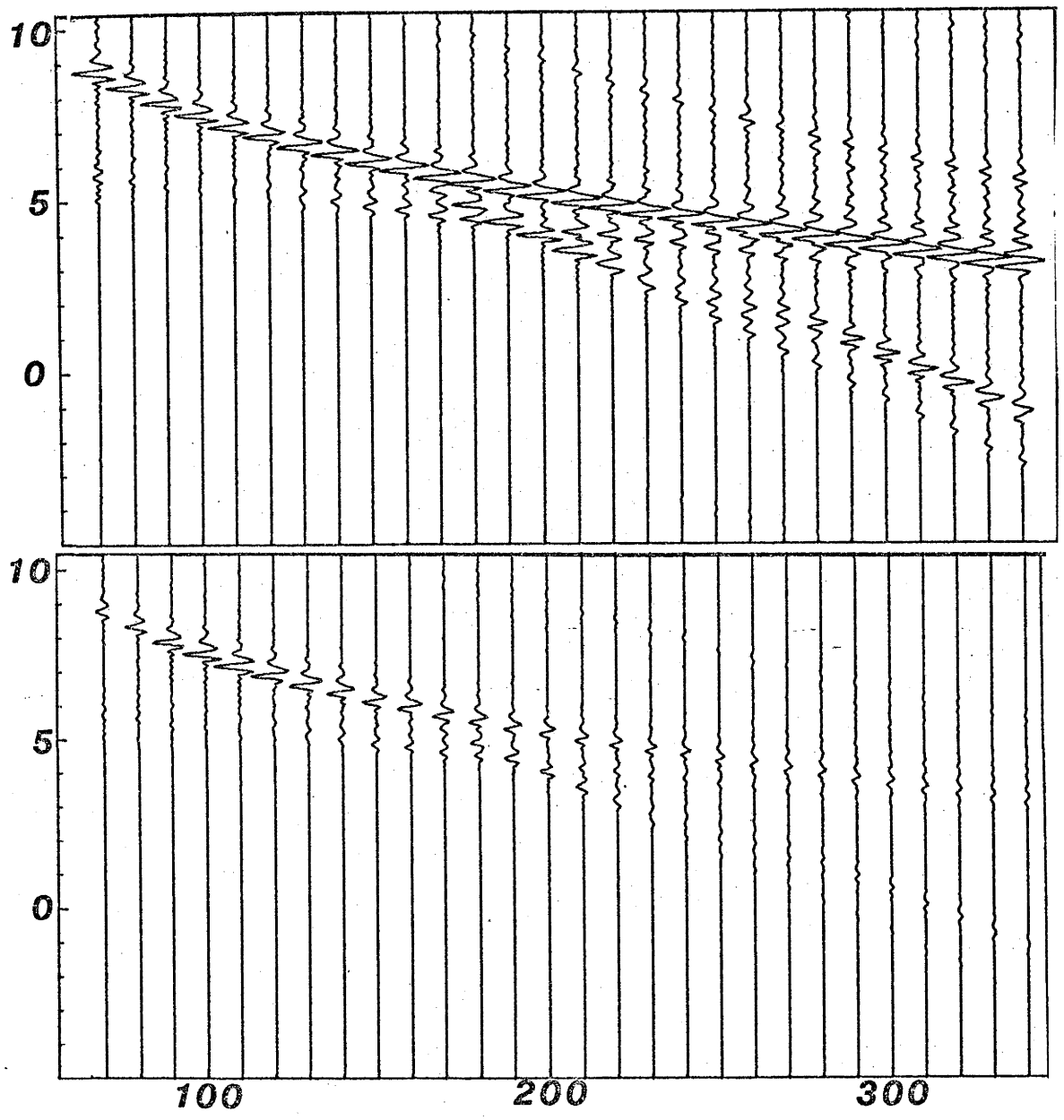

Figure 5.21

The Reflectivity synthetic seismogram of the CQEW velocity model.

velocity zone were unsuccessful. The low frequency character of these waves, together with the nature of the Mohorovicic discontinuity implied by the Pn wavegroups, suggested that the Pj arrivals may correspond to seismic energy tunnelled through the "high velocity layer" at the Moho. Another possibility is that these arrivals are PmPmP rays - the low frequency character possibly due to the filtering effects of the near surface sediments. Both the travel time curve obtained by doubling the distances and times of the Pm arrivals, and the associated apparent velocity do not fit the Pj arrivals. This could, however, be due to lateral variations in the crustal structure of the region.

The alternative explanation is the tunnelling of the seismic waves through the high velocity layer below the Moho. Fuchs and Schulz (1976) investigated the theory of this type of wave tunnelling, as related to the Mohorovicic discontinuity. Richards (1973) demonstrated how Full Wave theory could be used to study wave tunnelling at the core/mantle boundary.

The non-raytheoretical tunnelling of Pm energy through the high velocity zone at the Moho would allow this energy to be refracted in the velocity gradient around 45 km depth. This energy would have to then undergo tunnelling once again to be observed at the surface. The twofold tunnelling could explain the low frequency emergent nature of the Pj wavegroup, while the additional travel path explains the offset in distance and time from the Pm cusp.

Both these explanations are dependent on the exact structure and topography of the Mohorovicic discontinuity. The existance of lateral variations of Moho structure would tend to favour the PmPmP hypothesis.

CHAPTER 6

THE APPLICATION OF FULL WAVE THEORY TO THE EXPLANATION OF THE Pn PHASE IN EXPLOSION SEISMOLOGY.

6.1 INTRODUCTION

The observed amplitude of Pn arrivals in crustal refraction surveys varies considerably, from almost undiscernible onsets, to onsets with amplitudes comparable to those of the Pg wavegroup. Figure 6-1 shows an example from a Central Queensland refraction profile, of a Pn onset with an amplitude approximately equal to the Pg arrival.

The Pn arrival was initially thought to be a headwave refracted along the underside of the Moho, but the advent of synthetic seismograms has conclusively demonstrated that the energy propagated in this head wave mode is insufficient to explain this wavegroup. The amplitude of the wave energy refracted in the lower (faster) medium can be substantially increased by introducing a velocity gradient in this medium. The Pn energy then "dives" below the interface into the refracting layer, and for this reason it has been called a diving wave (see Giese 1978). The increase in amplitude of the Pn wavegroup due to the introduction of a positive velocity gradient below the Moho is shown in Figure 6-2. Figure 2a is a synthetic seismogram calculated by the Reflectivity method for a model having a homogeneous layer (i.e. no vertical velocity gradient) below the Moho, while 2b has a positive velocity gradient of 0.02 km/s/km. Although this increases the amplitude of the Pn wavegroup which is predicted by the synthetic seismograms, it is insufficient to explain the relative amplitudes observed in some refraction profiles. Braile and Smith (1975) have presented a series of Reflectivity synthetic seismograms which clearly indicate the behaviour of Pn amplitude associated with differing sub-Moho velocity structure. A positive velocity gradient below the Moho also introduces the possibility of a whispering gallery type wave phenomenon.

To investigate the nature of the Pn amplitudes, which in some cases are anomalously high relative to the Pg amplitudes, recourse will be had to full wave theory (Scholte, 1956; Richards, 1973, 1976). Ray theory treats the propagation of seismic disturbances in terms of hypothetical rays, which have no effective volume. However, if the

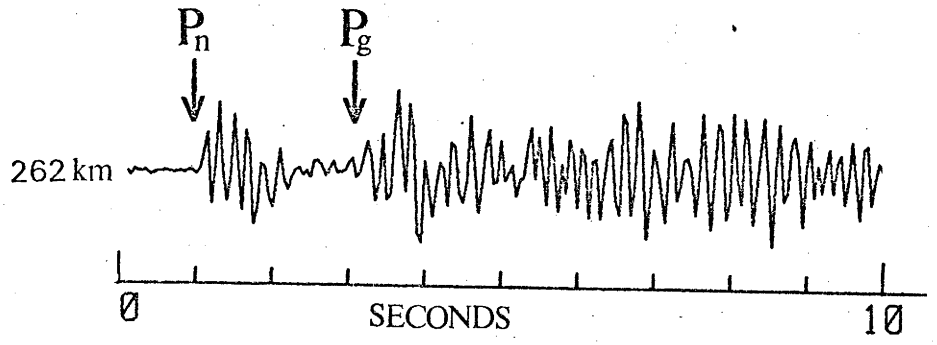

Figure 6.1

An example of a Pn arrival with comparable amplitude to the following Pg arrival.

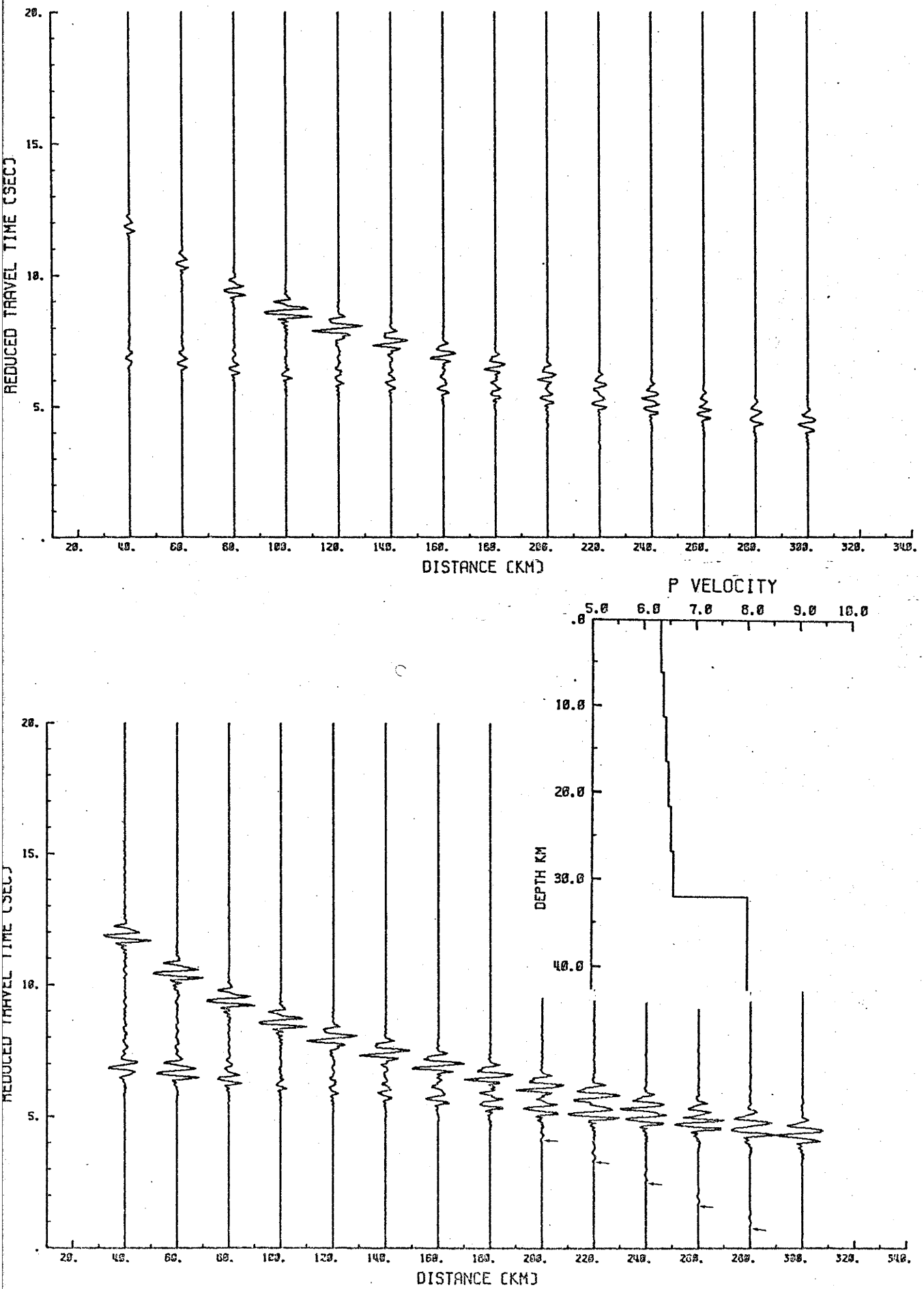

Figure 6.2 The amplitude of the P arrival in a model having (a) a homogeneous sub-Moho velocity.

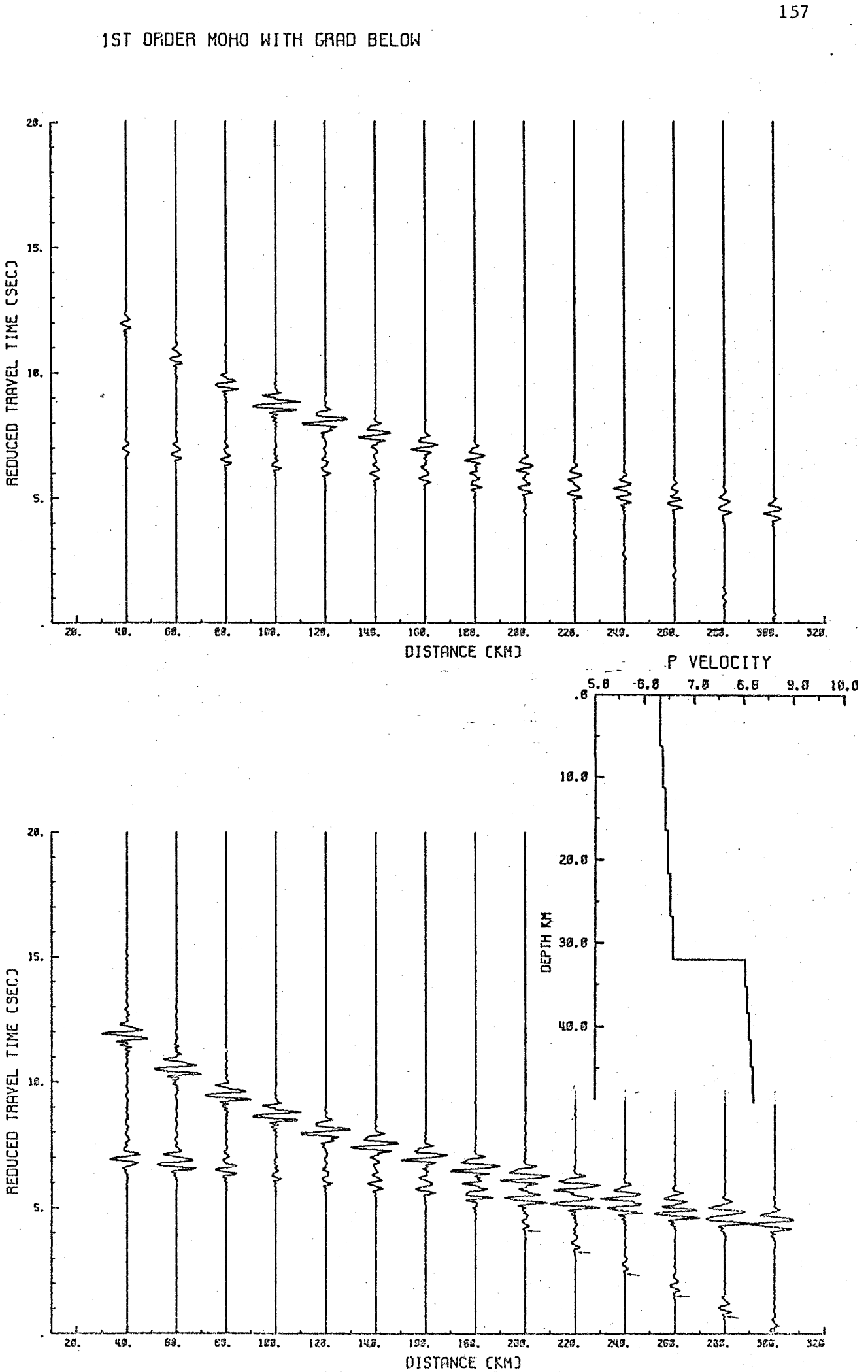

Figure 6.2 The amplitude of the P arrival in a model having (b) a sub-Moho velocity of 0.02 km/s/km.

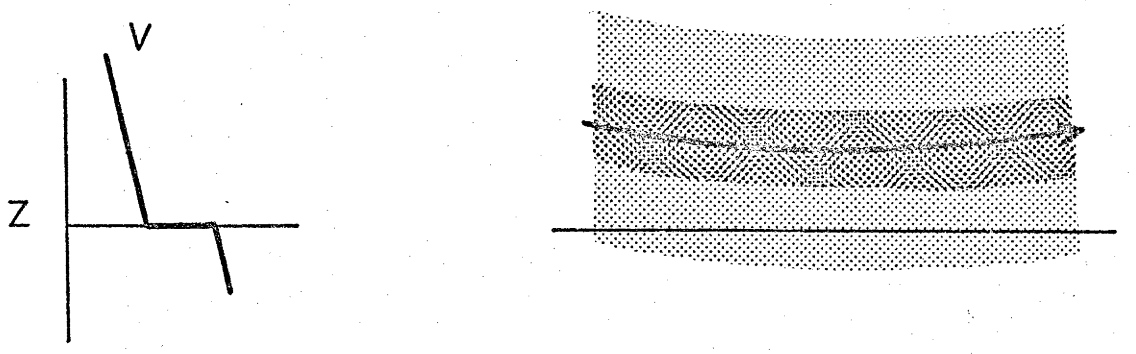

Figure 6.3

The volume of influence of a seismic wave.

disturbances are considered to be waves, then these seismic waves have, in addition to a wavelength, an effective breadth and depth of influence in the two dimensions perpendicular to the direction of propagation. This defines a "volume of influence", within which the wave acts. The total velocity structure within this volume will be "felt" by the wave, and hence affect its propagation. Figure 6-3 illustrates the interaction of a ray with an interface directly below its turning point. According to ray theory this ray would not interact with the interface, but the volume of influence of the wave includes this velocity discontinuity. This figure also indicates that the effect of this non-ray theoretical interaction will most strongly influence a wave travelling semi-parallel to the velocity interface over an extended distance; as is the case when a seismic wave bottoms near a discontinuity.

Interest with regard to Pn amplitudes lies in the tunnelling of Pm wave energy into a Pn type ray-path. Figure 6-4 shows two types of non-raytheoretical wave tunnelling phenomena. For the purpose of this discussion, attention will be restricted to the case of Figure 6-4a, where a retrograde (Pm) wave is reflected by a first order velocity discontinuity, and a non-raytheoretical Pn-type wave tunnels into the uppermost mantle.

6.2 GENERALIZATION OF TRANSMISSION AND REFLECTION COEFFICIENTS.

Richards (1976) has utilized the Langer approximation (Langer 1949, 1956) to calculate reflection and transmission coefficients which accurately incorporate non-raytheoretical effects. The WKBJ approximation, which has often been (explicitly or implicitly) used in the analysis of interface coefficients, does not account for (i) any curvature of the interface, (ii) the velocity structure above and below the discontinuity, (iii) and the wave's effective volume.

Richards (1974) has expressed the displacement $\hat{\underset{\sim}{u}}$ in terms of the scalar potential function P for compressional waves, and the vector potentials S (for SV) and H (for SH) waves

$$\hat{\underset{\sim}{u}} \simeq \rho^{-\frac{1}{2}}[\underset{\sim}{\nabla} P + \underset{\sim}{\nabla}\times\underset{\sim}{\nabla}\times (rS,0,0)] + \mu^{-\frac{1}{2}} \underset{\sim}{\nabla} \times (r\underset{\sim}{H},0,0) \qquad (6.1)$$

where ρ is the density and μ is the rigidity of the medium. Considering only the compressional wave potential, P, and separating variables in the usual manner, we obtain for the radial wavefunction of P

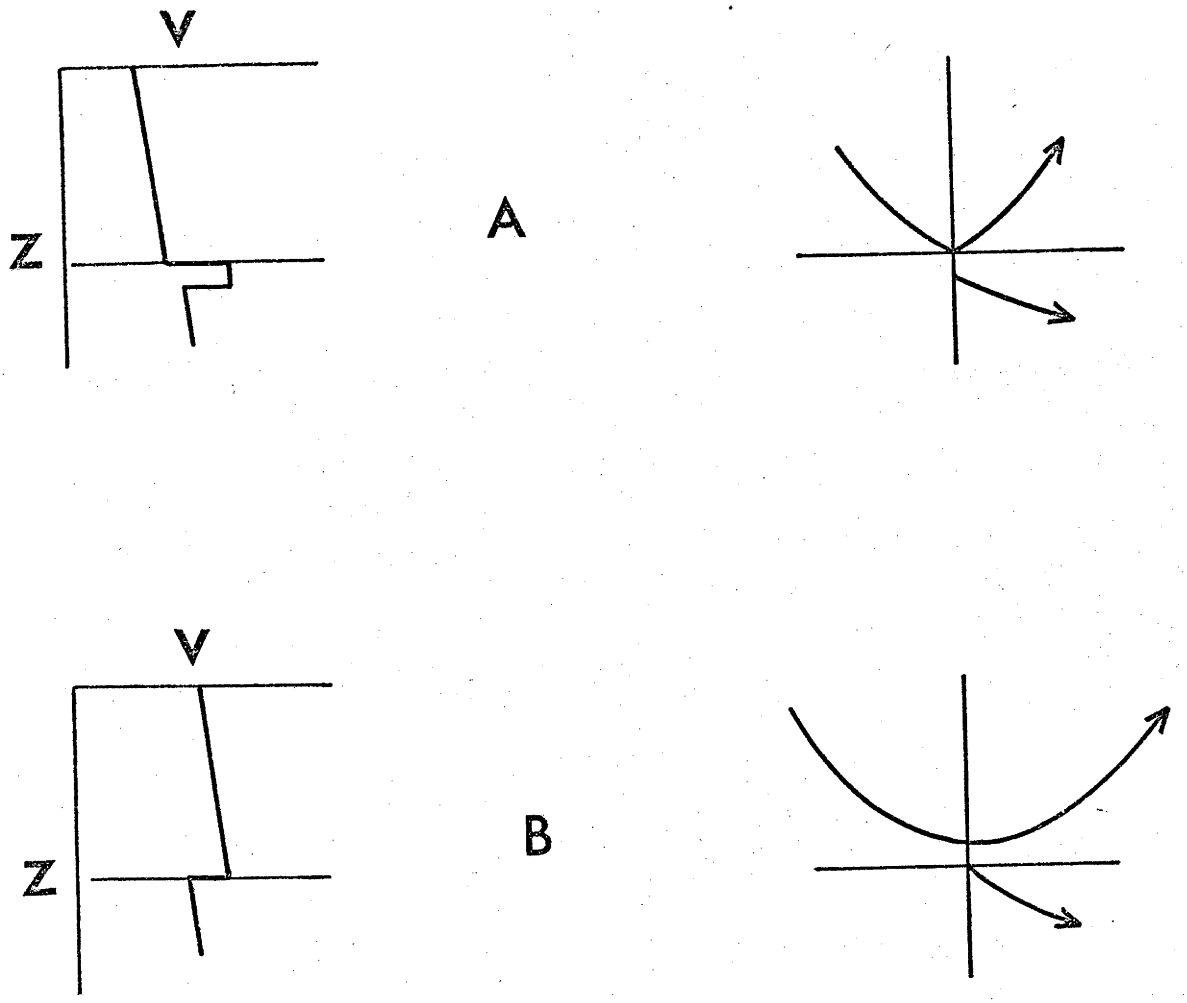

Figure 6-4

Two types of non-raytheoretical wave tunnelling.

$$\frac{d^2}{dr^2}(rR) + \omega^2 \left[1/\alpha^2 - \frac{n(n+1)}{\omega^2 r^2}\right] rR = 0 \qquad (6.2)$$

The WKBJ solution to the Schroedinger type equation is

$$R \simeq U = Q^{-\frac{1}{2}} r^{-1} \exp(\pm \imath \omega \xi)$$

$$Q = (1/\alpha^2 - p^2/r^2)^{\frac{1}{2}} \qquad \xi = \int_{r_p}^{r} Q \, dr$$

and r_p is the turning point radius, r is source/receiver radius. The Langer approximation to equation (3) gives

$$R \simeq V = Q^{-\frac{1}{2}} r^{-1} \xi^{\frac{1}{2}} H^{j}_{1/3}(\omega\xi)$$

where $H^{j}_{1/3}$ is the third order Hankel function of the j-th kind. Richards (1976) applied the Langer approximation to the calculation of transmission and reflection coefficients. Considering the simplest case of an acoustic transmission coefficient at an interface between two homogeneous media, we obtain

$$\frac{C}{A} = \frac{2 \rho_2 \alpha_2 \cos i_1}{\rho_2 \alpha_2 \cos i_1 + \rho_1 \alpha_1 \cos i_2}$$

By replacing the cosines in the above relation by generalized cosines, which are normalized radial derivatives of the radial wavefunction, the calculation of these coefficients became valid at high angles of incidence. The substitution

$$\cos i \rightarrow \frac{\alpha}{\imath\omega} \frac{\partial V^{(j)}}{\partial r}$$

modifies the above coefficient to incorporate the non-ray theoretical effects. The generalized cosines can be expressed in terms of Hankel functions as

$$C^j \rightarrow \frac{(1-\alpha^2 p^2)^{\frac{1}{2}}}{r^2} \exp(\pm \imath \pi/6) \frac{H^{(j)}_{2/3}(\omega\xi)}{H^{(j)}_{2/3}(\omega\xi)}$$

As Pn waves travel considerable distances in close proximity to the Mohorovicic discontinuity, where they interact with this discontinutiy at high angles of incidence, it is appropriate to use full wave theory to investigate the amplitude behaviour of the coefficients relevant to the Pn waves.

6.3 A COMPARISON OF THE LANGER AND WKBJ TRANSMISSION COEFFICIENTS

In Figure 6-5, two velocity models are shown which have been used

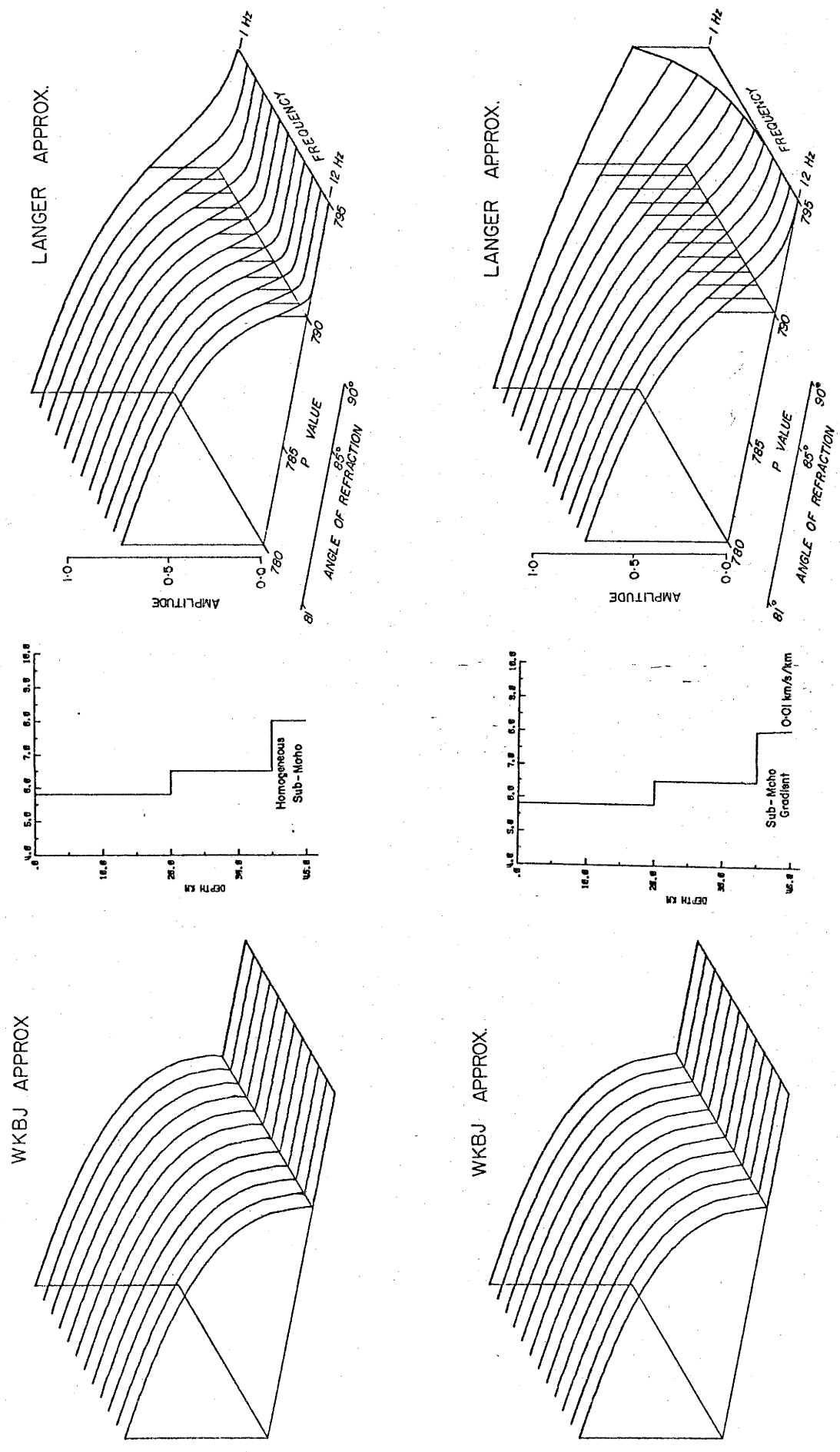

Figure 6.5

A comparison of the Langer and WKBJ approximations.

to investigate the difference between the WKBJ and Langer approximations. Model A has a homogeneous layer below the Moho, while Model B has a 0.01 km/s/km velocity gradient on the sub-Moho mantle. The transmission coefficient from the crust into the mantle ($\tilde{P}\tilde{P}$) and from the mantle back into the crust ($\check{P}\hat{P}$) have been calculated by both the WKBJ and Langer approximations for varying ray parameter and frequency. The product of these two coefficients, which is the transmission product relevant to Pn amplitudes, is plotted in Figure 6-5.

The WKBJ approximation is frequency independent, as can be seen from the left-hand diagrams of Figure 6-5. Non-raytheoretical effects such as the effective wave volume, and the curvature of the Moho account for the difference between the top left and top right diagrams. The critical value of the ray parameter, p_c, marks the point at which ray theory indicates that rays having larger angles of incidence (larger p) will not transmit energy into the mantle. However, calculations using the Langer approximation demonstrate that, depending on the wave frequency, energy is tunnelled into the mantle in a non-raytheoretical path for ray parameter values larger than the critical value, and this tunnelling becomes quite pronounced at the lower frequencies. This is to be expected on physical grounds, as at low frequencies the wavelength, and hence the volume of influence, becomes proportionally larger.

The introduction of a relatively small velocity gradient in the sub-Moho produces a profound change in the calculated transmission coefficients produced by the Langer approximation. The WKBJ coefficients are unaffected (the upper and lower left-hand diagrams of Figure 6-5 are the same), as the WKBJ approximation does not "see" this velocity gradient.

6.4 WHISPERING GALLERY EFFECT.

Choy (1977) investigated the whispering gallery effect associated with the SKS phase. This phenomenon also occurs within a positive velocity gradient underlying a discontinuity such as the Moho. Figure 6-6 illustrates the first few, of an infinite series of ray paths which have similar travel times, and therefore combine to create the amplitudes characteristic of the whispering gallery phenomenon. (Cerveny and Ravindra (1971) have also called this an interference head wave.)

Choy (1977) and Cormier (1977) demonstrated that the infinite series can be expressed

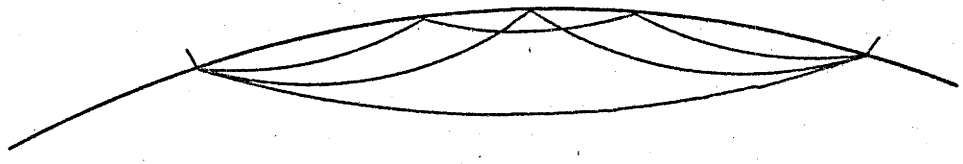

Figure 6.6

The first few of an infinite series of whispering gallery raypaths, which have similar travel times.

$$\grave{P}\grave{P}*\acute{P}\acute{P}*(1 + \acute{P}\grave{P} = (\acute{P}\grave{P})^2 + \ldots) = \frac{\grave{P}\grave{P}*\acute{P}\acute{P}}{1 - \acute{P}\grave{P}}$$

and using this, the result of the infinite series of coefficients can be calculated. The amplitude of this whispering gallery phenomena depends largely on the existence of a positive velocity gradient below a first order discontinuity. If there is no sub-Moho gradient, or if the velocity below the Moho is negative, then this wave phenomena would become inefficient. The effect of having a second order, rather than a first order discontinuity, would remove the possibility of the whispering gallery type phenomena.

Additionally, any topography on the Moho would seriously diminish the possibility of the whispering gallery series adding together in phase to produce the characteristically large amplitudes. Compound Moho structures, such as the interleaving of high and low velocity layers (which has been suggested to increase the Pm amplitude (Giese 1977)), would also tend to have a detrimental effect on the amplitude of the whispering gallery phenomena.

6.5 Conclusions.

An understanding of the nature of the Pn wavegroup is important for an understanding of the crust's formation. Theories, such as crustal underplating, depend largely for their testing on the uppermost mantle velocity models derived from studies of Pn waves. Two phenomena have been discussed which could contribute to the amplitude of the Pn wavegroup. The tunnelling of Pm energy into a Pn type path is most effective near the Pm cusp, where the Pm energy is greatest, but also contributes a greater distance. The whispering gallery phenomenum propagates energy very efficiently in a positive velocity gradient underlying a first order discontinuity; however, its effectiveness in the case of the Mohorovicic discontinuity, where the structure is often more complicated, is, as yet undertermined.

CHAPTER 7

THE APPLICATION OF SYNTHETIC SEISMOGRAMS TO THE INTERPRETATION OF THE UPPER MANTLE P WAVE VELOCITY STRUCTURE IN NORTHERN AUSTRALIA.

7.1 INTRODUCTION.

The exact nature of the velocity structure of the upper mantle is an area of considerable geophysical importance, as it bears upon the problems of mantle composition and mantle convection. Implied regional differences in the upper mantle velocity structure may be attributed either to lack of the resolving power of refraction seismic studies, or alternatively, may be indicative of the lateral variations in the upper mantle. For a better understanding of the geophysical and geochemical processes in the upper mantle, it is crucial that velocity models from different refraction studies accurately define the velocity structure in their region.

During the period from 1974 to 1977, a long range seismic project was conducted in Central Australia along the profile shown in Figure 7-1. Earthquakes from the Banda Sea region to the north were used as seismic sources for the experiment. Details of the experiment are described in Hales, Muirhead, Rynn, & Gettrust (1975), and in Hales, Muirhead, & Rynn (1980). An analysis of the data obtained has been presented in Hales et al.,(1980). This study resulted in the construction of an upper mantle compressional wave velocity model for the northern Australian region, which will hereafter be referred to as model CAP8. The analysis which resulted in this model was based largely on travel-time modelling, using geometrical raytracing techniques. This chapter further interprets the data from this experiment, using synthetic seismograms to provide additional constraints on the upper mantle velocity model.

7.2 A COMPARISON OF MODEL CAP8 WITH SELECTED UPPER MANTLE MODELS.

The region between the southern-most part of the Banda Sea Arc and northern Australia is known to be representive of continental lithosphere, (Simpson, 1973; Cardwell & Isacks, 1978), and the crust in the survey area is typical of stable continental regions. For this reason, complications due to large station residuals, and "non pure-path" effects along the refraction profile are minimized. The profile runs nearly perpendicular to

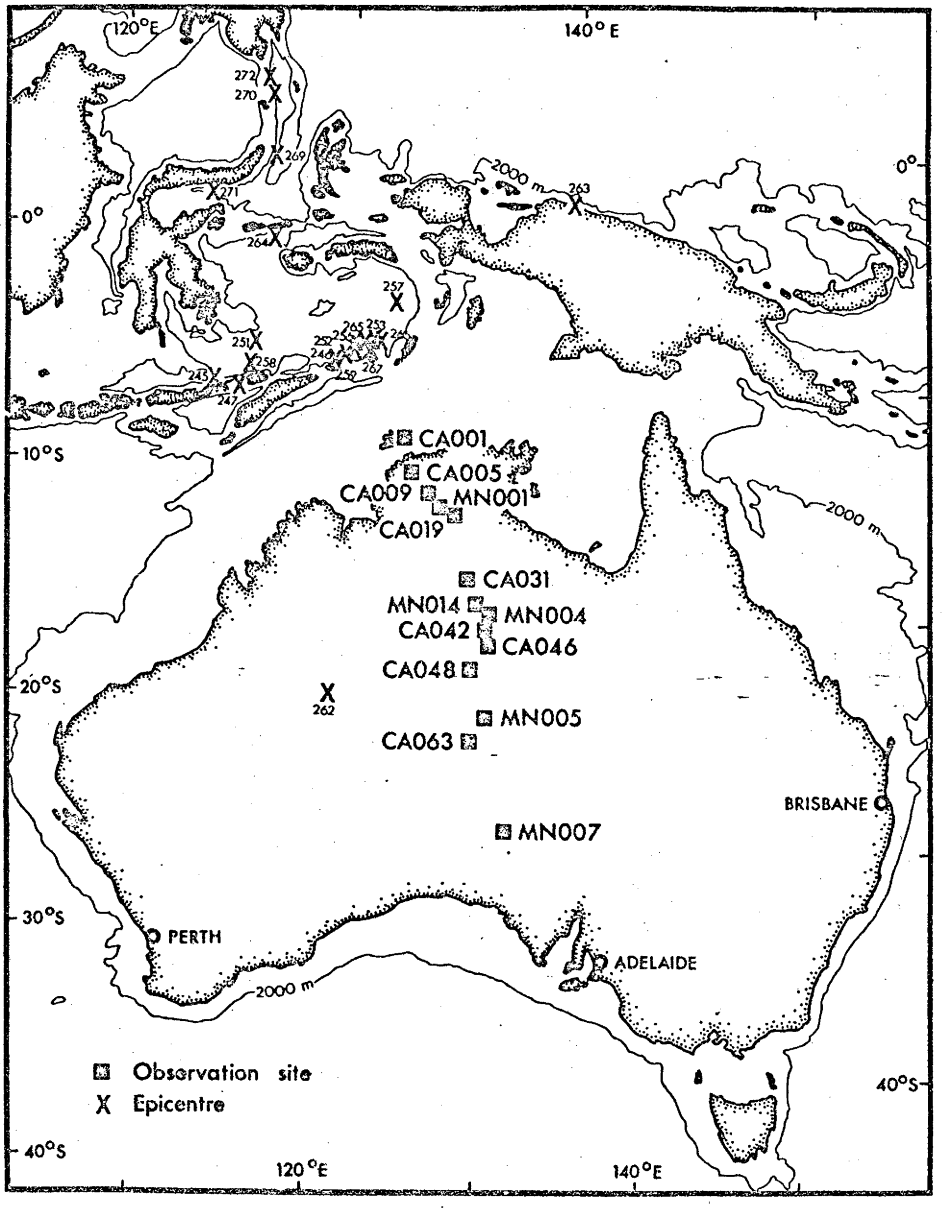

Figure 7.1

Recorder locations and earthquake epicentres for Central Australia Project - subarray 0. (After Hales et al., 1980a)

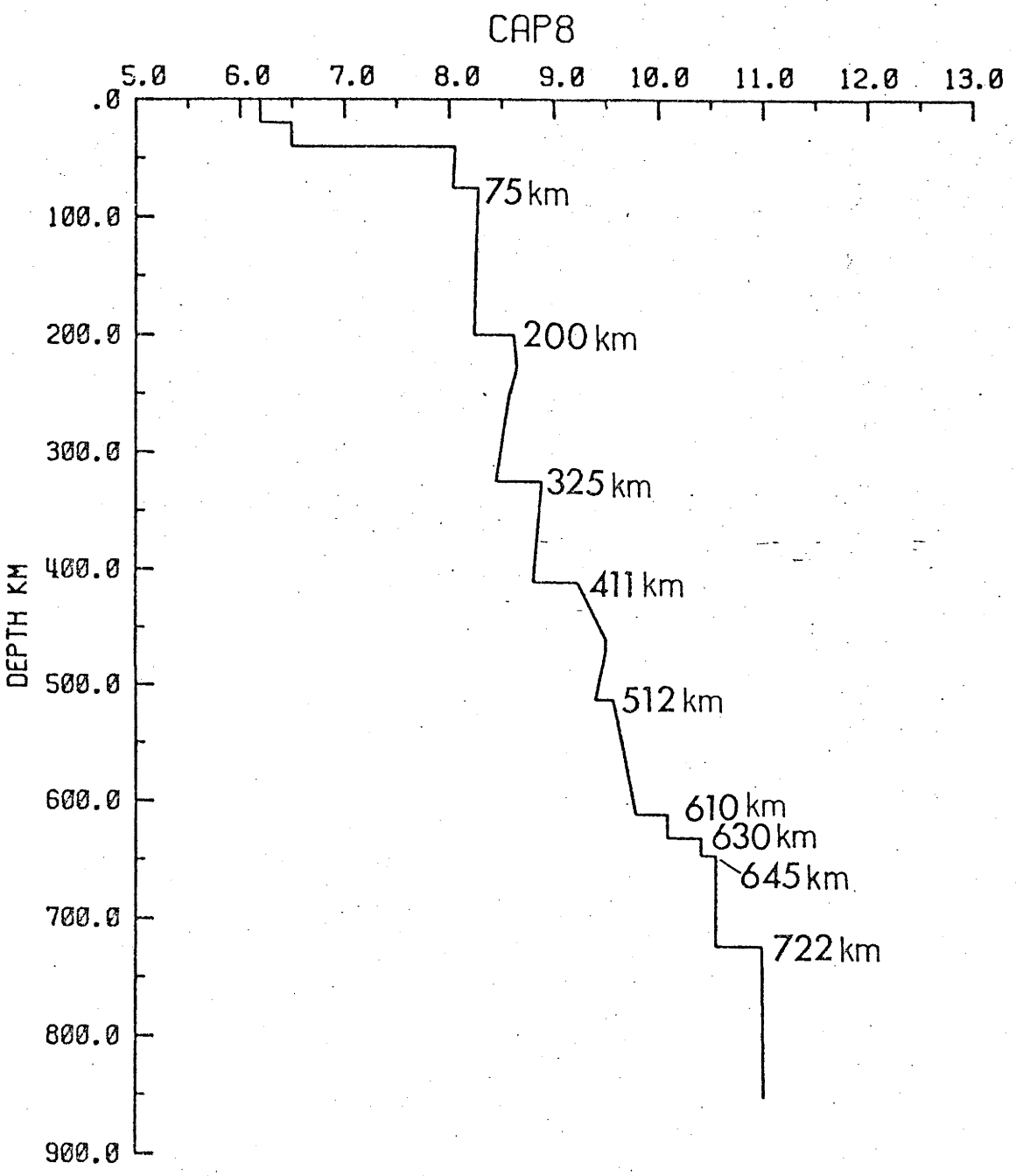

Figure 7.2

The CAP8 compressional wave velocity model.

the axis of the southern part of the Banda Sea Arc, and also roughly parallel to the direction of motion of the Indian-Australian plate in this region. As the Benioff Zone of the southern part of the Banda Sea Arc (where most events of this study occurred) dips to the north, a relatively constant source geometry has been maintained, and for the majority of events, the undesirable effects of propagation through the back-arc region have been avoided. For the above reasons, the experiment was conducted in an ideal location for the determination of an upper mantle velocity structure typical of a stable continental region.

The model CAP8 (Figure 7-2) displays a considerable degree of complexity. The range of epicentral distances for the events in this study does not allow an accurate determination of the velocity structure above a depth of 150 km, so the velocity structure above this depth will not be considered. In the CAP8 model, the 200 km discontinuity is a first order discontinuity, with a velocity increase of 4.4%, followed beneath by a relatively thin layer having a positive velocity gradient. Below this layer, a negative velocity gradient introduces a substantial low velocity zone, which is terminated by the 325 km first order discontinuity, representing a 5.0% velocity increase. Another layer with a weaker negative velocity gradient separates the 325 km and 411 km discontinuities. The 411 km discontinuity is a first order increase of 4.6% in velocity, below which a generally positive velocity gradient extends down to the 512 km discontinuity. A positive velocity gradient extends between this depth and 610 km, where a series of first order discontinuites at 610, 630 and 645 km combine to produce an overall increase of 7.4% in velocity. A homogeneous layer has been modelled above the first order 722 km discontinuity, and a slight velocity gradient below.

Model CAP8 is compared with some selected upper mantle models in Figure 7-3. Simpson (1973) gives a more extensive comparison of upper mantle models; however, for the purposes of this comparison, three recent models, representative of the main classes of upper mantle analyses, have been selected.

Burdick & Helmberger (1978) have used synthetic seismograms to carefully model long and short period waveform data from selected events with determined source parameters. Their model, designated T7, could be expected to accurately reflect the main features of the upper mantle velocity structure in the tectonically active region of the western USA. The pronounced low velocity zone in the upper-most mantle is associated

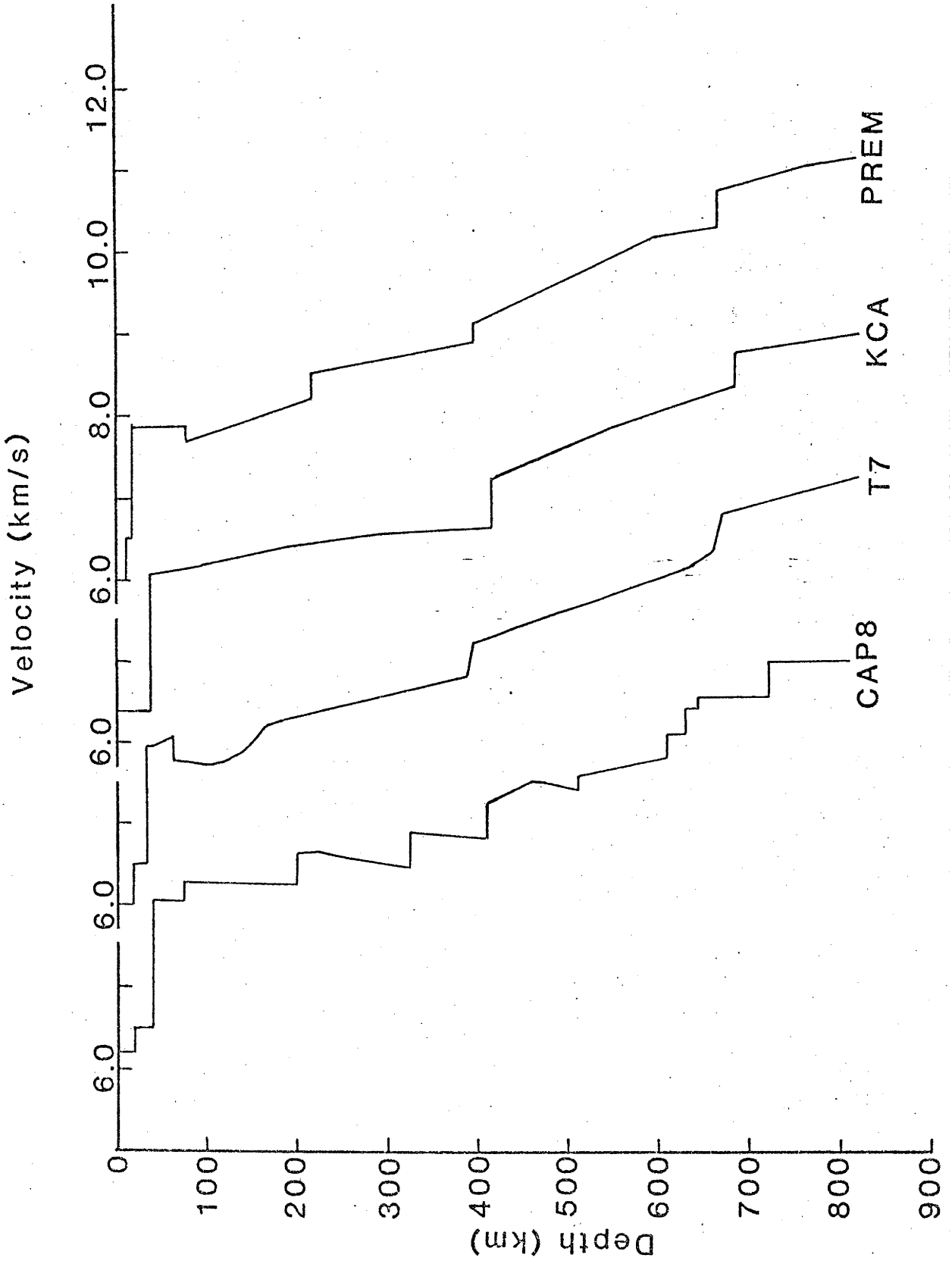

Figure 7.3

A comparison of CAP8 with the upper models T7 and KCA and the reference Earth model PREM.

with the tectonic activity of this region. Below this feature, the model has a particularly simple structure, dominated by the relatively strong positive velocity gradient, which is interrupted only by the "400 km" and "650 km" discontinuities. The waveform modelling performed by Burdick and Helmberger necessitated a reduction in the velocity step of the "400 km" discontinuity, and the removal of a small "500 km" structure, which had been present in their starting model. Their data did not require any discontinuity at 325 km depth.

The study conducted by King & Calcagnile (1976) utilized sources that were believed to be nuclear explosions within the USSR, and which had been recorded at the NORSAR array. Their study, conducted over a shield region using short period data, resulted in a considerably simpler model (KCA) than CAP8. The restriction of the use of only surface sources, however, implies some loss of resolving power in comparison with an analysis which uses sources distributed in depth, (see Gerver & Markushevich, 1966). This model is also characterized by a general positive velocity gradient, which is interrupted by discontinuities at 420 km and 690 km. The 690 km discontinuity of the KCA model is significantly deeper than the series of discontinuities in the CAP8 model which correspond to the "650 km" discontinuity. Their data ranged in epicentral distance from 12° to 40°, with observations over small (~100 km) intervals. The "200 km" refraction branch may not have been observed, due to the lack of data at epicentral distances less than 12°, so its absence from the KCA model is not considered significant. No other refraction branches were observed in the particularly dense array of observations which King & Calcagnile used in their study.

The Proposed Reference Earth Model (designated here as PREM) of Dziewonski and Anderson (1979) has been taken as representative of the gross Earth models, and this model satisfies a large suite of free oscillation, surface wave, and body wave data. This model is compared with the CAP8 model to detect any significant velocity variations that exist between the CAP8 model, and a globally averaged velocity model. The PREM has, as would be expected, a simpler velocity structure, with first order discontinuities at 200, 400 and 680 km depth. No "325 km" discontinuity is incorporated into the PREM model, which has a positive velocity gradient between the 200 and 400 km structures. A "400 km" discontinuity is represented by a substantially smaller velocity increase than given in model CAP8. The 680 km discontinuity of the PREM model is also

significantly deeper than the "650 km" discontinuity of model CAP8, and has positive velocity gradients modelled above and below.

The average velocity above 411 km for the CAP8 model is slightly higher than that of the PREM model, while below 411 km the reverse is true. This introduces an effective rotation of the travel-time distance curves of the CAP8 model, with first onsets at distances less than 2300 km (for a surface source) being earlier for the CAP8 model, and the first onsets beyond this distance being later, than those of PREM.

A comparison of the large suite of proposed upper mantle models establishes that significant differences in velocity structure exist between the models; however, the majority have several features in common. These include rapid increases in velocity at depths of around 200, 400 and 650 km, separated by regions of positive velocity gradients. Some models show a pronounced low velocity zone around 100 km depth, which may be correlated with tectonically active regions. The "400 km" and "650 km" discontinuities are common to most models, (with some variation in depth), and typically represent increases of about 5% and 7% respectively, set within positive velocity gradients.

The prominent exception to this is the CAP8 model, which Hales et al.,(1980) describe as "a series of steps [in velocity], between which the velocity is constant, or even decreases slightly with increasing depth". The petrological and thermal implications of the existence of negative velocity gradients between these discontinuities make it important to reconsider whether these negative velocity gradients are required by the data.

7.3 COMPARISON OF CENTRAL AUSTRALIA PROJECT DATA WITH SYNTHETIC SEISMOGRAMS.

Synthetic seismograms of selected events studied by Hales et al., (1980), have been generated by employing a variety of techniques, using the CAP8 velocity model, and assuming an explosive source function. With the exception of event 245, and as noted in the figure captions, ISC source locations have been used throughout this study. Lack of knowledge of source mechanisms for the events has precluded the possibility of detailed waveform modelling, such as performed by Burdick and Helmberger (1978). Significant variations in the character of the signal are observed between adjacent seismic recorders. King & Calcagnile (1978) commented on the variation of signal character that existed in the short period data across

the NORSAR array, where array elements are within kilometres of each other, and where considerably greater attention would have been paid to the siting of the seismometers than can be achieved at a temporary recording site. The application of the synthetic seismograms has therefore been restricted to a comparison of the relative amplitudes of various refraction branches.

Three different synthetic techniques have been employed to generate synthetic seismograms for comparison with the recorded data. These are the Generalized Ray Method (Wiggins & Helmberger, 1974), Full Wave Theory (Richards, 1973), and the "WKBJ" method (Chapman, 1978). The resulting synthetic seismograms differ somewhat in detail, (see Choy et al., 1979; Burdick & Orcutt, 1979); however, for the purpose of this study, the amplitudes of the refraction onsets derived by these three methods are sufficiently similar to enable any method to be used. All three of these methods have limitations with respect to their performance in dealing with layers having high velocity gradients, as each of these techniques makes assumptions which are invalid in a strongly inhomogeneous medium. However, it is not the purpose of this paper to compare the application of these techniques to the interpretation of upper mantle refraction surveys. Examples of these three different techniques can be seen in the accompaning figures.

A comparison of the record sections from selected events, (Table II of Hales et al.,1980), with the synthetic seismograms generated for the CAP8 model has been made, with particular attention being paid to the comparison of amplitudes. Modifications suggested by this comparison have been applied to the CAP8 model in such a way as to minimize perturbations to the resultant travel times. The derived model, denoted CAPRI, is shown in Figure 7-4, (with the CAP8 model dotted). It is characterized by positive velocity gradients, and, with the exception of the 406 km discontinuity, by second order type discontinuities. Record sections are compared below with the synthetic seismograms of both the CAP8 and CAPRI velocity models. In comparing the synthetic seismograms with the record sections, two points should be borne in mind. Firstly, all sections are trace normalized so that the synthetic seismograms can be directly compared with the traces of the record sections. This has undesirable effects in the situation where only one arrival occurs on a particular synthetic seismogram trace, (as noted in the caption of Figure 7-6). The second point is that the direct branch, which leaves the source with a near horizontal take-off angle, has not been synthesized in any of the synthetic

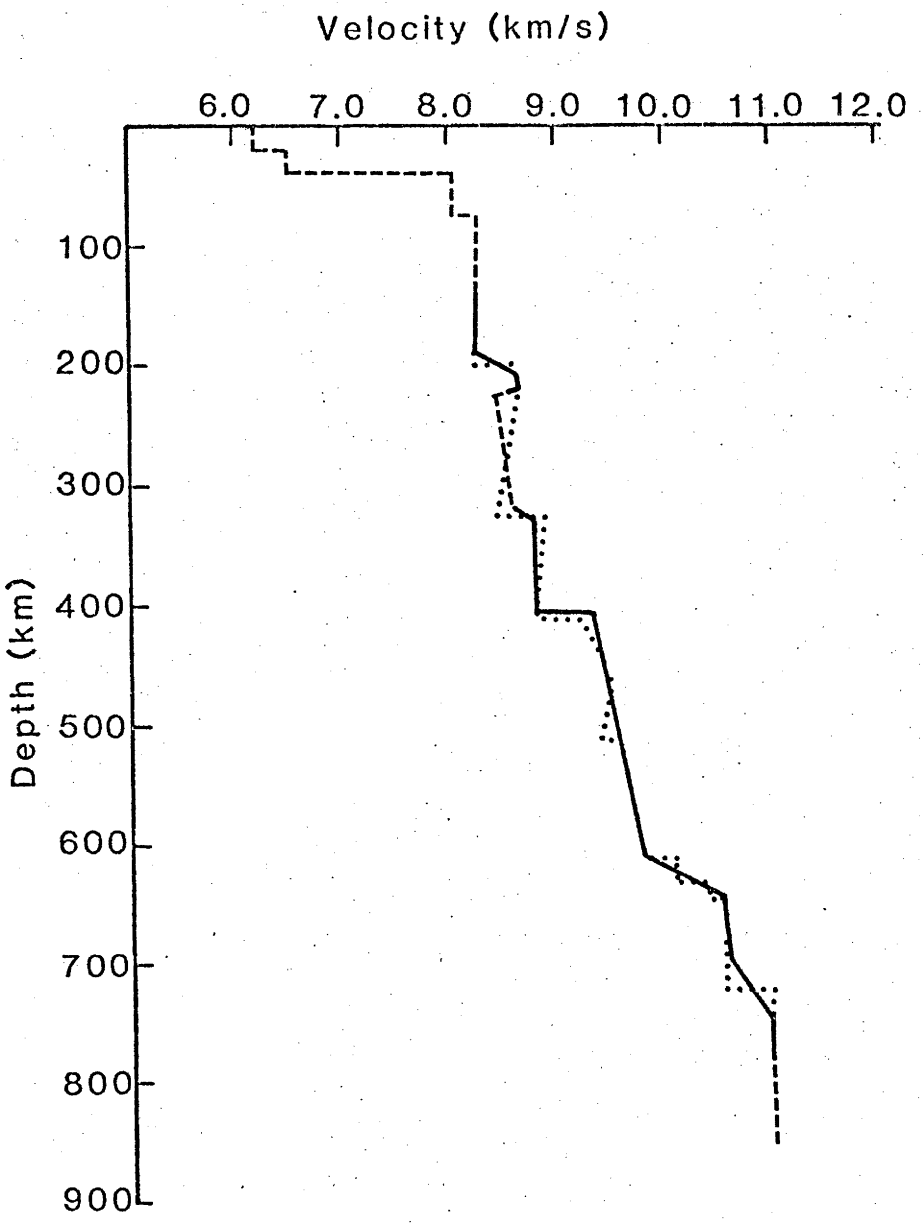

Figure 7.4

The CAPRI compressional wave velocity model. The dashed curve represents that part of the velocity model undetermined by this study. The dotted curve is the CAP8 velocity model of Hales et al., (1980).

Table 7-1. The CAPRI velocity model.

depth (km)	velocity (km/s)
0	6.2
20	6.2
20	6.5
40	6.5
40	8.06
75	8.04
75	8.28
190	8.24
210	8.66
220	8.66
225	8.45
320	8.60
330	8.80
406	8.80
406	9.33
610	9.80
645	10.55
700	10.60
750	10.99

seismograms, and is shown as a dotted line in the figures.

Event 256 (Figure 7-5)

The CAP8 synthetic seismogram of this event displays a prominent retrograde branch from the "200 km" discontinuity in the distance range between 1000 and 1500 km. This is not well corroborated by the data. In the synthetic seismogram of the CAPRI model, the relative amplitude of this retrograde branch has been reduced by distributing the velocity increase of this discontinuity over a 20 km depth range. In doing this, the cusp of the "200 km" triplication has been shifted to larger epicentral distances, as shown in the raytracing curves. The cusp of the "200 km" branch in the CAPRI synthetic seismogram terminates around 650 km, whereas the CAP8 cusp extends back to distances less than 500 km. The record section shows some evidence for this cusp on the trace of CA001, around 500 km distance. The prograde "200 km" refraction branch shows a dramatic decrease in amplitude around 1450 km. The sharper drop in velocity of the CAPRI profile near 230 km depth models this amplitude decay more successfully than the CAP8 velocity structure. Beyond 1500 km, small amplitude arrivals are observed on this refraction branch in the record section. Seismic scattering from the "high velocity zone" at 200 km depth could account for the propagation of this energy beyond the ray theoretical distance. There is little evidence in this record section for the branches of the 325 km discontinuity, although this branch is more clearly defined in the record section of event 245.

A strong cusp is associated with the "400 km" branch in the data - the large amplitude of this cusp extending forward to at least 1300 km. The CAP8 synthetic seismogram shows a rapid decrease in the cusp amplitudes of this branch near 1500 km, while the larger "400 km" discontinuity of the CAPRI model has extended this cusp forward to 1200 km. The refraction branches corresponding to the deeper discontinuities have not been synthesized, as they are not well defined in this record section.

Event 245 (Figure 7-6)

The depth of this event as determined by the ISC, is 241 km, and it lies within the low velocity zone below the "200 km" discontinuity. Hales et al.,(1980) adjusted the estimated focal depth of this event to 269 km, and this depth will be used in the present study. The record section shows three strong branches, corresponding to the direct branch, and

Fig. 7-5.

A comparison of the record section of event #256 with the synthetic seismograms of the CAP8 model (calculated by the WKBJ technique) and the CAPRI model (calculated by Full Wave theory). The record section shows the travel-time-distance curve of the CAP8 (dotted line) and CAPRI (solid line) velocity models; the ISC event origin time has been adjusted by 0.4 seconds for both travel-time-distance curve, to fit the observed arrival times. On this, and later diagrams, the traces in the three sections are trace normalized, and the dotted curve on the synthetic seismograms represents the direct branch, (rays leaving the source at a near horizontal take-off angle), which has not been synthesized. The time axes of the synthetic seismogram sections of this, and later figures, are relative to an arbitary origin time. The annotation on the branches of the travel-time-distance curves on the record section indicate the depth of the velocity discontinuity responsible for the branches.

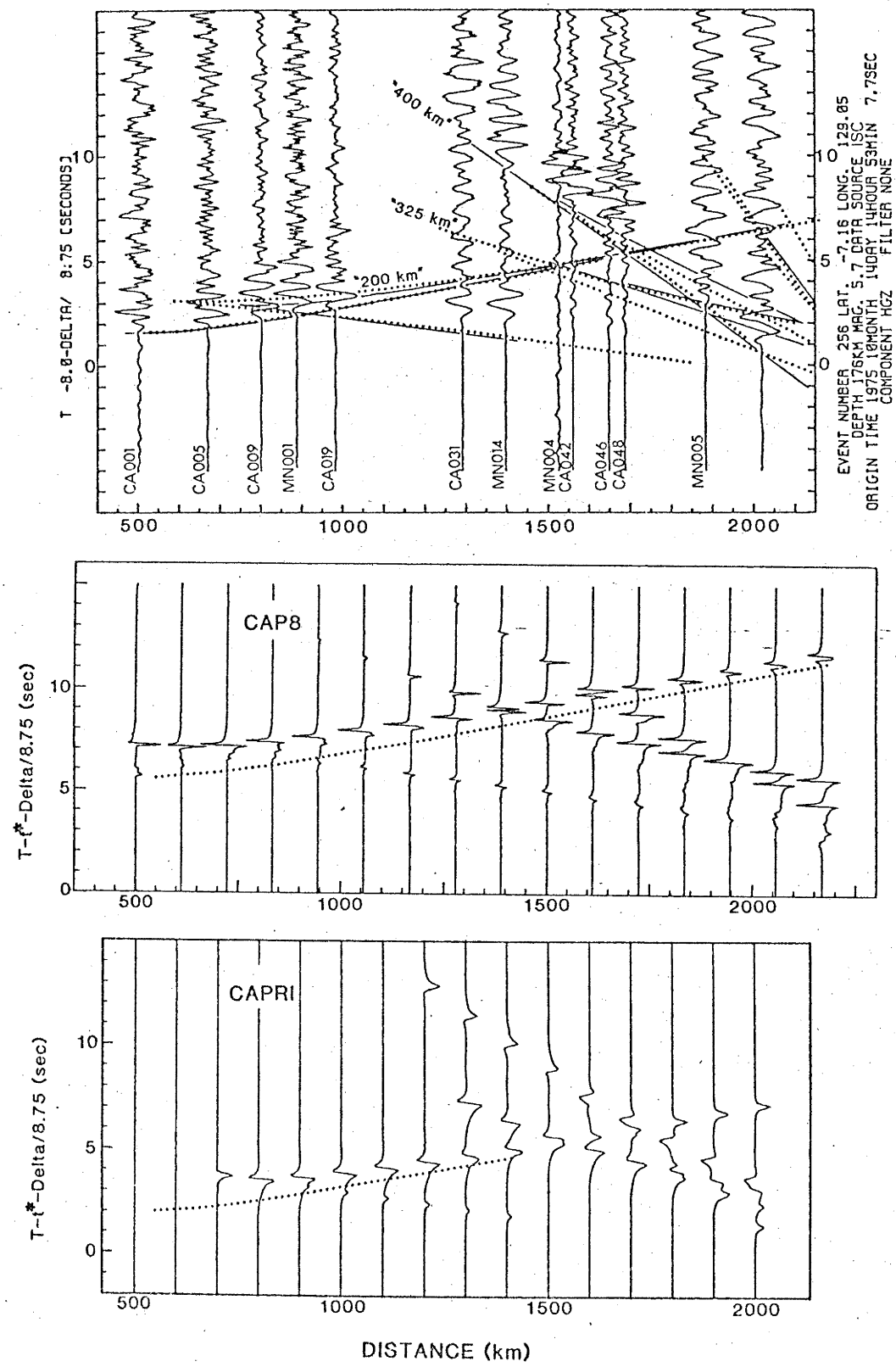
T -8.0-DELTA/ 8.75 (SECONDS)
"400 km"
"325 km"
"200 km"
CA001
CA005
CA009
MN001
CA019
CA031
MN014
MN004
CA042
CA046
CA048
MN005
EVENT NUMBER 256 LAT. -7.16 LONG. 128.85
DEPTH 176KM MAG. 5.7 DATA SOURCE ISC
ORIGIN TIME 1975 18MONTH 14DAY 14HOUR 53MIN 7.7SEC
COMPONENT HGZ FILTER NONE
CAP8
CAPRI
T-t*-Delta/8.75 (sec)
DISTANCE (km)

Figure 7.6

A comparison of the record section of event #245 with synthetic seismograms of the CAP8 and CAPRI velocity models, both calculated by Full Wave theory. The record section shows the travel-time-distance curve of the CAP8 (dotted line) and CAPRI (solid line) velocity models; the ISC event origin time has been adjusted by 1.75 seconds for both travel time distance curves, to fit the observed arrival times. The trace indicated by the star on the CAP8 synthetic seismogram has a low amplitude relative to the other arrivals, but has been amplified owing to the trace normalization, as it is the only arrival on this trace.

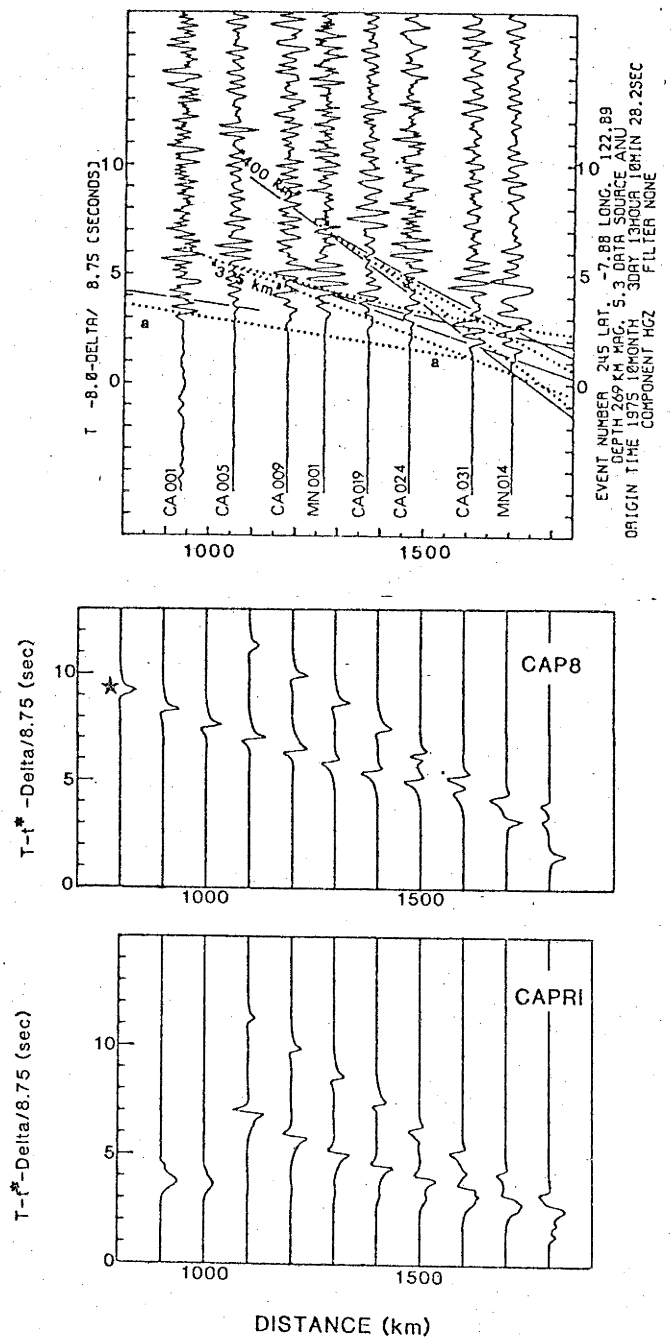
T -8.0-DELTA/ 8.75 (SECONDS)
CA 001
CA 005
CA 009
MN 001
CA 019
CA 024
CA 031
MN 014
400 KM
35 KM
1000
1500
EVENT NUMBER 245 LAT. -7.88 LONG. 122.89
DEPTH 269 KM MAG. 5.3 DATA SOURCE ANU
ORIGIN TIME 1975 10MONTH 3DAY 13HOUR 10MIN 28.2SEC
COMPONENT HGZ FILTER NONE
T-t* -Delta/8.75 (sec)
CAP8
CAPRI
DISTANCE (km)

branches of the "325 km" and "400 km" discontinuities.

The existence of relatively strong energy on the direct branch (a-a), coming from the low velocity zone below the "200 km" discontinuity, is difficult to explain. The a-a branch of the CAP8 model raytracing, extending to distances of the order of 1300 km, is dependent on the propagation of rays over a distance of several hundred kilometres in the CAP8 model layer (227km - 8.648 km/s, 230km - 8.646 km/s) which is three kilometres thick. Wave theory suggests that this branch would have insignificant energy. The prominent arrivals on this direct branch have been interpreted as indicating a positive velocity gradient in the low velocity zone underlying the "200 km" structure, but more data will be required to fully resolve this portion of the upper mantle velocity profile. The CAPRI model therefore has a positive velocity gradient at the source depth of this event, so that rays on this a-a branch leave the source travelling downwards, and are turned in the positive velocity gradient above the "325 km" discontinuity. The CAPRI travel time distance curve indicates that the ray theoretical arrivals on this a-a branch terminate around 1100 km, but the full wave synthetic seismogram shows that low-amplitude, low-frequency arrivals extend to a distance of 1500 km. These correspond to energy which has tunnelled through the "high velocity layer" below 200 km depth in the CAPRI model.

The strong cusp of the 325 km branch predicted by the CAP8 synthetics extends to smaller epicentral distances than observed in the data. This suggests that the velocity increase at this depth is not as large as modelled by CAP8. The cusp of the "400 km" branch is well modelled by the CAP8 synthetic seismogram, decreasing in amplitude at distances less than 1300 km. The amplitude of the "325 km" cusp is not significantly larger than that of the "400 km" cusp in the record section, whereas the synthetic seismogram of the CAP8 model gives a larger amplitude for the cusp of the "325 km" triplication branch than for the "400 km" cusp. This is further evidence that the velocity increase of the "325 km" discontinuity in CAP8 is too large to be reconciled with the data.

Event 258 (Figure 7-7)

The record section of this event serves to constrain the branches of the "400 km" discontinuity. The cusp from this discontinuity extends back to 800 km in the CAPRI synthetic seismogram, while in tha CAP8 synthetic, this cusp terminates at 1000 km epicentral distance. The trace

Figure 7.7

A comparison of the record section of event #258 with the synthetic seismograms of the CAP8 model (calculated by a saddle point approximation technique) and the CAPRI model (calculated by Full Wave theory). The record section shows the travel-time-distance curve of the CAP8 (dotted line) and the CAPRI (solid line) velocity models; the ISC event origin time has been adjusted by -1.0 seconds for both travel-time-distance curves, to fit the observed arrival times. As with Figure 7.6, the star beside an arrival indicates that this arrival has a relatively low amplitude.

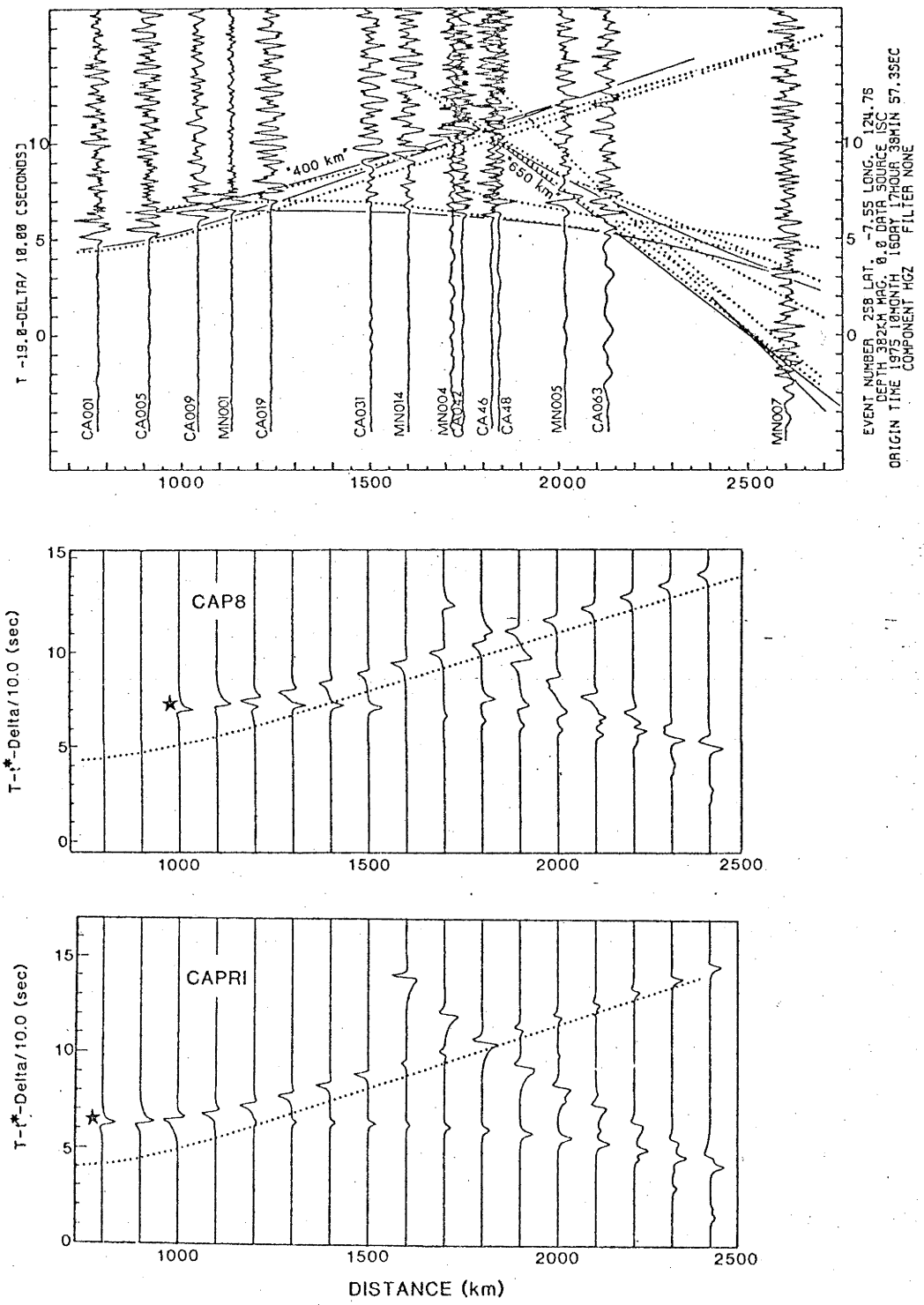
T -19.8-DELTA/ 10.00 (SECONDS)
400 km
650 km
CA001
CA005
CA009
MN001
CA019
CA031
MN014
MN004
CA032
CA46
CA48
MN005
CA063
MN007
1000
1500
2000
2500
EVENT NUMBER 25B LAT. -7.55 LONG. 124.7S
DEPTH 382KM MAG. 0.0 DATA SOURCE ISC
ORIGIN TIME 1975 10MONTH 16DAY 17HOUR 38MIN 57.3SEC
COMPONENT HGZ FILTER NONE
CAP8
T-t*-Delta/10.0 (sec)
CAPRI
DISTANCE (km)

of CA001 gives evidence of this cusp at an epicentral distance less than 800 km.

Traces CA048 and MN005 display arrivals which have been modelled by a discontinuity at 512 km depth in the CAP8 model. However, the evidence on these two traces was considered insufficient to maintain this feature in the CAPRI model. A great deal of complexity arises from the branches of the deeper discontinuities, and this record section does not serve to resolve them.

Event 251 (Figure 7-8)

This event, having an ISC source depth of 609 km, has been used by Hales et al.,(1980) to constrain the velocity at the source depth, using the method of Gutenberg. The "650 km" discontinuity has been modelled by three first order velocity increases in the CAP8 model at 610, 630, and 645 km depth. There is not a great deal of support in the record section of this event for the 610 km branch. Arrivals on the 630 km branch are relatively strong in the distance range 1500-2000 km, whereas, as noted by Hales et al., the onsets on the prograde 645 km branch are very weak. There is no doubt that the more complicated velocity structure of the CAP8 model is more consistent with the data of this event than is the CAPRI velocity model. However, event 281 (Figure 7-9) from the region south of the Celebes, has a similar depth (ISC depth 595 km), and the CAP8 model, derived from event 251, does not fit the record section of this event very satisfactorily. The CAPRI model, it should be noted, does no better; however, the complicated structure of the "650 km" discontinuity in the CAP8 model has been replaced by a single second order type discontinuity in the CAPRI model, as it is felt the the present data are incapable of resolving the finer detail of the "650 km" discontinuity.

Event 247 (Figure 7-10)

Both synthetic seismograms of this event show a small but evident arrival on the "75 km" branch, which the data does not corroborate. This indicates that either the "75 km" discontinuity does not exist near the source region of this event, or lateral variations in structure near the source region redirect the energy of this branch. As this event occurred in the northern region of the Banda Sea Arc, the seismic waves of the shallower branches could have been disrupted by the Benioff zone of the southern part of the Banda Sea Arc. The amplitudes of the "200 km" cusp

Figure 7.8

A comparison of the record section of event #251 with the synthetic seismograms of the CAP8 model (calculated by WKBJ technique) and the CAPRI model (calculated by Generalized Ray Theory). The record section shows the travel-time-distance curves of the CAP8 (dotted line), and the CAPRI (solid line) velocity model; the ISC event origin time has been adjusted by 1.35 seconds for both travel time distance curves, to fit the observed arrival times. As with Figure 7.6, the star beside an arrival indicates that this arrival has a relatively low amplitude.

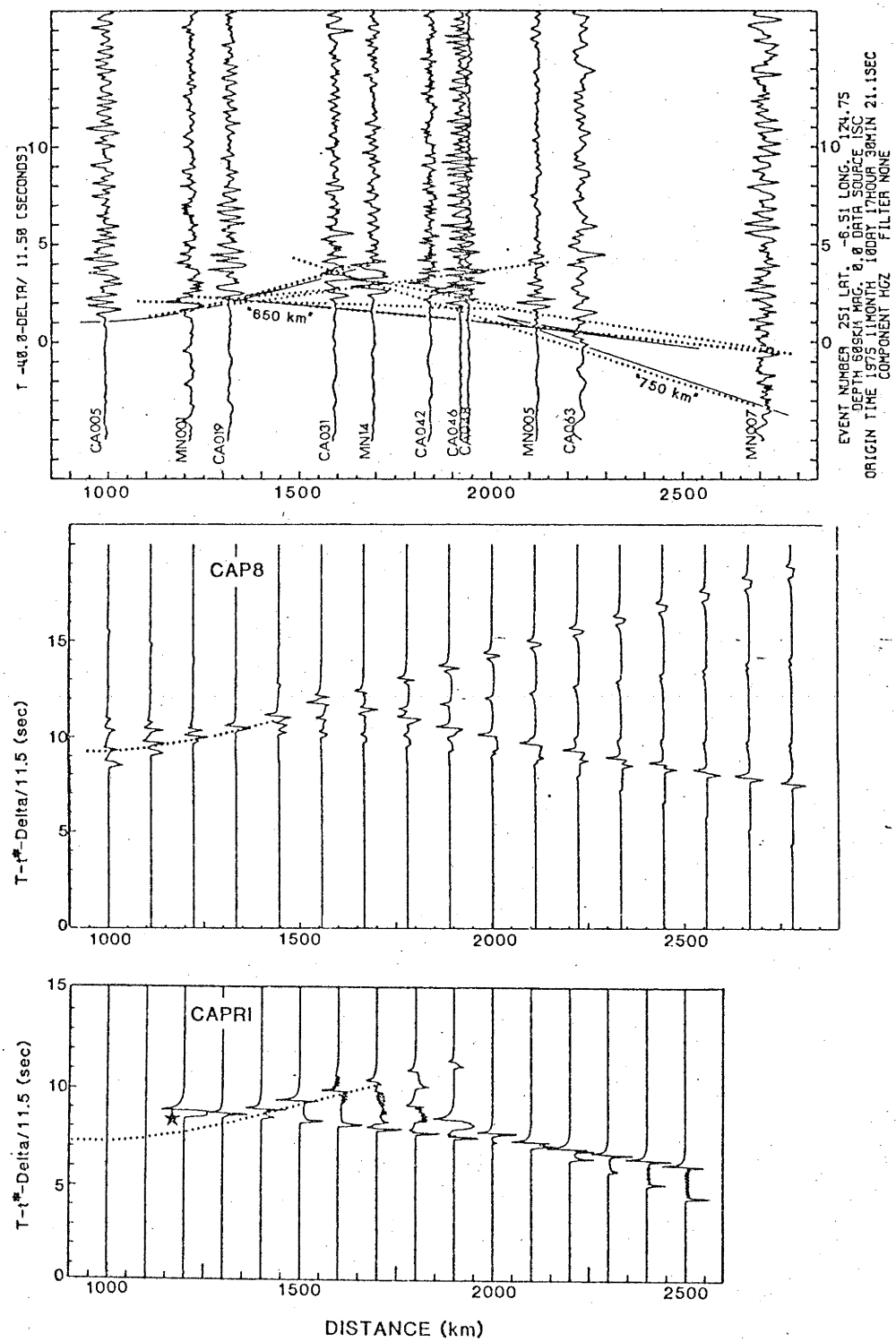
T -40.0-DELTA/ 11.58 (SECONDS)
650 km*
750 km*
CA005
MN09
CA019
CA031
MN14
CA042
CA046
CA218
MN005
CA063
MN007
EVENT NUMBER 251 LAT. -6.51 LONG. 124.75
DEPTH 686KM MAG. 0.0 DATA SOURCE ISC
ORIGIN TIME 1975 11MONTH 10DAY 17HOUR 30MIN 21.1SEC
COMPONENT HGZ FILTER NONE
CAP8
CAPRI
T-t*-Delta/11.5 (sec)
DISTANCE (km)

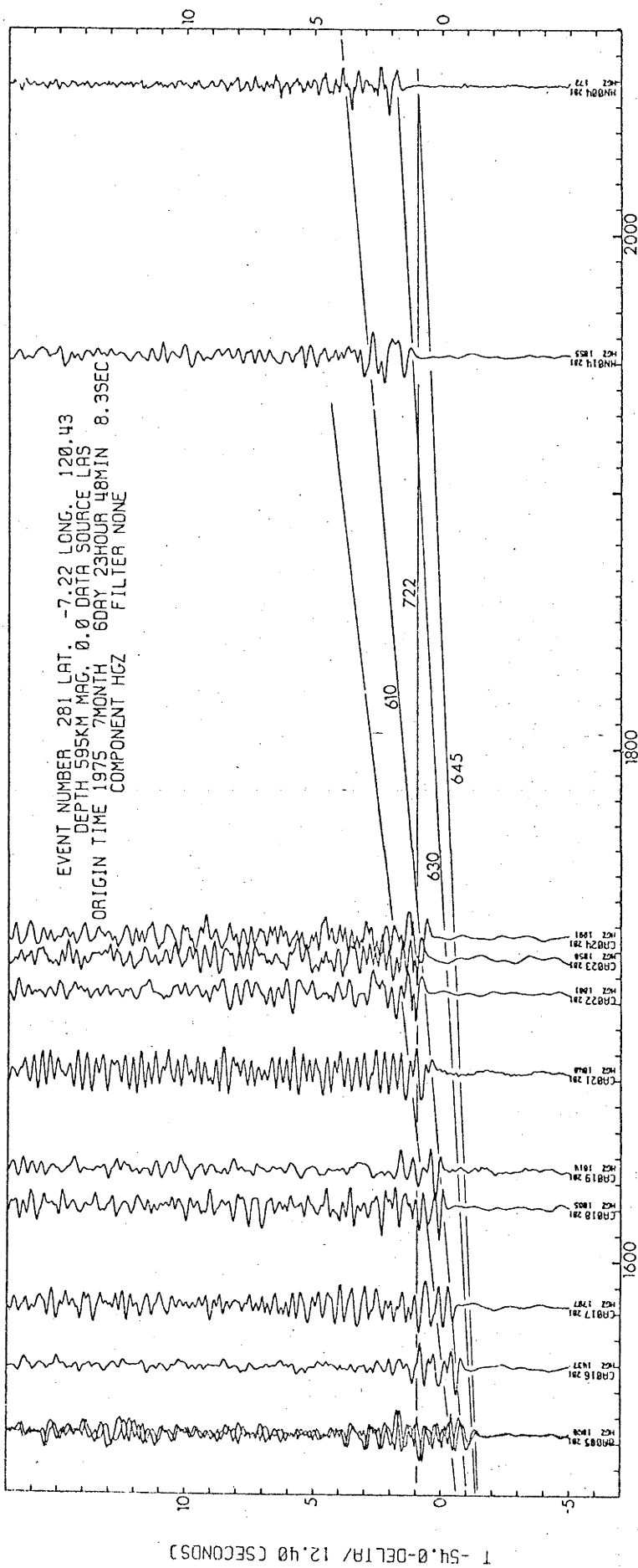

Figure 7.9

Record section of event 281 with the CAP8 velocity model superimposed.

Figure 7.10

A comparison of the record section of event #247 with the synthetic seismograms of the CAP8 model (calculated by Generalized Ray theory), and the CAPRI model (calculated by Full Wave theory). The record section shows the travel-time-distance curves of the CAP8 (dotted line) and the CAPRI (solid line) velocity models.

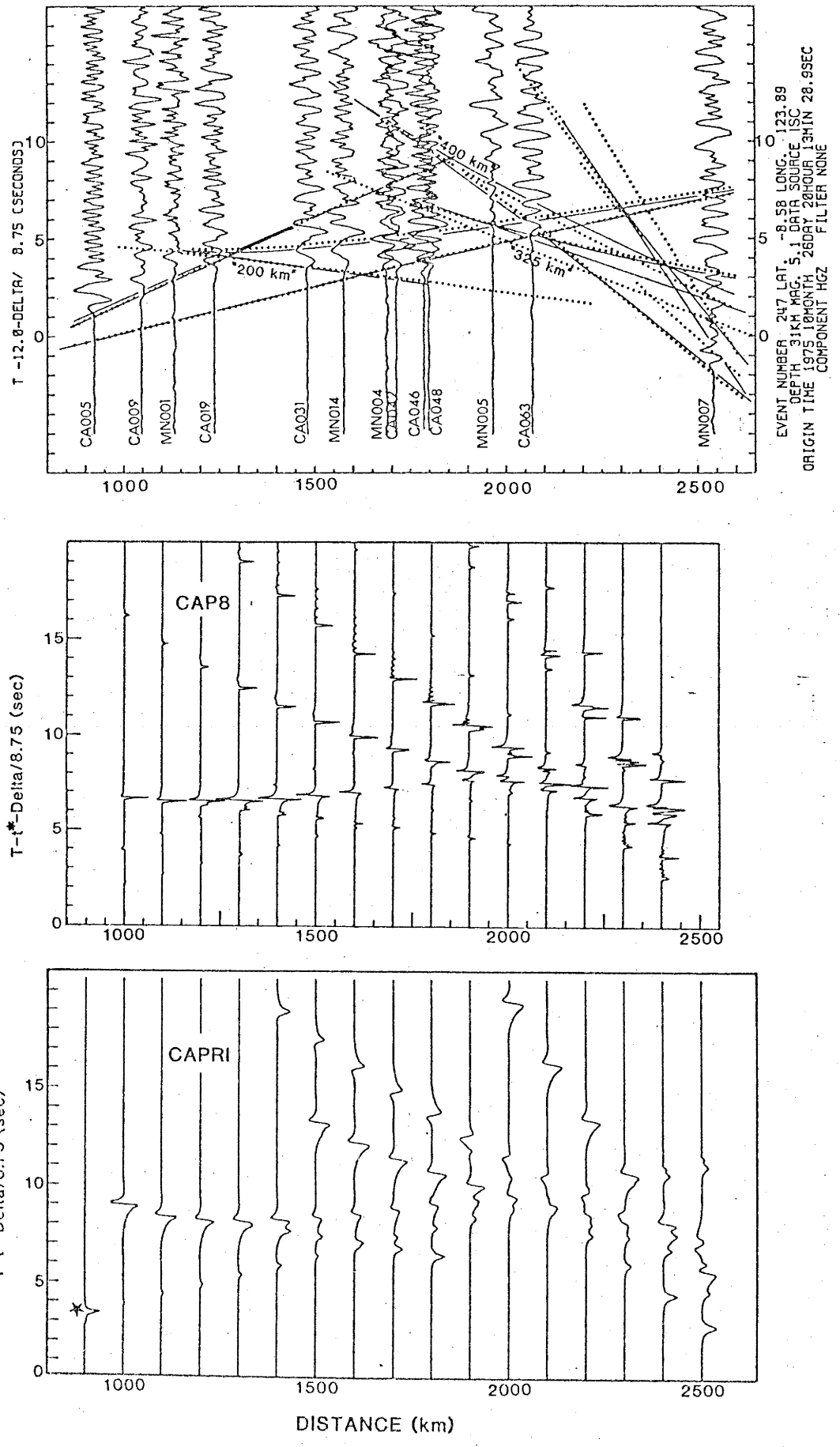
T -12.8-DELTA/ 8.75 (SECONDS)
CA005
CA009
MN001
CA019
CA031
MN014
MN004
CA047
CA046
CA048
MN005
CA063
MN007
200 km
400 km
325 km
1000
1500
2000
2500
EVENT NUMBER 247 LAT. -8.58 LONG. 123.89
DEPTH 31KM MAG. 5.1 DATA SOURCE ISC
ORIGIN TIME 1975 10MONTH 26DAY 20HOUR 13MIN 28.9SEC
COMPONENT HGZ FILTER NONE
CAP8
T-t*-Delta/8.75 (sec)
CAPRI
T-t*-Delta/8.75 (sec)
DISTANCE (km)

are relatively smaller than exhibited by the CAP8 synthetic seismogram. The CAPRI synthetic seismogram has reduced the relative amplitude of the "200 km" retrograde branch by replacing the first order discontinuity with a second order type discontinuity.

Arrivals on the prograde "200 km" branch decrease markedly in amplitude beyond 1800 km, while the CAP8 synthetic seismogram shows a relatively slow decrease in amplitude of this branch around this distance. This suggests that the onset of the low velocity zone below "200 km" is sharper than predicted by the gradual negative velocity gradient at this depth in the CAP8 model. Large amplitudes are associated with the 325 km branch in the CAP8 synthetic seismogram, but little evidence for onsets of this branch can be seen in the record section of event 247. No strong "400 km" refraction branch is observed in this record section, in contrast to those of events 256 and 266. However, the trace of MN014 does show evidence for a cusp of this branch, although at a somewhat later time than predicted by both the CAP8 and CAPRI velocity models. The refraction branches corresponding to the deeper discontinuties are not well resolved in this record section.

Event 266 (Figure 7-11).

The most noticeable feature of this record section is the prominent cusp of the "400 km" discontinuity, which extends back to an epicentral distance of around 1300 km. This feature is well modelled by a first order velocity discontinuity. There is no indication of the corresponding "325 km" triplication in this record section. Onsets on the prograde "200 km" branch are observed to drop to neglible amplitudes beyond 1500 km epicentral distance, and this supports the view that the low velocity zone beneath the "200 km" discontinuity begins more abruptly than indicated in the CAP8 model. A relatively strong onset which may correspond to the cusp from the "650 km" discontinuity is observed between 1900 and 2100 km (traces MN005 and CA063), but there is no indication of the "750 km" cusp on the record at 2100 km, although this may occur at a slightly greater epicentral distance.

Event 270 (Figure 7-12).

The record section of this event serves to constrain the apparent velocity of the prograde "750 km" branch. The onsets on this branch are seen to be stronger than the synthetic seismogram indicates, implying that

Figure 7.11

A comparison of the record section of event #266 with the synthetic seismograms of the CAP8 and CAPRI velocity models, both calculated by Full Wave theory. The record section shows the travel-time-distance curves of the CAP8 (dotted line) and the CAPRI (solid line) velocity models; the ISC event origin time has been adjusted by +0.8 seconds for both travel-time-distance curves, to fit the observed arrival times.

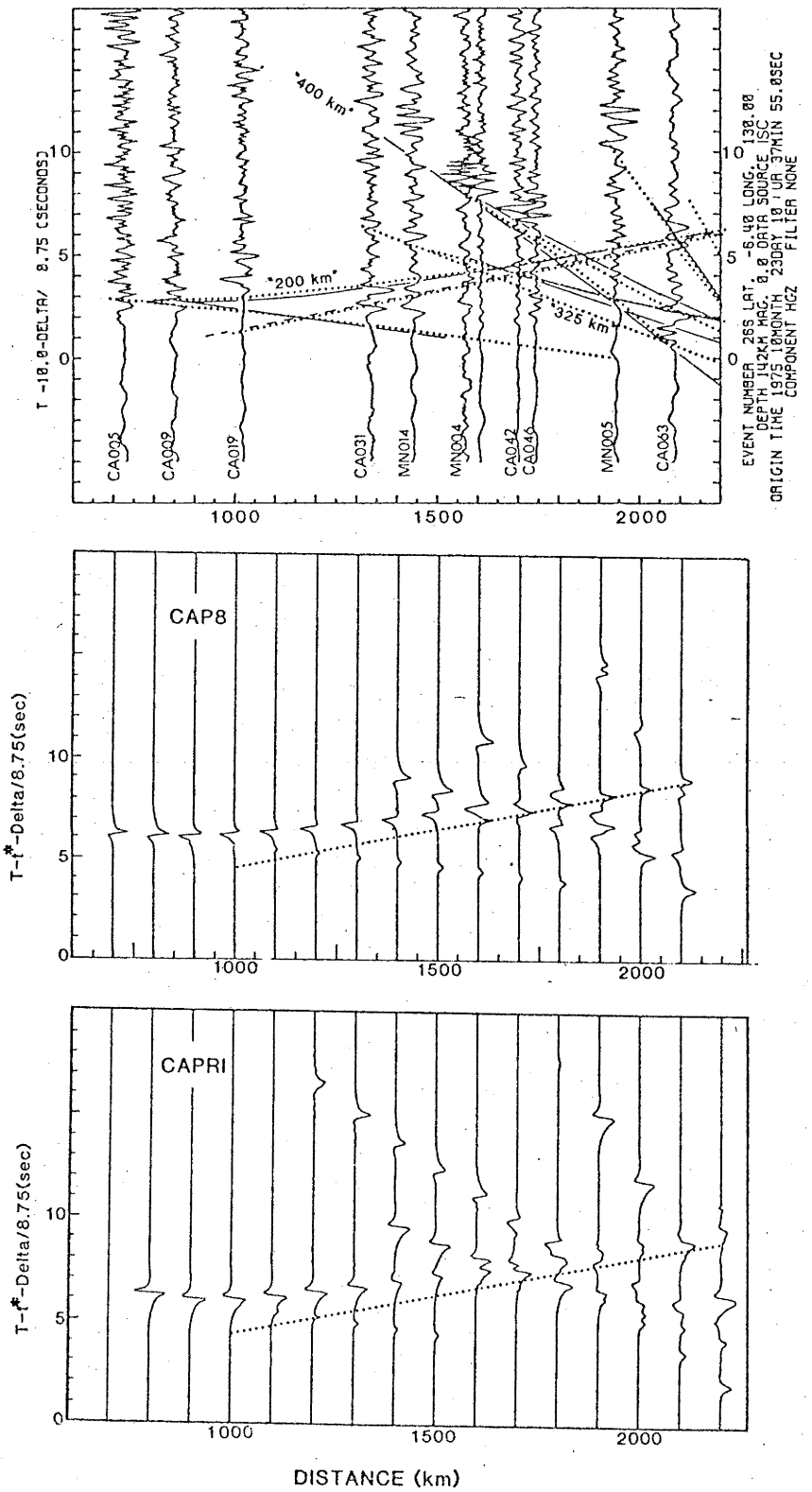
T -10.0-DELTA/ 8.75 (SECONDS)
"400 km"
"200 km"
325 km
CA035
CA009
CA019
CA031
MN014
MN004
CA042
CA046
MN005
CA063
1000
1500
2000
EVENT NUMBER 26S LAT. -6.40 LONG. 130.00
DEPTH 142KM MAG. 0.0 DATA SOURCE ISC
ORIGIN TIME 1975 10MONTH 23DAY 18 HR 37MIN 55.0SEC
COMPONENT HGZ FILTER NONE
CAP8
CAPRI
T-t*-Delta/8.75(sec)
DISTANCE (km)

Figure 7.12

A comparison of the record section of event #270 with the synthetic seismograms of the CAP8 model (calculated by the WKBJ method) and the CAPRI model (calculated by Full Wave theory). The record section shows the travel-time-distance curve of the CAP8 (dotted line) and CAPRI (solid line) velocity models; the ISC event origin time has been adjusted by 0.95 seconds for both travel-time-distance curves, to fit the observed arrival times.

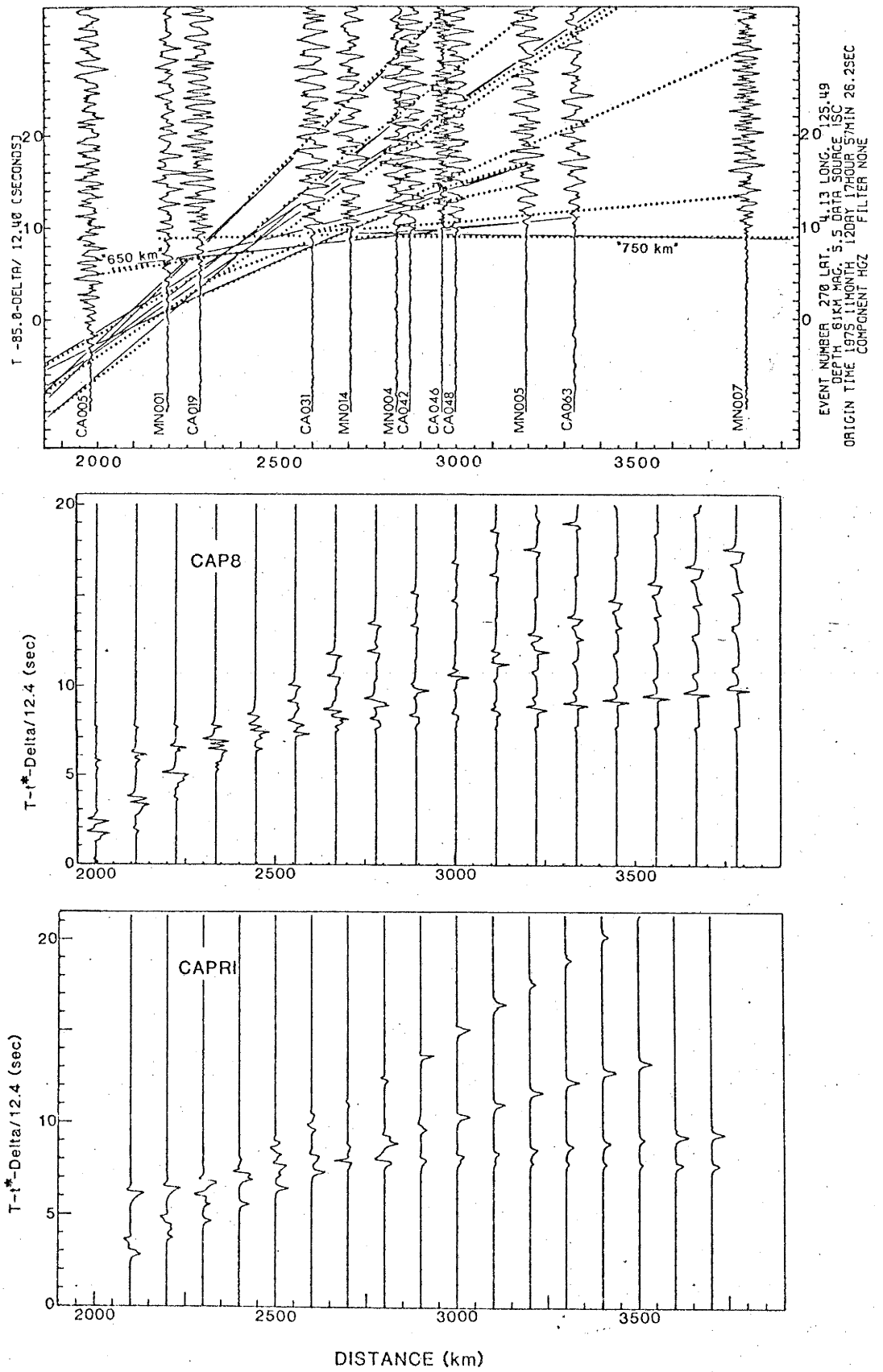
T -85.0-DELTA/ 12.48 (SECONDS)
650 km
750 km
CA005
MN001
CA019
CA031
MN014
MN004
CA042
CA046
CA048
MN005
CA063
MN007
2000
2500
3000
3500
EVENT NUMBER 278 LAT. 4.13 LONG. 125.49
DEPTH 61KM MAG. 5.5 DATA SOURCE ISC
ORIGIN TIME 1975 11MONTH 12DAY 17HOUR 57MIN 26.2SEC
COMPONENT HGZ FILTER NONE
CAP8
T-t*-Delta/12.4 (sec)
CAPRI
T-t*-Delta/12.4 (sec)
DISTANCE (km)

the velocity gradient below this feature may be more positive. There is some indication of a cusp of the "750 km" feature, but no corresponding increase in amplitudes is observed for the "650 km" triplication. The epicenter of this event lies to the north of the Banda Sea Arc, and the shallower branches of this record section, as in the record section of event 247, have possibly been disrupted by the wave propagation through the Benioff zones.

7.4 THE CAPRI MODEL AND ITS PETROLOGICAL IMPLICATIONS.

The first order "200 km" discontinuity of the CAP8 velocity profile has been remodelled as a zone of positive velocity increase between the depth interval of 190 and 210 km. The comparison of the synthetic seismograms and the data suggests that this velocity increase is not first order; however, there are insufficient data to provide any constraint on the exact velocity gradient. Detailed waveform modelling together with careful determination of the focal mechanism may provide this answer in the future. Below this increase, a relatively sharp negative jump in velocity has been modelled at around 220 km depth in the CAPRI model, to explain the abrupt decrease in amplitude on the prograde "200 km" refraction branch.

Anderson (1979a) named the "200 km" structure the Lehmann discontinuity. Anderson (1979b, 1980) has interpreted the velocity increase at this depth in terms of a chemical discontinuity in the upper mantle mineralogy, with a peridotitic mantle above and an eclogitic composition below. However, the velocity contrast of these two mineralogies is insufficient to explain the observed seismic discontinuity, (I. Jackson, personal communication, 1980). High pressure petrological investigations of the constituent minerals of the pyrolite model do not indicate any phase transformation that could explain this discontinuity. Ringwood (1975) points out that no phase transformations have been discovered in the pressure range appropiate to the depths from 150 to 330 km, despite an intensive study. Recently Liu (1980b) has attributed the Lehmann discontinuity to the onset of the solid solution transition phase between the pyroxene and garnet components of a pyrolite upper mantle, but this requires a temperature at a depth of 200 km in excess of 1600°C - significantly higher than current thermal models would indicate, (Graham & Dobizykowski, 1976), and approaching the predicted solidus of pyrolite at this depth, (Ringwood, 1975). Furthermore, at the temperature of 1600°C,

the transformation of pyroxene to garnet is spread out over a large depth range, contrary to the observed seismic feature. Ringwood (1975) argues that this transformation occurs at depths considerably shallower than 150 km. Liu's explanation differs markedly from Anderson's explanation, in that Liu argues discontinuity is a phase change, and not a chemical discontinuity. An alternative explanation of this feature in terms of a chemical change is that the material below "200 km" depth is of a primitive pyrolitic composition, whereas the material above "200 km" is more peridotitic, having been depleted in its low melting point components, (Ringwood, 1975). However, this model is also unsatisfactory, as it cannot explain a velocity increase greater than 0.2 km/s (Jackson, personal communication, 1980).

The two alternative petrological explanations hinge largely on the question as to whether there exist significant proportions of eclogite in the upper mantle. A wide range of evidence, reviewed by Ringwood (1975), suggests that the upper mantle is dominantly composed of peridotite, with eclogite being widely distributed as local segregations, but relatively minor in total volume. The work of Graham (1970) also strongly implies that the upper mantle mineralogy is dominated by peridotite.

The Lehmann discontinuity is now thought to be a fairly persistent global feature (Anderson, 1979a); however, different refraction studies have indicated substantially differing depths for this discontinuity, (Simpson 1973). If the Lehmann discontinuity does represent the zone of decoupling between the lithosphere and the underlying mantle, as Hales (1977) and Anderson (1979a,b) have suggested, then any topographic relief on this feature may impose severe constraints on the possible plate motions. It is difficult to explain the association of the upper mantle low velocity zones in the depth range 100 to 200 km, with the tectonically active regions, unless the mantle material above the "200 km" discontinuity moves with the related continental features. However, any significant topography on the "200 km" discontinuity may tend to impede this motion. Further studies of the regional variations in the depth of this discontinuity are needed to clarify this point, as the existence of topographic coupling would suggest that the mantle material below this discontinuity must convect at a rate similar to that of the lithospheric plates.

It is well known that the velocity structure within a low velocity zone cannot be uniquely determined from refraction data, unless there is a

distribution of sources through the low velocity zone, (see Gerver & Markushevich, 1966). However, two features of the upper mantle low velocity zone in the region below the Lehmann discontinuity have been suggested from studying the observed amplitudes. Firstly, a more abrupt onset of the low velocity zone is indicated by the rapid amplitude decay of the prograde "200 km" branch, as discussed in relation to the record section of events 256 and 247. Secondly, the record section of event 245 has been interpreted as indicating that the velocity gradient at the source depth of this event is positive. The low velocity zone of the CAP8 and CAPRI models are significantly deeper than the low velocity zones of most other upper mantle models. However, the data of Simpson (1973) suggest that there is no low velocity zone in the depth range of 80 to 160 km, so that the low velocity zone below the "200 km" discontinuity is the first significant low velocity zone beneath the Australian continental shield region.

The commonly accepted explanation for the low velocity zone in the upper mantle is partial melting along grain boundaries, although Goetze (1977) noted that critical petrological experiments to verify this idea have not been performed, and other mechanisms may well play an important role. The abrupt onset of the low velocity zone in the CAPRI model is difficult to explain in terms of partial melting, which one would intuitively expect to have a more gradational onset. However, the disposition of the Lehmann discontinuity may have a causal bearing on the formation of the low velocity zone, as the barrier to convection which may be imposed by the discontinuity could cause a concentration of heat below the discontinuity. It is, however, difficult to maintain this negative velocity gradient for any depth range by invoking a super-critical thermal gradient, without having temperatures that exceed the solidus.

The 325 km discontinuity of the CAP8 model poses some difficulties in its seismological interpretation. The record section of event 245 shows unquestionable evidence for the refraction branches corresponding to this discontinuity, while the record section of event 256 shows virtually no evidence for the corresponding branches. The data suggest, however, that this discontinuity, (if it does exist), has a smaller velocity increase than modelled in CAP8. A possible explanation for the transitory nature of the observations of these refraction branches is that a small amount of topographic relief on the discontinuity scatters the refracted energy of the corresponding branches, and this scattered energy may or may not be

observed.

The CAPRI model has a relatively minor second order discontinuity at a depth of 325 km. Other areas of seismic evidence for a discontinuity at this depth have been considered in maintaining this feature in the CAPRI velocity profile. Array studies using the N-th root processing technique (Muirhead, 1968; Muirhead and Ram Datt, 1976), have detected the existence of a change in wave-slowness of the first arrivals, as well as later arrivals, which are attributed to the "325 km" structure. Shear wave studies (Hendrajaya, personal communication, 1980) also indicate a relatively strong discontinuity at this depth. The S wave branches have a greater separation than the corresponding P wave refraction branches, allowing the prograde S wave refractions of the "325 km" feature to become first arrivals for observable distances, whereas the corresponding P onsets are first arrivals over only a very limited distance range. For these reasons, the discontinuity at 325 km depth has been maintained in the CAPRI model, but has been reduced in overall velocity increase.

Ringwood (1975) has suggested that the petrological explanation for this discontinuity may be the transformation of pyroxene to garnet. His estimated depth of this phase transformation is around 330 km, which agrees well with the modelled depth of the discontinuity; however, as Liebermann (1979) points out, there is no unambiguous way of identifying any specific phase transformation with a particular seismic discontinuity. Akaogi & Akimoto (1977) found that the rapid increase in the density of this phase transformation occurs near 17 GPa (170 kbars), and therefore would be associated with a discontinuity nearer 500 km depth.

The "400 km" discontinuity of the CAP8 model has been modelled in the CAPRI velocity profile as a first order discontinuity at a depth of 406 km, with a larger velocity increase than that given in CAP8. The prominent cusp displayed in the record section of events of 256 and 266, indicates that this velocity discontinuity is much sharper than the other observed upper mantle discontinuities. The velocity increase of the CAPRI model at 406 km depth is 5.8%, and this is larger than the velocity increase of the "400 km" discontinuity in the PREM model, of similar magnitude to that of the T7 model, but smaller than that of the KCA model.

The commonly accepted petrological explanation of the "400 km" discontinuity, among those who advocate a pyrolitic upper mantle, is the transformation of olivine to the beta structure. Ringwood (1975) estimates the increase of velocity due to this transformation to be 0.43 km/s

distributed 'over a depth interval of about 30 km, centred on 400 km [depth]' but suggests that 'a first order discontinuity could arise from the presence .... of a reaction point.' The particularly pronounced cusp indicates a sharp velocity increase, which in wave propagation terms implies that the increase occurs over less than half a wavelength (< 6 km). More speculatively, Anderson (1979b) has proposed that this discontinuity is caused by the pyroxene to garnet transformation, although Akaogi & Akimoto (1977) and Liu (1980b) have suggested that this transformation occurs at pressures too great to explain the "400 km" feature, and that this phase transition is relatively gradual, in contrast with the observed sharpness of the seismic discontinuity.

The prominent cusps produced by the "400 km" discontinuity argue against significant scattering at this depth. However, it is difficult to reconcile having topographic relief on the "325 km" discontinuity, without postulating some corresponding relief on the "400 km" discontinity, if the topography is the result of convection. Nevertheless, the larger velocity increase at the depth of the "400 km" discontinuity may compensate for any local scattering effects, and still produce the strong cusps which are observed. An alternative petrological explanation (Ringwood, 1975) can explain relief on the "325 km" discontinuity without incurring any topography on the "400 km" feature. If the "325 km" feature is caused by the transformation of pyroxene to garnet, then this reaction is dependent on the amount of Al present in the mantle mineralogy at this depth, and local variations of the Al content could be responsible for topography on this discontinuity, whereas this would not affect the olivine to beta structure transformation associated with the "400 km" discontinuity.

The CAP8 model has a first order discontinuity at a depth of 512 km, but this feature was not incorporated into the CAPRI model. As already mentioned, Burdick and Helmberger (1978) have also found this discontinuity unnecessary in modelling the upper mantle velocity structure of the western United States. Additional data, ideally events located around 500 km depth, will be required to resolve this feature.

Liu (1980b) proposes the high pressure boundary of the pyroxene - garnet transformation as the explanation of the "512 km" discontinuity. An explanation for this discontinuity cannot be easily given in terms of an eclogitic composition at this depth, (Liu 1980b). The higher pressure boundary of the garnet-pyroxene system has been shown by Akaogi & Akamoto (1977) to be relatively gradual, being achieved over a pressure interval of

7 GPa (70 kbars). This may explain why this transformation is not clearly observed in the seismic sections. An alternative phase transformation that will occur for a peridotitic mantle is the conversion of the olivine component from the beta to the spinel structure. A 2% increase in density has been estimated for this transformation (Liu, 1977a), and if the corresponding velocity increase is significantly less than 2%, then it is questionable whether this would be seismically observed as a discontinuity.

The three first order discontinuities of the "650 km" feature of the CAP8 model have been replaced by a single second order type discontinuity in the CAPRI model, although as already noted in relation to event 251, a more complicated structure is indicated by the data. It is interesting to note that the data of King & Calcagnile (1978) show a remarkably well constrained triplication branch from the "650 km" structure, (given at a depth of 690 km in their model), in which no indication of any multiple structure in the triplication branch can be seen. However, it is difficult to resolve this structure using surface sources.

Two conflicting petrological explanations for the "650 km" discontinuity have been advocated. The view that the "650 km" discontinuity is the result of a phase change has long been popular, although some controversy existed over which particular transformation was responsible. Liu (1977b) has shown that this feature can be explained in terms of the decomposition of the spinel phase to perovskite plus rock salt structure, and also the transformation of garnet to an ilmenite type structure. Anderson (1976) stated that the "650 km" was 'primarily due to phase changes in the pyroxene - garnet [mineral assemblages]'. The alternative explanation, recently proposed by Liu (1979 a,b), is that the "650 km" discontinuity is a chemical transition, with the composition above the "650 km" discontinuity being predominantly of the spinel phase (with or without the garnet phase), and the denser perovskite phase below this discontinuity. Anderson (1979b) considers the "650 km" discontinuity as the termination of his proposed eclogite layer which commenced at the "200 km" discontinuity, with a peridotitic mantle composition below the "650 km" discontinuity. Experiments by Yagi, Mao, & Bell (1978), using a technique that carefully calibrates pressure, have indicated that the most likely explanation of the "650 km" discontinuity is the transformation of spinel structure to the pervoskite structure.

The velocity model CAPRI is unable to distinguish between the

various petrological possibilities, but the fact that the velocity increase is thought to be distributed over a depth interval of about 35 km may impose some petrological constraint. If the "650 km" discontinuity represents a chemical change, then it may also represent a barrier to mantle convection, implying the need for at least a two cell structure in mantle convection models.

The first order "750 km" discontinuity of the CAP8 model has been smoothed to a second order type discontinuity in the CAPRI velocity model, because no clear evidence for a strong triplication cusp associated with this feature can be seen in the data. Apart from the observed change in the apparent velocity that occurs in the data at a cross-over of around 2700 km epicentral distance, the resolution of the data at this depth is poor. As with the "200 km" discontinuity, the velocity gradient of this feature is not constrained by comparison of the synthetic seismograms with the data, and the velocity increase has been arbitarily distributed over an interval of 50 km. The present data provide no control over the form of the velocity profile below 750 km, apart from the fact that a more positive gradient is suggested in order to explain the larger amplitudes on the prograde "750 km" branch. Ram Datt and Muirhead (1977), using the Warramunga Seismic Array, have also found evidence for this discontinuity in the upper mantle velocity profile, although they have modelled this discontinuity at a greater depth.

It is clear that as one progresses deeper into the mantle the geophysical and geochemical constraints become less restrictive, and the number of possibile explanations of any feature grows. The "750 km" discontinuity is no exception. Liu (1977a,1980a) has suggested the transformation of Al ilmenite-type solid solution to orthorhombic perovskite structure may be the explanation for this discontinuity, although this interpretation implies that the discontinuity at around 650 km depth is not a chemical change. Alternatively, if the "650 km" discontinuity represents the chemical change with spinel (± garnet) above and rock salt below, then the "750 km" discontinuity may be a chemical change with rock salt above and perovskite below. Yet another interpretation is that the region between the "650 km" and "750 km" features is a zone of mixing between the spinel and perovskite mineralogies. Liu (1980b) has suggested that chemical interactions between the constituent minerals are necessary to explain the large number of discontinuities in the mantle, and this may offer another explanation of

the "750 km" feature.

CHAPTER 8

THE AMPLITUDE OF RETROGRADE BRANCHES IN UPPER MANTLE REFRACTION STUDIES.

8.1 INTRODUCTION.

Synthetic seismograms have recently been used in several studies to provide additional constraints on upper mantle velocity models by comparing the observed amplitudes of short period data with the amplitudes predicted by the synthetic seismograms, (see for example Wiggins & Helmberger 1973, McMechan 1979, Chapter 7). It is obvious when comparing synthetic seismograms with the short period data that the predicted amplitudes of the arrivals on the retrograde triplication branches are significantly larger than the corresponding recorded amplitudes. This is not the case with long period data, as clearly demonstrated by the detailed waveform modelling of Burdick and Helmberger (1978).

Amplitudes of the prograde refraction branches of the synthetic seismograms can be increased relative to the amplitude of the retrograde branches by the introducion of stronger positive velocity gradients between discontinuities; but while this improves the situation, it does not explain why clear arrivals on retrograde branches away from the cusps are not observed in short period upper mantle refraction data.

The relative attenuation of the energy on the retrograde branch can be quantified by considering it as a Q mechanism. In this sense, Q pertains to both the intrinsic attenuation, and the attenuation by other mechanisms such as scattering. Two possible physical explanations of this attenuation have been investigated.

8.2 PHASE TRANSITION ATTENUATION.

It is widely accepted that some upper mantle seismic discontinuities correspond to phase changes in the mantle mineralogy, (Ringwood, 1975; Lui, 1977). A physical mechanism which predicts low Q zones associated with solid/solid phase transitions is the phase relaxation process (Vaisnys, 1968). In a system containing two phases in equilibrium, any increase or decrease in pressure, such as that caused by the passage of a seismic wave, will tend to preferentially move the equilibrium towards the denser or less dense phase, respectively. The relaxation time accompanying this change causes the strain to lag the stress, and this

contributes to the attenuation of the seismic wave.

Vaisnys (1968) has considered this process in detail, and concluded that because the frequency of peak attenuation for the phase transitions (as determined by the kinetics of the reaction) is well below the seismic bandwidth, this phenomenon would be unimportant at seismic frequencies. Jackson and Anderson (1970) reappraised the case, and suggested that the peak frequency for solid/solid phase relaxation may be higher than that of the liquid/solid case, which Vaisnys had used as the analogue. They therefore did not dismiss this mechanism as being incapable of explaining seismic attenuation.

An interesting corollary of the hypothesis that layers of higher attenution accompany phase transitions is that the lower Q of the upper mantle relative to that of the whole mantle is a direct result of the greater number of phase transitions that occur in the upper mantle.

The phase transition mechanism will only be operative over the range of depths in which the two phases are in equilibrium. Of all the observed upper mantle discontinuities, there is general consensus that the "400 km" discontinuity is the result of the transformation of olivine to the beta Mg_2SiO_4 structure. The "400 km" discontinuity in the Australian region is observed to be particularly sharp relative to other upper mantle features, (see Chapter 7). In spite of the large amplitude cusp observed from this discontinuity, the recorded arrivals on the retrograde branch away from this cusp are significantly lower than predicted by synthetic seismograms of derived models. A zone of higher attenuation caused by the co-existence of the alpha and beta olivine phases could be responsible for attenuation of this retrograde energy. On the other hand, there are difficulties in explaining the "200 km" discontinuity in terms of a phase transition, (Ringwood, 1975; see Chapter 9), and Liu (1979) has proposed that the "650 km" discontinuity may be the result of a chemical change, rather than a phase change. It is observed that the relative attenuation of the energy on the retrograde branches from these discontinuities is analogous to that of the "400 km" discontinuity, and this strongly suggests that a similar attenuation process is operative at all the upper mantle discontinuities.

8.3 SCATTERING ATTENUATION.

Cleary, King & Haddon (1975) have considered the mechanism of scattering in relation to the observation of seismic codas, while Cleary

and Haddon (1972) have re-interpreted PKIKP precursors in terms of scattering near the core mantle boundary. Numerous other studies have investigated the phenomena of seismic scattering (see Appendix C of Pilant, 1979). There is no doubt that scattering is an important mechanism in any consideration of mantle attenuation, but while it is easy to attribute some portion of the seismic attenuation to a Chernov-type scattering process, it is more difficult to explain why this mechanism should selectively attenuate the energy on retrograde branches. To do so, the heterogeneity responsible for this scattering, must be causally associated with the discontinuities. Rays from the retrograde branches bottom at, or within, the velocity transition, and hence would have a greater proportion of their energy scattered by heterogeneities at or above this discontinuity than rays which travel through this region in a more vertical path.

Upper mantle seismic discontinuities have been traditionally explained in terms of either phase transitions or changes in chemical composition. In both cases, it is possible that mantle convection is responsible for the generation of heterogeneities near discontinuities. Whole mantle convection is widely concluded to be necessary to explain the observed surface heat flow, (Smith, 1980); but while the whole mantle is most likely to be convecting, it is probable that more than one convection cell is involved.

8.4 APPLICATION OF SYNTHETIC SEISMOGRAMS.

Simpson, Mereu and King (1974) studied a large suite of events recorded at the Warramunga Seismic Array from earthquakes to the north of Australia. When inverting this data, they were able to accurately model the arrival times and slowness values, but found that for any reasonable model, the observed amplitudes of the retrograde branches of the "400 km" and "650 km" discontinuities were notably smaller than predicted by the application of geometric ray theory to the models. To explain this amplitude anomaly, they proposed a model having layers of low Q above these discontinuities, (Mereu, Simpson and King, 1974). The relatively low amplitude of the upper portion of the replicated travel time curve has been verified from a large suite of data recorded from a long range upper mantle refraction profile conducted in Central Australia, (Hales et al.,1976; Hales et al.,1980).

A numerical study has been undertaken to investigate the effect of a zone of higher attenuation associated with a discontinuity, on the

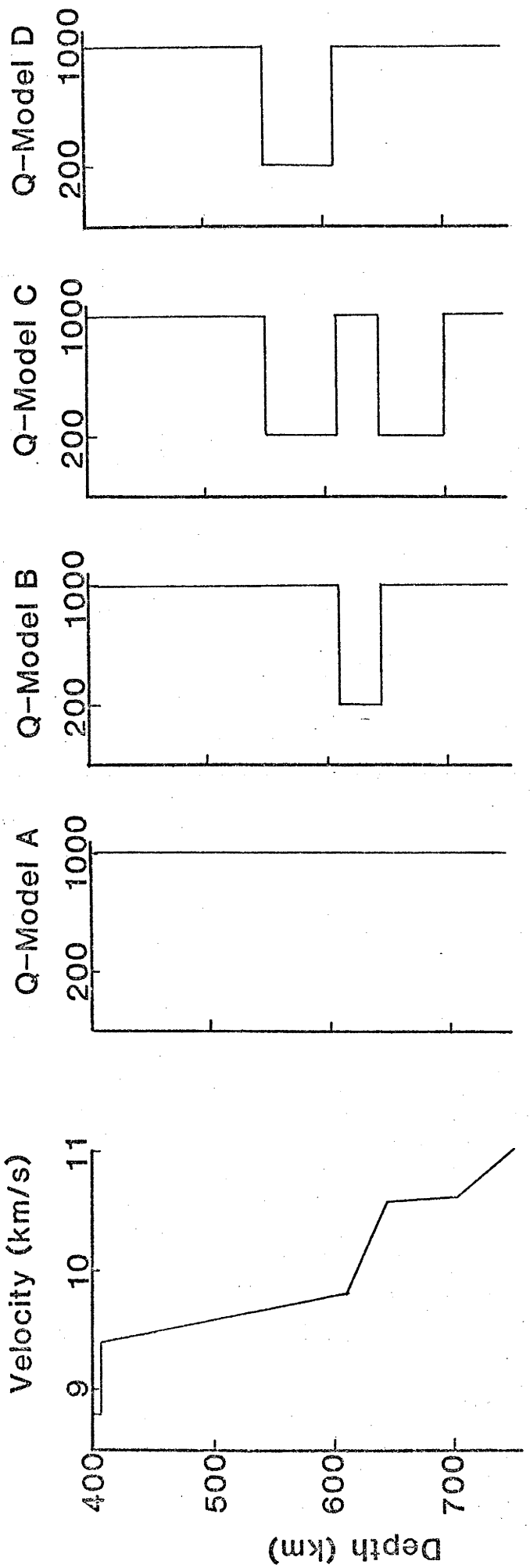

Figure 8.1

The CAPRI velocity model around the "650 km" discontinuity, with the four attenuation models studied.

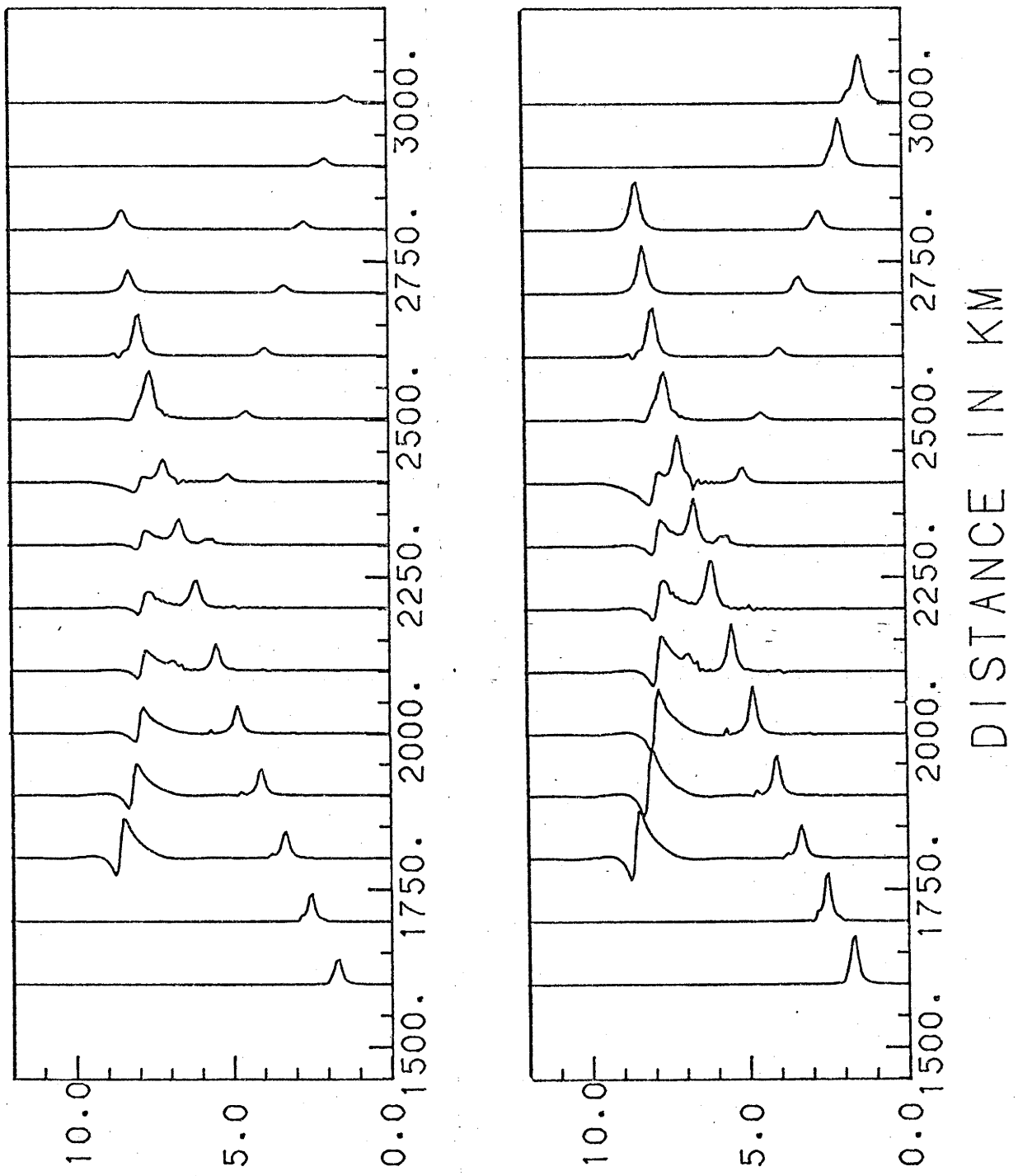

Figure 8.2

A synthetic seismogram of the "650 km" discontinuity of the CAPRI model, calculated by Full Wave theory, using attenuation model A.

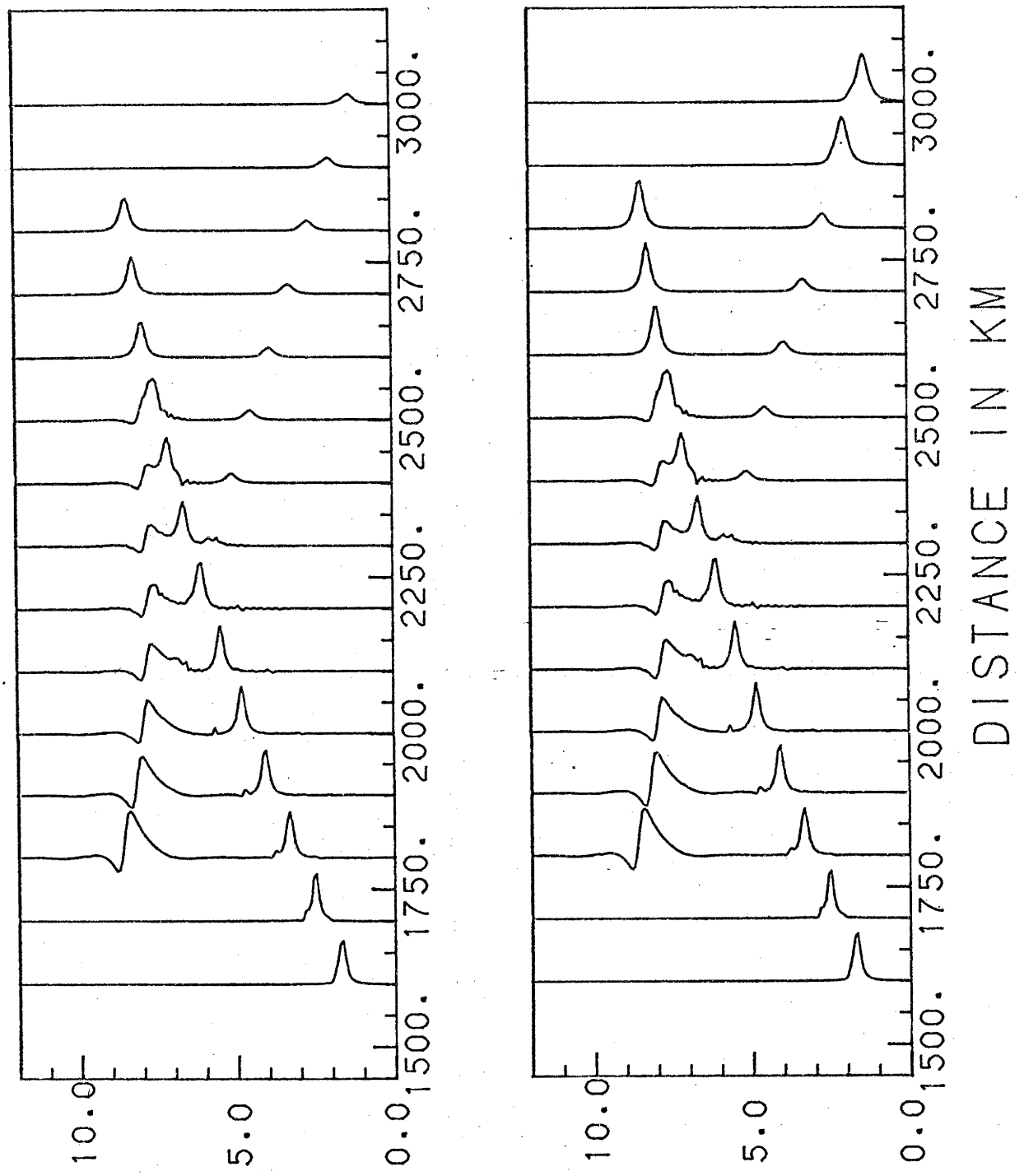

Figure 8.3

A synthetic seismogram of the "650 km" discontinuity of the CAPRI model, calculated by Full Wave theory, using attenuation model B.

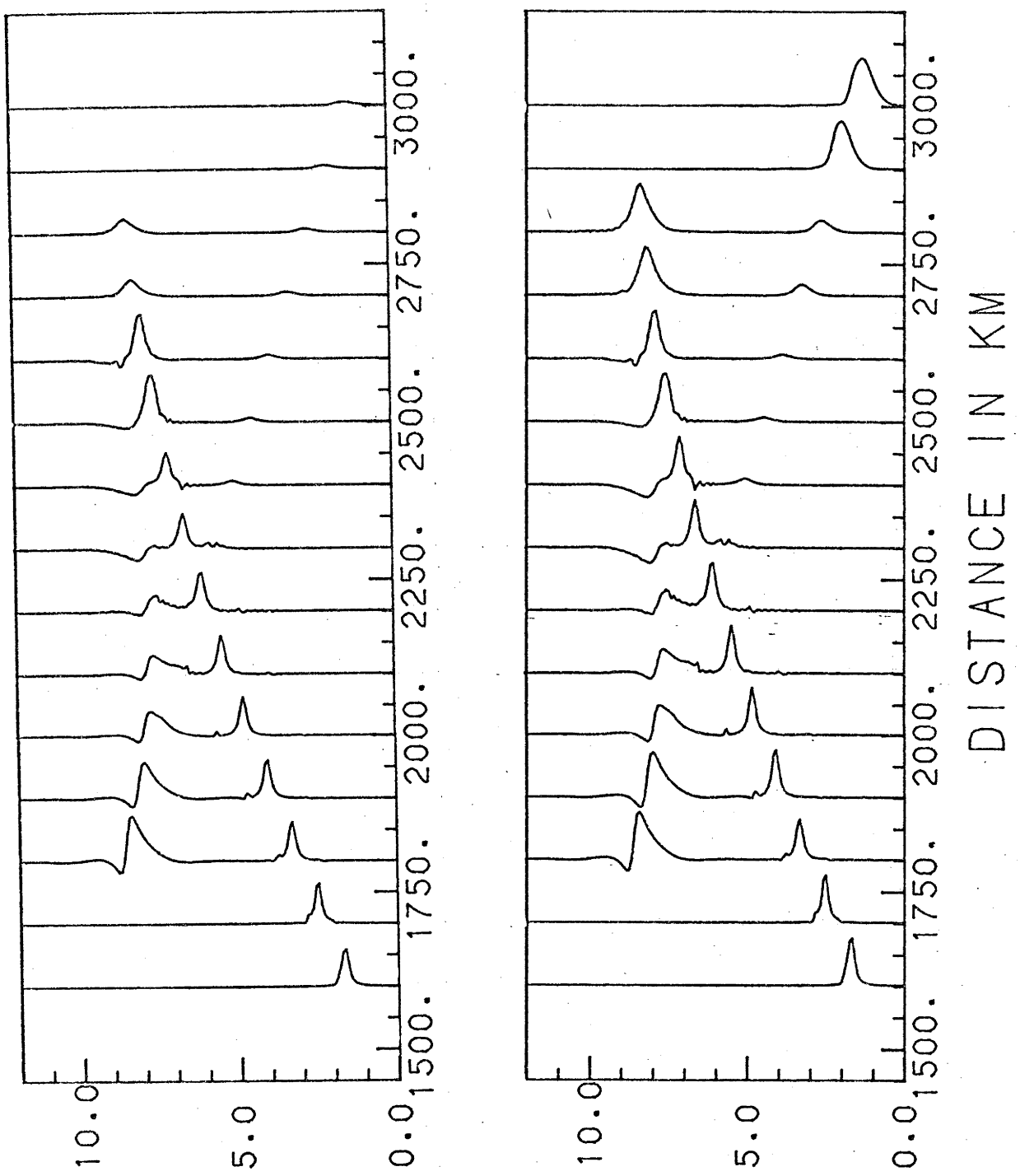

Figure 8.4

A synthetic seismogram of the "650 km" discontinuity of the CAPRI model, calculated by Full Wave theory, using attenuation model C.

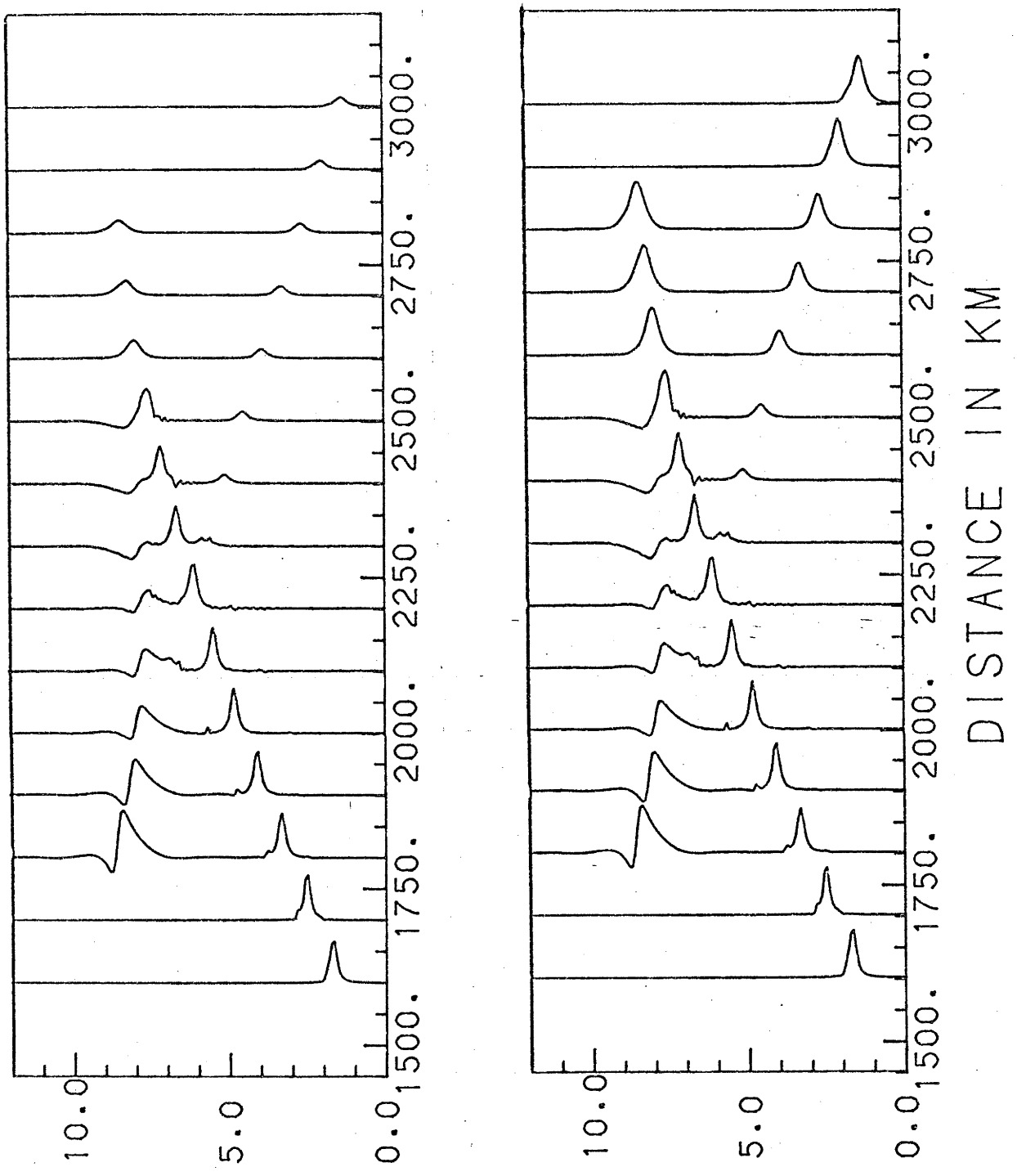

Figure 8.5

A synthetic seismogram of the "650 km" discontinuity of the CAPRI model, calculated by Full Wave theory, using attenuation model D.

relative amplitude of retrograde branches. Figure 8-1 shows the CAPRI velocity profile used for this study, together with the three different Q models which have been investigated. A comparison of the synthetic seismograms (Figs. 8-2 to 8-5) indicates that the model having a low Q zone above the velocity discontinuity produces the highest relative attenuation of retrograde arrivals. The reason for this is that the retrograde rays (BC branch) have a longer transit time through the region above the velocity transition, than within the zone of rapid increase. Along the AB branch, only those rays arriving near B will travel through a low Q zone above the transition, while on the CD branch, the rays travel in a more vertical path through the low Q zone, and therefore suffer relatively less attenuation. The numerical experiment therefore suggests that a region of low Q responsible for the attenuation of the energy on the retrograde branches, most probably lies above the seismic discontinuity.

8.5 DISCUSSION.

The result of the above numerical study argues against the phase transition mechanism being primarily responsible for the observed attenuation of the retrograde branch energy. It is difficult to envisage an attenuation mechanism other than scattering which would be operative above a seismic discontinuity.

Quite different mechanisms would have to be postulated to explain this scattering, depending on whether the discontinuity was a phase or chemical transformation. A phase transformation is unlikely to inhibit convection, (Richter, 1973; Schubert et al.,1975). Stevenson & Turner (1979) have suggested that an endothermic phase transformation to the higher pressure component may actively help mantle convection, creating topographic relief on the discontinuity. The very high viscosity of the mantle material, and semi-infinite Prandtl number of mantle convection suggests that the type of convection involves relatively narrow "plumes" of material convecting around an essentially stable core (see for example Jarvis and McKenzie, 1980). As the downgoing or uprising "plumes" are most likely to be associated with the regions beneath the plate boundaries, it is difficult to explain the existence of topographic relief on seismic discontinuities in the regions away from the plate boundaries, in terms of convection through a phase transition.

A chemical discontinuity, on the other hand, is likely to be a barrier to convection, and hence a boundary layer for the mantle convection

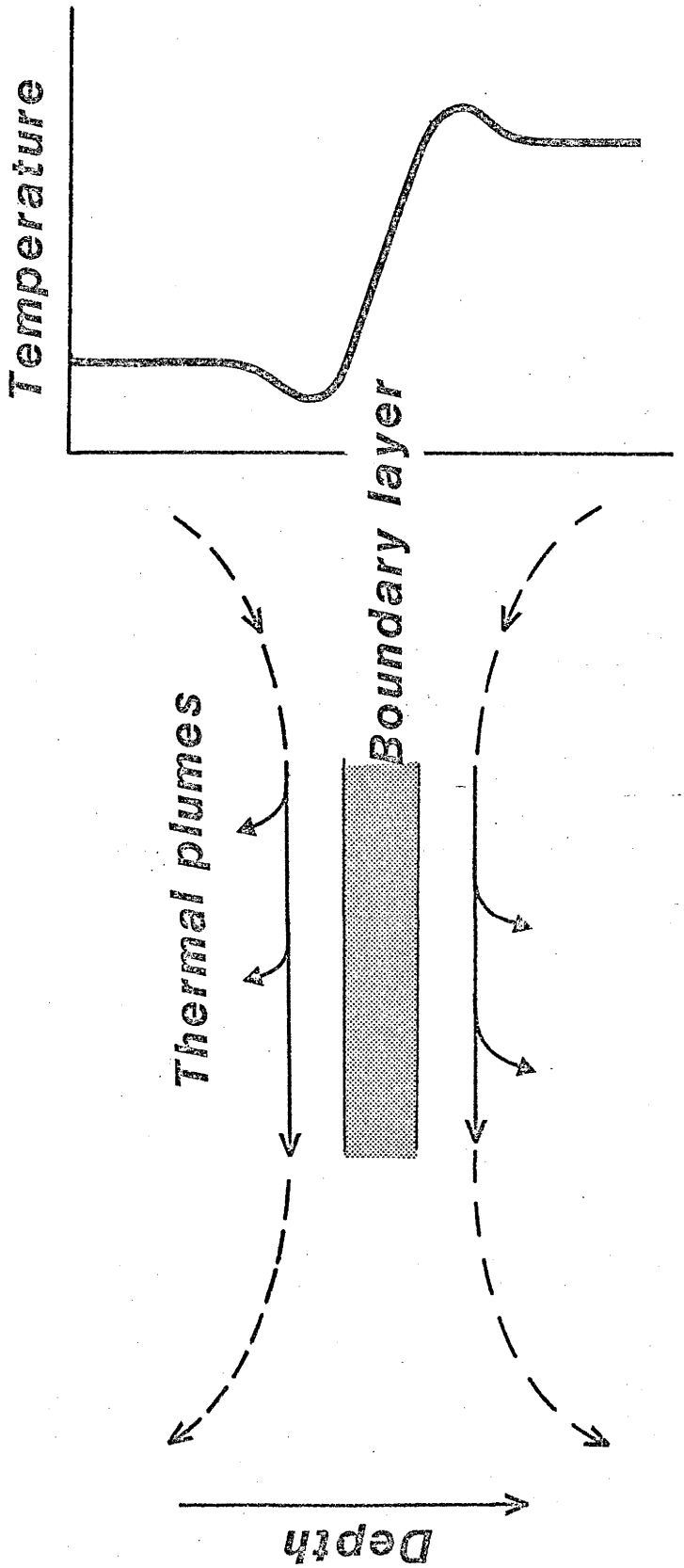

Figure 8.6

A schematic diagram of the formation of thermal plumes at the boundary layer of a chemical discontinuity.

cells. Figure 8-6 sketches the convective flow at the boundary layer of a chemical discontinuity, and the associated thermal profile. The thermal gradient across the boundary layer is super-adiabatic, but is stabilized by the density distribution resulting from mixing. Above and below this boundary layer, two marginally stable layers exist. Linden and Shirtcliffe (1978) suggest that "blobs or thermals arise on the outer edge" of these layers. A photographic example of this phenomenon observed in a model experiment can be seen in Fig. 3b of Griffiths (1979). It is interesting to note in this context that Busse (1979) states "Howard's (1966) mechanism for the onset of an oscillatory instability of the thermal boundary layers at the top and bottom boundaries of a convection layer is the only mechanism discussed in the literature that could operate in the limit of infinite Prandtl numbers". The formation of these incipient plumes may explain the relative attenuation of the energy on the retrograde branches.

However, not all upper mantle seismic discontinuities are considered to be chemical discontinuities, and a seismic discontinuity caused by a phase transition would not be expected to develop a similar boundary layer structure. This hypothesis does not explain the attenuation of the energy on the retrograde branches from seismic discontinuities caused by a phase transformation. However, phase transformations are sensitive to the exact composition of the mantle material, and small local variations of mantle mineralogy could account for some "topography" on a phase discontinuity.

The numerical modelling suggests that the optimum location of the low Q region responsible for the attenuation of the retrograde energy is above the discontinuity. However, fluid dynamic experiments have demonstrated that these thermal "blobs" form both above and below the convective boundary layer. Clearly further numerical and experimental modelling will be required to explore the extent to which the production of scattering heterogeneities by convective instability is operative in the upper mantle. The cause of this attenuation will have to be more fully understood before waveform modelling can be successfully applied to short period data.

CHAPTER 9

UPPER MANTLE ANISOTROPY AND LITHOSPHERIC DECOUPLING

9.1 INTRODUCTION.

It has been suggested by several authors that the lithosphere underlying continental shield regions extends to depths of the order of 200 km. It has been postulated (Ringwood, 1962 Jordan, 1975, 1978) that the lithosphere (tectosphere) beneath stable continental shields is depleted in low melting point components, is cooler than the normal mantle material at this depth, and hence would translate with the continental plates by virtue of its higher viscosity and lower density. Body and surface wave studies of the upper mantle structure beneath shield regions have not indicated any significant low velocity zone above a depth of 200 km. A detailed study of the shear wave velocity structure beneath the Australian shield by Hales, Muirhead & Rynn (1980b) has not found evidence for any region of low shear wave velocity above a depth of 150 km.

Lehmann (1959,1962) first postulated the existence of a seismic discontinuity in the upper mantle at a depth of around 200 km. This feature has subsequently been observed in many upper mantle refraction surveys, commonly at depths shallower than 200 km. Anderson (1979a) has named this upper mantle feature the Lehmann discontinuity. Hales (1977) suggested that the relative motion of the Australian continental lithosphere over the underlying mantle material occurs "below a discontinuity in the P wave velocity at a depth of about 200 km". As it is observed that continents can move with velocities comparable to oceanic plates, the question that must be answered is where this zone of relative motion of the continental lithosphere over the underlying mantle occurs, and what is the relation of the "200 km" discontinuity to this zone.

9.2 SEISMIC OBSERVATIONS.

Hales et al., (1980a) have analysed the data obtained from a long range upper mantle refraction profile conducted in Central Australia. The upper mantle velocity model (Model 8) derived from this analysis has a velocity discontinuity at a depth of 200 km, with an increase in the compressional wave velocity of 0.38 km/s. The depth of this feature has been constrained by the recorded arrivals of an event on the 14th October

1977 (Event #256). The record section (Figure 9-1) of this event, which has been located by the ISC in the depth range of 176 ± 5 km, on the basis of 164 readings, clearly indicates that the "200 km" discontinuity is significantly below 176 km depth. The method of Gutenberg (1953) constrains the velocity at the source depth of this event to be less than or equal to 8.28 km/s. Beneath the "200 km" discontinuity, the velocity is well constrained by this and other events to be 8.62 km/s, indicating that a velocity increase across the "200 km" discontinuity is in excess of 0.3 km/s.

The "200 km" prograde refraction branch, corresponding to rays which bottom below the "200 km" discontinuity, shows an abrupt decrease in amplitude at an epicentral distance of around 1700 km (depending on the source depth). Figure 12 of Hales et al.,(1980a) shows a fit of the travel time distance curve derived from their model 5, to the record section for event 256. Model 5 did not incorporate any discontinuous increase in velocity around a depth of 200 km, so that this figure serves to indicate the ease with which the "200 km" discontinuity can remain undetected, especially in studies employing only shallow events. Hales et al., (1980a) have modelled the "200 km" structure as a velocity "knee" with a layer having a negative velocity gradient below. Using synthetic seismograms to model amplitudes, it has been shown (Chapter 7), that the amplitude decay of the "200 km" prograde branch can be explained by a low velocity zone which commences more sharply, around 30 km beneath the "200 km" discontinuity. The exact nature of the velocity profile within the low velocity zone cannot be determined from the present refraction data. However, the synthetic seismogram modelling indicates that the negative velocity gradient commencing at a depth of 230 km must be sharper than that of the Hales et al., (1980a) model, in order to explain this rapid decrease in amplitude near 1700 km distance.

A sharp velocity increase at a depth of around 200 km, followed beneath by a velocity decrease, is a peculiar seismological feature. Similar "knees" in the velocity models of other upper mantle studies can be found - but usually at shallower depths. Lewis and Meyer (1968) have a comparable structure at a depth of around 130 km, while in the model of Wiggins and Helmberger (1978), this structure is at a depth of around 150 km. The abrupt decrease in amplitude of the "200 km" branch has also been observed in other upper mantle refraction profiles, although the low velocity zone which is implied by this decrease has not been incorporated

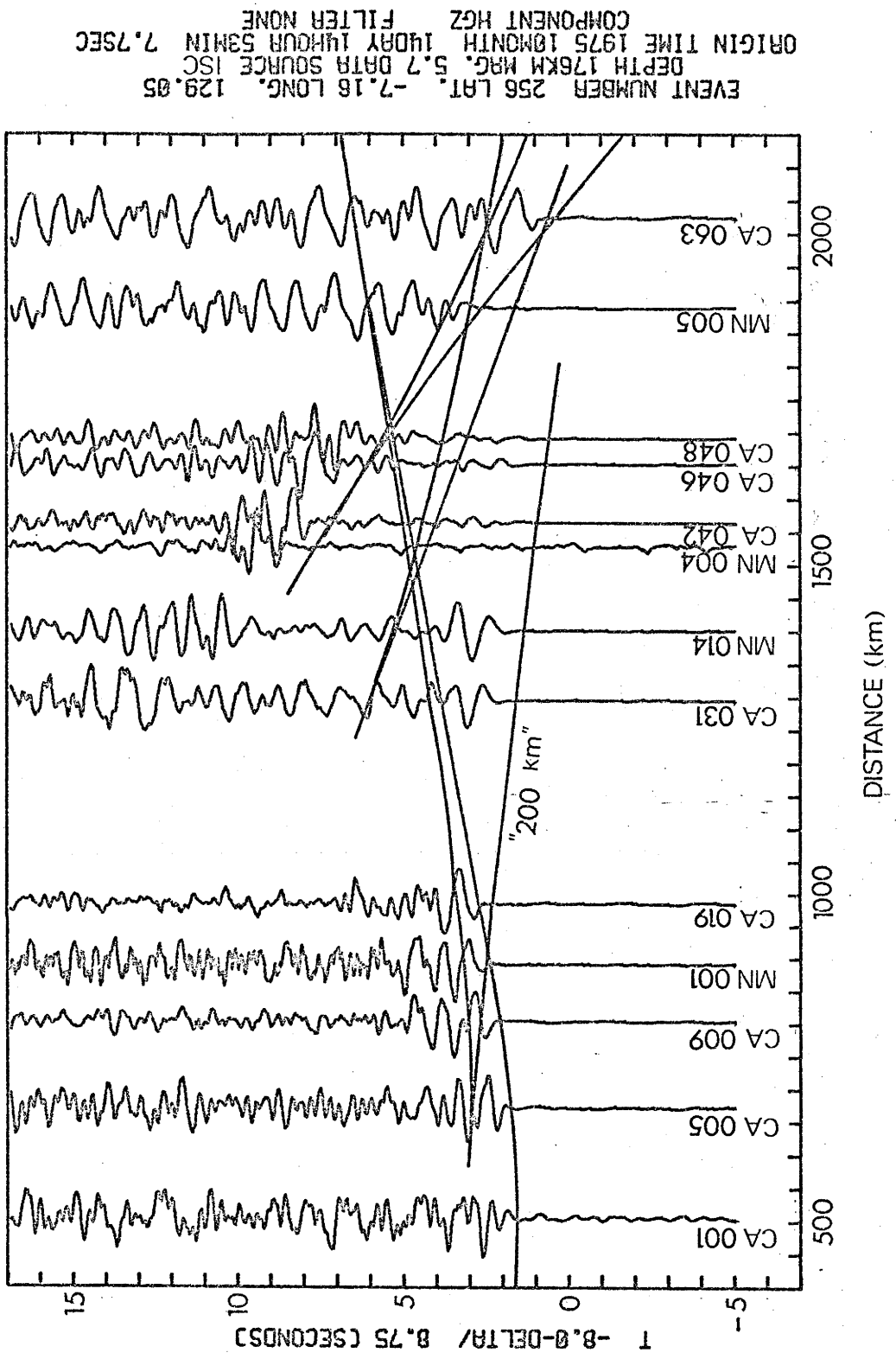

Figure 9.1

Vertical component record section of event 256 from the Banda Sea arc, with the travel time curve of CAP8 superimposed. The branch labelled "200 km" corresponds to rays refracted below the "200 km" discontinuity. This branch displays a rapid decrease in amplitude beyond an epicentral distance of 1,400 km, corresponding to the onset of a negative velocity gradient beneath the "200 km" discontinuity (see Figure 2).

in the models resulting from these studies. Examples of this abrupt decay in the amplitude of the prograde "200 km" branch can be clearly seen in Figure 8 of Masse et al., (1972) and in Figures 11 and 12 of Johnson (1967). It is, however, interesting that no convincing evidence of this type of velocity structure has been observed in the data of any of the Early Rise Experiment profiles, (Warren et al., 1968), which traverse North America with an excellent coverage of azimuth.

Further seismological support for the existence of a negative velocity gradient around 200 km depth has been obtained from the S to P conversion evident in records from teleseismic events. Sacks et al., (1979) have studied these converted phases recorded at the NORSAR array, and have interpreted precursors to the S onset as being S to P conversions from a negative velocity gradient at a depth of 250 ± 15 km.

Long range refraction surveys for oceanic paths have also indicated a similar velocity structure, but at a considerably shallower depth. Both Asada & Shimamura (1976) and Hales et al., (1970) have an analogous feature in the velocity models derived from oceanic refraction surveys. These velocity models both have a discontinuous jump to a compressional velocity of around 8.6 km/s, followed beneath by a low velocity zone, with the depth of this "knee" in both cases being around 75 km. Leeds and others (1974,1975) have derived a model for the variation of the lithospheric thickness over the Pacific basin from surface wave studies. Their model indicates a thickening of the oceanic lithosphere from around 76 km in the younger regions, to 104 km in the older regions of the oceanic basin.

9.3 CONVENTIONAL INTERPRETATIONS - A REVIEW.

Traditionally, seismic discontinuities in the Earth's mantle have been explained in terms of isochemical changes in mineralogy, changes in chemical composition, or a combination of both. Such phenomena of possible relevance to a consideration of the "200 km" discontinuity are reviewed below.

(i) Exsolution of $M_3^{2+}Al_2Si_3O_{12}$ (M=Mg,Fe,Ca) garnet from aluminous pyroxenes.

The pressure-sensitivity of the Al_2O_3 content of pyroxenes coexisting with garnet provides the basis of pyroxene geobarometry, and accordingly has been widely studied, (see MacGregor, 1979; and Akaogi & Akimoto, 1979 for recent reviews). Along the 1200° C isotherm, for

example, the Al_2O_3 content of orthopyroxene coexisting with garnet in both synthetic and natural systems decreases, rather rapidly from 5-7% near 2.5 GPa (25 kbar) to 1.5-2.5% near 4 GPa, and then more gradually to ~0.7% at 7 GPa and 0.4% in Ca-poor clinopyroxene at 14 GPa (Akaogi & Akimoto, 1979). However, Green and Ringwood (1962, see also Ringwood, 1975) have shown that the orthopyroxene Al_2O_3 isopleths in the garnet pyrolite stability field are sub-parallel to the Clark and Ringwood (1964) Precambrian shield geotherm - suggesting approximate constancy (at the 1.0-1.5% level) of orthopyroxene alumina content over the 2-5 GPa pressure range. The low alumina content of such orthopyroxene and the evidence for its gradual reduction with increasing pressure beyond 5 GPa exclude any possibility that exsolution of pyrope-rich $M_3^{2+}Al_2Si_3O_{12}$(M=Mg, Fe, Ca) garnet from aluminous orthopyroxene is responsible for the discontinuous increase in compressional wave velocity near 200 km depth.

(ii) Formation of complex $M_3^{2+vi}(Al_2)Si_3O_{12}$ - $M_3^{2+vi}(MSi)Si_3O_{12}$ garnet solid solutions.

The formation of dense garnet solid solutions containing substantial proportions of octahedrally coordinated silicon was first demonstrated by Ringwood (1967, see also 1975) and has been further studied by Akaogi and Akimoto (1977,1979). Ringwood's study of the crystallisation of a glass of 90% $MgSiO_3$-10%Al_2O_3 composition revealed a rapid increase in both the garnet lattice parameter and the proportion of garnet near 10 GPa. More recent work of Akaogi and Akimoto (1977) confirms the high pressure solubility of $MSiO_3$ pyroxene in the garnet structure, but suggests that such solution occurs gradually over the pressure range 4-14 GPa (40-140 kbar), with a pronounced increase in the proportion of garnet (and hence the density and P-wave velocity) in the 14-19 GPa pressure interval. The fact that the garnet lherzolite nodules of deepest origin (~200 km depth, 7 GPa pressure) brought to the Earth's surface by the Lesotho (see Akaogi & Akimoto, 1979), Kao (MacGregor, 1979) and other kimberlite pipes contain 3.02-3.07 silicon atoms per 12 oxygen atoms provides marginal evidence for the initiation of $M_3^{2+}(Al_2)Si_3O_{12}$ - $M_3^{2+}(M^{2+}Si)\ Si_3O_{12}$ solid solution near this depth. There is, however, no indication from either the laboratory experiments or the garnet bearing nodules of any abrupt increase in the $M_3^{2+}(M^{2+}Si)Si_3O_{12}$ content of garnet near 200 km depth in the Earth's mantle. This observation, together with the absence of other mineralogical changes in garnet lherzolite in the relevant pressure range, suggests that

phase transformations are not responsible for the rapid increase in P-wave velocity near 200 km depth in the continental mantle.

(iii) Compositional change: harzburgite to garnet lherzolite.

The long and complex geochemical history of sub-continental uppermost mantle, the geochemistry of ultramafic nodules from kimberlite pipes, and the absence of significant seismic low-velocity zones beneath Precambrian shields all suggest that the sub-continental uppermost mantle is likely to be strongly (but somewhat variably) stripped of its low melting-point fraction. Under these circumstances, a transition would be expected, perhaps near 200 km depth, from barren harzburgite above, to fertile garnet lherzolite below (e.g. Ringwood, 1966,1975). The densities and P-wave velocities for these assemblages have been estimated to be 3.31 g/cm^3 and 8.32 km/s for harzburgite and 3.38 g/cm^3 and 8.38 km/s for pyrolite (Ringwood, 1966,1975). More recently, Jordan (1979), in a comprehensive review of the density and elasticity of garnet lherzolites, has shown that removal (by 20% partial melting) of the basaltic fraction of pyrolite, decreases the density of the residium by $\sim$ 0.05 g/cm^3, but leaves the P-wave velocity almost unchanged. The small change in P-wave velocity accompanying such differentiation is due to the near-cancellation between the velocity decrease associated with garnet removal and the velocity increase associated with the more magnesian composition of the residual olivine and orthopyroxene (Jordan, 1979).

It is quite clear that, although the sub-continental upper mantle must be chemically zoned as a result of differentiation, there is virtually no possibility that a P-wave velocity discontinuity of order 0.3 km/s near 200 km depth, can be explained in these terms.

(iv) Compositional change: garnet lherzolite (or harzburgite) to eclogite.

Anderson (1979a,b) has recently suggested that the Lehmann discontinuity might represent a change in chemical composition from garnet lherzolite (or harzburgite) above the discontinuity to eclogite below.

Compressional-wave velocities for mantle-derived eclogites measured by Kanamori and Mizutani (1965), Christensen (1974) and Manghnani et al. (1974 - samples 11, 14 and 15) span the range 8.27-8.50 km/s at 1.0 GPa (10 kbar) with anisotropy being less than 2%. Shear wave velocities are more variable (4.49-4.86 km/s at 1.0 GPa). The Nové Dvory (Czechoslovakia) eclogite studied by Christensen to 3.0 GPa is representative of the highest

P-wave velocity (most jadeitic pyroxene) eclogites with ρ=3.56 g/cm^3 V_p=8.33 km/s and V_s=4.59 km/s at standard temperature and pressure.

For comparison, our preferred parameters for garnet pyrolite are ρ=3.40 g/cm^3, V_p=8.31 km/s and V_s=4.82 km/s (these differ slightly from those of Jordan (1979) as a consequence of our use of pyrope elastic moduli measured by Leitner et al., (1980).

Our analysis thus strongly reinforces the observations of Kanamori and Mizutani (1965), Ringwood (1975), and Anderson (1979a) concerning the indistinguishability of garnet lherzolite and eclogite P-wave velocities. We conclude that a change in chemical composition from garnet lherzolite to eclogite might produce a significant decrease in shear wave velocity but that no discernible change in compressional wave velocity would be expected. Under these circumstances, we see no possibility that the Lehmann discontinuity reflects a chemical change of this type.

(v) Base of pronounced low-velocity zone

Many seismic models for upper mantle velocities beneath tectonically active continental regions (such as the western United States) include a substantial rapid increase in seismic wave velocities in the depth range 150-200 km (e.g. Archambeau et al., 1969; Helmberger and Wiggins, 1971). In most such models, the discontinuity represents the base of a pronounced low-velocity zone, so that a large part of the velocity contrast across the discontinuity is accounted for by a return to "normal" upper mantle velocities, (e.g. at substantially subsolidus temperatures) below the discontinuity. The previously mentioned (Section 2) absence of significant low-velocity zones, shallower than 200 km depth, beneath Precambrian shield regions precludes such an interpretation of the Lehmann discontinuity.

9.4 SEISMIC WAVE VELOCITIES FOR GARNET PYROLITE

The arguments presented above clearly demonstrate the difficulty of accounting for the observed 0.3 km/s increase in V_p at $\sim$200 km in terms of any of the conventional explanations. In order to proceed further in understanding the nature of the seismic feature near 200 km depth, we now compare the CAPRI velocity-depth model (Chapter 7) with calculated P-wave velocities for an assumed garnet pyrolite upper mantle.

For purposes of this calculation, the following procedure was adopted.

(i) A compressional-wave velocity (V_p) of 8.31$\pm$0.05km/s at STP was

employed.

(ii) It was assumed that V_p varies linearly with pressure (to $\sim$10 GPa) and temperature (to $\sim$1400° C). Since volumetric strains will be no greater than 8% at 10 GPa, the use of finite strain equations of state should not be strictly necessary. The general tendency for both pressure and temperature derivatives of the elastic wave velocity to decrease with increasing pressure and temperature suggests that linear extrapolation, using derivatives measured near STP, may result in slight over-estimation of velocities at the upper end of the extrapolation. Any relaxation of ultrasonically determined shear moduli for upper mantle seismic wave propagation would similarly result in an over-estimation of the seismic velocities.

The pressure and temperature derivatives, used in the calculation,

$\delta V_p/\delta P = 0.106$ km/s/GPa

$\delta V_p/\delta T = -0.55 \times 10^{-3}$ km/s/K

represent a weighted average (57% olivine, 17% orthopyroxene, 12% clinopyroxene, 14% garnet) of the mineral pressure and temperature derivatives. Christensen's (1974) data for Stillwater bronzitite ($\delta V_p/\delta P$ = 0.137 km/s/GPa) are used in preference to the much higher value $\delta V_p/\delta P$ = 0.207 km/s/GPa derived from the single-crystal study of Frisillo and Barsch (1972). The latter value is grossly inconsistent with the expectation (Birch, 1969) that $(1/V_p)(\delta V_p/\delta P)$ be approximately equal to

$$\frac{39K + 16\mu}{6K(3K + 4\mu)}$$

This relation yields an expected $\delta V_p/\delta P$ of 0.138 km/s/GPa - in excellent agreement with Christensen's value. Furthermore, even if the unusually large single-crystal pressure derivatives (dK/dP = 9.6!) were, in fact, appropriate at STP, it seems highly improbably that such a high derivative would be maintained over a substantial pressure range. The use of the Frisillo and Barsch data for orthopyroxene (see Hales et al., 1980) would increase the garnet pyrolite $\delta V_p/\delta P$ to 0.128 km/s/GPa and hence raise the velocity at 200 km depth by approximately 0.14 km/s. Further experimental work on single-crystal and polycrystalline orthopyroxene is clearly necessary for resolution of this uncertainty. Olivine and garnet pressure and temperature derivatives were drawn from the work of Kumazawa and Anderson (1969), Graham and Barsch (1969), and Bonczar et al., (1977). A clinopyroxene ($\delta V_p/\delta P$) of 0.119 km/s/GPa was obtained by comparison of

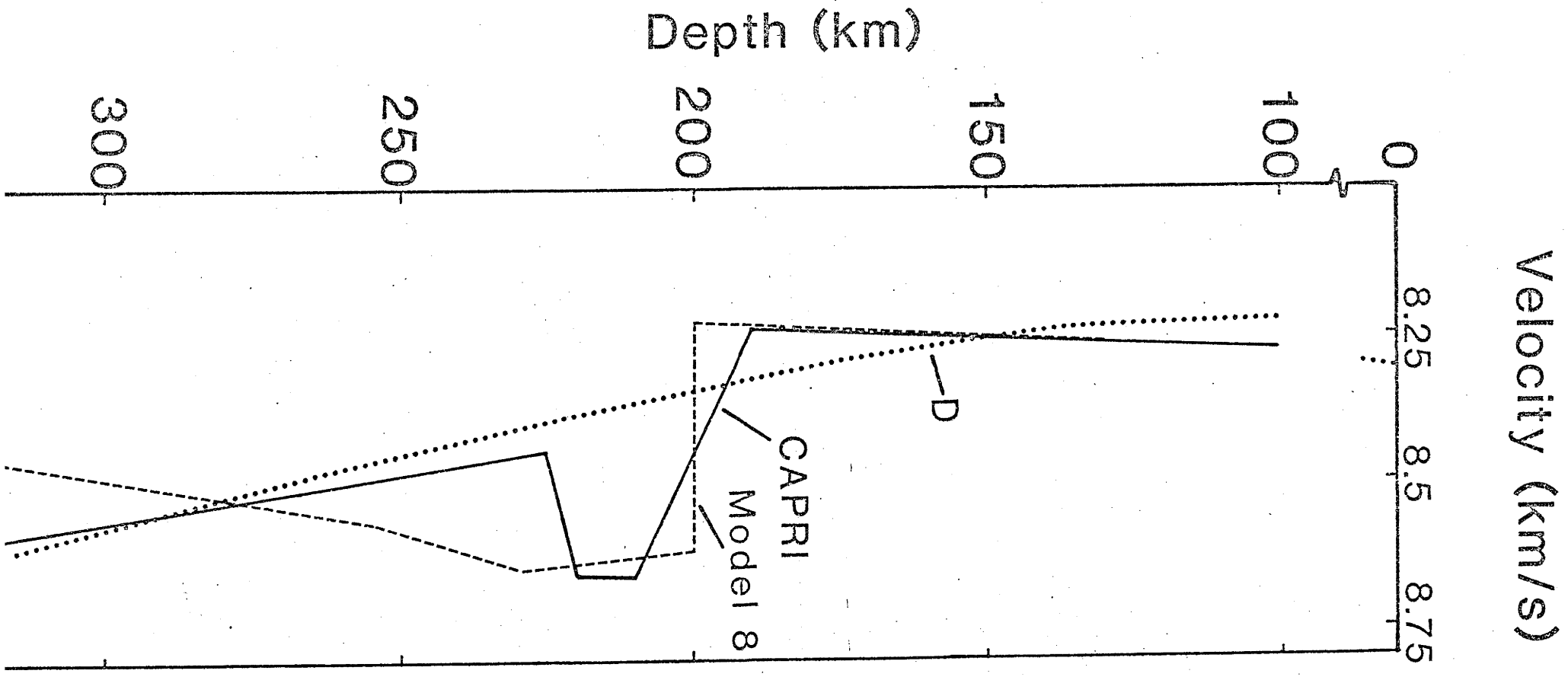

Figure 9.2

A comparison of the CAP8 and CAPRI compressional wave velocity-depth models with calculated velocities (D) for a garnet pyrolite upper mantle based on the geotherm presented in the text.

Christensen's (1974) data for Novè Dvory eclogite with the Bonczar et al. data for garnet. Otherwise, it was assumed that the orthopyroxene derivatives are appropriate for clinopyroxene.

(iii) Initial calculations employed the geotherm of Harte (1978) which is said to be consistent with a wide variety of geophysical and geochemical observations. The resulting compressional-wave velocity profile was broadly consistent with the CAPRI model in the 75-190 km and 225-320 km depth ranges but failed to explain the high velocities in the 190-225 km interval. Variation of the geotherm within reasonable limits (e.g. Jordan, 1979) allowed a more satisfactory fit ("D", Fig. 9-2) to the CAPRI velocities in the 75-190 km and 225-320 km depth ranges. The required geotherm,

depth (km)	temperature (degrees C)
100	770
150	1050
200	1180
250	1320
300	1420

is intermediate between, and qualitatively similar to, Jordan's (1979) S1 and S2 conductive geotherms, and would intersect adiabats for the oceanic upper mantle at depths between 300 and 400 km.

The clear implication of the comparison presented in Fig. 9-2 is the adequacy of a garnet pyrolite composition and mineralogy combined with a reasonable geotherm as an explanation of compressional-wave velocities for all but a narrow interval (190-225 km) of the 75-300 km depth range. Similar difficulties in explaining high velocities just below 200 km are evident in the studies of Graham (1970, Fig. 3), and Ahrens (1973) who noted that none of his calculated models "predict the 8.65 km/s P-velocity maximum ... at 200 km depth in profile HWNE" (of Wiggins and Helmberger, 1973). Likewise, Green and Liebermann (1976, pp.87-88) comment on the difficulty of explaining compressional wave velocities >8.5 km/s in some seismic models of the oceanic lithosphere, in terms of the calculated elastic properties of petrologically appropriate isotropic aggregates.

It should be noted, in passing, that the match between the calculated velocities and the CAPRI model, other than in the 190-225 km depth range, precludes neither a more barren harzburgitic chemistry above

200 km, nor a gradual increase in the $M_3^{2+}(M^{2+}Si)Si_3O_{12}$ component of the garnet with increasing depth below 200-250 km.

9.5 SEISMIC VELOCITY ANISOTROPY?

It is clear from this comparison and the discussion of Section 2 that we are concerned, not with a seismic discontinuity in the usual sense, but rather with a zone of order 50 km in thickness, characterised by higher velocities than both overlying and underlying mantle.

In section 3, the difficulty involved in explaining the 0.3 km/s velocity increase near 200 km, in terms of mineralogical or chemical changes, was demonstrated. The decidedly negative velocity gradient below 230 km is equally difficult to explain in conventional terms. In Chapter 7 it has been inferred that this velocity gradient must be more negative than that (dV_p/dz = -0.002 km/s/km) of Hales et al., (1980) in order to produce synthetic seismograms consistent with the observed rapid decrease in first arrival amplitudes near Δ = 1700 km. Using P-wave velocity pressure and temperature derivatives appropriate for garnet pyrolite (section 4), we find that an improbably large temperature gradient, of at least 9° C/km, would be required if the negative velocity gradient of CAP8 were to be explained in terms of the combined effects of pressure and temperature.

On the other hand, this sub-continental "high-velocity zone" bears a strong qualitative resemblance (see Section 2) to shallower high velocity lids capping low-velocity zones in many velocity models for the sub-oceanic upper mantle. These considerations, and the variability of its observation (Section 2), suggest that this unusual seismic feature might be explained in terms of seismic velocity anisotropy associated with deformation-induced preferred orientation of olivine (and possibly orthopyroxene) crystals in a shear zone, at 200-250 km depth, which is responsible for decoupling of the continental lithosphere from the underlying mantle. Support for this hypothesis derives from the following observations:

(i) Extensive field and laboratory studies of deformed peridotites from the Lanzo massif in Northern Italy, (believed to represent sub-continental mantle), have established a firm relationship between the observed 7% velocity anisotropy, the fabric and the flow coordinates (see Peselnick et al., 1974, Nicolas and Poirier (1976), and references therein). The velocity anisotropy is associated with a preferred orientation of the fast 100 axes of olivine crystals at a low inclination ($\sim$10°, Fig. 9-4) to the flow direction during high temperature (1200° C)

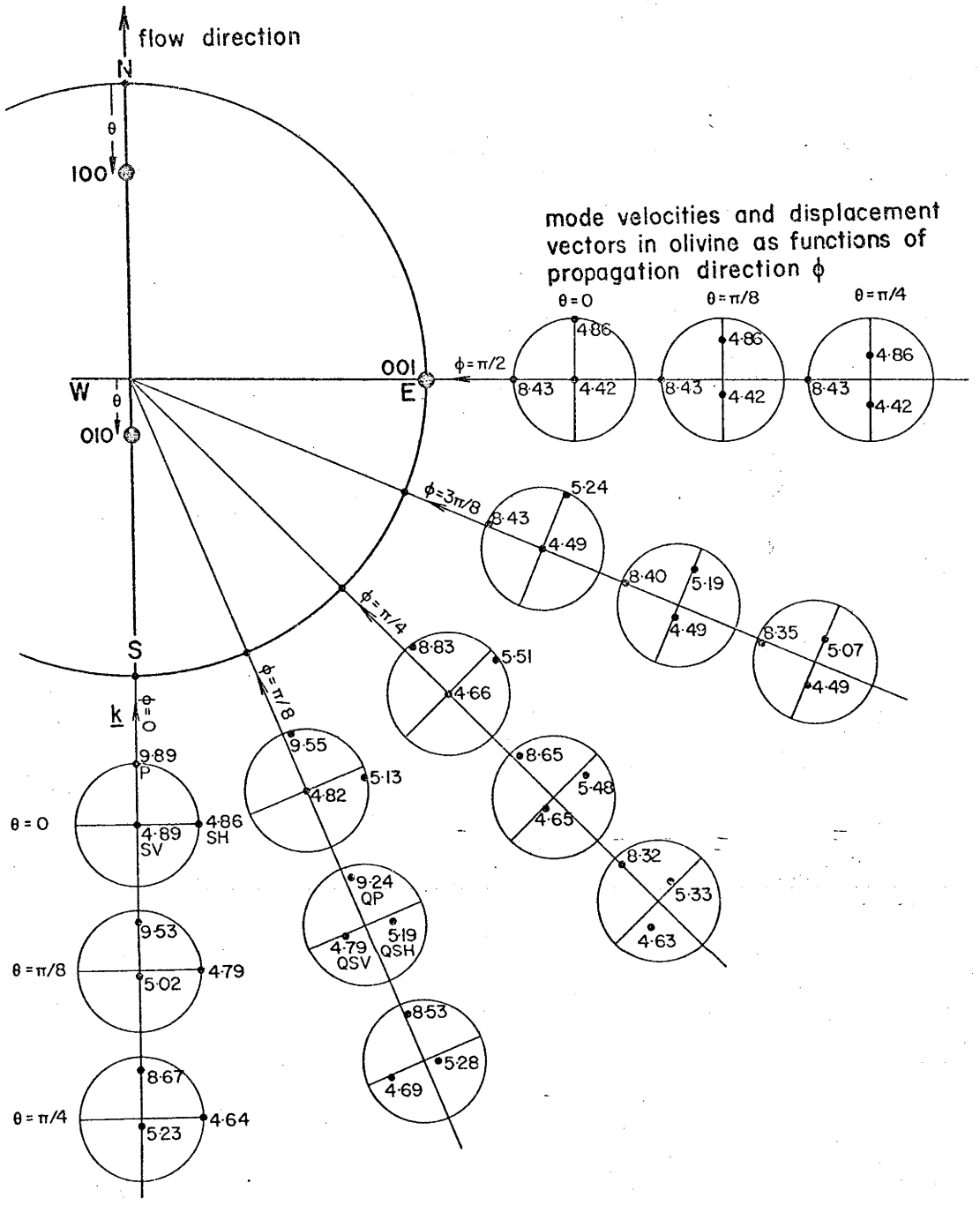

Figure 9.3

Seismic anisotropy and shear-wave birefringence of olivine. The crystal orientation is the expected preferred orientation of olivine (see text) in the Australian upper mantle: flow plane horizontal, plate movement over underlying mantle due North. The olivine C-axis (001) lies East-West while the inclination θ of the a-axis (001) to the flow direction is varied between 0 and π/4 (see text). Mode velocities and displacement vectors for horizontal propagation vectors k are calculated as functions of azimuth φ and inclination θ from the single crystal moduli of Kumazawa and Anderson (1969). The particle displacement vectors for the three independent propagation modes for each (φ,θ) pair are plotted (dots) on a stereographic projection and labelled with the appropriate velocities (in km/s). It is important to note that off-axis propagation directions involve modes for which particle displacement is neither parallel nor orthogonal to the propagation vector. Such coupled modes are labelled QP, QSH, QSV (Crampin, 1977). The results may be applied in the SW quadrant by virtue of the mirror symmetry of olivine about the plane normal to 001.

deformation at an inferred strain rate of 10^{-14}/s.

(ii) Experiments conducted over a wide range of temperature and strain rate (Ave Lallemant and Carter, 1970; Nicolas et al., 1973; Ave Lallemant, 1975; Nicolas and Poirier, 1976) have demonstrated the development of strong preferred orientation of olivine ([010]$||\sigma_1$ and [100]$||\sigma_3$) as a consequence of laboratory deformation of dunite. At high temperatures and moderate strain rates (moderate flow stress), the preferred orientation appears to be derived primarily from syntectonic recrystallisation driven by strain accumulation, due principally to dislocation glide on the system (010)[100]. The coincidence of principal axes of stress and strain in most laboratory deformation experiments (e.g. Ave Lallemant and Carter, 1970; Ave Lallemant, 1975) results in an ambiguity concerning predicted fabric orientation in the field which may resolve the apparent conflict between the orientations of the natural and laboratory fabrics mentioned above.

(iii) Studies of the azimuthal variation of compressional-wave velocities in the oceanic upper mantle (e.g. Hess, 1964; Raitt et al, 1969) have established beyond doubt the velocity anisotropy of the sub-oceanic mantle. The fast direction in each case is sub-parallel to the spreading direction i.e. normal to the mid-ocean ridge. The azimuthal range in Pn velocities ($\sim$ 0.3 km/s) and the association of fast velocities with the direction of plate movement over underlying mantle are both appropriate for explanation of the high P-wave velocities at 200-250 km depth along a north-south profile beneath the Australian plate (Fig. 9-3).

(iv) The seismic implications of the development of such an olivine preferred orientation are more fully explored in Fig. 9-3. For small inclinations of the fast [100] axis to the flow direction (N), propagation directions within 45 degrees of the flow direction display compressional (or quasi-compressional) mode velocities significantly higher than 8.42 km/s which is the Voigt-Reuss-Hill (VRH) average. Also noteworthy is the considerable shear wave birefringence - the difference in quasi-shear mode velocities being as great as 0.7km/s for some propagation directions. Thorough characterization (Babuska, 1972) of an essentially monominerallic sample of Twin Sisters dunite with a strong preferred orientation revealed a high degree of seismic anisotropy ($7.98<V_p<9.24$ km/s, $4.57<V_s<5.01$ km/s) and shear wave birefringence (maximium $\Delta V_s=0.38$ km/s). In upper mantle garnet peridotite, the magnitude of these effects will be reduced as a consequence of the reduced proportion of olivine. Nevertheless, the

results of Fig. 9-3 provide a firm semi-quantitative basis for testing of the preferred orientation hypothesis.

The model certainly provides a qualitative explanation of the high compressional wave velocities for approximately N-S propagation at depths of 200-250 km in the Australian upper mantle. The results presented in Fig. 9-3 (see especially $\phi=\theta=22.5°$) suggest that significant shear wave birefringence might also be observed (on both horizontal and vertical components) at appropriate azimuths.

(v) Both the chemistries and textures of deep-seated ultramafic modules contained in kimberlite pipes provide evidence supportive of the view that decoupling of the continental lithosphere and the underlying mantle is concentrated at depths near 200 km (Boyd, 1973). The observation that ultramafic nodules of deepest origin ($\sim$ 200 km), brought to the surface by South African kimberlites varying in age by more than 1000 million years (e.g. Danchin, 1979; MacGregor, 1979), display more primitive chemistry than their shallower counterparts, suggests that the former are derived from a zone of the mantle which is continuously replenished from a large mantle reservoir. Furthermore, while the highly sheared mosaic textures of the deepest-seated xenoliths are probably not representative of steady-state mantle deformation processes (Goetze, 1975), the contrasting fabrics of these and the shallower relatively undeformed coarse-grained xenoliths (e.g. Nicolas and Poirier, 1976) suggest a major discontinuity in the mechanical properties of sub-continental mantle at about 200 km depth.

(v) The combination of more primitive chemistry below 200 km depth and the general characteristics of upper mantle geotherms suggests that the zone between 200 km and $\sim$300 km depth may be characterised by higher homologous temperatures (T/Tm) for olivine than for the shallower and the deeper mantle. Under these circumstances, it is a plausible zone for strain concentration, although the relative roles of dislocation creep - syntectonic recrystallisation (which may be subject to strain hardening) and grain boundary sliding (Chopra and Paterson, 1980) remain to be determined. Anderson (1979b) similarly concludes that the viscosity of sub-continental mantle should attain a minimum value near 200-250 km depth.

9.6 CONCLUSIONS.

The hypothesis that deformation-induced seismic anisotropy is responsible for the high compressional-wave velocities observed near

200-250 km depth in models derived from some continental seismic refraction profiles urgently needs further testing. For example, on the Australian continent, existing seismological data provide only very limited information concerning possible azimuthal variation in the character of the velocity profile near 200 km depth. Although of significantly lower quality than the recent Central Australia Project (Hales et al.,1980), data from the earlier studies (Denham et al.,1972; Simpson, 1973), in which the Ord River explosions were monitored along lines trending approximately NNE-SSW (Ord-Perth), and NNW-SSE (Ord-Adelaide), also provide clear evidence of a major discontinuity in the 150-200 km depth interval. By contrast with this relative abundance of information for approximately N-S profiles, the recording of the Mt Fitton explosion at Meekatharra (Finlayson et al.,1974) is the only published datum suggestive of the observation of the "200 km" discontinuity along an approximately E-W profile. Carefully controlled experiments over a wide range of azimuths (such as those conducted by Raitt et al., (1969) on the sub-oceanic mantle) will be required to test for anisotropy and possible shear wave birefringence of the continental upper mantle.

It may be anticipated, however, that observation of sub-continental upper mantle seismic anisotropy will be subject to considerable variability. Spatial variation of the abundances of key volatile species (such as H_2O), mantle geotherms and strain rates may result in variability of the dominant upper mantle deformation mechanism, with some plausible flow mechanisms (such as grain boundary sliding) having little tendency to produce a strong preferred orientation. Even where an appropriate mechanism (such as dislocation creep - syntectonic recrystallisation) is dominant, the development of an observable seismic anisotropy may be dependent upon a long, consistent and current history of relative motion of the lithospheric plate with respect to underlying mantle.

Such anisotropy beneath both continental and oceanic lithosphere, would facilitate seismic mapping of the vertical extent of the lithosphere, and ultimately provide considerable insight into the rheological behaviour of the upper mantle.

CHAPTER 10

CONCLUSION.

The application of synthetic seismograms has increased dramatically over the past 10 years, and this increase shows no sign of abatement. To date, the emphasis has largely been on those methods which assume a laterally homogeneous structure in the velocity model. However, present indications are that the techniques capable of handling laterally inhomogeneous models will become more general. Techniques such as the Asymptotic Ray theory and the Finite Difference method, which have not been discussed in this thesis, have the ability to handle a generally inhomogeneous medium. However, both these methods suffer from other limitations.

Synthetic seismogram modelling using three dimensional models will present problems associated with the conceptual difficulty of three dimensional wave propagation, quite apart from the increased number of possible models which will have to be investigated. Synthetic seismogram modelling is expensive in terms of time, and often money, and will become more so with this increased range of possible models. If the computation times of synthetic seismograms increases significantly, some cost-benefit analysis will be required to evaluate the necessity of synthetic seismogram refinement of Earth models.

Waveform modelling at long periods is currently proving to be a powerful tool in Earth modelling at the lower resolution of long period waves. It is clear that the application of waveform modelling to short period data will require a greater understanding of the processes of seismic scattering, as scattering obviously contributes fundamentally to the complexity of the short period records. The quantification of this scattering will require a great deal of further work.

There is also a need for faster synthetic seismogram methods, with which trial models can be iteratively corrected. The WKBJ method fills this need to some extent. However, the limits of applicability of these faster methods must be fully understood, and it is only by comparing the results of the application of a variety of methods to the same problem that the validity of the methods can be checked.

BIBLIOGRAPHY

AHRENS, T.J., 1973. Petrological properties of the upper 670 km of the Earth's Mantle: Geophysical Implications. Phys.Earth Planet.Inter., 7, 167-186.

AKAOGI, M. and AKIMOTO, S., 1977. Pyroxene-garnet solid-solution equilibria in the systems $Mg_4Si_4O_{12}$-$Mg_3Al_2Si_3O_{12}$ and $Fe_4Si_4O_{12}$-$Fe_3Al_2Si_3O_{12}$ at high pressures and temperatures. Phys.Earth Planet. Inter., 15, 90-106.

AKAOGI, M. and AKIMOTO, S., 1979. High-pressure phase equilibria in a garnet lherzolite, with special reference to Mg^{2+}-Fe^{2+} partitioning among constituent minerals. Phys.Earth Planet.Inter., 19, 31-51.

ANDERSON, D.L., 1976.

The 650 km mantle discontinuity. Geophys. Res. Lett., 3, 347-349.

ANDERSON, D.L., 1979a. The deep structure of continents. J.Geophys.Res., 84, 7555-7560.

ANDERSON, D.L., 1979b. The upper mantle transition region: eclogite? Geophys.Res.Lett., 6, 433-436.

ANSELL, J.H., 1979. On the decoupling of P and S waves in inhomogenous elastic media. Geophys.J.R.astr.Soc., 59, 399-409.

ARCHAMBEAU, C.B., FLINN, E.A., & LAMBERT, D.G., 1969. Fine structure of the upper Mantle. J.Geophys.Res., 74, 5825-5864.

ASADA, T., & SHIMAMURA, H., 1976. Observations of earthquakes and explosions at the bottom of the western Pacific: structure of oceanic lithosphere revealed by Longshot Experiment. in: The Geophysics of the Pacific Ocean Basin and its Margin. ed. Sutton, G.H., et al., Amer. Geophys. Union Geophys.Monograph., 19, 135-153, AGU, Washington.

AVE'LALLEMANT, H. G., 1975. Mechanisms of preferred orientations of olivine in tectonite peridotite. Geology, 3, 653-656.

AVE'LALLEMANT, H.G., & CARTER, N.L., 1970. Syntectonic recrystallisation of olivine and modes of flow in the upper mantle. Geol.Soc.Amer.Bull., 81, 2203-2230.

BABUSKA, V., FIALA, J., KUMAZAWA, M., OHNO, I., & SUMINO, Y., 1978. Elastic property of garnet solid-solution series. Phys.Earth Planet. Inter., 16, 157-176.

BACKUS, G.E., 1965. Possible forms of seismic anisotropy in the uppermost mantle under oceans. J.Geophys.Res., 70, 3429-3439.

BAMFORD, D., 1973a. Refraction data on Western Germany - a time term interpretation. J.Geophys., 39, 907-927.

BAMFORD, D., 1973b. An example of the iterative approach to time term analysis. Geophys.J.R.astr.Soc., 31, 365-372.

BAMFORD, D., 1976. Mosaic time term analysis. Geophys.J.R.astr.Soc., 44, 433-446.

BAMFORD, D., 1977. Pn velocity anisotropy in a continental upper mantle. Geophys.J.R.astr.Soc., 49, 29-48.

BAMFORD, D.,1978. Interpretation of wide angle reflection travel times in realistic crust-mantle structures. J. Geophys., 44,219-230.

BAMFORD, D., JENTSCH, M., PRODEHL, C., 1979. Pn anisotropy studies in northern Britain and the eastern and western United States. Geophys. J. R. astr. Soc., 57, 397-429.

BATH, M., 1968. Mathematical aspects of seismology. Developments in solid Earth Geopyhsics, 4, Elsevier, Amsterdam.

BIRCH, F., 1969. Density and composition of the upper mantle: first approximation as an olivine layer, in: The earth's crust and upper mantle. ed. Hart, P.J., Amer. Geophys. Union Geophys. Monogr.,13, 18-36, AGU, Washington.

BONCZAR, L.J., GRAHAM, E.K., & WANG, H., 1977. The pressure and temperature dependence of the elastic constants of pyrope. J.Geophys.Res., 82, 2529-2534.

BOYD, F.R., 1973. A pyroxene geotherm. Geochim.Cosmochim.Acta, 37, 2533-2546.

BURDICK, L. J., & HELMBERGER, D. V. 1978. The upper Mantle P velocity structure of the western United States J. Geophys. Res., 83, 1699-1712.

BURDICK, L. J., & ORCUTT, J. A., 1979. A comparsion of the generalized ray and reflectivity methods of waveform synthesis. Geophys. J. R. astr. Soc., 58, 261-278.

BUSSE, F.H., 1979. High Prandtl number convection. Phys.Earth Planet. Int., 19, 149-157.

CAGNIARD, L., 1939. Reflextion et refraction des Ondes seismiques progressives. Gauthier-Villars, Paris.

CAGNIARD, L., FLYNN, E.A., and DIX, C.H., 1962. Reflection and refraction of progressive seismic waves. McGraw-Hill, New York.

CARDWELL, R. K., & ISACKS, B. L., 1978. Geometry of the subducted lithosphere beneath the Banda Sea in Eastern Indonesia from seismicity and fault plane solutions. J. Geophys. Res., 83, 2825-2838.

CERVENY,V., 1979. Accuracy of ray theoretical seismograms. J. Geophys., 46, 135-146.

CHAPMAN, C.H., 1973. The earth flattening transformation in body wave theory. Geophys.J.R.astr.Soc., 35, 55-70.

CHAPMAN, C.H., 1974. Generalized Ray Theory for an inhomogeneous medium. Geophys.J.R.astr.Soc., 36, 573-704.

CHAPMAN, C.H., 1976a. Exact and approximate Generalized Ray Theory in vertically inhomogeneous media. Geophys.J.R.astr.Soc., 46, 201-233.

CHAPMAN, C.H., 1976b. A first motion alternative to geometrical ray theory. Geophys. Res. Letters, 3, 153-156.

CHAPMAN, C.H., 1978. A new method for computing synthetic seismograms. Geophys.J.R.astr.Soc., 54, 481-518.

CHAPMAN, C.H. and PHINNEY, R.A., 1972. Diffracted signals and their numerical solution. In B.A. Bolt (Ed) Seismology: Body waves and sources. (Methods of computational physics Vol 12) Academic Press, New York.

CHERNOV, L.A., 1960. Wave Propagation in a random medium. pp.168. McGraw Hill, New York.

CHOPRA, P.N. and PATERSON, M.S., 1980. The experimental deformation of dunite. Tectonophysics, in press.

CHOY, C, 1977. Theoretical seismograms of core phases calculated by frequency-dependent full wave theory, and their interpretation. Geophys.J.R.astr.Soc., 51, 275-312.

CHOY, G. L., CORMIER, V. F., KIND, R., MULLER, G., & RICHARDS, P. G., 1979. A comparsion of synthetic seismograms of core phases generated by the full wave theory and by the reflectivity methods. Geophys. J. R. astr. Soc., 61, 21-39.

CHRISTENSEN, N.I., 1974. Compressional wave velocities in possible mantle rocks to pressures of 30 kilobars. J.Geophys.Res., 79, 407-412.

CLARK, S.P., & RINGWOOD, A.E., 1964. Density distribution and constitution of the mantle. Revs.Geophys., 2, 35-88.

CLEARY, J., 1973. Australian crustal structure. Tectonophysics, 20, 241-248.

COLLINS, C.D.N., 1978. Central structure of the central Bowen Basin, Queensland. BMR Jour. of Australian Geol. and Geophys, 3, 203-209.

CONNELLY, J.B., and COLLINS, C.D.N., 1973. Bowen Basin seismic refraction survey, May-June, 1973: Operational report. BMR, Australia, Record 1973/212, unpublished.

CORMIER, V.F., and RICHARDS, P.G., 1977. Full wave theory applied to a

discontinous velocity increase: the inner core boundary. J.Geophys., 43, 3-31.

CRAMPIN, S., 1977. A review of the effects of anisotropic layering on the propagation of seismic waves. Geophys.J.R.astr.Soc., 49, 9-27.

CUNNINGHAM, A.B., 1974. Refraction data from single ended refraction profiles. Geophysics, 39, 292-301.

DANCHIN, R.V., 1979. Mineral and bulk chemistry of garnet lherzolite and garnet harzburgite xenoliths from the Premier mine, South Africa, pp.104-126, in: The mantle sample: inclusions in kimberlites and other volcanics, Ed. F.R. Boyd and H.O.A. Meyer, American Geophysical Union, Washington.

DE HOOP, A.T., 1960. A modification of Cagniard's method for solving seismic pulse problems. Appl.Sci.Res., Section B, 8, 349-356.

DENHAM, D., SIMPSON, D.W., GREGSON, P.J., & SUTTON, D.J.,1972. Travel times and amplitudes from explosions in Northern Australia. Geophys. J. R. astr. Soc., 28, 225-235.

DEY-SARKAR, S.K., and CHAPMAN, C.H., 1978. A simple method for the computation of body wave seismograms. Bull.Seism.Soc.Am., 68, 1577-1593.

DICKENS, J.M., & MALONE, E.J., 1973. Geology of the Bowen Basin, Queensland. BMR Bull. 130.

DOBRIN, M.B., 1960. Introduction to Geophysical Prospecting. McGraw-Hill, New York.

DOOLEY, J.C., 1976. Variations in crustal mass over the Australian region. BMR Jour.of Australian Geol. & Geophys., 1, 291-296.

DUNKIN, J.W., 1965. Computation of modal solutions in layered elastic media at high frequencies. Bull.Seism.Soc.Am., 55, 335-358.

DZIEWONSKI, A. M., & ANDERSON, D. L., 1979. A proposal for an interim Reference Earth Model. Working Paper, IASPEI Commission on Reference Earth Models.

FINLAYSON, D.M., 1968. First arrival data from the Carpentaria region upper mantle project (CRUMP). J.Geol.Soc.Aust., 15, 33-50.

FINLAYSON, D.M., CULL, J.P., & DRUMMOND, B.J., 1974. Upper mantle structure from the Trans-Australia seismic survey (TASS) and other seismic refraction data. J. Geol. Soc. Aust., 21, 447-458.

FINLAYSON, D.M., COLLINS, C.D.N., and DENHAM, D., 1980. Crustal structure under the Lachlan Fold Belt, Southeastern Australia. Phys.Earth.Planet.Inter., 21, 321-342.

FRISILLO, A.L., & BARSCH, G.R., 1972. Measurement of single-crystal

elastic constants of bronzite as a function of pressure and temperature. J.Geophys.Res., 77, 6360-6384.

FUCHS, K., 1968. Das Reflexions und Transmission-sver-mogen eines geschichteten Mediums mit beliebiger Tiefen-Verteilung der elastichen Moduln und der Dichte für schragen Einfall ebener Wellen. J.Geophys., 34, 389-413.

FUCHS, K., and MULLER, G., 1971. Computation of synthetic seismograms with the Reflectivity method, and comparison with observations. Geophys.J.R. astr.Soc., 23, 417-433.

FUCHS, K., & SCHULZ, K., 1976. Tunnelling of low frequency waves through the sub-crustal lithosphere. J. Geophys., 42, 175-190.

GERVER, M. L., & MARKUSHEVICH, V. M., 1966. Determination of a seismic wave velocity from the travel time curve. Geophys. J., 11, 165-173.

GIESE, P., 1978. Models of crustal structure and the main wave groups. in: Explosion seismology in Central Europe, Data and results. European Seismological Commission, Monograph 1, Springer-Verlag, Berlin.

GIESE, P., PRODEHL, C., SCHRODER, H., & STEIN, A., 1978. Presentation of record sections. in: Explosion seismology in Central Europe, Data and results. European Seismological Commission, Monograph 1, Springer-Verlag, Berlin.

GILBERT, F., and HELMBERGER, D.V., 1972. Generalized Ray Theory for a layered sphere. Geophys.J.R.astr. Soc., 27, 57-80.

GOETZE, C., 1975. Sheared lherzolites: From the point of view of rock mechanics. Geology, 3, 172-173.

GOETZE, C., 1977. A brief summary of our present day understanding of the effect of volatiles and partial melting on the mechanical properties of the uppper Mantle. in: High pressure Research, Applications in geophysics, (ed. Manghnan and Akimoto) ACADEMIC PRESS, New York.

GRAHAM, E.K., 1970. Elasticity and composition of the upper mantle. Geophys.J.Roy. astr.Soc., 20, 285-302.

GRAHAM, E.K., & BARSCH, G.R., 1969. Elastic constants of single-crystal forsterite as a function of temperature and pressure. J.Geophys.Res., 74, 5949-5960.

GRAHAM, E. K., & DOBRZYROWSKI, D., 1976. Temperatures in the Mantle as infered from simple compositional models. Am. Mineralogist, 61, 549-559.

GRANT, F.S. and WEST, G.F., 1965. Interpretation theory in applied geophysics. McGraw-Hill, New York.

GREEN, D.H. and LIEBERMANN, R.C., 1976. Phase equilibria and elastic

properties of a pyrolite model for the oceanic upper mantle. Tectonophysics, 32, 61-92.

GREEN, D.H., & RINGWOOD, A.E., 1967. The stability fields of aluminous pyroxene peridotite and garnet peridotite and their relevance in upper mantle structure. Earth Planet.Sci.Letts., 3, 151-160.

GRIFFITHS, R.W., 1979. The transport of multiple components through thermohaline diffusive interfaces. Deep-Sea Research, 26A, 383-397.

GUTENBERG, B., 1953. Wave velocities between 50 and 600 kilometres. Bull.Seism.Soc.Am., 3, 223-232.

HALES, A.L., 1977. Director's Report, Research School of Earth Sciences Annual Report, 1977. Australian National University, Canberra, unpublished.

HALES, A.L., HELSLEY, C.E., & NATION, J.B., 1970. P travel times for an oceanic path. J.Geophys.Res., 75, 7362-7381.

HALES, A. L., MUIRHEAD, K. J., RYNN, J. M., & GETTRUST, J. F., 1975. Upper mantle travel times in Australia - a preliminary report. Phys. Earth Planet. Inter., 11, 109-118.

HALES, A. L., & RYNN, J. M. W., 1978. A long range controlled source seismic profile in northern Australia. Geophys. J. R. astr. Soc., 55, 633-644.

HALES, A.L., MUIRHEAD, K.J., & RYNN, J.M.W., 1980a. A compressional velocity distribution for the upper mantle. Tectonophysics, 63, 309-348.

HALES, A.L., MUIRHEAD, K.J., & RYNN, J.M.W., 1980b. Crust and upper mantle shear wave velocities from controlled sources. Submitted to Geophys. J. Roy.astr.Soc.

HARKRIDER, D.G., 1964. Surface waves in multilayered elastic media. 1. Rayleigh and Love waves from buried sources in a multi layered elastic halfspace. Bull.Seism.Soc.Am., 54, 627-679.

HASKELL, N.A., 1953. The dispersion of surface waves on multilayered media. Bull.Seism.Soc.Am., 43, 17-34.

HARTE, B., 1978. Kimberlite nodules, upper mantle petrology, and geotherms. Phil.Trans.R.Soc.Lond., A.288, 487-500.

HELMBERGER, D.V., 1968. The crust mantle transition in the Bering Sea. Bull.Seism.Soc.Am., 58, 179-214.

HELMBERGER, D.V., & WIGGINS, R.A., 1971. Upper Mantle structure of midwestern United States. J.Geophys.Res., 76, 3229-3245.

HELMBERGER, D.V., & BURDICK, L.J., 1979. Synthetic seismograms. Ann. Rev. Earth Planet. Sci., 7, 417-442.

HESS, H., 1964. Seismic anisotropy in the uppermost mantle under oceans. Nature, 203, 629-631.

HILL, D.P., 1972. An earth flattening transformation for waves from a point source. Bull.Seism.Soc.Am., 62, 1195-1210.

HOWARD, L.N., 1966. Convection at high Raleigh number. In: H. Gorton (Editor) Proc. 11th Int.Congr.of Applied Mechanics, Munich, 1964. Springer, Berlin, 166pp, 109-115.

JARVIS, K., & McKENZIE, D.P., 1980. Convection in a compressible fluid with infinite Prandtl number. J.Fluid Mechanics, 96, 515-583.

JOHNSON, L.R., 1967. Array measurements of P velocities in the upper mantle. J.Geophys.Res., 72, 6309-6325.

JOHNSON, L.R., 1974. Green's Function for Lambs problem. Geophys.J.R.astr. Soc., 37, 99-131.

JORDAN, T.H., 1975. The continental tectosphere. Rev.Geophys.Space Phys.,13,1-12

JORDAN, T.H., 1978. Composition and development of continental tectosphere. Nature, 274, 544-548.

JORDAN, T.H., 1979. Mineralogies, densities, and seismic velocities of garnet lherzolites and their geophysical implications. in: The mantle sample: inclusions in kimberlites and other volcanics. ed. F.R. Boyd and H.O.A. Meyer, Amer. Geophys. Union, Washington.

KANAMORI, H., & MIZUTANI, H., 1965. Ultrasonic measurement of elastic constants of rocks under high pressures. Bull.Earthquake Res.Inst., 43, 173-194.

KENNETT, B.L.N., 1975. The effects of attenuation on seismograms. Bull.Seism.Soc.Am., 65, 1643-1651.

KENNETT, B.L., 1977. The inversion of long range seismic profiles. J. Geophys., 43, 243-256.

KIND, R., 1976. Computation of Reflection coefficients for layered media. J.Geophys., 42, 191-200.

KIND, R., 1978. The reflectivity method for a buried source. J.Geophys., 44, 603-612.

KIND, R., 1979. Extensions of the Reflectivity Method. J.Geophys., 45, 373-380.

KING, D. W. & CALCAGNILE, G., 1976 P-wave velocities in the upper Mantle beneath Fennoscandia and Western Russia. Geophys. J. R. astr. Soc., 46, 407-432.

KNOPOFF, L., 1964. A matrix method for elastic wave problems. Bull.Seism.

Soc.Am., 54, 431-438.

KUMAZAWA, M., & ANDERSON, O.L., 1969. Elastic moduli, pressure derivatives and temperature derivatives of single-crystal olivine and single-crystal forsterite. J.Geophys.Res., 74, 5961-5972.

LANGER, R.E., 1951. Asymptotic solutions of a differential equation in the theory of microwave propagation. Comm. Pure Applied Math., 3, 427-438.

LEEDS, A.R., KNOPOFF, L., KAUSEL, E.G., 1974. Variations of the upper mantle structure under the Pacific Ocean. Science, 186, 141-143.

LEEDS, A.R., 1975. Lithospheric thickness in the western Pacific. Phys. Earth Planet. Inter., 11, 61-64.

LEHMANN, I., 1959. Velocities of longitudinal waves in the upper part of the earth's mantle. Ann.Geophys., 15, 93-118.

LEHMANN, I., 1962. The travel times of the longitudinal waves of the Logan and Blanca atomic explosions, and their velocities in the upper mantle. Bull.Seism.Soc.Am., 52, 519-526.

LEWIS, B.T.R., & MEYER, R.P., 1968. A seismic investigation of the upper mantle to the west of Lake Superior. Bull.Seism.Soc.Am., 58, 565-596.

LIEBERMANN, R. C.,1979 Elasticity of the Mantle. in; The Earth: its Origin, Structure, and Evolution. Ed. McElhinny. ACADEMIC PRESS, New York.

LINDEN, P.F., & SHIRTCLIFFE, T.C.L., 1978. The diffusive interface in a double-diffusive convection. J.Fluid Mech., 87, 417-432.

LIU, LIN-GUN, 1977a. The system Enstatite-Pyrope at high pressure and temperature, and the mineralogy of the Earth's Mantle. Earth & Planet. Sci. Letters, 36, 237-245.

LIU, LIN-GUN, 1977b. Mineralogy and chemistry of the Earth's Mantle above 1000 km. Geophys. J. R. astr. Soc., 48, 53-62.

LIU, LIN-GUN, 1979a. Calculations of high pressure phase transformations in the system MgO-SiO_2 and implications for the Mantle discontinuities. Phys. Earth & Planet. Int., 19, 319-330.

LIU, LIN-GUN, 1979b. On the 650 km seismic discontinuity. Earth & Planet. Sci. Letters, 42, 202-208.

LIU, LIN-GUN, 1980a. Phase transformations and the constitution of the deep Mantle. in; The Earth: its Origin, Structure, and Evolution. Ed. McElhinny. ACADEMIC PRESS, New York.

LIU, LIN-GUN, 1980b. The pyroxene garnet transformation and its implication for the 200 km discontinuity. in press.

LIU, LIN-GUN, 1980c. On the interpretation of Mantle discontinuities. Phys. Earth Planet. Inter. (in press)

LONGMAN, I.M., 1970. Computation of theoretical seismograms. Geophys.J. R.astr.Soc., 21, 295-305.

MALONE, E.J., 1964. Depositional environment of the Bowen Basin. J. Geol. Soc. Aust., 11, 263-282.

MALONE, E.J., 1966. Fitroy region, Queensland, Resource series. Dept. Nat. Development.

MANGHNANI, M.H., RAMANANANTOANDRO, R., & CLARK, S.P.,1974. Compressional and shear wave velocities in granulite facies rocks and eclogites to 10 kbar. J.Geophys.Res., 79, 5427-5446.

MASSE, R.P., LANDISMAN, M., & JENKINS, J.B., 1972. An investigation of the upper mantle compressional velocity distribution beneath the Basin and Range Province. Geophys.J.Roy. astr.Soc., 30, 19-36.

MacGREGOR, I.D., 1979. Mafic and ultramafic xenoliths from the Kao kimberlite pipe, pp.156-172, in: The mantle sample: inclusions in kimberlites and other volcanics. ed. F.R. Boyd and H.O.A. Meyer, Amer. Geophys. Union, Washington.

McMECHAN, G. A., 1979. An amplitude constrained P-wave velocity profile for the upper mantle beneath the eastern United States. Bull. Seism. Soc. Am. 69, 1733-1744.

MELLMAN, G.R., 1978. A method for waveform inversion of bodywave seismograms. Ph.D. Thesis, Calif.Inst.Technology, unpublished.

MEREU, R.F., SIMPSON, D.W., & KING, D.W., 1974. Q and its effect on the observations of upper mantle travel time branches. Earth Planet.Sci. Letters, 21, 439-447.

MUIRHEAD, K. J., 1968. Eliminating false alarms when detecting seismic events automatically. Nature, 186, 706.

MUIRHEAD, K.J., & SIMPSON, D.W., 1972. A three quarter Watt seismic station. Bull. Seis. Soc. Am., 62, 985-990.

MUIRHEAD, K. J., & RAM DATT, 1976. The Nth root process applied to seismic array data. Geophys. J. R. astr. Soc., 47, 197-210.

MULLER, G., 1977. Earth-flattening approximation for body waves derived from geometrical ray theory-improvements, corrections, and range of applicability. J.Geophys., 42, 429-436.

NAYFEH, A.H., 1973. Perturbation methods. Wiley, New York.

NICOLAS, A., BOUDIER, F., and BOULLIER, A.M., 1973. Mechanisms of flow in naturally and experimentally deformed peridotites. Am. J. Sci., 273,

853-876.

NICOLAS, A., & POIRIER, J.P., 1976. Crystalline plasticity and solid-state flow in metamorphic rocks, 444pp. Wiley-Interscience, London, 1976.

O'NEILL, M.E., and HILL, D.P., 1979. Causal absorption: its effect on synthetic seismograms computed by the reflectivity method. Bull.Seism. Soc.Am., 69, 17-25.

PAO, Y., and GAJEWSKI, R.R., 1977. The Generalized Ray Theory and transient responses to layered elastic solids. Physical Acoustics, ed. Mason, W.P., and Thurston, R.N., Vol.XIII, pp.183-265.

PESELNICK, L., NICOLAS, A., & STEVENSON, P.R., 1974. Velocity anisotropy in a mantle peridotite from the Ivrea zone: application to upper mantle anisotropy. J.Geophys.Res., 79, 1175-1182.

PILANT, W.L., 1979. Elastic Waves in the Earth. Developments in Solid Earth Geophysics 11. Elsevier Sci.Publ.Co., Amsterdam.

PHINNEY, R.A. and ALEXANDER, S., 1966. P wave diffraction theory and the structure of the core mantle boundary. J. Geophys. Res., 71, 5943-5958.

PHINNEY, R.A., CHOWDHURY, K.R., FRAZER, L.N., 1979. Transformation and analysis of record sections. Abs IUGG IASPEI, Dec 1979.

PILANT, W., 1979. Elastic Waves in the Earth. Developments in Solid Earth Geophysics No. 11, Elsevier, Amsterdam.

RAITT, R.W., SHOR, G.G, FRANCIS, T.J.G., & MORRIS, G.B., 1969. Anisotropy of the Pacific upper mantle. J.Geophys.Res., 74, 3095-3106.

RAM DATT & MUIRHEAD, K. J., 1977. Evidence of multiphases in the P-travel time curve beyond 30 degrees. Phys. Earth Planet. Inter., 15, 28-38.

RICHARDS, P. G., 1973. Calculation of body waves for caustics and tunnelling in core phases. Geophys. J. R. astr. Soc., 35, 243-264.

RICHARDS, P.G., 1974. Weakly coupled potentials for high frequency elastic waves in continuously stratified media. Bull.Seism.Soc.Am., 64, 1575-1588.

RICHARDS, P.G., 1976. On the adequacy of plane wave reflection/transmission coefficients in the analysis of seismic body waves. Bull.Seism. Soc.Am., 66,701-717.

RINGWOOD, A.E., 1966. The chemical composition and origin of the earth, pp.287-356, in: Advances in earth science (P. Hurley, Ed.), M.I.T. Press, Cambridge, Massachusetts.

RINGWOOD, A.E., 1967. The pyroxene-garnet transformation in the earth's mantle. Earth Planet.Sci.Lett., 2, 255-263.

RINGWOOD, A.E., 1975. Composition and petrology of the earth's mantle, 604

pp, McGraw Hill, New York.

SACKS, I.S., SNOKE, J.A., HUSEBYE, E.S., 1979. Lithosphere thickness beneath the Baltic Shield. Tectonophysics, 56, 101-110.

SCHEIBNER, E., 1974. Fossil fracture zones segmentation, and correlation problems in the Tasman Fold Belt System. Denmead, A.K., Tweedale, G.W., and Wilson, A.F., eds., The Tasman Geosyncline, - a symposium. Geol. Soc.Aust., Qld. Div.

SCHEIDEGGER, A.E., and WILLMORE, P.L., 1957. The use of a least square method for the interpretation of data from seismic surveys. Geophysics, 22, 9-22.

SCHOLTE, J.G.J., 1956. On seismic waves in a spherical earth. Koninkl. Med.Meteorol.Inst.Publ. 65, 1-55.

SHIRLEY, J.E., 1979. Crustal structure of north Queensland from gravity anomalies. BMR J. Aust. Geol. Geophys., 4, 309-321.

SIMPSON, D.W., 1973. Ph. D. Thesis, Australian National University. (unpublished 1973).

SIMPSON, D.W., MEREU, R.F., & KING, D.W., 1974. An array study of P wave velocities in the upper mantle transition zone beneath northeastern Australia. Bull. Seis. Soc Am., 64, 1757-1788.

SMITH, P.J., 1980. The case for layered convection. Nature, 283, 524.

SPENCER, T., 1960. The method of generalized reflection and transmission coefficients. Geophysics, 25, 625-641.

STEVENSON, D.J. & TURNER, J.S., 1979. Fluid models of mantle convection. In: The Earth: its origin, structure and evolution. ed. M.W. McElhinny, p.227-263.

TATEL, H.E., & TUVE, M.A., 1955. Seismic exploration of a continental crust. Geol. Soc. Am. Spec. Paper 62, 35-50.

THOMPSON, W.T., 1950. Transmission of elastic waves through a stratified medium. J.Appl.Phys., 21, 89-93.

VAN DER MOLEN, I., 1979. Some physical properties of granite at high pressures and temperatures. Ph. D. Thesis, Australian National University, unpublished.

WARREN, D.H., HEALY, J.H., HOFFMANN, J.C., KEMPE, R., RAUULA, S., & STUART, D.J., 1968. Project Early Rise, travel times and amplitudes. U.S.Geological Survey Open File Report, 150 pp., Menlo Park, California.

WEBB, A.W., 1969. Metallogenic Epochs in eastern Queensland. Proc. Aust. Inst. Min. Met., 230, 29-36.

WHITCOMBE, D.N. and MAGUIRE, P.K.H., 1979. The response of the time term

method to simulated crustal structures. Bull. Seis. Soc. Am., 69, 1455-1473.

WIGGINS, R.A., 1976. Body wave amplitude calculations II. Geophys. J. R. astr. Soc., 46, 1-10

WIGGINS, R.A., & HELMBERGER, D.V., 1973. Upper mantle structure of western United States. J.Geophys. Res., 78, 1870-1880.

WIGGINS, R. A., & HELMBERGER, D. V., 1974. Synthetic seismograms computation by expansion in generalized rays. Geophys. J. R. astr. Soc., 37, 73-90.

WIGGINS, R.A., and MADRID, J.A., 1974. Body wave amplitude calculations. Geophys. J. R. astr. Soc., 37, 423-433.

WILL, M., 1978. Calculation of travel times and ray paths for lateral inhomogeneous media. in: Explosion seismology in Central Europe, Data and results. European Seismological Commission, Monograph 1, Springer-Verlag, Berlin.

WILLMORE, P.L., 1969. Comments on how necessary are large-scale refraction experiments? Geophys.J.R.astr.Soc., 18, 227.

WILLMORE, P.L., and BANCROFT, A.M., 1960. The time term approach to refraction seismology. Geophys.J.R.astr. Soc., 3, 419-432.

YAGI, T., MAO, H. K., & BELL, P. M., 1978. Structure and crystal chemistry of perovskite-type $MgSiO_3$. Phys. Chem. Minerals, 3, 97-110.